### PROGRESS IN BIOMEDICAL OPTICS AND IMAGING

Vol. 2, No. 16 ISSN 1605-7422

## Biomarkers and Biological Spectral Imaging

Gregory H. Bearman Darryl J. Bornhop Richard M. Levenson Chairs/Editors

23 January 2001 San Jose, USA

Sponsored by U.S. Air Force Office of Scientific Research SPIE—The International Society for Optical Engineering

### **DISTRIBUTION STATEMENT A**

Approved for Public Release Distribution Unlimited

Proceedings of SPIE Volume 4259

20030106 110

#### REPORT DOCUMENTATION PAGE AFRL-SR-AR-TR-02-Public reporting burden for this collection of information is estimated to everage 1 hour per response, including the ting gathering and instituting the date needed, and completing and reviewing the collection of information. Send common in information, including suggestions for reducing this burden to Westington Headquestern Service, Directorate for in 1215 Juliana Device Highway, Suble 1204, Artington, VA 22202-4302, and to the Office of Management and Budget Paperwork Reduction Project (0704-0185) Weshington, DC 20503. 0427 PLEASE DO NOT RETURN YOUR FORM TO THE ABOVE ADDRESS. 3. DATES COVERED (From - To) 1. REPORT DATE (DD-MM-YYYY) 2. REPORT DATE 18-01-2001 - 17-01-2002 17-07-2002 Final Technical Report 4. TITLE AND SUBTITLE 54. CONTRACT NUMBER 56. GRANT NUMBER Biomarkers and Biological Spectral Imaging F49620-01-1-0153 5c. PROGRAM ELEMENT NUMBER 5d. PROJECT NUMBER 6. AUTHOR(S) 50. TASK NUMBER Gregory H. Bearman Darryl J. Bornhop Richard M. Levenson 51. WORK UNIT NUMBER 8. PERFORMING ORGANIZATION 7. PERFORMING ORGANIZATION NAME(S) AND ADDRESS(ES) REPORT NUMBER Society of Photo-Optical Instrumentation Engineers Volume 4259 PO Box 10 Bellingham, WA 98227-0010 10. SPONSOR/MONITOR'S ACRONYM(S) 9. SPONSORING/MONITORING AGENCY NAME(S) AND ADDRESS(ES) Air Force Office of Scientific Research AFOSR/NL 11. SPONSORING/MONITORING 801 N. Randolph Street, Room 732 AGENCY REPORT NUMBER Arlington, VA 22203-1977 12. DISTRIBUTION AVAILABILITY STATEMENT Approved for Public Release 13. SUPPLEMENTARY NOTES ISBN 0-8194-3937-1 14. ABSTRACT This proceedings contains papers on the following topics: spectral imaging data, multivariate data processingexogenous optical contrast agents, imaging of ions and metabolites by fluorescence microscopy. 15. SUBJECT TERMS biomedical optics 18. NUMBER 19a. NAME OF RESPONSIBLE PERSON OF PAGES 16. SECURITY CLASSIFICATION OF: 17. LIMITATION OF a. REPORT b. ABSTRACT |C. THIS PAGE Janice Gaines Walker

Standard Form 298 (Rev. 8-98) Prescribed by ANSI-Sid Z39-18

19b. TELEPONE NUMBER (Include area code)

(360)676 - 3290

166

SAR

Non-

lassfied

### PROGRESS IN BIOMEDICAL OPTICS AND IMAGING

Vol. 2, No. 16

# Biomarkers and Biological Spectral Imaging

Gregory H. Bearman Darryl J. Bornhop Richard M. Levenson Chairs/Editors

23 January 2001 San Jose, USA

Sponsored by U.S. Air Force Office of Scientific Research SPIE—The International Society for Optical Engineering

Published by SPIE—The International Society for Optical Engineering

Proceedings of SPIE Volume 4259

SPIE is an international technical society dedicated to advancing engineering and scientific applications of optical, photonic, imaging, electronic, and optoelectronic technologies.



The papers appearing in this book compose the proceedings of the technical conference cited on the cover and title page of this volume. They reflect the authors' opinions and are published as presented, in the interests of timely dissemination. Their inclusion in this publication does not necessarily constitute endorsement by the editors or by SPIE. Papers were selected by the conference program committee to be presented in oral or poster format, and were subject to review by volume editors or program committees.

Please use the following format to cite material from this book:

Author(s), "Title of paper," in *Biomarkers and Biological Spectral Imaging*, Gregory H. Bearman, Darryl J. Bornhop, Richard M. Levenson, Editors, Proceedings of SPIE Vol. 4259, page numbers (2001).

ISSN 1605-7422 ISBN 0-8194-3937-1

Published by SPIE—The International Society for Optical Engineering P.O. Box 10, Bellingham, Washington 98227-0010 USA Telephone 1 360/676-3290 (Pacific Time) • Fax 1 360/647-1445 http://www.spie.org/

Copyright© 2001, The Society of Photo-Optical Instrumentation Engineers.

Copying of material in this book for internal or personal use, or for the internal or personal use of specific clients, beyond the fair use provisions granted by the U.S. Copyright Law is authorized by SPIE subject to payment of copying fees. The Transactional Reporting Service base fee for this volume is \$15.00 per article (or portion thereof), which should be paid directly to the Copyright Clearance Center (CCC), 222 Rosewood Drive, Danvers, MA 01923 USA. Payment may also be made electronically through CCC Online at http://www.directory.net/copyright/. Other copying for republication, resale, advertising or promotion, or any form of systematic or multiple reproduction of any material in this book is prohibited except with permission in writing from the publisher. The CCC fee code is 1605-7422/01/\$15.00.

Printed in the United States of America.

#### **Contents**

vii	Conference	Committees
VII	Comerence	Committees

#### Part A Spectral Imaging: Instrumentation, Applications, and Analysis

### SESSION 1 NEW INSTRUMENTATION TO OBTAIN SPECTRAL IMAGING DATA, INCLUDING CALIBRATION TECHNIQUES AND IMPLEMENTATION OF MATCHED FILTER IMAGING

- Beyond image cubes: an agile lamp for practical 100% photon-efficient spectral imaging [4259-02]
  - P. J. Miller, R. M. Levenson, Cambridge Research & Instrumentation, Inc. (USA)
- Compact hyperspectral imager for low-light applications [4259-03]
   P. Herman, Univ. of Maryland/Baltimore (USA) amd Charles Univ. (Czech Republic);
   H. M. Malak, W. E. Moore, Microcosm, Inc. (USA); J. Vecer, Charles Univ. (Czech Republic)
- Signal-to-noise analysis of various imaging systems [4259-05]
   P. J. Miller, Cambridge Research & Instrumentation, Inc. (USA); A. R. Harvey, Cranfield Univ. (UK)

### SESSION 2 MULTIVARIATE DATA PROCESSING AND ANALYSIS ALGORITHMS, CLASSIFICATION, AND MATCHED FILTERING

- Cancer screening through the use of enhanced visual systems [4259-07]
  U. Utzinger, M. Bueeler, Univ. of Texas at Austin (USA); D. L. Heintzelman, Indiana Univ. School of Medicine (USA); A. Gillenwater, Univ. of Texas M.D. Anderson Cancer Ctr. (USA); R. R. Richards-Kortum, Univ. of Texas at Austin (USA)
- Virtual reality techniques for the visualization of biomedical imaging data [4259-09] M. A. Shaw, W. B. Spillman, Jr., K. E. Meissner, J. Gabbard, Virginia Polytechnic Institute and State Univ. (USA)
- Cellular automata for the analysis of biomedical hyperspectral images [4259-10]
   W. B. Spillman, Jr., K. E. Meissner, S. C. Smith, S. Conner, R. O. Claus, Virginia Polytechnic Institute and State Univ. (USA)
- Near-infrared spectroscopic approach to assess tissue viability following a thermal injury [4259-11]
   L. Leonardi, M. G. Sowa, J. R. Payette, M. D. Hewko, B. J. Schattka, A. Matas, H. H. Mantsch, National Research Council Canada

### SESSION 3 APPLICATIONS IN CELL BIOLOGY, PATHOLOGY, CYTOGENETICS, GFP, RETINAL IMAGING, OPTICAL BIOPSY, AND PHARMACOLOGY

- Combined spectroscopic imaging and chemometric approach for automatically partitioning tissue types in human prostate tissue biopsies [4259-12]

  A. S. Haka, National Institutes of Health (USA) and Massachusetts Institute of Technology (USA); L. H. Kidder, Spectral Dimensions, Inc. (USA); E. N. Lewis, Spectral Dimensions, Inc. (USA) and National Institutes of Health (USA)
- 56 Spectral karyotyping (SKY) in hematological neoplasia [4259-13]
  B. S. Preiss, R. K. Pedersen, G. B. Kerndrup, Odense Univ. Hospital (Denmark)
- 60 Structure of mouse spleen investigated by 7-color fluorescence imaging [4259-15]
  H. Tsurui, Juntendo Univ. School of Medicine (Japan) and CREST/Japan Science and
  Technology Corp.; S. Niwa, Sumitomo Electric Industries, Ltd. (Japan); S. Hirose, Juntendo
  Univ. (Japan); K. Okumura, Juntendo Univ. School of Medicine (Japan) and CREST/Japan
  Science and Technology Corp.; T. Shirai, Juntendo Univ. School of Medicine (Japan)
- Multimodal multispectral imaging of the cervix in vivo for the detection of neoplasia
   [4259-17]
   A. Agrawal, T. Harrell, S. B. Bambot, M. Faupel, SpectRx, Inc. (USA); D. Ferris, Medical College of Georgia (USA)
- 75 Skin hydration imaging using a long-wavelength near-infrared digital camera [4259-18] M. Attas, T. Posthumus, B. J. Schattka, M. G. Sowa, H. H. Mantsch, National Research Council Canada; S. L. Zhang, Unilever Research (USA)
- Brain tissue charcterization using spectral imaging: a potential clinical tool [4259-19]
  A. Mahadevan-Jansen, J. D. Mongin, E. D. Jansen, D. Pedrotty, W.-C. Lin, Vanderbilt Univ. (USA)

#### Part B Molecular Probes and Dyes

#### SESSION 4 EXOGENOUS OPTICAL CONTRAST AGENTS

- 92 Influence of the refractive index on EGFP fluorescence lifetimes in mixtures of water and glycerol [4259-20]
  K. Suhling, D. M. Davis, Z. Petrášek, J. Siegel, D. Phillips, Imperial College of Science, Technology and Medicine (UK)
- Time-domain measurement of fluorescence lifetime variation with pH [4259-21]
  A. G. Ryder, S. Power, T. J. Glynn, J. J. Morrison, National Univ. of Ireland
- New approach to optical imaging of tumors [4259-23]
  S. A. Achilefu, J. E. Bugaj, R. B. Dorshow, H. N. Jimenez, R. Rajagopalan, Mallinckrodt, Inc. (USA)
- Monoclonal antibody-tagged receptor-targeted contrast agents for detection of cancers [4259-26]
   N. S. Soukos, M. R. Hamblin, T. F. Deutsch, T. Hasan, Massachusetts General Hospital/Harvard Medical School (USA)

R. Rajagopalan, S. A. Achilefu, H. N. Jimenez, E. G. Webb, M. A. Schmidt, J. E. Bugaj, R. B. Dorshow, Mallinckrodt, Inc. (USA)

IMAGING OF IONS AND METABOLITES BY FLUORESCENCE MICROSCOPY/SPECTROSCOPY

Dimensions of calcium release domains in frog skeletal muscle fibers [4259-22]
J. L. Vergara, M. DiFranco, D. Novo, Univ. of California/Los Angeles School of Medcine (USA)

Fluorescent pH probes, fluorescent proteins, and intrinsic cellular fluorochromes are tools to study cytosolic pH (pH<sup>cyt</sup>) in mammalian cells [4259-35]
G. M. Martinez, Texas Tech Univ. (USA); L. S. Gollahon, Texas Tech Univ. (USA) and Southwest Cancer Ctr. (USA); R. Martínez-Zaguilán, Texas Tech Univ. (USA) and Southwest Cancer Ctr. (USA)

Usefulness of indocyanine green as an infrared marker [4259-36]

Y. Fukami, M. Heya, K. Awazu, Osaka Univ. (Japan)

Targeted Type 1 phototherapeutic agents using azido-peptide bioconjugates [4259-37]

129

163

166

Addendum

Author Index

#### **Conference Committees**

#### Part A Spectral Imaging: Instrumentation, Applications, and Analysis

Conference Chairs

**Gregory H. Bearman,** Jet Propulsion Laboratory (USA) **Richard M. Levenson,** Cambridge Research & Instrumentation, Inc. (USA)

#### Program Committee

Scott E. Fraser, California Institute of Technology (USA)
Yuval Garini, Applied Spectral Imaging (Israel)
E. Neil Lewis, Spectral Dimensions, Inc. (USA)
Urs Utzinger, University of Texas at Austin (USA)

#### Session Chairs

- New Instrumentation to Obtain Spectral Imaging Data, including Calibration Techniques and Implementation of Matched Filter Imaging Gregory H. Bearman, Jet Propulsion Laboratory (USA) Yuval Garini, Applied Spectral Imaging (Israel)
- 2 Multivariate Data Processing and Analysis Algorithms, Classification, and Matched Filtering

E. Neil Lewis, Spectral Dimensions, Inc. (USA)

Applications in Cell Biology, Pathology, Cytogenetics, GFP, Retinal Imaging, Optical Biopsy, and Pharmacology
Scott E. Fraser, California Institute of Technology (USA)
Richard M. Levenson, Cambridge Research & Instrumentation, Inc. (USA)
Urs Utzinger, University of Texas at Austin (USA)

#### Part B Molecular Probes and Dyes

Conference Chair

Darryl J. Bornhop, Texas Tech University (USA)

#### Program Committee

Samuel A. Achilefu, Mallinckrodt, Inc. (USA)
Raul Martinez-Zaguilan, Texas Tech University Health Sciences Center (USA)

#### Session Chairs

- 4 Exogenous Optical Contrast Agents
  Samuel I. Achilefu, Mallinckrodt, Inc. (USA)
- Imaging of Ions and Metabolites by Fluorescence Microscopy/Spectroscopy

  Raul Martinez-Zaguilan, Texas Tech University Health Sciences Center (USA)

# Beyond image cubes: an agile lamp for practical, 100% photon-efficient spectral imaging

Peter J. Miller, Richard M Levenson, Cambridge Research & Instrumentation, Inc. 35-B Cabot Rd, Woburn MA 01801

#### **ABSTRACT**

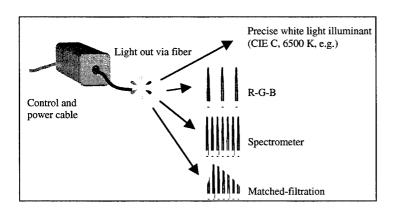
Hardware for obtaining spectral image cubes using filters or interferometers, though capable of revealing subtle aspects of composition, is typically expensive, bulky, slow, and often provides poor spatial resolution. In addition, a great deal of computer processing is needed to extract information from the raw data: interferometers must perform FFTs on megapixel data sets; all approaches involve calculations of spectral indices in order to classify or analyze the scene into its components. Consequently, spectral imaging techniques have been adopted only by a small, pioneering community.

We report on a novel agile lamp for imaging which produces illumination having any desired spectral flux distribution ranging from pure spectral bands to precisely-tailored, complex polychromatic functions. This lamp, together with a CCD camera, is suitable for use in most spectral imaging applications, and by enabling one to directly image the scene in the spectral measure of interest, it eliminates the need for computer processing. Using matched filtering, one can obtain full information from all spectral bands in a handful of exposures with optimal signal-to-noise. The lamp is long-lived and spectrally stable. It will be affordable, compact, and rugged, and its spectral output can be adjusted within one millisecond. Finally, as there is no interferometer or other optics involved, imaging is 100% photon-efficient. Use of spectrally agile lamps in various multispectral applications is expected.

Keywords: spectral, imaging, matched filters, tunable, illumination, segmentation.

#### 1. INTRODUCTION

Most spectral imaging of two-dimensional scenes is presently performed with tunable filters<sup>1-4</sup>, interferometers<sup>5,6</sup>, or dispersive apparatus<sup>7</sup> to measure or calculate an image cube comprising a spatial representation of the scene at a variety of wavelengths. Subsequent computer analysis such as classification or pixel unmixing is used to determine the information of interest. An interesting exception is the ISIS system<sup>8,9</sup> where the apparatus directly records the parameter of interest by subjecting the light to a spectral filter matched to that parameter, then measuring the beam intensity. Yet even this instrument has its drawbacks: it is costly, complex, and images only a line of a scene at a time.



In general, the power of spectral imaging to reveal subtle features has enabled fruitful research, but to date few applications have been identified where the benefits of spectral imaging are sufficient to outweigh the cost, complexity, and reduced measurement speed that it entails. Fundamentally, most spectral imaging approaches are intrusive in the sense that their use excludes conventional, non-spectral operating modes; at best, these systems add additional equipment to bypass the spectral apparatus. Thus anyone considering use of spectral imaging in a practical application must choose between a conventional approach and a spectral approach. This has proven a barrier to adoption of spectral measures.

The present work explores a different approach to spectral imaging, based on tailored spectral illumination, that can use conventional (non-spectral), RGB, photometric, colorimetric, spectral imaging, and matched filtering modes interchangeably. Several of these modes can be combined fruitfully, in a way that nearly eliminates the need for computer processing in order to obtain the sample parameters of interest. This approach appears quite practical and offers an easy migration path from conventional to spectral techniques.

#### 2. PRINCIPLE OF OPERATION

Figure 1 illustrates the principle of tailored spectral illumination. A spectrally agile lamp produces light across a spectral range, with independent control of the intensity at each wavelength band. The lamp can produce light in a single wavelength band, or in multiple bands, or in all bands at once. Indeed, it has as its goal the production of essentially arbitrary distributions of spectral radiance, under computer control.

The construction and design of the illuminator will be addressed in a subsequent paper, but its performance is briefly summarized here. Reconfiguring to a new spectral radiance distribution takes approximately 1 ms, and the brightness at any wavelength can be adjusted over a range of greater than 2500:1. The prototype instrument has 29 bands spanning the visible range in 10-nm steps, but other ranges and spectral resolutions are possible. The adjustment of flux is linearized to 3% or less, and the output intensity of the lamp is stable within 1% after warm-up. Its optics are designed to ensure the output is free of spectro-spatial artifacts such as color shifts across the image.

The overall imaging system consists of a spectral illuminator, sample and associated optics, a monochrome imaging detector, and control electronics such as a PC.

#### 3. CALIBRATION

The signal induced at the detector by light in an infinitesimal spectral band centered at  $\lambda_0$  and having width  $d\lambda$  is given by

$$D(\lambda_0) = I(\lambda_0) S(\lambda_0) R(\lambda_0) d\lambda$$
 [1]

where D() is the signal produced at the detector, I() is the illumination flux, S() is the spectral response of the sample, and R() is the detector responsivity at wavelength  $\lambda$ . S( $\lambda$ ) may indicate reflection, transmission or scatter, depending on how the sample is being illuminated and viewed, (i.e. by a transmissive, reflective, or scattering arrangement). In the present context, these are equivalent so long as the wavelength of light is substantially unaltered by its interaction with the sample.

One can rewrite the above equation in terms of discrete bands, provided that the bands are chosen to be sufficiently narrow that neither sample response nor detector responsivity varies greatly within a given band. Then one may write the expression for the contribution from light in the j-th band as

$$D(j) = I(j) S(j) R(j) d\lambda_i$$
 [2]

To obtain calibrated values for  $S(\lambda)$ , one normalizes the sample readings by readings taken using a standard such as a white card (for reflection measurements) or a transparent reference (for transmission measurements). This normalization is performed on a band-by-band basis, and typically for the standard  $S(\lambda) = 1$ , leading to a signal of

$$D(j) = I(j) R(j) d\lambda_{j}$$
 [3]

when the standard is read. From this measurement, one can determine the sample property S(j) by taking the ratio of the detector readings when the sample is present, relative to when the standard is absent, as:

$$S(j)_{\text{measured}} = D(j)_{\text{sample}} / D(j)_{\text{standard}} = I(j) S(j) R(j) d\lambda_j / I(j) R(j) d\lambda_j = S(j)$$
[4]

This is typically done by setting the spectral illuminator to produce each wavelength band in turn while recording the detector reading D(j), under both sample and standard conditions; the point-by-point ratio yields the sample response S(j).

But the readings  $D(j)_{standard}$  are especially significant for the present system. They indicate the reading for a given spectral band at the illuminator setting used for that exposure. Since the illuminator output is continuously variable, it is possible to adjust the illuminator settings so as to attain a sought-for reading at the detector, which we denote as K. By doing so in all bands, and recording the illuminator brightness settings C(j) required to meet this condition, one can calculate a calibration table of scale factors  $\alpha(j)$ :

$$\alpha(j) = K / C(j)$$
 [5]

The scale factor  $\alpha(j)$  is the detector response per unit of illuminator flux in band j, and it will be used in several of the operating modes discussed below. Once the values for  $\alpha(j)$  have been determined, there is no need to repeat the measurement of the standard unless the apparatus is disturbed or altered.

#### 4. RGB, PHOTOMETRIC AND COLORIMETRIC USES

The spectral illuminator can be used in several, complementary operating modes. All are compatible with conventional (non-spectral) imaging. First, if all wavelength bands are turned on, one can perform white-light observations, either using the detector or visually. However, since the intensity in each spectral band is adjustable, it is straightforward to produce illumination that matches the CIE A, daylight, CIE C, or other desired illuminant, weighted by the spectral response of the detector. This is achieved by setting the individual bands in the spectral illuminator according to:

$$C(j) = F(j) \alpha(j)$$
 [6]

where F(j) is the spectral distribution of the desired illuminant. This calculation includes all corrections for the spectral response of the detector. In this mode, the spectral illuminator provides a well-known, standard illuminant whose overall intensity level can be adjusted over a wide range without altering the color temperature.

The settings of the spectral illuminator may be further weighted by the luminosity function L(), by operating with

$$C(j) = F(j) L(j) \alpha(j)$$
 [7]

in which case the detector will produce a luminance image of the sample, when illuminated by the chosen illuminant. Similarly, the spectral illuminator settings may be weighted by a chosen illuminant times the tristimulus functions X(), Y(), and Z():

$$C(i) = X(i) F(i) \alpha(i)$$
[8a]

$$C(j) = Y(j) F(j) \alpha(j)$$
[8b]

$$C(j) = Z(j) F(j) \alpha(j)$$
 [8c]

and by sequentially imaging the sample under the conditions [8a], [8b], and [8c], precise colorimetric values are obtained at every pixel in the scene. From the colorimetric values, one can derive RGB values of extremely high fidelity by a linear transform, specifically multiplying the [XYZ] values at each pixel by the inverse of the chromaticity matrix of the target primaries. The resulting color images have essentially zero color error, since the illuminant was controlled, the spectral response of the detector is corrected for, and the RGB values are derived directly from tristimulus values. This stands in contrast to conventional RGB images, where the primaries used for acquisition bear only a rough resemblance to the ideal curves.

Alternatively, when less exacting color is sought, one may take three exposures, during which time the spectral illuminator is set with channels corresponding to red, green, and blue turned on, in sequence. This can be done at video rate or faster, given the response time of the illuminator (1 ms).

#### 5. USE IN COLLECTING IMAGE CUBES

A spectral illumination system can be readily used to obtain image cubes, by turning on one band at a time and recording the corresponding image at the detector for each band in turn. This operating mode is essentially standard band-sequential spectral imaging, albeit with the benefit that light is filtered before reaching the sample, rather than when passing from the sample to the detector.

There appear to be some benefits to using a spectral illuminator approach. Only light of the target spectral band is presented to the sample, minimizing overall flux at the sample. This is useful for measurement of light-sensitive samples, as is the case with retinal imaging. Since there are no lossy optics between the sample and the detector, nearly all photons that exit the sample will reach the detector. Hence, a photon-efficiency of nearly 100% can be achieved.

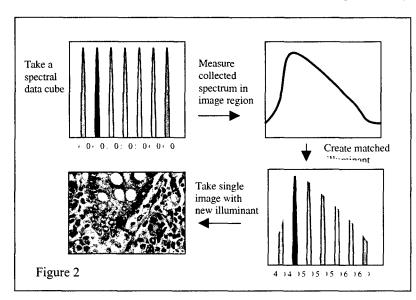
#### 6. USE IN MATCHED-FILTER IMAGING

The spectral illuminator is ideal for implementation of matched filter algorithms <sup>10, 11</sup> that extract full spectral information from many bands at once. For each exposure, the spectral illuminator settings are chosen to produce the desired matched filter corresponding to a selected species or class. The light reaching the detector is the product of the illumination function times the sample spectral function S() at each wavelength, summed across all bands. By simply measuring the flux at the detector, one obtains the weighted spectral function of interest for the sample. There is no need for computer processing to extract the information from an image cube, and the operating speed is directly improved as a result.

This is an extremely powerful imaging mode, for which there is no analogy in systems based on tunable filters or interferometers. It most nearly resembles the ISIS instrument, but whereas ISIS produced a line image by means of dispersive optics with a spatial light modulator to provide the spectral weighting, a spectral illuminator system obtains a full high-resolution image of a two-dimensional scene simply by imaging it under the properly tailored illumination. As a result, a full weighted spectral image can be obtained at video rates.

Since the contribution of the spectral bands is summed optically, without lengthy computations; and the use of multiple spectral bands does not call for additional exposures, just more bands in the tailored illumination; there is no penalty for utilizing the full spectral signatures of the species involved. So, unlike nearly all alternative approaches, there is no trade-off between using many bands for high accuracy, and the desire for a practical, high-speed system.

There is a natural fit between this imaging mode and the image-cube mode just discussed. Specifically, first one would take an image cube of a region in band-sequential fashion (with flux in only one spectral band at a time)and then analyze that image cube using a technique such as projection pursuit to determine a matched filter set that maximally distinguishes the species of interest. Subsequently, one may image other samples rapidly, with full spectral information, by recording the



detector response while programming the spectral illuminator to the matched filter settings derived from the image cube data. This is especially valuable in cases where the spectral signatures may change somewhat over time (of from batch to batch), but will be reproducible within a sample (or batch) that contains many regions. Only once is it necessary to obtain and process the image cube, while all subsequent regions can be rapidly imaged utilizing the matched filter thus obtained.

This process is illustrated in Figure 2. One can analogize that the characteristic spectrum of a given target species is akin to the ridges and valleys on a key. The acquisition of an image cube, and the analysis of that data to generate a matched filter, corresponds to determining (or more properly, estimating) the exact shape of

the key for the species being sought. By setting the spectral illuminator to produce the specified matched filter, and imaging other sample regions, one is tries the sample with the key measures the presence (or degree) of response. The latter activity occurs with great speed and great selectivity since the entire key is tried at once.

The same apparatus is employed for the determination of the key shape, and the subsequent use of the key; only the settings of the spectral illuminator are altered, which is done rapidly, under computer control.

#### 7. VISUAL IMAGING MODES

A spectrally-tailored illuminator can be used for visual imaging of samples, without any camera or detector. At the simplest level, it is a lamp with reproducible color temperature and quantitative spectral distribution. As discussed in Section 4, one can also implement a variety of illuminants such as CIE A, C, daylight, and so on. Further, the overall intensity can be adjusted up or down as needed without changing the spectral qualities of the light. This mode entails a different calibration

protocol. Normally, the imaging detector is used to derive the illuminator calibration constants  $\alpha(j)$ ; this is convenient and insures that one compensates for the spectral response of the detector, which is desirable. However, to produce illuminants such as CIE A for visual use, a detector with known spectral response must be used, and its own spectral response factored out, when deriving the calibration constants.

Another mode exists in applications where one wishes to highlight or exaggerate the difference between regions with similar spectra. An example is the detection of counterfeits, where two objects may be metamers (or nearly so). That is, they have the same apparent color under one type of illumination but their colors appear different under another illuminant. This arises when one color-matches to an object using pigments of a different chemical makeup. Such a counterfeit can be detected by spectral analysis, but this is cumbersome and unnecessary. Because the pigments have different spectra, the counterfeit cannot perfectly match the sample for all illumination conditions; and by setting the spectral illuminator to blink alternately between a pair of suitable states, one can identify counterfeits by the contrast (or lack thereof) at the blink frequency. Suitable states can be determined by acquiring image cubes of both spectra, then deriving a pair of illuminants  $C_1(j)$  and  $C_2(j)$  which meet the conditions:

$$\begin{split} & \Sigma_{\text{all } j} \left\{ C_{1}(j) \, S_{\text{real}}(j) \, X(j) \right\} \, = \, \Sigma_{\text{all } j} \left\{ C_{2}(j) \, S_{\text{real}}(j) \, X(j) \right\} \\ & \Sigma_{\text{all } j} \left\{ C_{1}(j) \, S_{\text{real}}(j) \, Y(j) \right\} \, = \, \Sigma_{\text{all } j} \left\{ C_{2}(j) \, S_{\text{real}}(j) \, Y(j) \right\} \\ & \Sigma_{\text{all } j} \left\{ C_{1}(j) \, S_{\text{real}}(j) \, Z(j) \right\} \, = \, \Sigma_{\text{all } j} \left\{ C_{2}(j) \, S_{\text{real}}(j) \, Z(j) \right\} \end{split} \tag{9b}$$

and

$$\begin{split} & \Sigma_{\text{all } j} \left\{ C_1(j) \ S_{\text{real}}(j) \ X(j) \right\} \ \neq \ \Sigma_{\text{all } j} \left\{ C_2(j) \ S_{\text{counterfeig}}(j) \ X(j) \right\} \\ & \Sigma_{\text{all } j} \left\{ C_1(j) \ S_{\text{real}}(j) \ Y(j) \right\} \ \neq \ \Sigma_{\text{all } j} \left\{ C_2(j) \ S_{\text{counterfeit}}(j) \ Y(j) \right\} \\ & \Sigma_{\text{all } j} \left\{ C_1(j) \ S_{\text{real}}(j) \ Z(j) \right\} \ \neq \ \Sigma_{\text{all } j} \left\{ C_2(j) \ S_{\text{counterfeit}}(j) \ Z(j) \right\} \end{split}$$

$$[10a]$$

The former conditions express the requirement that the real object have identical appearance under either illuminant, while the latter require that there be a difference in appearance for the counterfeit.

TABLE 1.	Spectral Illuminator	Filter Wheel	Tunable Filter	Imaging Interferometry	Dispersive Imagers	ISIS
Acquisition Speed	very high (>2 processed regions/sec)	medium (0.1 — 0.5 processed regions/sec)	medium (0.1 processed regions/sec)	medium-low (0.025 — 0.1 processed regions/sec)	medium (>5 processed lines/sec)	high (>50 processed lines/sec)
(spectral components)	low (< \$5k)	low (< \$3k)	moderate (< \$10k)	high (> \$25k)	moderate (< \$10k)	very high (> \$100k)
Complexity	low	low	medium	medium	medium	high
Spatial Resolution	very high (> 4 Mpixel)	medium (<1 Mpixel)	high (2 Mpixel)	medium (<1 Mpixel)	varies	varies (swept-slit)
Spectral Resolution	medium (5 — 30 nm)	varies (2 — 100 nm)	medium (5 — 30 nm)	varies (0.25— 20 nm)	varies (0.05-10 nm)	medium
Ease-of- integration	easy	medium	medium to hard	medium to hard	medium	hard
Spectral Sensitivity	medium (29 bands)	low (4 — 10 bands)	varies (3 — 50 bands)	varies (10-256 bands)	high (>128 bands)	high (>50 bands)
Computing burden	low-medium	medium	high	very high	very high	low
Notes	illuminant only	mechanical	polarized light	requires transform	swept-slit system	swept-slit system

#### 8. COMPARISON WITH EXISTING TECNHIQUES

Tailored spectral illumination is compared in Table 1 against existing techniques including filter wheels, tunable filters (LCTF or AOTF), imaging interferometry, dispersive, and the ISIS system. In terms of acquisition speed, cost, complexity,

computing burden, spatial resolution, and ease-of-integration, the spectral illuminator is unsurpassed. Its greatest limitations are that it cannot be used at all for emission-side fluorescence spectroscopy or Raman spectroscopy; nor where there are other illuminants, such as airborne remote sensing, agriculture, and the like. One can well imagine its use in biomedical applications such as retinal imaging, colposcopy, and in endoscopic procedures; it may prove useful for imaging of the skin, if ambient light can be adequately excluded.

As the spectral illuminator is a non-imaging optical apparatus, it is considerably simpler, more economical, and easier to integrate into an instrument than the equipment used in competitive approaches such as tunable filters, interferometers, and the like. Also, it eliminates the intensive computing burden of alternative methods, greatly increasing instrument throughput and further reducing system cost. Taken together, these factors result in a much more practical and robust system. Consequently it should be competitive for a wider array of uses, including industrial and clinical applications.

Perhaps the most striking feature of tailored illumination is that it is compatible with established (non-spectral) methods, by the expedient of operating it as a simple broadband lamp. The importance of this cannot be overstressed: most spectral devices cannot provide the conventional features and operating modes that the user community is familiar with. Or, the familiar feature is available, but with greatly reduced speed, sensitivity, or ease-of-use due to the presence of the spectral equipment. Overall, a user must set aside their normal favored practices to pursue a multispectral approach. This has proven a severe barrier to adoption in all but the research environment, since their practical benefits are not yet accepted widely in the user community. For multispectral methods to access wider markets, an evolutionary, rather than revolutionary approach is needed, and this is offered by the spectral illuminator.

#### 9. CONCLUSIONS

The concept of a tailored spectral illuminator has been presented, along with an exploration of the operating modes that are thus enabled. Construction of the illuminator will be addressed in a separate paper. A system of this type is may be operated as a broadband (white-light) source; it provides precise illumination as a CIE A, C, or other illuminant; it corrects for spectral response of the imaging detector used; it enables quantitative colorimetry and precision RGB imagery; it can be used to acquire image cubes by operating it as a band-sequential spectrometer; it can be used to perform matched filter imaging without the need for any computing whatsoever; and it can be used to highlight visual contrast for detection of metamers.

The spectral illuminator is rugged, practical, and easily integrated into a variety of instruments. Particular emphasis is placed on the fact that it is backward-compatible with existing (non-spectral) measures, so as to provide an easy adoption path from present techniques to multispectral-aware techniques.

#### **ACKNOWLEDGEMENTS**

This work was funded by CRI internal research and development funds, and by NIH grant 1R44-CA88684-01. Cliff Hoyt was responsible in large part for the concept of using tailored spectral illumination, and many of the ideas used in designing a practical device of this type.

#### REFERENCES

- 1. Gat N. Imaging spectroscopy using tunable filters: a review, In: Wavelet Applications VII, HH Szu, M Vetterli, WJ Campbell, JR Buss, (Ed.), Proc. SPIE Vol. 4056, p. 50-64, 2000.
- 2. Kasili P, Mobley J, Cullum BM, Vo-Dinh T. Bioimaging system using acousto-optic tunable filter, In: *Biomedical Diagnostic, Guidance, and Surgical-Assist Systems II*, T Vo-Dinh, WS Grundfest, DA Benaron, (Ed.), Proc. SPIE Vol. **3911**, p. 345-354, 2000.

- 3. Wachman ES, Niu W and Farkas DL. AOTF microscope for imaging with increased speed and spectral versatility, *Biophysical Journal*; 73:1215-1222, 1997.
- 4. Hoyt C. Liquid crystal tunable filters clear the way for imaging multiprobe fluorescence, *Biophotonics International*; July/August: p. 49-51, 1996.
- 5. Buican TN, Real-time Fourier transform spectrometry for fluorescence imaging and flow cytometry, In: *Bioimaging and Two-Dimensional Spectroscopy*, LC Smith, (Ed.), Proc. SPIE Vol. **1205**, p. 126-133, 1990.
- 6. Garini Y, Katzir N, Cabib D, Buckwald RA, Soenksen DG and Malik Z. Spectral Bio-Imaging, In: XF Wang and B Herman (Ed), Fluorescence Imaging Spectroscopy and Microscopy. Chemical Analysis Series. 137, John Wiley & Sons, Inc, 1996
- 7. Herrala E, Okkonen JT, Hyvarinen TS, Aikio M, Lammasniemi J. Imaging spectrometer for process industry applications, In: *Optical Measurements and Sensors for the Process Industries*, C Gorecki, RW Preater; (Ed.), Proc. SPIE Vol. **2248**, p. 33-40, 1994.
- 8. Stallard BR, Gentry SM, Sweatt WC, Motomatsu SE, Boye CA, Principals and satellite applications of the information-efficient spectral imaging sensor, SAND97-1493, Sandia National Laboratories Report, Albuquerque, NM, 1997.
- 9. Sweatt WC, Boye CA, Gentry SM, Descour MR, Stallard BR, Grotbeck CL, ISIS; An information-efficient spectral imaging system, In: *Imaging Spectrometry IV*, MR Descour, SS Shen (Eds.), Proc. SPIE, Vol. **3438**, p. 98-106, San Diego, 1998.
- 10. Gentry SM, Levenson RM, Biomedical applications of the information-efficient spectral imaging sensor (ISIS), <u>Proc. SPIE</u>, **3603**: 129-142, 1999.
- 11. Jimenez LO, Landgrebe D, High Dimensional Feature Reduction via Projection Pursuit, TR-ECE 96-5, School of Electrical Engineering, Purdue University, West Lafayette, IN 47907-1285, (dynamo.ecn.purdue.edu/~biehl/MultiSpec), 1995.

### Compact hyperspectral imager for low light applications

Petr Herman <sup>a,b</sup>, Henryk Malak <sup>c</sup>, Wayne E. Moore <sup>c</sup>, Jaroslav Vecer <sup>b</sup>

<sup>a</sup> Center for Fluorescence Spectroscopy, University of Maryland at Baltimore, 725 W.Lombard Street,
Baltimore, MD 21201; <sup>b</sup>Institute of Physics, Charles University, Ke Karlovu 5, 121 16 Prague 2, Czech
Republic; <sup>c</sup> Microcosm Inc., 9140 Guilford Rd. Columbia, MD 21046

#### **ABSTRACT**

A high-performance hyperspectral imaging module with high light throughput suitable for microscopy and analytical imaging was built and tested. The imager utilizes the phenomenon of optical activity. The new technique provides information from a continuous spectral range of 250 – 1000nm. Similar spectral range extended to the near IR is also achievable. The imager has the form of a small module which can be inserted between a microscope or other imaging system and a camera. We have tested an 8-bit CCD video-rate camera with satisfactory results. The resulting instrument is simple, robust, and highly compact. The imager module is placed in-line to the microscope imaging system and does not introduce observable image aberrations. The imager is transparent to conventional imaging operations, thus with the imager in-place there is no need for reconfiguration of the microscope or switching between conventional and hyperspectral video/digital imaging modes. The presented spectral imager answers the need for a sensitive, compact, and affordable imaging spectrometer. The instrument is suited for applications requiring parallel acquisition of highly resolved concurrent spatial and spectral information such as high throughput screening, biochip analysis, remote sensing, semiconductor testing, etc. Images, spectral maps, and spectra of various fluorescent objects are presented.

**Keywords:** Hyperspectral, spectral imaging, imaging spectrograph, optical activity

#### 1. INTRODUCTION

Spectral imaging has found its place in applications ranging from astronomy and airborne monitoring to forensic and biomedical sciences or industrial quality and process monitoring. There is growing need for a sensitive hyperspectral imager with high spatial and spectral resolution which can perform well under low light conditions.

Spectral imagers can be divided into two major categories. The first category contains sequential techniques. The simplest can utilize a set of fixed bandpass filters for spectral filtering<sup>1,2</sup>, other can employ tunable filters based on liquid crystals (LQTF)<sup>3</sup> or acousto-optic modulators (AOTF). Still another approach can utilize spectrographs coupled to imaging devices. The second large family of spectral imaging methods is interferometers. Such devices comprise different embodiments of optical-path-difference (OPD) generators. The OPD can be generated e.g. by a movement of some element of the interferometer, or can be induced by an external perturbation of the optical medium. An example of such a device could be an imaging interferometer based on a liquid crystal retarder<sup>10</sup>.

We present a new spectroscopic imaging technique based on the phenomenon of optical activity. Although the principle of operation is different, the imager provides a multiplex/multichannel capability and therefore resembles interferometric imagers. Besides the small size, wide spectral range, and high light throughput, another advantage of the presented hyperspectral imager is that it can be inserted into the light beam without changing its direction or introducing optical aberrations. An inactive hyperspectral module is optically passive and does not interfere with conventional imaging operations. This feature makes switching between conventional and hyperspectral imaging modes extremely easy.

#### 2. PRINCIPLE

A principle of the new method was first described by Herman and Vecer<sup>11</sup> and is schematically depicted in Figure 1. The method utilizes a phenomenon known as the dispersion of optical rotation. The polarization plane of linearly polarized light rotates during propagation through the optically active medium (rotator) and the rotation angle  $\varphi(\lambda)$  depends on the

wavelength of the radiation. Having polarized polychromatic radiation with the total intensity  $I = \int I(\lambda)d\lambda$ , the polarization planes of different spectral components become angularly dispersed after passage through the rotator. Therefore the total output intensity R of light emerging from the output polarizer (analyzer) is:

$$R = \int_{\lambda} I(\lambda) \cos^2 \left[ \varphi_o + \varphi(\lambda) \right] d\lambda , \qquad (1)$$

where  $I(\lambda)$  is a spectrum of the analyzed light,  $\varphi_0$  denotes a fixed angle between polarization planes of the polarizer and analyzer. For practical purposes it is advantageous to set polarizer and analyzer to the parallel position, e.g.  $\varphi_0$ = 0. By choosing an appropriate material and configuration of the rotator, it is possible to construct a rotator with variable rotation power. This means that the rotation angle  $\varphi(\lambda)$  can be varied by changing a proper physical parameter p of the rotator,  $\varphi(\lambda) = \varphi(\lambda, p)$ . The p is a generalized variable embodying a concept of controlling the optical rotation by some direct or indirect means. Parameter p can represent a physical state or characteristic of the rotator or it can represent another influence used to control the rotation of the rotator. More specifically the parameter p could represent thickness of the material, concentration of the optically active medium, magnetic field for magneto-optic rotators, etc. With a variable rotator, the output light intensity can be measured as a function of p:

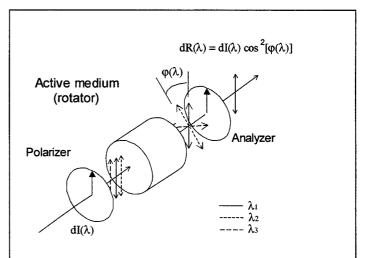


Figure 1: Schematic representation of the new method for the spectral analysis of light

$$R(p) = \int_{\lambda} I(\lambda) \cos^2 \left[ \varphi(\lambda, p) \right] d\lambda.$$
 (2)

The function R(p) we further call a "rotogram". Once the rotogram R(p) is measured for a set of values of p, the spectrum  $I(\lambda)$  is calculated from Eq.(2).

The rotator should be made from material exhibiting high dispersion of optical rotation and high overall optical rotation. Generally, the higher dispersion of the rotation the material has, and the higher overall rotation the analyzed light

experiences, the higher spectral resolution and accuracy can be expected. In other words, in order to spectrally resolve two closely spaced spectral lines, their initially coincident polarization planes have to exit the rotator with significantly different polarization angles. The material of the rotator should also be transparent for light in the desired spectral region. In the presented embodiment of the hyperspectral imager we have used a rotator made from crystalline quartz. Although a number of other optically active materials exists<sup>12,13</sup>, we have chosen crystalline quartz since our intention was to build an imager capable of operation over the

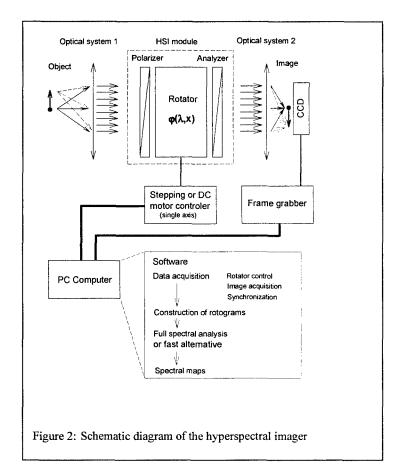
Table 1: Specific optical rotation for crystalline  $quartz^{12}$ 

Wavelength (nm)	Specific optical rotation D(λ) (deg/mm) 236.0		
214			
325	80.5		
527	27.5		
760	12.7		

continuous UV/VIS/NIR region. Quartz is transparent from deep UV to IR and when light propagates along the crystalline axis, the crystal exhibits optical activity with significant dispersion of the specific optical rotation  $D(\lambda)$ . This is an important requirement for a good spectral resolution. As seen from Table 1,  $D(\lambda)$  of quartz decreases with increasing wavelength. The polarization plane of light with shorter wavelength rotates more than the polarization plane of light with longer wavelength. The rotation angle can be expressed as:

$$\varphi(\lambda, d) = d \cdot D(\lambda), \tag{3}$$

where d is thickness of the medium.



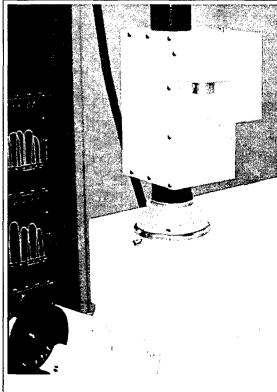


Figure 3: HSI module mounted on the camera port of a Zeiss Axiotron microscope.

When d=0 the rotator dos not exhibit any overall optical activity and does not rotate the polarization plane of light at any wavelength, e.g.  $\varphi(\lambda,0)=0$ . This is an important property, since at this position the rotator does not modify polarization state of the beam. Examination of the Equation 2 shows, that the measured output intensity equals the total light intensity entering the rotator,  $I=\int I(\lambda)d\lambda$ . Such rotator has several advantages. Quartz is a highly stable, optically homogenous, material with very small temperature dependence of its optical properties. The design of the rotator gives superior

uniformity of the polarization plane rotation across the aperture. The surfaces of the rotator can be manufactured to the highest optical quality and AR coated. Those are important requirements for diffraction-limited, aberration-free imaging through the rotator. When a two-dimensional detector is placed in the image plane located behind the HSI module, Figure 2., the multiple detector elements enable rotograms at all pixels to be collected simultaneously. The multiplexing action of the instrument allows all the spectral frequencies to be measured concurrently. This means, that the data stack built from images acquired for different values of d, can be transformed according to Equation (1) to the spectral cube. Then, based on a calculated spectrum in the each pixel location, additional classification of the image can be performed.

#### 3. CONSTRUCTION OF THE SPECTRAL IMAGER

A schematic diagram of the hyperspectral imager is shown in Figure 2. The hardware part of the imager consists of a compact HSI module shown in Figure 3, input and output optics, and a camera which is not shown in Figure 3. The HSI module contains a computer controlled quartz rotator with replaceable elements, and two high-quality Glan-Taylor polarizers. Since the module does not change the direction of the light beam, it can be inserted in-line anywhere between the Optical system 1 and the Optical system 2 of Figure 2. The Optical system 1 can be any kind of an infinity-corrected optical system. It could be e.g. infinity corrected microscope objective or conventional camera lens or telescope with an optical adapter, which provides an infinity correction. The Optical system 2 forms an image on the 2D detector.

The module is compact, having a volume of approx. 22 cubic inches, and is equipped it with a standard 8-bit BW video-rate camera. We have chosen an 8-bit video camera in order to demonstrate and verify capability of the imager under

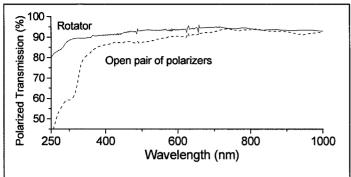


Figure 4: Transmission of the optical components in the HSI module for linearly polarized light.

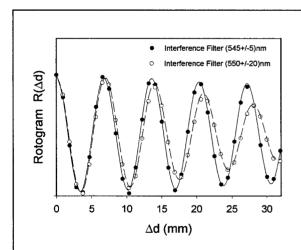
most unfavorable conditions. We understand that using a high dynamic range, slow-scan CCD would enhance performance of the imager. Since we wanted to preserve the field of view of the camera, the HSI unit was designed with a clear aperture of 15x15mm. The size of the HSI unit can be also considerably scaled down, if needed, by limiting the aperture of the crystals and replacing the bulky Glan-Thomson polarizers by a polarizing film. The latter would, however, compromise the light throughput, since transmission of the sheet polarizers is typically lower in the UV/VIS region than transmission of calcite polarizers. The movable element comprising the rotator was mounted on a linear translation stage with positional accuracy of 5µm. This corresponds to the accuracy of the polarization-plane

rotation of about 1degree at 250nm.<sup>12</sup> In order to extend usable spectral range farther to the UV region, a higher positional accuracy would be required to in order to obtained well-sampled rotograms.

The transmission response of the optical components in the HSI module is presented in Figure 4. The HSI module has an overall polarized transmission of 35% at 250nm and over 75% for wavelength longer than 400nm. For standard microscopy applications, however, the spectral range is further limited below approx. 360nm by transmission of the microscope objective and optics. To take advantage of use the full spectral range of the imager, UV optics would be required.

#### 4. RESULTS AND DISCUSSION

A performace of the new hyperspectral imaging technology is demonstrated in Figures 5-10. In order to demostrate sensitivity of the imager to the changes in the spectral position and spectral bandwith of the well-defined input radiation, we



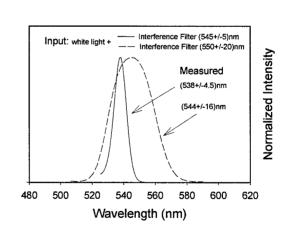


Figure 5: Sensitivity to the position and half-width of the spectral peak. Sample was illuminated by a white light from Xe-arc lamp. Signal was collected through an interference filter (545 +/-5) nm (solid line) or (550+/-20) nm (dashed line) inserted in the emission path. The left panel shows rotograms, the right panel shows corresponding calculated spectra.

illuminated sample with a white light and collected the reflected signal through two different interference filters, Figure 5. One of the filters had a peak transmission located at 545nm and symetrical bandwith of 10nm. The second IF filter had a

peak transmission red-shifted 5nm to 550nm and broader bandwith of 40nm. The left panel of Figure 5 shows rotograms measured at the same spatial location in the image. It is seen, that as the efective optical thickness  $\Delta d$  of the rotator changes, the detector receives varying light intensity  $R(\Delta d)$ . An examination of Equation (2) reveals, that for a monochromatic input light the rotogram  $R(\Delta d)$  should have a pure cosine square form. Any attenuation of amplitudes of the oscillations is a signiture of a finite spectral bandwith of the light. Such predicted behavior is clearly seen from rotograms in Figure 5. The effect is more pronounced for the rotogram taken through 40nm bandwith filter. The wavelength of the light is reflected in the periodicity of the oscillations. One period in the rotogram represents rotation of the polarization plane by  $\pi$ . Since specific rotation of quartz decreases with increasing wavelength, Table 1, the period of oscillations increases for longer wavelength. Due to the good rotational dispersion of quartz, a 5nm wavelength shift results in a significant change of the rotogram periodicity. Spectra recovered from the measured rotograrotograms are presented in the right panel of Figure 5. The spectra mimic well the transmission profiles of the interference filters used. The slight blue shift of the spectral maxima

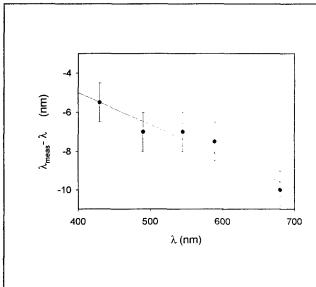


Fig 6: Deviation of a measured wavelength from the expected value for an uncalibrated HSI unit.

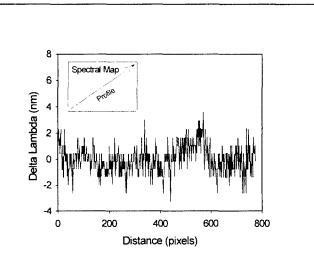


Fig 7: Uniformity of the spectral image. Spectral profile is taken diagonally across the spectral map of a diffuser illuminated by a white light. Signal was collected through an interference filter (545 +/-5) nm inserted in the emission path.

agree with the wavelength calibration curve of the imager, Figure 6. The shift can be eliminated by a proper wavelength calibration.

We have also examined flattness of the spectral field of the imager. Figure 7 shows diagonal profile across the spectral map for a sample illuminated by a white light and observed through a filter with known transmittance. The spectral map was found to be flat with standard deviation of approx. 1 nm from the mean value. Similar results were obtained also for other wavelengths from the spectral range of the imager (not shown).

Figure 8 shows low magnification image (10x) of a mixture of Ludox microcrystals stained by Rhodamine 110 ( $\lambda_{max}$  = 525nm, in solution), and Rhodamine B ( $\lambda_{max}$  = 580nm). The fluorescence intensity image was taken with the hyperspectral module present in the lightpath and set to the "zero state" when the imager is spectrally passive and transmits undistorted intensity images. The upper right panel shows a pseudocolored spectral map. The resulting spectral map closely resembles visual impressions or images of the object taken by a RGB camera. The stack of images can be processed and pre-clasified within several seconds using a high-speed approximation on a PC computer. The full spectral analysis can then be performed on a pre-classified image which highly reduces processing time. It is seen that the spectral map shows sharp spectral contrast between different components. The lower panels of Fig.8 show unnormalized rotograms and normalized calculated spectra at three different locations, indicated in the images. The measured spectra agree well with spectra of the chosen dyes and both spectral components are correctly resolved in the overlaying region.

Figure 9 shows hyperspectral image analysis of the 15 $\mu$ m Focal Check double-stained fluorescent microspheres (Molecular Probes, Inc.) The beads are stained dark-red throughout ( $\lambda_{cm} = 680$ nm)and green on the surface ( $\lambda_{cm} = 515$ nm).

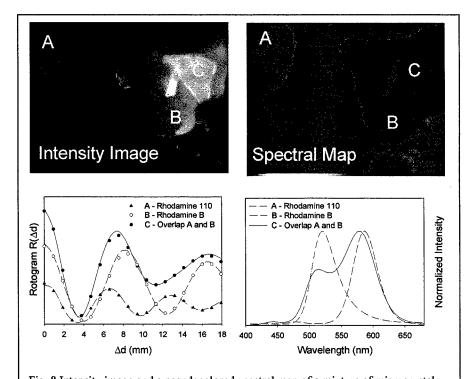


Fig. 8 Intensity image and a pseudocolored spectral map of a mixture of microcrystals stained by Rhodamine 110 and Rhodamine B. The lower panels shows rotograms and corresponding spectra collected from the places indicated in the images. Excitation was done by a Xe arc-lamp at 450nm, emission was collected through 480nm long-pass filter.

Intensity image presented in the left panel was taken through the HSI module in the zero-state and does not indicate any optical distortions caused by the imager. The pseudocolored spectral map correctly indicated different spectral properties of the beads surface (not shown). Since the image was taken in the fluorescence wide-field mode, we cannot eliminate contribution of the out-of-focus light. Then it is reasonable to expect some contribution of the signal from the surface of the sphere to be present in the signal taken from the inside of the bead. This effect is seen from the spectra in Figure 9. The spectra exhibit different proportions of the red and green components in the center and at the surface of the spheres. As expected, both green and red emission was detected with the green emission dominating the signal from the surface of the bead. The oposite is true for signal from the bead interior. Part of the red signal collected from the surface of the bead was caused by the 5x5pixels data integration area. The measured positions of spectral peaks

agree reasonably well with expected values from literature being 516nm and 662nm for green and red fluorescence, respectively. Positions of peaks were stable and reproducible within several nanometers for different preparations of beads. Since the measurements are reproducible, any measured wavelength inconsistency can be eliminated by a proper calibration procedure.

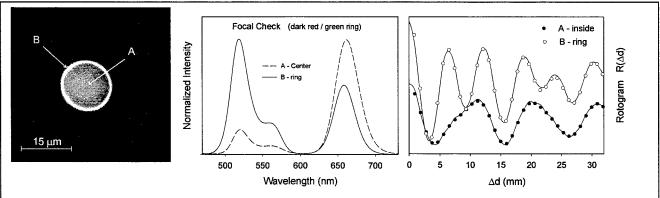


Figure 9: Image of the 15um Focal Check fluorescent bead stained dark-red throughput with green fluorescent ring. The left panel shows an intensity image taken through the HSI unit in the "spectrally pasive" position. The right panel shows spectra recovered from spots marked in the image. The spectra were recovered from 5x5 pixel spot. Fluorescence was excited by a Hg arc-lamp through (450+/-20)nm excitation filter. Emission was collected through 500nm long-pass filter.

The next example shows a bovine pulmonary artery endothelial cell stained by a MitoTracker Red CMXRos ( $\lambda_{em} \sim$  600nm), which labels mitochondria, BODIPY FL phallacidin which selectively stains F-actin filaments ( $\lambda_{em} \sim 515$ nm), and

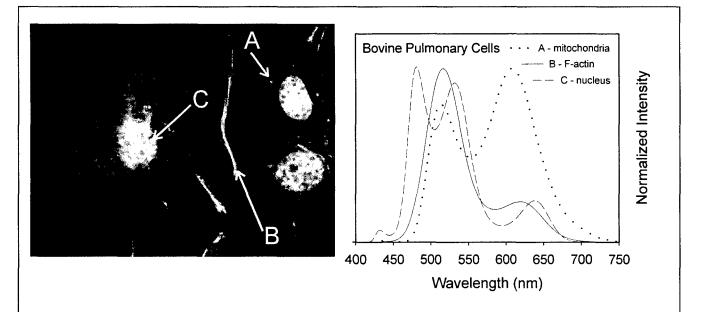


Figure 10: Bovine pulmonary artery endothelial cells stained by MitoTracker Red CMXRos to label the mitochondria, BODIPY FL phallacidin to label the F-actin filaments and DAPI to label the nucleus. The image was acquired using 460nm long-pass filter and 400/40nm excitation from 100W Hg-arc lamp. The strong emission of DAPI was spectrally truncated in order to see all three spectral components simultaneously. The slide was purchased from Molecular Probes, Inc.

DAPI which stains the cell nucleus ( $\lambda_{em} \sim 460$ nm), Figure 10. When excited with a single excitation wavelength at 365nm, the strong blue DAPI fluorescence with a maximum close to 460nm is dominating the signal. This leaves little of the dynamic range of our 8-bit detection system for detection of the other two weak components. In order to partially equalize intensities from different components, we had to red-shift the excitation wavelength out of the excitation maximum of DAPI and collect only the red tail of the DAPI emission through 460nm long-pass filter. The left panel of Figure 10 shows fluorescence intensity image taken through the HSI module. We could detect fine cell structures and no deterioration of the spatial resolution caused by the HSI module was detected. The RGB color map correctly indicated different colors for the three type of stains. Spectra measured at three characteristic regions are shown in the right panel of Figure 10. Red spots in the color map, location A, exhibited bimodal spectra with one maximum located around 605nm a weaker one close to 515nm. The red peak correlates with the emission of MitoTracker Red CMXRos and the green peak with the emission of the BODIPY FL phallacidin. Green spots in the color map, location B, are represented by a solid-line spectrum. By comparing the dotted and the solid line, it is seen that the spectrum has the same location of the two fluorescence maxima. The green component is dominating in this case. Existence of the two peaks in the spectra can be explained by an overlap of the different fluorescent structures and by a contribution of signal from structures located out of the focal plane. A spectrum recovered from nucleus (dashed line) exhibits three peaks. One is located near 470nm and can be attributed to the tail of the DAPI emission "shaped" by a 460nm long-pass filter. Other two peaks are close to the emission of the BODIPY FL phallacidin and MitoTracker Red CMXRos. The noticeable shift of the peaks we attribute to the effect of photobleaching, which was observed during the experiment. Photobleaching distorts rotograms and is known to interfere with the measurement.

#### 5. CONCLUSIONS

We have demonstrated capability of a new spectral-imaging technique based on the optical activity and rotational dispersion of light. A small and simple adapter based on the new technology can convert almost any imaging device into a high light-throughput hyperspectral imager. On several examples it was shown that a hyperspectral module connected to a microscope and equipped with an 8-bit video-rate CCD camera yields meaningful spectral data under fluorescence microscopy light conditions. Future replacement of the quartz rotator will result in a highly compact hyperspectral module without moving parts suitable for high data acquisition rate applications. Such research is underway at Microcosm, Inc.

#### 6. ACKNOWLEDGEMENTS

This work was funded by Microcosm, Inc. The authors would like to thank all people from Microcosm, Inc., who helped to build the prototype of the hyperspectral imager.

#### 7. REFERENCES

- 1. J. Fung, W. Hyun, P. Dandekar, R.A.Pedersen, and H.U. Weier, "Spectral imaging in preconception/preimnplantation genetic diagnostics of aneuploidy: multicolor, multichromosome screening of single cells", *J.Assist. Reprod. Genet.* 15, pp.323-330, 1998
- 2. B.W. Chwirot, Z. Michniewicz, M. Kowalska, and J. Nussbeutel, "Detection of colonic malignant lesions by digital imaging of UV laser-induced autofluorescence", *Photochem Photobiol.* **69**, pp.336-340, 1999
- 3. R.L. Ornberg, B.M. Woerner, D.A. Edwards, "Analysis of stained objects in histological sections by spectral imaging and differential absorption", *J Histochem Cytochem.* 47, pp1307-1314, 1999
- 4. E.S. Wachman, W. Niu, and D.L. Farkas, "AOTF microscope for imaging with increased speed and spectral versatility", *Biophys J.* 73, pp.1215-22, 1997
- 5. R.S. Balaban, I. Kurtz, H.E. Cascio, and P.D. Smith, "Microscopic spectral imaging using a video camera", *J Microsc.* 141, pp31-39, 1986
- 6. D. Schweitzer, M. Hammer, and M. Scibor, "Imaging spectrometry in ophthalmology-principle and applications in microcirculation and in investigation of pigments", *Ophthalmic Res.* **28 Suppl 2**, pp. 37-44, 1996
- C. Favard, P. Valisa, M. Egret-Charlier, S. Sharonov, C. Herben, M. Manfait, E. Da Silva, and P. Vigny, "A new UV-visible confocal laser scanning microspectrofluorometer designed for spectral cellular imaging", *Biospectroscopy* 5, pp.101-115, 1999
- 8. E.N. Lewis, P.J. Treado, R.C. Reeder, G.M. Story, A.E. Dowrey, C. Marcott, and I.W. Levin, "Fourier transform spectroscopic imaging using an infrared focal-plane array detector", *Anal Chem.* 67, pp. 3377-3381, 1995
- D. Cabib, R.A. Buckwald, Y. Garini, D.G. Soenksen, "Spatially resolved Fourier transform spectroscopy (spectral imaging): a powerful tool for quantitative analytical microscopy", Optical diagnostics of living cells and biofluids, D. L. Farkas, R. C. Leif, A. V. Priezzhev, T. Asakura, and B. J. Tromberg editors, Proc. SPIE, 2678, pp.278-291, 1996
- 10. J.P. Miler, "High-performance birefringent imaging spectrometer", Spectral Imaging: Instrumentation Applications and Analysis, G. H. Bearman, D. Cabib, and R. M. Levenson Editors, Proc. SPIE, 3920, pp. 32-39, 2000
- 11. P. Herman, J. Vecer, "Method and device for spectral analysis of light", Czech patent 284282, 1998
- 12. Weast, R. C. ed., CRC Handbook of Chemistry and Physics, CRC Press, Inc., Boca Raton, 1986
- 13. Washburn E.W. ed., International Critical tables, vol. 7, McGraw-Hill Book Co., New York, 1926

### Signal to noise analysis of various imaging systems

Peter J. Miller, Cambridge Research & Instrumentation, Inc. 35-B Cabot Rd., Woburn MA 01801

Dr Andy R. Harvey Cranfield University, RMCS, Shrivenham, Oxfordshire SN6 8LA, UK

#### ABSTRACT

Recent papers comparing the relative signal to noise performance of filters and interferometers for visible and near-IR spectral imaging have reached divergent conclusions. Others have presented the proposition that interferometer systems, by capturing light from multiple spectral channels bands at once, inherently outperform filter-type systems, which capture a single channel at a time. In this paper, a general analysis is provided that establishes a basis for comparison between band-sequential spectrometers and imaging interferometers in the shot-noise limit (set by Poisson statistics of the number of electrons produced at the detector), and in practice. It is shown that factors such as lamp flicker and sample stability can introduce much more error than shot noise does. Thus, one must be aware that the use of shot-noise limited detectors does not ensure shot-noise limited images.

Keywords: Keywords: noise, spectral imaging, interferometry, liquid crystal, tunable filter.

#### 1. INTRODUCTION

The signal to noise of multiple-probe fluorescence imaging experiments has been analyzed for the case of an imaging interferometer and a band-sequential filter instrument<sup>1</sup>. This analysis concluded that pixel classification error rates were significantly lower for the interferometer. Others challenged key aspects of that analysis including how the classification error was derived from the signal-to-noise of the raw image planes<sup>2</sup>. Yet while pointing out the limitations of certain assumptions in the original analysis, the latter group overlooked an error in the derivation of signal-to-noise for the raw image planes, which is of sufficient magnitude to explain the disparity between the supposed advantage of interferometric instruments, and the empirical evidence that the two types of instruments yield comparable results in practice.

Here we derive the signal-to-noise of individual spectral bands for an interferometer, a band-sequential spectrometer, and a spectral illuminator instrument in several operating regimes. First, we consider the light-starved regime encountered in fluorescence or Raman imaging. Here, throughput is limited by integration time, and one seeks to maximize signal-to-noise for a given number of incident photons. Next, we consider the bright-field regime. When there is plenty of light, throughput is paced by readout speed, and one seeks to maximize the signal-to-noise per readout.

Then, consider the case where one wishes to implement a matched filter or other linear-algebraic weighted sum of the readings in several spectral bands. Finally, we look at experimental factors that reduce signal-to-noise in practice, and indicate when these factors, rather than shot-noise statistics, determine the overall measurement noise

#### 2. SPECTRAL SHOT NOISE OF INTERFEROMETERS

An idealized interferometer produces a sequence of signal readings  $e_s(x)$  at a detector while various path differences x are introduced between two beams that are subsequently interfered. From this sequence of readings, termed an interferogram, one obtains a spectrum  $e_s(\lambda)$  by Fourier transformation. All wavelengths of light are present at full strength when the path difference x=0, which point is termed the grand maximum. At other settings, the intensity varies according to  $\delta$  and to the intensity of each spectral component according to

$$e_s(x) = e_s(0) \int_{all} (1 + \cos(2\pi x/\lambda))/2 d\lambda$$
 [1]

In practice, a finite set of measurements is made and the calculation of the spectrum is done using a discrete Fourier transform rather than a Fourier integral. Further, a given measurement  $e_s(x)$  includes contributions from detector noise and shot noise, so the actual measured interferogram is

$$e_s(x) = e_0 \int_{all} (1 + \cos(2\pi x/\lambda))/2 d\lambda + n_d(x) + n_s(x)$$
 [2]

where e<sub>0</sub> denotes the idealized grand-maximum reading.

Shot noise derives from the fact that the detector counts a discrete number of electrons E, for which successive measurements of the same underlying population vary with a standard deviation given by E<sup>1/2</sup>, in accordance with Poisson statistics. Hence one may consider a measurement to have a noise level given by

$$n_s = E^{1/2}$$
 [3]

In the subsequent analysis, detector read-out noise  $n_d$  is taken to be insignificant. This assumption is valid when  $n_d \ll E^{1/2}$ , which for cooled silicon CCD detectors ( $n_d \approx 10$  electrons) means that signal levels greatly exceed 100 electrons.

Note that the RMS value of the shot noise level  $n_s(x)$  is not constant, but varies according to the square root of the photon count, and so is modulated by  $[\int (1 + \cos(2\pi x/\lambda))/2 \, d\lambda]^{1/2}$ . Like the interferogram itself, the shot noise varies with x, which makes the analysis more complicated. Even the exact RMS level of shot noise cannot be stated in general. Since the integrand varies according to the sample being viewed, a precise signal-to-noise analysis requires knowing the spectral distribution. However, for a given grand-maximum level, the impact of spectral distribution upon the mean value of  $n_s$  is not strong. The results derived here are exact for very broadband light or for monochromatic light, while intermediate distributions may see RMS values that are at most few percent different.

The interferogram signal e<sub>s</sub>(x) is given by

$$e_s(x) = A T \left[ \int_{all} F(\lambda) \epsilon(\lambda) \left( 1 + \cos(2\pi x/\lambda) \right) / 2 d\lambda \right] t + n_s(x)$$
 [4]

where  $\varepsilon(\lambda)$  indicates the quantum efficiency of the detector, A is the detector area, T is the transmission of the optical system, and  $F(\lambda)$  is the spectral flux density incident upon the system, and t is the integration time of each measurement in the sequence. After the Fourier transform, one obtains a spectral distribution

$$e_s(\lambda) = A T \left[ \int_{band} F(\lambda) \, \epsilon(\lambda) / 2 \, d\lambda \right] t + n_s(\lambda)$$
 [5]

or in terms of discrete spectral bands

$$e_s(k) = A T F(k) \varepsilon(k) t / 2 + n_s(k)$$
 [6]

where F(k) and  $\varepsilon(k)$  denote the integrated flux and mean quantum efficiency of the detector, respectively, across the k-th band of wavelengths; and  $n_s(k)$  indicates the shot noise in that band of the transformed signal.

Having determined the signal level, we turn to the question of the RMS noise in the spectrum. While the signal depends only on the flux in that band, the RMS value of the shot noise depends on the flux in all bands as will now be shown. The mean signal level in the interferogram is

$$e_{s}(x)_{mean} = A T \left[ \int_{all} F(\lambda) \varepsilon(\lambda) / 2d\lambda \right] t = A T (F \cdot \varepsilon) t / 2$$
 [7]

where  $F \cdot \epsilon$  indicates the vector dot product of  $F(\lambda)$  and  $\epsilon(\lambda)$  across all N spectral bands. This yields a RMS shot noise in the interferogram signal of

RMS 
$$n_s(x) = [e_s(x)_{mean}]^{1/2} = [A T (\mathbf{F} \cdot \mathbf{\epsilon}) t / 2]^{1/2}$$
 [8]

and an interferogram signal-to-noise ratio of

$$SNR_{x} = [A T (\mathbf{F} \cdot \mathbf{\epsilon}) t / 2]^{1/2}$$

The shot noise  $n_s(x)$  in the interferogram is uncorrelated from sample to sample; and spectrally random (white), so it is distributed equally across all N spectral channels. Noise in the N spectral channels adds incoherently (as the root-sum-of-squares), so each spectral channel has an RMS noise of

RMS 
$$n_s(k) = [RMS \ n_s(x)] / N^{1/2}(\lambda) = \{ [A \ T \ (F. \ \epsilon) \ t] / 2N \}^{1/2}$$
 [10]

and broadband noise across all N channels is  $\{[A T (F. \varepsilon) t] / 2\}^{1/2}$ , which is the observed value in the interferogram signal. Now we can write the signal to noise in band k as

$$\begin{aligned} SNR_k &= e_s(k) / [RMS \ n_s(k)] = \{A \ T \ F(k) \ \epsilon(k) \ t \ / \ 2\} \ / \ \{A \ T \ (\textbf{F.} \ \epsilon) \ t] \ / \ 2N\}^{1/2} \\ &= \{A \ T \ t \ / \ 2\}^{1/2} \cdot \{[F(k) \ \epsilon(k) \ N] / [\textbf{F.} \ \epsilon]\}^{1/2} \\ &= \{A \ T \ t \ \epsilon_0 \ / \ 2\}^{1/2} \cdot \{[F(k) \ RQE(k) \ N] / [\textbf{F.} \ RQE]\}^{1/2} \end{aligned} \qquad [11a]$$

In the last equation,  $\varepsilon$  has been broken into two terms, a mean quantum efficiency  $\varepsilon_0$  and a spectral variation RQE(k). One can see that the SNR depends on two terms, one of which is spectrally independent and incorporates the detector size, optics transmission, mean quantum efficiency, and integration time; and the other of which reflects the relative proportion of the total flux that falls within that band (weighted for relative detector efficiency).

In the case of broadband light, the signal flux is equal in all bands and the second term in equation [11c] is  $RQE(k)^{1/2}$ . All channels have identical signal levels, and each enjoys a signal to noise ratio of

$$SNR_{k} = \{A T t \varepsilon(k) / 2\}^{1/2} - broadband light$$

while for monochromatic light the second term has value N<sup>1/2</sup> for the channel containing the light, and has 0 otherwise, so

SNR<sub>k</sub> = 
$$\{A \text{ T t } \varepsilon(k) \text{ N / 2}\}^{1/2}$$
 - monochromatic (signal channel) [13a]  
= 0 - monochromatic (other channels) [13b]

This is physically sensible, if one recalls that all channels contribute to the noise, while only the light in a given band contributes to the band's signal. So, the best SNR for any given band is obtained when there is no other light present to add noise. This is a critical result, since it implies that an instrument designer should exclude light from all non-information bearing channels in order to realize the best SNR.

Similarly, the SNR in the monochromatic signal channel is physically sensible, since a total of N measurements were made of the signal, each with an average transmission of T/2; this yields an improvement of  $N^{1/2}$  in the estimate of signal strength, compared to a single measurement. Other channels have no signal, and shot noise due to photons in the signal channel is distributed equally amongst all channels.

To understand the implications of [11c] in cases intermediate between the monochromatic and broadband cases, it can be helpful to idealize that any given spectral band either has flux, or not; and of the total N bands, M have flux while N-M are dark. We also idealize a 'gray' detector, that is, one for which  $\varepsilon(k) = \varepsilon_0$  for all bands. Thus simplified, we can write

$$SNR_k = \left\{ A T P \varepsilon_0 / 2 \right\}^{1/2} \cdot \left\{ N/M \right\}^{1/2} - M \text{ bands present}$$
 [14]

#### 3. SPECTRAL SHOT NOISE OF BAND-SEQUENTIAL SPECTROMETERS

For a band-sequential spectrometer, the analysis is much easier. The signal when tuned to band k is simply

$$e_s(k) = A T \varepsilon(k) F(k) t + n_s(k)$$
 [15]

and the RMS value of the shot noise n<sub>s</sub>(k) given by Poisson statistics is simply the square root of this, or

RMS 
$$n_s(k) = [A T \varepsilon(k) F(k) t]^{1/2}$$

to yield a signal-to-noise ratio of

SNR<sub>k</sub> = 
$$e_s(k) / [RMS n_s(k)] = [A T \varepsilon(k) F(k) t]^{1/2}$$
 [17]

Note that for a filter-based instrument, both signal and noise are zero in unpopulated bands. In this case, it is not sensible to describe a signal-to-noise, as the shot-noise model predicts that both the signal and the noise are zero, so the SNR is indefinite. Instead we must speak of the threshold detection limit set by the transmission and the RMS detector read-out noise,  $n_d(k) / T$ .

#### 4. IMPLICATIONS IN THE LIGHT-STARVED REGIME

In equations [11c] and [17], one sees that the SNR varies with observation time as  $t^{1/2}$ , improving as more photons are measured. Thus, if these equations hold, it is always possible to improve the SNR by longer observation; indeed, the fact that more observations provide a better estimate of the mean of a population is a truism of experimental statistics. Thus, any comparison of SNR between instruments must assess differences in SNR for the same overall data acquisition time. When one is in the light-starved regime, exposure times are long relative to the time needed to read out the detector, or to reconfigure the apparatus to change the wavelength (or path difference) between readings. Thus we may formulate the problem as achieving the best SNR while keeping the total time for all exposures held constant.

We denote the total time available as P, this being the period over which one may update the overall spectral measurement. For the interferometer, the exposure times are all equal, and if one wishes to obtain an N-band spectrum the exposure time for each reading is simply t = P/N; substituting this into equation [11c] one obtains

SNR<sub>k</sub> = {A T P 
$$\varepsilon_0$$
 / 2N}<sup>1/2</sup> · {[F(k) RQE(k)]/[F . RQE]}<sup>1/2</sup> - general [18a]  
= {A T P  $\varepsilon_0$  / 2N}<sup>1/2</sup> · {N / M}<sup>1/2</sup> - M bands present [18b]

For the band-sequential spectrometer using exposure times of t = P/N, one obtains from equation [17] the result

$$SNR_{k} = [A T P \epsilon(k) F(k) P/N]^{1/2} = \{A T P \epsilon(k)\}^{1/2} \cdot \{1/N\}^{1/2}$$
[19]

Comparison of Equations 18b and 19 indicates that an interferometric approach is favored when N > 2M, meaning less than half the spectral bands are populated, and a band-sequential approach is favored when the source spectrum is denser than this. Examples of such situations include species identification, when an experiment labels a region with one of several spectrally distinct probes, and the goal of the instrument is to determine which probe is present. Thus, an interferometric approach may be most suitable in fluorescence, rather than bright field, where typically most bands are populated.

Of course, if there is a priori knowledge that only certain bands may be present, the filter instrument will omit those bands which cannot contain signal; this effectively defines a new N' for the filter system, purged of the bands known to be vacant. In this case, the band-sequential approach is once again favored. There is no equivalent for an interferometric system, as it must measure all the points in the interferogram.

#### 5. IMPLICATIONS IN THE BRIGHT-FIELD REGIME

When there is adequate light, exposure times may be considered negligible and throughput is set by readout-speed. Consequently, one seeks to maximize the signal-to-noise per readout, or more precisely, to utilize the available dynamic range of the detector as fully as possible. For example, in the bright-field regime, one should select exposure times of each band in a band-sequential spectrometer to ensure the detector is fully exposed in all cases. Similarly, the interferometer should be set so that full exposure is obtained for the grand maximum setting x=0. Typically this is performed with a reference sample such as a blank slide or a Spectralon target, for which the transmission (or reflection) is unity. If we denote the detector's total well depth (in electrons) as W, and the sample transmission (or reflection) in band k as  $S_k$ , one will obtain the following SNRs:

$$SNR_k = W^{1/2} \left( \varepsilon_k S_k F_k \right) / \left[ \left( \varepsilon \cdot F \right) \left( \Sigma \varepsilon_k F_k S_k \right) \right]^{1/2} - interferometer$$
 [20]

$$SNR_k = W^{1/2} S_k^{1/2} - band-sequential$$
 [21]

The band-sequential result is readily understood as the shot noise in the fully utilized detector, correcting for the detector's dynamic range being more or less completely utilized, according to the transmission  $S_k$  of the sample relative to the reference

for which the exposure was optimized. Note that the precision of the readout digitization must exceed the SNR given in [21] to achieve this noise level,

The interferometer presents an interesting, if less lucid, case. The leading term  $W^{1/2}$  is scaled by a ratio. The numerator is the flux in band k. The denominator term is the square root of two terms, comprising the broadband flux in the reference case multiplied by the broadband flux with the sample present. Thus, the denominator is the geometric mean of the broadband flux under sample and reference conditions. In the simplified case where M of the N bands are populated, it reduces to:

$$SNR_k = (W S_k / M)^{1/2}$$
 [22]

That is, the signal to noise is reduced by  $1/M^{1/2}$  relative to the band-sequential spectrometer, because the dynamic range of the detector has to be shared amongst the M active bands. This is physically sensible since otherwise the detector would saturate when all bands are transmitted fully. Equation [22] also illustrates that the interferogram must be recorded with a precision that is at least a factor of  $M^{1/2}$  greater than the desired SNR of the resultant spectra.

Beyond these generalities, one may note that the best course in the bright-field limit is simply to use a detector that has a large well-depth W. Indeed, this is always beneficial from a shot-noise point of view, and is favored experimentally provided that cost and other performance aspects do not prohibit the detector selection on these grounds.

#### 6. PRACTICAL NOISE SOURCES

In practice, the SNR achieved is frequently less than that suggested by the above analyses. There are several reasons for this, the simplest being inadequate stability of other experimental factors such as illumination source and the sample itself. We term noise arising from such sources 'excess noise', as they produce noise exceeding that expected from the idealized shot noise case.

It is instructive to give some concrete examples. Modern CCDs have well depths W ranging from 15,000 – 90,000 electrons, for which the shot noise SNR ranges from 120:1 to 300:1. Yet typical arc lamps exhibit fluctuations of 1% or more. So if one exposes the CCD fully, the actual signal-to-noise level is not set by shot noise, but by lamp flicker. Similarly, photobleaching of fluorophores in excess of 1 part in 120 (or 1 part in 300) will introduce errors that dominate over shot noise. Maintaining such levels of stability over the full acquisition time for an image cube or interferogram is a demanding, if not outright impossible, requirement in fluorescence experiments.

To achieve shot-noise limited performance, experimental noise must be small compared to the shot noise. It turns out that the sensitivity to experimental factors is not the same for the two approaches. Using Equation [9] and [17] one may compare the SNR of interferogram readings to the SNR of an individual band k in a spectral stack taken by a band-sequential imager; the SNRs compare by the ratio:

$$SNR_{interferogram} / SNR_{spectral band k} = [A T (\mathbf{F.\epsilon}) t / 2]^{1/2} / [A T \epsilon(k) F(k) t]^{1/2} = [\mathbf{F.\epsilon} / 2F(k)\epsilon(k)]^{1/2}$$
 [23]

When the total flux across all bands is greater than twice the flux in band k, the interferogram must have a higher SNR. Conversely, if there is only flux in a single band, the spectral band measurement must have higher SNR.

Note that Equation [23] is both a statement of the relative SNR levels, and of the relative SNR requirements for all other elements of the experiment in order to realize shot-noise limited performance. For a band-sequential spectrometer, the SNR of the spectrum is degraded by experimental factors such as lamp flicker and sample aging, to the exact degree that such factors are present. So, lamp flicker of 1 percent will place a 1 percent limit on the SNR of the resultant spectrum.

For an interferometer, however, the relationship is more complex since the SNR in the interferograms and in the calculated spectrum are not the same. In general, the degree of stability required depends on the spectral distribution, with the highest stability being required when imaging a broadband distribution. The ratio given by Equation [23] is highest in the limit of a gray scene, attaining a value of  $(N/2)^{1/2}$ , meaning greater experimental stability is required for an interferometer approach.

To make a detailed comparison between interferometers and band-sequential spectrometers in the presence of excess noise, one may assess the disparity between the experimental SNR and the required SNR for achieving shot-noise performance in each case, given by Equation [9] for interferograms and by Equation [17] for band-sequential spectrometers, and recognize

that the overall SNR will depart from the shot noise limit by the amount of the disparity. Interferometers place a more stringent requirement on the experiment than do band-sequential spectrometers, as shown in Equation [23].

#### **ACKNOWLEDGEMENTS**

This work was funded by CRI internal research and development funds.

#### REFERENCES

- 1. Garini Y, Gil A, Bar-Am I, Cabib D, Katzir N. Signal to noise analysis of multiple color fluorescence imaging microscopy. Cytometry 1999; 35:214–226.
- 2. Castleman K R, Eils R, Morrison L, Piper J, Saracoglu K, Schulze M A, Speicher M R. Classification Accuracy in Multiple Color Fluorescence Imaging Microscopy. Cytometry 2000; 41:139–147.

### Cancer Screening Through the Use of Enhanced Visual Systems

Urs Utzinger<sup>a</sup>, Michael Bueeler<sup>a</sup>, Douglas L. Heintzelman<sup>b</sup>, Ann Gillenwater<sup>c</sup> and Rebecca Richards-Kortum<sup>a</sup>

<sup>a</sup>The University of Texas at Austin, Biomedical Engineering, Austin, TX

<sup>b</sup>Indiana University School of Medicine, Indianapolis, IN

<sup>c</sup>Gynecologic Oncology, The University of Texas M. D. Anderson Cancer Center, Houston, TX

#### **ABSTRACT**

The human eyes are not made to detect disease, however visual perception is the most common screening method for early cancer detection. With optimal illumination and observation configuration there is significant improvement of optical contrast between normal and pre-cancerous tissue in the oral cavity, both for reflected or fluorescent light.

Keywords: neoplasia, screening, spectroscopy, diagnosis, visual perception

#### **SUMMARY**

The human eyes are not made to detect disease, however visual perception is the most common screening method for early cancer detection. We have shown there is significant optical contrast between normal and pre-cancerous tissue in the oral cavity and the cervix, owing to differences in the spectrum of reflected or fluorescent light.

If multi spectral data is presented to the human eye the content is reduced to three bands associated with the three types of cone photoreceptors. Since their spectral sensitivities broadly overlaps one can only extract a fraction of the existing chromatic information [1,2,3]. Multi spectral datasets were used as input to a model [4,5] which simulates the perceived contrast on the level of the photoreceptors. This simulation allowed selected illumination and detection characteristics such as bandwidth and wavelength combinations.

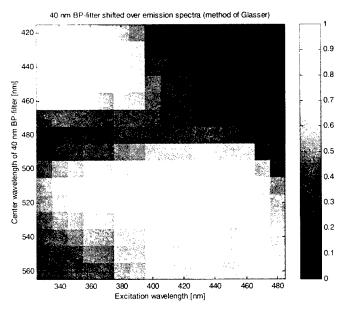


Figure 1: Map of average contrast-values from color stimuli produced by 40 nm BP-filters shifted over the emission spectra. The ordinate represents the excitation light and the abscissa the observed fluorescence.

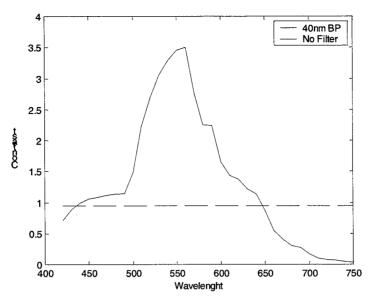


Figure 2: Average contrast-values from color stimuli produced by 40 nm BP-filters shifted over reflectance spectra. White light illuminates the tissue while the observation is bandpass filtered.

The contrast perceived from reflectance spectra of the oral mucosa can be improved by more than a factor of 2 with wavelength selective observation between 500 and 600 nm. Contrast perceived from fluorescence spectra is greatest when observed at 430 nm excitation / 510 nm emission with a bandpass of 60 nm.

Thus, there is significant potential to gain contrast by engineering simple enhanced visual devices that preserve the inherent contrast between abnormal and normal tissue.

#### REFERENCES

- 1. Guenther Wyszecki, W.S. Stiles, Color Science: Concepts and Methods, Quantitative Data and Formulae, (Second Edition, Wiley-Interscience Publication)
- 2. K.R. Boff, L. Kaufman, J.P. Thomas, Handbook of perception and human performance, Vol. 1 Sensory Processes and Perception, (John Wiley and Sons)
- 3. P.K. Kaiser, R.M. Boynton, Human Color Vision (Optical Society of America, 1996)
- 4. Jordan J.R., W. Geisler, and A.C. Bovik, "Color as a source of information in the stereo correspondance process," Vision Res. 20 1955-1970
- 5. Geisler W. Discrimination Information in Natural Radiance Spectra, In Vision Models for Target Detection and Recog., (Info. Display Series, World Scientific Publishing) 117-131

# Virtual Reality Techniques for the Visualization of Biomedical Imaging Data

M. A. Shaw<sup>ac</sup>, W. B. Spillman Jr.<sup>a,b</sup>, K. E. Meissner<sup>a</sup>, J. Gabbard<sup>ac</sup>

<sup>a</sup>The Optical Sciences and Engineering Research Center, Virginia Polytechnic Institute and State University; <sup>b</sup>Department of Physics, <sup>c</sup>Research Graduate Studies, Virginia Polytechnic Institute and State University

#### **Abstract**

The Optical Sciences & Engineering Research Center (OSER) at Virginia Polytechnic and State University investigates advanced laser surgery optics, biocompatible material for implants, and diagnostic patches and other diagnostic and drug delivery tools. The Center employs optics to provide new biological research tools for visualization, measurement, analysis and manipulation. The Center's Research into Multispectral Medical Analysis and Visualization techniques will allow human and veterinary medical professionals to diagnose various conditions of the body in much the same way that satellite information is used to study earth resources. Each pixel in the image has an associated spectra. Advanced image analysis techniques are combined with cross-correlation of the spectra with signatures of known conditions, allowing automated diagnostic assistance to physicians. The analysis and visualization system consists of five components: data acquisition, data storage, data standardization, data analysis, and data visualization. OSER research efforts will be directed toward investigations of these system components as an integrated tool for next generation medical diagnosis. OSER will research critical data quality and data storage issues, mult-spectral sensor technologies, data analysis techniques, and diagnostic visualization systems including the VT-CAVE, (www.cave.vt.edu). The VT-CAVE is Virginia Tech's configuration of Fakespace Systems, Inc Virtual Reality system.

#### Introduction

The Optical Sciences and Engineering Research Center (OSER) was recently formed at Virginia Tech. The center is a collaborative effort between Virginia Tech and the Carilion Biomedical Institute. OSER is specifically tasked with conducting research and engineering activities involving optics and other disciplines to create knowledge and technology to benefit the medical, biomedical and veterinary fields, while supporting the practical goals of improving services and reducing the costs of health care.

Multispectral medical analysis and visualization can allow human and veterinary medical professionals to diagnose various conditions of the body in much the same way that information from satellites can be studied to yield information about the earth's surface (vegetation, pollution, and mineral resources, for example). Each pixel in the image has an associated spectra. Advanced image analysis techniques are combined with cross-correlation of the spectra with signatures of known conditions, allowing automated diagnostic assistance to physicians.

#### **Multispectral Medical Vizualization**

Advances in sensor technology using multispectral and hyperspectral data acquistion systems can be combined with immersive data visualization techniques to produce enhanced reconstructions of a patient's condition for diagnostic purposes. These emerging systems will require developments in sensors, data standards, data management, computational data analysis, and improved data visualization systems.

Advances in multispectral and hyperspectral technology produce data rich images. These images can be combined using computational techniques to produce information rich products. Data compression and transmittal standards and processes for these images must be developed to ensure quality is maintained. Furthermore, the computational algorithms combined with immersive stereoscopic visualization techniques can result in enhanced diagnostic capabilities. A rigorous information system is required to support this research and development effort. The system must be modifiable, flexible, robust, scalable, maintainable, and have a set of supporting process in place to ensure data integrity, quality control, and availability.

The critical challenge is the development of techniques that will provide the clinician an enhanced diagnostic space. This will require development of new methods for information portrayal derived from new sensor technologies. Display of enhanced three dimensional image elements within an immersive environment and interactive analysis techniques must be developed. Finally, this new diagnostic space must provide access to all available patient and other critical information within the work area to provide a complete decision support capability.

#### **Medical Visualization System Components**

The goal of a multispectral data visualization system is to provide enhanced diagnosis capabilities for use by the medical practitioner. The system consists of five components: 1. multispectral data acquisition; 2. data management; 3. data reduction; 4. data analysis; and 5. stereoscopic visualization, (Figure 1.). The data acquisition and visualization systems will provide enhanced capabilities for portraying multispectral data abstractions within a natural three-dimensional stereoscopic immersive display system.

#### Multispectral Data Acquisition

Multispectral imaging systems acquire full spectral data at each pixel of an image. Thus, a three-dimensional data cube is built with the axes being x, y and wavelength ( $\lambda$ ). The multispectral data acquisition system used at OSER was custom built by OKSI (Torrance, CA). It consists of a TE-cooled, blue enhanced Silicon CCD array, a liquid crystal tunable filter (LCTF), camera optics, and a laptop computer for control and storage. Either a visible LCTF (400nm – 720nm) or a near-infrared LCTF (600nm – 1050nm) may be fitted on the camera system. The image acquisition time depends on the integration time at each wavelength band, but is generally on the order of one minute. An image cube is 512 x 512 x 33 (39) for the visible (NIR) and occupies approximately 17MB (20MB).

#### **Data Management**

The massive amounts of data generated by the enhanced sensor systems must be managed and stored in a manner that preserves the quality and unique identifying characteristics of each data set. The meta data describing the sensor data must include machine calibration records, patient identification, patient condition at the time of the measurement, a complete

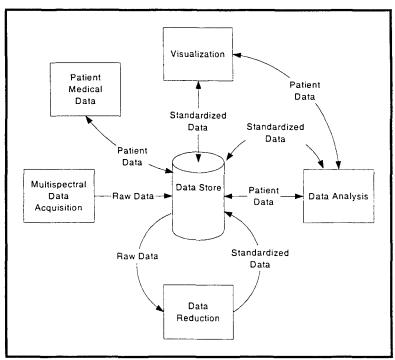


Figure 1. Component Diagram of a multispectral medical data acquisition, analysis, and Visualization system.

record of data reduction and/or computational modification to the original data. This information is critical to ensuring data quality is maintained by preserving the chain of events and processes that result in the analytical or visualization product being evaluated by the clinician.

The OSER system will support the research effort and therefore data provenance is critical when evaluating data anomalies and determination of the efficacy of computational algorithms. The data maintained by the OSER data management system will be invaluable for evaluating new diagnostic tolls as techniques are developed by the research team.

Also included in the data structure will be a complete set of patient records. This information will be available to the analyst and diagnostician during computational analysis and also within the virtual environment to provide an effective and complete virtual diagnostic space.

The availability of this information is critical to the proper analysis of factors that may contribute to the variances in the sensing system. Changes in tissue response due to the physiological state of the patient due must be available to the development team.

#### **Data Reduction**

Data reduction transforms raw multispectral sensor derived data into more useful forms. The techniques used during transformation will be preserved along with the resulting data set to ensure data provenance is preserved for quality control. The data reduction products will include data transformation into industry standard formats for data analysis, image visualization, and three-dimension virtual reconstruction.

#### **Data Analysis**

The data analysis component will consist of integrated commercial-off-the-shelf (COTS), open-source, and custom software to be used for computational analysis. The analytical component will be tightly coupled with the visualization system to allow interactive stereoscopic visualization. This capability will be available both at desktop workstation and with the VT-CAVE immersive environment.

The data analysis toolkit will include both COTS and custom computer applications. Appropriate software applications used by the remote sensing industry will be applied (and customized as necessary) to support the multispectral diagnostic development effort. It is expected that research into the efficacy of applying these reliable remote sensing techniques to medical multispectral data is a promising research area.

#### Visualization

Data visualization is the science of turning sets of complex data into high-density visual information and understanding. Current and emerging technologies allow the generation of virtual environments (VEs) that provide access to traditional data visualization analysis techniques and the ability to combine these capabilities with scaled digital models, video, and other multimedia within an interactive immersive, stereographic environment.

Advanced visualization has become a mainstream tool in applications where complex data sets need to be studied and manipulated. The ability to provide human-scale display, immersion, visual databases, spatial integration, and collaboration solutions will have a significant impact on clinical and diagnostic procedures. The technology provides immediate sensation of the spatial relationships between data. Data can be portrayed using techniques that can either abstract complex data into recognizable patterns or portray information in a natural and therefore more understandable context.

The use of VEs for data fusion is an area of active research. The technology currently provides capabilities for:

- interactive work environments with access to traditional data analysis techniques,
- any combination of spatially related data (or abstractions of the data), computational products, or data classifications,
- 3D data models from other sources,
- 3D models produced by voxelation of image slices
- video.
- images.
- audio and 3D audio,
- scale models of environments, structures, sensors, and devices,
- interactivity at any scale or from any viewpoint,
- textual labels, visual, and audio information that would help investigate, understand, and communicate a medical investigation,
- interactive devices that can be developed specifically to aid in the dissection of discrete data images,
- interactive tools to manipulate and navigate the VE scene graph, and,
- interactive collaborative work sessions with remote sites.

The OSER will be using desktop workstations and Virginia Tech's VT-CAVE immersive system for medical visualization and diagnostic analysis. The CAVE(tm) is a multi-person, room-sized, high-resolution, 3D video and audio environment. In the current configuration, graphics are rear projected in stereo onto three walls and the floor, and viewed with stereo

glasses. As a viewer wearing a position sensor moves within its display boundaries, the correct perspective and stereo projections of the environment are updated by a supercomputer, and the images move with and surround the viewer. Hence stereo projections create 3D images that appear to have a presence both inside and outside the projection-room continuously. To the viewer with stereo glasses the projection screens become transparent and the 3D image space appears to extend to infinity

Specifically, the CAVE(tm) is a theater 10x10x9 feet, made up of three rear-projection screens for the front, right and left walls and a down-projection screen for the floor. Electrohome Marquis 8000 projectors throw full-color workstation fields (1024x768 stereo) at 96 Hz onto the screens, giving approximately 2,000 linear pixel resolution to the surrounding composite image. Computer-controlled audio provides a sonification capability to multiple speakers. A user's head and hand are tracked with Ascension tethered electro magnetic sensors. Stereographics' LCD stereo shutter glasses are used to separate the alternate fields going to the eyes. A Silicon Graphics Power Onyx with three Infinite Reality Engines is used to create the imagery that is projected onto the walls and floor. (http://www.sv.vt.edu/future/vt-cave/whatis/)

#### Conclusion

The goal of a multispectral data visualization system is to provide enhanced diagnosis capabilities for use by the medical practitioner. The system consists of five components: 1. multispectral data acquisition; 2. data management; 3. data reduction; 4. data analysis; and 5. stereoscopic visualization. The full spectra imaging system is combined with the data analysis and interactive visualization to provide means for evaluating sensor response, computational alogorithms, and efficacy of the portrayal techniques as a diagnostic tool. The data management component provides a platform for storage of raw and computational data and the resulting visualization products. This component also provides the patient information necessary to a comprehensive diagnostic space. Finally the data reduction component provides the required procedures for standardizing and reducing the data acquired from the sensor systems. The stereoscopic workstations and the VT-CAVE, a multi-person, room-sized, high-resolution, 3D video and audio environment, will be used for medical data visualizations and research into diagnostic procedures.

In conjuction with this data visualization work, we investigate an intriguing method for analyzing hyperspectral data in talk 4259-10, "Cellular Automata for the Analysis of Biomedical Hyperspectral Images", later in this session. Here, cellular automata are used to rapidly scan hyperspectral images and quantify the extent of conditions of medical interest. This technique can lead to a large reduction in the computational time spent analyzing large hyperspectral images.

# Cellular Automata for the Analysis of Biomedical Hyperspectral Images

W. B. Spillman Jr., K. E. Meissner, S. C. Smith, S. Conner, R. O. Claus

Optical Sciences and Engineering Research (OSER) Center, Virginia Polytechnic Institute and State University

# **ABSTRACT**

In this paper, we describe a technique whereby cellular automata are used to rapidly scan hyperspectral medical images and quantify the extent of conditions of medical interest. The cellular automata population uses the condition of interest as 'food' and only grows in those areas of the image where the food is present. The size of the cellular automata population can be correlated with the fractional area of the image containing the condition of interest. The technique has the potential to significantly reduce the computational overhead required to analyze a hyperspectral image. A simple model of the technique will be described and the results of its operation on a specific hyperspectral image presented.

#### INTRODUCTION

Increasing emphasis is being placed on the creation of an automated physician's assistant to prescreen patients, compare current data with patient history and provide prediagnosis condition estimates to make more effective use of the physician's limited time. Hyperspectral imaging represents a very promising tool for the rapid prescreening of patients. However, processing the large amount of data contained within the hyperspectral image can take a significant amount of time. The majority of this time is spent identifying the spectral signature of interest at each pixel of the image. Cellular automata have been used in other systems to detect defects and damage [as examples see 1,2].

In this application, the use of cellular automata can reduce the number of spectral identification calculations performed during the image analysis. A cellular automaton is a dynamical model of single cell life that uses the spectral signature of interest as food and is only affected by its local environment [3,4]. Here, the cellular automata are randomly seeded directly on the hyperspectral image and are given the ability to determine the amount of food within their local environment. By allowing individual cellular automaton to grow, move and reproduce in the presence of food, the technique is able to essentially ignore the areas of the image with no food. This is expected to result in a significant reduction of computational overhead and thus speed the image analysis process.

#### **OSER HYPERSPECTRAL IMAGING SYSTEM**

The hyperspectral imaging system used at OSER was purchased from Opto-Knowledge Systems, Inc. (Torrance, CA) and consists of a CCD array, a liquid crystal tunable filter (LCTF), and the necessary camera optics. The system is controlled by a laptop computer with a docking station and is tethered to control electronics for both the array and the LCTF. In its current configuration, the system has a working distance of approximately 0.5 m. and images an area of about 1.25 in. x 1.5 in. Depending on the filter, the system can acquire an image with up to 39 spectral bands in less than one minute. Figure 1 shows the system imaging blood samples during an experiment.

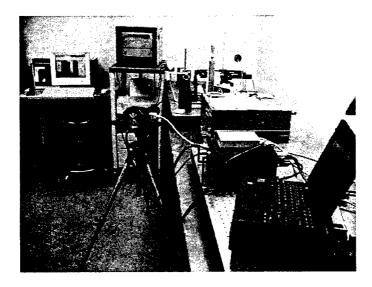


Figure 1: The OSER hyperspectral imaging system being used to identify fibrin in processed blood samples.

The detector array is a blue-enhanced Silicon CCD purchased from PixelVision, Inc. (Beaverton, OR). It is  $512 \times 512$  elements with each pixel being  $24 \mu m \times 24 \mu m$  in size. The system has a 2 stage TE cooler and is normally operated at -10°C. The signal is digitized to 16 bits. The array controller is tethered to both the camera as well as a laptop docking station.

The LCTFs were purchased from CRI, Inc. (Boston, MA). OSER currently has two LCTFs covering the ranges of 400nm - 720nm and 650nm - 1050nm. Both filters have a 10nm bandpass, a 50ms switching time and a 20mm clear aperture. The LCTF is controlled by external electronics that must be programmed for the desired wavelength sequence before use. Wavelength agility is a major advantage of using an LCTF. The filter does not have to scan the spectral region sequentially. The filter can skip wavelengths that are not of interest without incurring any time lost in data acquisition.

The system is controlled by a laptop computer and docking station. Custom software controls the data acquisition and synchronizes the LCTF and camera. Each image file is multiple megabytes in size, depending upon the number of spectral bands acquired, and is stored on the hard drive for analysis. Analysis can be performed on the laptop using custom tools developed under the ENVI/IDL software package.

# HYPERSPECTRAL IMAGE DATA

Hyperspectral data cubes (the cube dimensions being spatial, x and y, as well as spectral,  $\lambda$ ) have a full spectrum associated with each pixel in the image. This large amount of data accounts for the large image file size (up to 20MB for our system). This spectral data contains information about the analyte or condition of interest. In a general sense, image processing techniques seek to reduce the spectral data to a single value indicating the correlation to what is being investigated. These techniques include such functions as cross correlation with a known spectrum, Fourier Transforming the spectrum and filtering, etc. These data processing operations tend to be computationally expensive and dominate the time required for overall analysis of the image. The use of cellular automata will not improve image analysis by replacing these processing techniques. Rather, they can improve the efficiency of the overall process by eliminating a portion of the pixels undergoing the processing steps. Basically, the cellular automata use the results of the image processing techniques as "food" and populate the image in areas where food is the most abundant.

#### CELLULAR AUTOMATA

The functioning of a cellular automaton, or a finite state machine, involves three steps:

- observing its local environment and internal state
- using the observations as inputs to an internal set of rules
- performing some action.

More rigorously, each cellular automaton on a lattice site is defined by three discrete sets and two mappings [5]. The three sets are:

- {inputs}
- {internal state}
- {outputs}.

The two mappings are represented by:

- a state change function which maps the input and state at time, t, to a new state at time  $t+\Delta t$
- an output function that maps the input and state at time, t, to an output at time  $t+\Delta t$

The evolution of a collection of cellular automata takes place in discrete steps and can be carried out either globally (in parallel) or locally (sequentially). For the local or sequential case, the evolution of only one automaton is carried out at a time. For the global or parallel case, all automata are updated simultaneously via generations. In the example to follow, global updating will be used.

In this implementation, each individual cellular automaton begins with a set parameters and operates (lives) under a simple set of rules. The system is based on the energy level (or strength), E, of the automaton and the food, F, in the immediate neighborhood of the automaton. So, the automaton must have the ability to calculate the food value at its current location as well as adjacent locations. This calculation involves the previously mentioned processing step(s). The automaton requires food to offset loss of energy due to living and to strengthen. Without sufficient food, the automaton will eventually die. The set of operating parameters include:

- initial energy level, E<sub>0</sub>
- food retention efficiency, RE
- food ingestion efficiency, IE
- energy level required for life, LEL
- energy level required to move, MEL
- energy level required to reproduce, REL.

Each automaton then lives by the following rules during each generation (i<sup>th</sup> generation):

- change the internal state:  $E_i = (E_{i-1} \times RE) + (F_0 \times IE)$
- if able to reproduce, do so at most favorable unoccupied adjacent location:

```
if (E_i > REL)
```

calculate F in adjacent pixels

reproduce into the one with largest F

• if able to move but not reproduce, move to unoccupied adjacent location with more food:

```
if (REL > E_i > MEL)
```

calculate F in adjacent pixels

move if  $(F_{adjacent} > F_{current})$ 

- if multiple CAs try to occupy same location (move and/or reproduce), the strongest moves
- if unable to move or reproduce (MEL  $> E_i > LEL$ ), wait
- if below life level (LEL > E<sub>i</sub>), die

Thus, an individual automaton can spawn a colony, simply gain strength, migrate to a more favorable environment or cease to exist depending on the food in its own and adjacent pixels.

Image analysis is performed by seeding an image with many cellular automata and allowing the individuals to follow the rules of life for a number of generations. The flowchart in figure 2 demonstrates the cellular automata algorithm used During the generational process, each cellular automaton will seek a more favorable situation for itself if possible (i.e. move or grow). The group behavior of the individuals then yields the information about the spectral feature of interest. After the prescribed number of generations (usually on the order of 10's), the final population distribution of the cellular automata is recorded. The energy level of the CA at each pixel directly correlates to the strength of the spectral signature at that location. Additionally, the percentage of the image affected by the spectral signature is easily obtained by looking at the fractional coverage of the colonies of cellular automata. Thus, image analysis results from the group behavior demonstrated by individuals that operate by a simple set of rules and only observe their local environment.

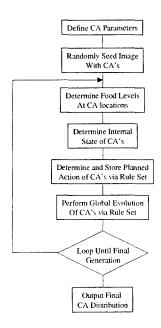


Figure 2: Flowchart showing algorithm for cellular automata image analysis.

# ILLUSTRATIVE EXAMPLE

We use a cartoon to illustrate the technique. A cellular automaton will be introduced into a 4 x 4 image and the system development will be traced. Figure 3 shows diagrams the system development.

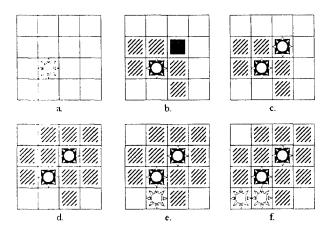


Figure 3: Illustrative example of a cellular automaton introduced into a 4x4 image. Cellular automaton are represented by the round image. Food is represented by a square with a darker color meaning higher food value. Hatched squares indicate a food value of zero. Unfilled squares have not had food value calculated.

In figure 3a, a single automaton is introduced onto the image. The automaton calculates the food at its location and, in this case, grows due to the presence of food. It then calculates food at the surrounding locations (figure 3b). Assuming the cellular automaton is strong enough to reproduce, it will do so into the location with the most food (figure 3c). This is the end of the first generation. In the next generation, the two cellular automata then grow due to the food. In the next generation, the new cellular automaton must

calculate the food in the adjacent areas (figure 3d). As shown in the figure, this involves four calculations. The original automaton would reproduce into the next best food area (figure 3e). This would end the second generation. In the next generation, the cellular automata would again grow. The only action possible would be for the original automaton to reproduce into the final location with food (figure 3f). This would be the stable state for the system. In this example, there are two locations (out of 16) that do not undergo the spectral calculation. Assuming the damage must occupy more than a single pixel, the cellular automata technique has identified all locations with the spectral signature of interest.

#### **BIOMEDICAL EXAMPLE**

As a basic example of this technique, processed blood samples were examined for the presence of fibrin in the serum. The blood sample have been centrifuged and processed. As seen in figure 4, the serum sample of interest is at the top of the tube followed by a serum separator. Finally, the hemoglobin sits at the bottom of the tube. Occasionally, the serum sample becomes corrupted with such compounds such as lipids, icterus or fibrin. Once corrupted, these samples cannot be properly analyzed by standard instrumentation. So, the ability to pre-screen these samples becomes quite important.

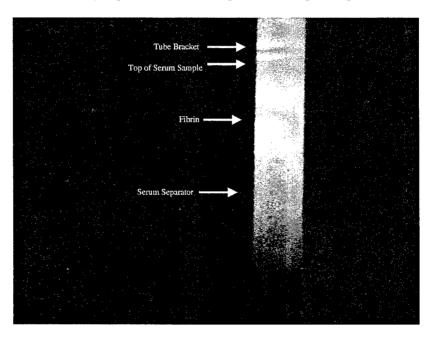


Figure 4: Picture of the processed blood sample used for hyperspectral analysis.

The serum sample sits above the serum separator. Within the serum are two large areas of fibrin (seen as brighter areas in the picture).

In the sample shown, there is a large amount of fibrin at the bottom of the serum sample. The goal is to identify the solid as fibrin and quantify the amount of fibrin in the sample using the cellular automata. The first step is to identify a spectral signature for fibrin. Here, Principal Component Regression (PCR) was used to identify the spectral signature of fibrin. Details of this step are omitted because the source of the spectral signature is immaterial to the cellular automata. Suffice to note that PCR produced a vector of wavelength weightings that are multiplied by a pixel's spectrum and summed. The result indicates the amount of fibrin or food at the location.

In this example, the hyperspectral image includes data in the 400nm – 570nm spectral region. The sample was back illuminated and the transmitted light imaged on the hyperspectral system. The section of the image chosen for analysis was 270 x 120 pixels. Cellular automata were randomly seeded over 20 percent of the image and were iterated for 20 generations. Figure 5 shows the resultant cellular automata

population. Clearly, the cellular automata colonized the fibrin within the serum sample. Although this is a rather simple image to analyze, it demonstrates the utility of the cellular automata technique.

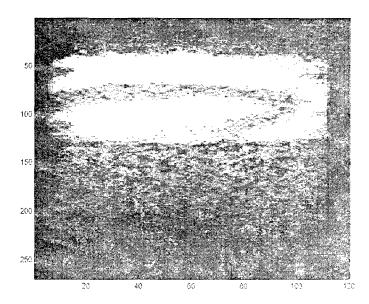


Figure 5: Final cellular automata population distribution after 20 generations of growth. The areas containing fibrin are heavily populated.

# **RESULTS AND DISCUSSION**

The rather simple example above illustrates that cellular automata can be utilized for the analysis of hyperspectral images. But, what advantages are realized? After 20 generations, cellular automata are still alive on 44% of the pixels. An analysis of the entire image indicates a nonzero food value on 92.5% of the pixels. However, the cellular automata calculated the food on only 87% of the pixels. Since this calculation tends to be computationally expensive, this 13% savings could amount to a significant amount of time.

The primary advantage of cellular automata is realized in image areas with little or no food. In these sparse areas, the cellular automata will calculate the food at the location they occupy. However, they will not even calculate the food in adjacent pixels because the food retention rate will weaken them such that they cannot move or reproduce. So, the rule set does not allow them to look around. Areas rich in food encourage the cellular automata to grow and reproduce rapidly. The ability of the cellular automata to migrate to richer food areas allows a random seeding to produce a consistent end population on the image. In general, the cellular automata technique will be more efficient as the percentage of the image containing food decreases. This is true to the point that the areas containing food become small enough that there is a significant probability that no cellular automata from the random seeding process or the migration process contact the area. Basically, an area of interest should occupy more than one pixel in a given area. It should also be noted that in the worst case this technique performs no more food calculations than there are pixels.

Naturally, the choice of parameters greatly affects the efficiency of the technique. All parameters must be balanced against the size of the food calculated. A normalized food calculation allows general values of the parameters to be applied. However, there is still significant dependence on the parameters of the cellular automata. For instance, setting a low value on the energy level required to move and a high value on food retention will cause the cellular automata to do more searching of adjacent pixels. So, the parameters must be investigated for each particular system.

#### SUMMARY AND CONCLUSIONS

We have described a method of using cellular automata for the analysis of hyperspectral images. This technique is easily implemented and can significantly reduce the computational overhead required for hyperspectral image analysis. The efficiency of the technique is attained through a reduction in the number of spectral identification calculations that must be performed. The ability of the cellular automata to reproduce and migrate allows them to essentially ignore areas of the image that do not show a high correlation to the spectral signature of interest. The technique was successfully applied to the identification of fibrin in a processed blood sample. Because fibrin was not present over the entire image, the cellular automata required a spectral identification calculation on only 87% of the pixels. This represents a significant savings in computational overhead. The efficiency of the technique will be even greater as the percentage of the image containing the spectral signature of interest becomes smaller.

#### **ACKNOWLEDGEMENTS**

This work was supported by a grant form the Optical Sciences and Engineering Center at Virginia Tech. The authors wish to thank Nahum Gat (OKSI) for his assistance with the hyperspectral imaging system and Prof. Robin Felder at the University of Virginia for use of the blood samples.

#### REFERENCES

- 1. Spillman, W. B. Jr, Huston, D. R., "Cellular Automata for Image Analysis of Damage in Large Structures," Opt. Eng. 37(3) 898-903 (1998).
- 2. D'Alotto, L. A., "Real Time Cellular Automata Computations for Detecting Defects," Proc. of SPIE 3645, 68-75 (1999).
- 3. Adami, C., Introduction to Artificial Life, Springer-Verlag, New York, 1998.
- 4. Bar-Yam, Y., Dynamics of Complex Systems, Addison-Wesley Publishing Company, New York, 1997.
- 5. Weisbuch, G., Complex Systems Dynamics, An Introduction to Automata Networks, Addison-Wesley Publishing Company, New York, 1991.

# A Near Infrared Spectroscopic Approach to Assess Tissue Viability Following a Thermal Injury

Lorenzo Leonardi\*, Michael G. Sowa, Jeri R. Payette, Mark D. Hewko, Bernhard J. Schattka, Anna Matas, and Henry H. Mantsch

Institute for Biodiagnostics, National Research Council Canada, Winnipeg, MB, Canada, R3B 1Y6

#### **ABSTRACT**

A recurrent problem in the assessment of thermal injuries is the ability to accurately identify the depth and extent of injury. Generally, the depth of a burn injury determines and is inversely related to the ability of the skin to restore and regenerate itself. Burns involve damage to the dermis in varying amounts, reducing the dermal blood supply and altering the skin hemodynamics. Near infrared spectroscopic imaging was used to non-invasively assess the changes that occur in the early (1-3 h) post-burn period. The study used an acute porcine model to investigate the potential of near infrared spectroscopic imaging to accurately distinguish between burns of varying severity. Data analysis was carried out using a two-way and three-way data decompositions techniques to investigate the spectral changes related to burns. Burn injuries drastically alter the physical and optical properties of the tissue. Thermal destruction of cutaneous vasculature disrupts perfusion and oxygen delivery to the affected tissue. The results demonstrated that near infrared spectroscopic imaging might provide a new tool for an objective clinical assessment of burn injuries.

Keywords: near infrared, spectroscopy, cutaneous burns, multivariate analysis

# 1. INTRODUCTION

The skin's ability to restore and regenerate itself following a thermal insult largely depends on the viable tissue underneath the wound. Depending on the depth of injury, a wound can either heal on its own given proper wound care or it may necessitate surgical intervention such as skin replacement. Burns involve damage to the dermis in varying amounts, reducing the dermal blood supply and altering the skin hemodynamics. Current clinical practice involves assessing the wound based on the visual appearance of the wound upon admission and reassessing as needed during the early post-burn period. The ability to accurately identify the degree of thermal injury, however, remains a challenge as there is no uniformly accepted method beyond visual judgement to assess the extent of injury. Visual observation requires sufficient clinical knowledge of burns and is often affected by the examiners past experience. Over the past few years, many modalities have been developed to aid in the assessment of burns, from tissue biopsies<sup>1</sup> to laser Doppler<sup>2,3</sup>, fluorescence<sup>4,5</sup> and thermography<sup>6</sup>. Although many of these techniques have demonstrated success in distinguishing superficial from full thickness burns, difficulty arises with burn types that occur somewhere in-between such as partial thickness burns.

Near infrared spectroscopic imaging provides a non-invasive means of assessing status of tissue following an insult. Near infrared devices present no added harm or inconvenience to the patient or the medical staff that is performing the diagnostic. The most relevant and observable tissue chromophores in this spectral region are hemoglobin and water. These chromophores provide vital tissue information related to oxygen delivery and utilization as well as tissue hydration. A number of people have used near infrared spectroscopy to monitor in-vivo tissue hemodynamics<sup>7-10</sup>. The main advantage of using near infrared light is the tissue sampling depth achieved. Near infrared light between 700-1100 nm can penetrate deep within tissue providing vital burn injury related information. Near infrared can be used to examine the altered blood circulation occurring deep within the tissue. Proper tissue perfusion and oxygenation are key elements in the wound healing process. Hemoglobin provides us with an endogenous marker of tissue oxygenation. The oxygenated (oxyhemoglobin) and deoxygenated (deoxyhemoglobin) states of hemoglobin have different extinction coefficients in the near infrared region. A near infrared spectrum of tissue contains information on the relative concentration of both species of hemoglobin. This porcine burn model study was designed to investigate the use of near infrared spectroscopic imaging to explore elements involved in distinguish between burns of varying severity in the early post-burn period.

# 2. METHODS AND METHODS

#### 2.1 Animal model

All procedures were performed in accordance with a protocol approved by the Institute for Biodiagnostics, National Research Council Canada and conformed to the guidelines set forth by the Canadian Council on Animal Care. Prior to the study, the animals were acclimatized for a period of 10 days. Adult Yorkshire cross swine (Rockwood, Manitoba), ranging between 40 and 50 kg were premidcated with an instramuscular injection of midazolam (0.3 mg/kg), atropine (0.02 mg/kg), and ketamine (20 mg/kg).

Anesthesia was then induced by mask and the pigs were intubated and mechanically ventilated. Isoflurane (1.5 - 2.5 %), was delivered through the ventilator (via 40-60% oxygen mixed with medical air at 3.0 L/min) to maintain anesthesia for the duration of the experiment. Systemic oxygen saturation, heart rate, and blood pressure were monitored throughout the experiment. Core body temperature was maintained at 39.0°C  $\pm 0.5$ °C. Blood samples for blood gas and electrolyte analyses were acquired prior to thermal injury and every hour thereafter. Eight sites, each 3 cm in diameter, were marked on the dorsal surface of the pig as previously described<sup>10</sup>. Burn injuries of varying degrees were then induced on four of the eight sites using a heated brass rod that was 3 cm in diameter. The brass rod was equilibrated in 100°C water and then applied to the skin with constant pressure (2000 g) for 3, 12, 20, and 75 seconds to reproducibly create superficial, intermediate partial, deep partial, and full thickness burns respectively. The remaining four uninjured sites were used as controls. The general burn layout, depicted in Figure 1, shows the relative positions of the burn and control sites. This was an acute and non-recovery study where the animal remained at a surgical depth of anesthesia throughout the protocol.

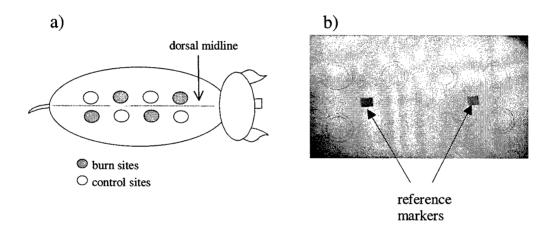


Figure 1: Layout of the burn and control sites on the dorsal surface of the animal. a) pictorial and b) photographic representation.

#### 2.2 Near infrared spectroscopic imaging

Near infrared reflectance images were acquired with a Photometric Series 200 CCD camera that consists of a 512 x 512 back-illuminated CCD detector array and a 14 bit analog-to digital converter (Photometrics, Tucson, AZ). Each near infrared image was collected as 256x256 arrays (2x2 binning) using a 200 msec exposure time. Wavelength selection was achieved using a 7 nm (FWHH) bandpass Lyot type liquid crystal tunable filter (LCTF) between 650 and 1050 nm at 10 nm increments (Cambridge Research Instruments, Cambridge, MA). The camera was equipped with a Nikon Micro AF60 lens with the f-stop set to 5.6 with uniform illumination provided by tungsten halogen lamps (Smith-Victor, Griffith, IN). The white-side of a Kodak Gray Card (Rochester, NY), was used as a reference. Depicted in Figure 2 is a diagram of the experimental setup with the animal and the spectroscopic imaging system. The near infrared spectroscopic imaging camera was mounted on a stage equipped with a railing system permitting camera movement in a reproducibly manner. Since the dorsal of the animal is fairly flat, two sets of spectroscopic images were acquired per time sequence. Each spectroscopic image contained two burn and two control sites in the field of view.

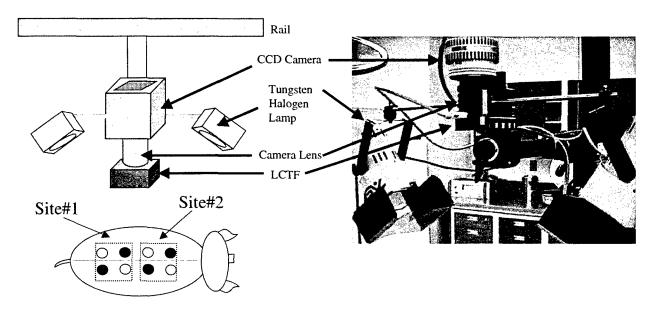


Figure 2: Near infrared spectroscopic imaging camera

# 2.3 Multivariate data processing

Collected from the dorsa of 5 animals were a time series of near infrared spectroscopic images. The first time point in the series was taken prior to thermal injury with subsequent images collected at fixed time intervals after the injury. The experimental design results in a rich set of data consisting of many variables (reflectance response over the 650 – 1050 nm wavelength range) observed on several occasions (longitudinal measurements) and measured over a large spatial area (images). In this manuscript, data exploratory methods, namely Principal Component Analysis (PCA) and Parallel Factor analysis (PARAFAC) are explored to investigate and attempt to separate the spatial, spectral and temporal changes in the near infrared spectroscopic images of thermally injured skin. The objective of the analysis is to identify regions that are temporally and spectroscopically correlated with thermal injuries and most importantly the degree of injury.

# 2.3.1 Principal Component Analysis (PCA)

Principal Component Analysis (PCA) is a well known data exploratory<sup>11-12</sup> method often used to examine spectral data in an attempt to identify the molecular species that contribute to the spectra and determine the magnitude or amount of each. The identification of the species that contribute to the response in a highly convolved series of spectra is particularly challenging when little or no information is available on the nature and relative concentrations of the constituents that make up the system. PCA attempts to determine the combination of variables or factors that describe the major trends based on the maximal change in the variance in the data. However, there is no certainty that the factors or trends correspond to a unique or distinct response. If the data contains two or more responses, there is no assurance that each response will be described by a principal component. It is more likely that each component will describe the responses as a linear combination of the "pure" components. Thus far, no one method exists that can deconstruct the data into it's "pure" components.

PCA is a two way method which decomposes a 2-D data set into a set of eigenvectors based on the maximal variance in the data. However, in the experimental design dorsal sites with varying degrees of thermal injury were monitored spectroscopically over time. The data has an intrinsic three-way structure consisting of the three variables; spatial information, observation time and the wavelengths at which the reflectance of the skin was monitored. PCA, as applied to spectroscopic image time series analysis, requires unfolding of the three-way data such that the spatial and temporal informations are combined. PCA requires an eigenvector decomposition of the covariance or correlation matrix of the spectroscopic image data. The data, represented by X, corresponds to a m x n matrix where each row is associated with an image-time pixel and each column a particular wavelength. To ensure scale invariance, the data are normalized prior to the formation of the covariance matrix. For a given data matrix X with m rows and n columns, the covariance matrix C (n x n) of X is defined as

$$C = \frac{X'X}{(m-1)} \tag{1}$$

where X' denotes the transpose of the matrix. The eigenvectors are determined using a singular value decomposition (SVD) of the covariance matrix C. SVD decomposes the matrix C into three matrices

$$C = UWV' (2)$$

where U is related to the scores, V the loadings, and W the variation explained by successive latent variables. The loadings are orthogonal projections of the latent variables in the data with scores representing the scalar weightings of each of the variables. With respect to the data, the scores are related to the spatial-temporal eigenvectors and the loadings the wavelength eigenvectors. The eigenvectors provide a measure of the percent variance accounted for by the kth principal component of the expansion of the multispectral image matrix. The eigenvectors are order in descending order such that earlier eigenvalues explain the major variations in the data. Therefore, the ordered set of linearly independent principal components accounts for successively smaller fractions of the variation in the tissue reflectance. The first 3 principal components of the multispectral image accounted for more than 95% of the variance, while principal components 4 and 5 accounted for less than 5% of the variance typically represented noise in the multispectral image. Generally, it is found that the data can be adequately described using far fewer eigenvectors than the original number of variables. Only the first 3 principal components of the multispectral image were retained for further analysis.

# 2.3.2 Parallel Factor Analysis (PARAFAC)

Parallel factor analysis (PARAFAC) extends the ideas and methods of standard two-way factor analysis to a multidimensional, in our case three-way, data set. PARAFAC avoids some of the intrinsic problems of two-way analysis such as unfolding the three-way data array into a two-way array and loss of information in the unfolded dimension. The advantage of PARAFAC over PCA is that decomposition of the original array into factors is done in each of the original dimensions, thus recovering information from all dimensions. In our case, parallel factor analysis is used to explore the time series of spectroscopic images collected by attempting to identifying the factors that contribute to the spectra and determining how these factors are affected by thermal insults. The technique is also used to investigate the temporal and spatial variation of these factors following the insult.

Two-way factor analysis approaches attempt to provide an interpretable model of the data by imposing physically meaningful constraints in the decomposition of the data. Generally, this is accomplished by rotating (performing a linear transformation) a truncated set of the latent components (often starting from the principle components) of the data subject to a set of physically meaningful constraints. The resulting factors are intended to retrieve the individual underlying "pure" components of the measured multicomponent system. Such approaches often suffer from rotational ambiguity when applied to spectroscopic data. In these instances the number of constraints are too few to provide a unique rotation or solution and therefore a number of possible factor models can exist. Parallel factor analysis is an N-way decomposition method originating from Psychometrics<sup>14</sup>, which is aimed at overcoming the rotational problem encountered by two-way methods. In the experimental design, varying degrees of thermal injuries were monitored over time using a near infrared spectroscopic imaging system. Intrinsically, the data has a three-way structure consisting of three variables, spatial information, observation time, and the wavelengths at which the images were collected. PARAFAC can exploit this structure while imposing further constraints in order to resolve the problem of rotational ambiguity. In spectroscopic applications, a nonnegativity constraint is usually invoked<sup>15</sup>. Such a constraint provides rotational solutions that may lead to physically meaningful factors and potentially, to the pure components that make up the system.

For clarity, a brief description of the mathematical nomenclature used to describe the variables will be presented. A scalar is indicated by lower-case italics, a vector by a bold lower-case letter, two-dimensional matrices by bold capital letters, and underlined bold capitals for three-dimensional matrices. The three-way data set involving spatial, time, and spectral absorbance can be represented by a triad of loading matrices in the three-way PARAFAC model,

Proc. SPIE Vol. 4259

$$x_{ijk} = \sum_{m=1}^{M} a_{im} b_{jm} c_{km} + e_{ijk}$$
 (3)

where  $a_{im}$ ,  $b_{jm}$ , and  $c_{km}$  are the loading elements of the decomposed data set consisting of M factors and E the data residual matrix. M represents the number of underlying factors or components in the data.

The three-way decomposition described in equation 3 represents the "pure" components contained within the data with respect to the a, b, and c factors. In the case of spectral data, the "pure" spectrum of each of the components contained within the data will be expressed as one of the matrices containing M spectra. Two-way decomposition methods produce one score and one loading matrix. The three-way PARAFAC decomposition produces one score and two loading matrices. A common notation for a three-way PARAFAC model uses Kronecker tensor products to describe the model.

$$\underline{X} = \sum_{m=1}^{M} a_m \otimes b_m \otimes c_m \tag{4}$$

The three matrices from the PARAFAC decomposition represent the spatial variation with thermal injury, the spectroscopic changes and the changes with time. The factors in the PARAFAC analysis are determined using an iterative alternating least squares method. The convergence criterion used in the PARAFAC analysis to terminate the iterative procedure utilizes the relative difference in the fit between two consecutive iterations. The iterative procedure terminates when this difference is below a value of 10<sup>-6</sup>. A constraint of nonnegativity was also placed on the wavelength factors of the PARAFAC analysis to ensure that the extracted wavelength factors or "pure" components have no region of negative optical density. This method requires an initial guess or starting value to determine the underlying factors or solution. To avoid a solution whereby a local minimum is reached, a random set of starting values are used for each run. The PARAFAC analysis is run twice using a random set of starting values for each run. A consistent set of solutions for each run helps ensure that the global solution is obtained. If essentially the same factors are obtained in each run, there is little probability that a local minimum was reached and the solution is unique. The PARAFAC analysis was run twice and the results compared to ensure that the global minimum was reached.

# 3. RESULTS AND DISCUSSION

Thermal injuries disrupt both the physical and optical properties of the tissue. The severe damage to the microvasculture due to a thermal insult results in dramatic hemodynamic changes such as impaired tissue perfusion. Both two-way and three-way data exploratory techniques, namely PCA and PARAFAC respectively, were used to investigate the spectroscopic changes induced by thermal injury. Prior to the analysis the data was mean center where the near infrared spectroscopic images were centered by subtracting the mean of each observation thus removing any offsets in the data. The advantage of mean centering the data is that the decomposition is done with respect to variations in the data instead of the level. Preprocessing is an important step in many multiway decomposition methods. A representative multispectral image series of preburn and postburn tissue is presented in Figure 3. Examination of the raw multispectral image series reveals little or no apparent visual clues to the extent of the thermal injury.

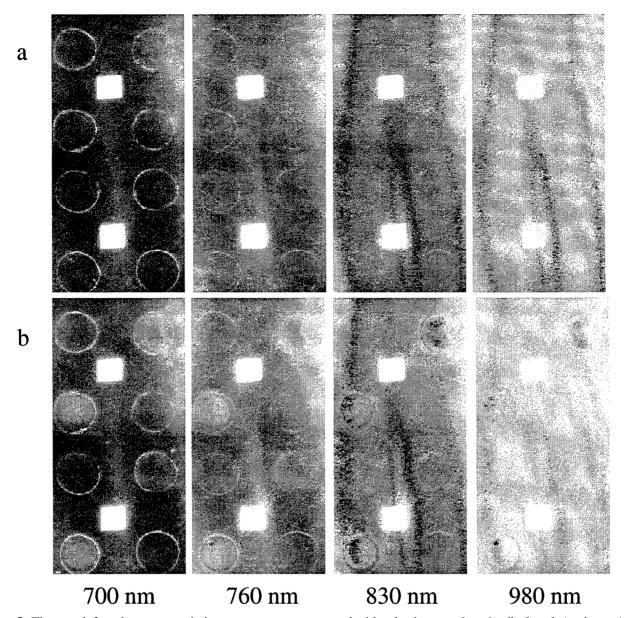
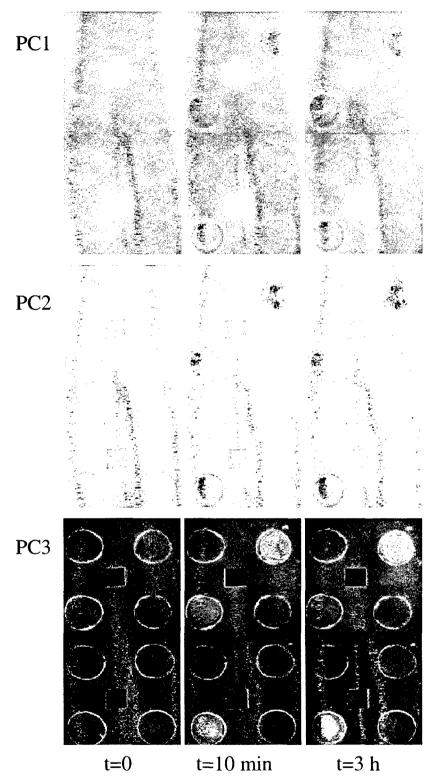


Figure 3: The near infrared spectroscopic images were mean centered with selective wavelengths displayed a) prior to (t=0) and b) immediately post (t=10 min).

# **Principal Component Analysis**

Principal component analysis of the mean centered data attempts to decomposes the near spectroscopic images into a set of uncorrelated principal components. Prior to the analysis, the three-way data was unfolded into a two-way array, which was then processed according to the method outlined in the previous section. The three-way spectroscopic data consisted of images (i) collected at various wavelengths (j) at different time (k) points or observations, processed as two-way data, namely as (i j) x (k). The first 3 principal components account for more than 95% of the total variance in the multispectral images sequence. The higher order principal components accounted for less than 5% of the variance thus representing noise in the data. Therefore, the first 3 principal components were retained in the PCA decomposition. The PCA score and loading factors from the unfolding consisting of images at different time intervals verses wavelength are shown in Figures 4 and 5.



**Figure 4:** PCA scores results for the unfolded image-time by wavelength spectroscopic data. The scores results are displayed with respect to the image PC for three different time intervals.

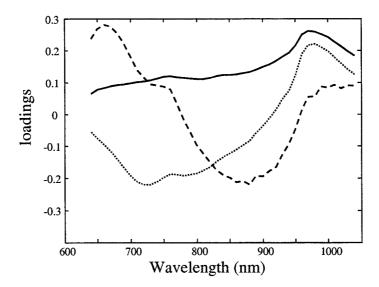


Figure 5: PCA loading results for the first three PC of the unfolded spectroscopic image sequence. These loading represent the wavelength components in the spectroscopic image data where the solid line depicts the first PC, the dotted line the second and the dash line the third.

The first PC denotes the common spectrum detected throughout the spectroscopic image data, accounting for approximately 90% of the variation. The preburn (t=0) PC looks fairly uniform, as would be expected since no injury has been induced. Following the injury, the magnitude of the first image loading factor is different for the sites with injuries. Thermal injuries destroy and damage tissue and one effect of this destruction is a change in the scattering properties of the tissue. This is evident in the first PC. However, other than the superficial burn, the scattering changes for the more severe burns are reasonably similar. Thus distinguishing burn severity solely on the first set of factors is difficult. A larger contrast between the burns is observed in the second set of factors which accounts for 5% of the variation. The loading displays distinct contributions at the 760 and 980 nm regions which are consistent with deoxyhemoglobin and water absorption. Unlike the first PC, the second image-time loading factors exhibits slight differences between the various burns. The full and deep partial thickness injuries display the largest change and are easily discerned from the intermediate and superficial injuries. Based on changes in the deoxyhemoglobin and water content in the tissue the second PC seems to classify the injuries into two categories, burns which will survive and burns which most probably will necrose. The third PC which accounts for approximately 1% of the variation can easily discern the full thickness injury from the remaining injuries. Full thickness injuries destroy the dermal layer and what little if any of the intact dermal vessels is insufficient to supply blood to the skin. The third PC is most probably a linear combination of the oxyhemoglobin, deoxyhemoglobin and water variations in the tissue. Two-way factor analysis approaches attempt to provide an interpretable model of the data and are intended to retrieve the individual underlying "pure" components of the measured multicomponent system. The results often achieved are factors, which are linear combinations of the "pure" components in the spectral data, as was evident in the third PC. Therefore, the non-uniqueness of the of eigenvector limits the usefulness of the information extracted about the system. The temporal information is a key parameter in many situations, in particular, in burn injury assessment. Burns injuries are a dynamic process whereby the burns can become progressively worse during the first few hours following the injury. To compute the PCs, the data was unfolded into a two-way array thus diminishing the information obtained about the time component.

# **Parallel Factor Analysis**

Parallel Factor Analysis is N-way method capable of simultaneously decomposing the data into N different factors, each corresponding to a different dimension of the data. In our case, the results from the three-way PARAFAC analysis produce a score and two loading vectors consisting of wavelength, time, and image factors, summarized in Figures 6. The loading wavelengths of Figure 6a reveal the two predominate spectral components that are retrieved by the PARAFAC analysis. Similar to the PCA analysis, the first wavelength factor, denoted by the solid line, is consistent with the general spectral shape obtained from reflectance tissue. Thus the first factor seems to consist of contributions from deoxyhemoglobin (760 nm) and water (980 nm) absorption. The second wavelength factor resembles an oxyhemoglobin spectrum with it's

particular broad near infrared charge transfer band between 800 and 1000 nm. These result suggest that two changes are occurring, one related to the basic spectrum often associated to the scattering and the other changes in the oxyhemoglobin contributions.

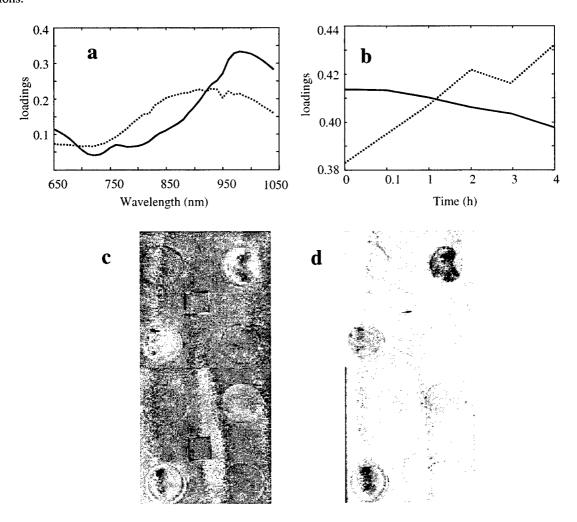


**Figure 6:** The spectroscopic image sequence of thermally injured skin was analyzed using a two-factor three-way PARAFAC method. These score and loadings represent the PARAFAC decomposition results for the a) wavelength factors, b) time factors, c) first image factor and d) second image factor

The PARAFAC analysis suggests that thermal injuries alter the oxyhemglobin contributions in the spectral responses. As stated earlier, burn injuries are a dynamic process whereby the injury can become progressively worse during the first few hours following the injury. The time loading factors, Figure 6b, describe the general trends of the two wavelength factors over the time course of the study. Thus providing a measure of the time-dependent variations associated with the first wavelength component. The first time loading factor, associated with the base spectral feature, exhibits a small increase with time. This suggests that the scattering properties of the tissue following the injury changed slightly over the course of the study. In contrast, the second time loading factor corresponding to oxyhemoglobin content of tissue exhibits a large change over time. This indicates that the burns have a dramatic effect on the oxygen availability and content in tissue and changes oxygen availability over time. The image loading factors, Figure 6c and d, are used to obtain an understanding of the contributions of the wavelength and time factors to the actual burns. In the first image loading factor, it is clear that the more severe burns, namely, partial and full thickness injuries are discernible from the mild superficial burn. Superficial burns only moderately alter the optical properties of the tissue. Damage is restricted to the epidermis whereas the other injuries involve damage to the dermis at varying levels. Clearly, the full thickness injury is distinguishable from the other burn injuries, since this type of burn total destroys the dermis and has a drastic effect on the scattering properties of the tissue. The partial thickness injuries are difficult to distinguish since both of these injuries involve relatively similar damage to the dermis. The second image loading factor identified with the oxyhemoglobin content of the tissue shows a decrease or negative contribution, in comparison to the surrounding tissue. Full thickness injuries, totally destroy the vascular structure causing the tissue to become avscular. This results in the tissue having very little oxygenated hemoglobin. This aspect of full thickness injuries is clearly depicted in the second image loading factor. Intermediate and deep partial thickness injury also damage the dermal layer, however not to the same extent. This is evident in the second image loading factor. Although the partial thickness burns appear very similar in the second image loading factor, a small difference exists between the intermediate and deep partial thickness with the latter exhibiting a greater reduction in the oxyhemoglobin contribution. The superficial burn, the least destructive of the burns shows a minimal change in the oxyhemoglobin in comparison to the more severe burns. In the PARAFAC model, the three loading factors consisting of wavelength, time, and image are not necessarily orthogonal is as is the case with PCA. The solution of the PARAFAC model, however is unique and does not suffer from the indeterminacy that arises in PCA. Furthermore, PARAFAC can exploit the three-way structure of the data while imposing further constraints such as non-negativity in order to resolve the problem of rotational ambiguity often encountered in PCA.

#### 4. SUMMARY

Two decomposition approaches were used to investigate and compare the spectroscopic time course following a thermal injury. Principal component analysis is a two-way method which attempts to decomposes the near spectroscopic images into a two sets of uncorrelated principal components. In general, the results obtained with the two-way analysis seem to suggest that burns alter the scattering properties as well as the oxy- and deoxyhemoglobin balance within the injured tissue. However, the principal components are not unique and seem to consist of a linear combination of the pure components. An inherent problem of two-way analysis with three-way data is the unfolding of the data into a two-way array. Unfolding of three-way data can be done in numerous manners with application of principal component analysis to each of these unfoldings will generally produce different results. As an alternative, a three-way parallel factor analysis was also used to investigate the near infrared spectroscopic image sequence. Like principal component analysis, parallel factor analysis could be done in an exploratory fashion requiring little or no prior information on the system other than that information required to determine the constraints imposed by the experimental design. The two-component three-way analysis extracts two wavelength factors, one resembling the a mean spectra consisting of a water and deoxyhemoglobin contribution and the other representing the oxyhemoglobin contribution to the spectra. Parallel factor analysis reveals that the spectral changes in the early post-burn period can be faithfully represented by two components that summarize the oxy- and deoxy- hemoglobin balance within the injured tissue. Analysis of the near infrared spectroscopic image data indicated that the oxy- and deoxy- hemoglobin balance in injured tissue changed over time following the injury. More importantly, the oxyhemoglobin contribution scaled with the degree or depth of thermal injury. Collectively, both decomposition methods suggest that near infrared spectroscopic images can be used to extract relevant information pertaining to the level of thermal damage to tissue.

#### ACKNOWLEDGMENTS

We are grateful for the expert technical assistance provided by Mrs. S. Germscheid, Mrs. L. Gregorash, and Mrs. R. Mariash.

# REFERENCES

- 1. M. Chvapil, D.P. Speer, J.A. Owen, and T.A. Chvapil, "Identification of the depth of burn injury by collagen stainability", Plast. Reconstr. Surg., 73, pp. 438-41, 1984.
- 2. D. Park, J. Hwang, K. Jang, D. Han, K. Ahn, and B. Baik, "Use of laser doppler flowmetry for estimation of the depth of burns", Plast. Reconstr. Surg., 101, pp. 1516-23, 1998.
- 3. E.K. Yeong, R. Mann, M. Goldberg, L. Engrav, and D. Heimbach, "Improved accuracy of burn wound assessment using laser Doppler", J. Trauma, 40, pp. 956-962, 1996.

- 4. J.E. Gatti, D. LaRossa, D.G. Silverman, and C.E. Hartford, "Evaluation of the burn wound with perfusion fluorometry", J. Trauma, 23, pp. 202-206, 1983.
- 5. R.L. Sheridan, K.T. Schomaker, L.C. Lucchina, J. Hurley, L.M. Yin, R.G. Tompkins, M. Jerath, A. Torri, K.W. Greaves, D.P. Bua, and N.S. Nishioka., "Burn depth estimation by use of indocyanine green fluorescence: initial human trial", J. Burn Care Rehab., 16, pp. 602-604, 1995.
- 6. B.R. Mason, A.J. Graff, and S.P. Pegg, "Colour thermography in the diagnosis of the depth of burn injury", Burns, 7, pp. 197-202, 1981.
- 7. R. A. De Blasi, M. Cope, C. Elwell, F. Safoue and M. Ferrari, "Noninvasive measurement of human forearm oxygen consumption by near infrared spectroscopy", Euro. J. Appl. Physiol. 67, pp. 20-25, 1993.
- 8. M.G. Sowa, J.R. Mansfield, G.B. Scarth and H.H. Mantsch, "Noninvasive assessment of regional and temporal variations in tissue oxygenation by near-infrared spectroscopy and imaging", Appl. Spectrosc., 51, pp. 143-152, 1997.
- 9. M.G. Sowa, J.R. Payette, M.D. Hewko, J.R. Mansfield and H.H. Mantsch., "Hemodynamic information obtained by statistical analysis of near-IR spectroscopic images", SPIE **3257**, pp. 296-306, 1998.
- 10. L. Leonardi, M.G. Sowa, J.R. Payette and H.H. Mantsch., "Near infrared spectroscopy and imaging: a new approach to assess burn injuries", Amer. Clin. Lab. 18, pp. 20-22, 2000.
- 11. J.E. Jackson, A user's guide to principal components. John Wiley, New York, 1991.
- 12. S. Wold, K. Esbensen, and P. Geladi, "Principal component analysis", Chemometrics. Intell. Lab., 2, pp.37-52, 1987.
- 13. J. Mandel, "Use of the singular value decomposition in regression analysis", Am. Statistician, 36, pp. 15-24, 1982.
- 14. R. A. Harshman and M. E. Lundy, Reseach Methods for Multimode Data Analysis, ed. H. C. Law, C. W. Snider, Jr. J. A. Hattie and R. P. Mc Donald, Praeger, New York, 1984.
- 15. L. Leonardi, M.G. Sowa, J. R. Payette, M. Hewko, B. Schattka, A. Matas, and H. H. Mantsch., "Applications of visible-near infrared spectroscopy in burn injury assessment", SPIE vol 3918, 83-90 (2000).

Tel: 204-984-5195, e-mail: larry.leonardi@ibd.nrc.ca

<sup>\*</sup>Address all correspondence to: Lorenzo Leonardi, Fax: 204-984-5472,

# A combined spectroscopic imaging and chemometric approach for automatically partitioning tissue types in human prostate tissue biopsies

Abigail S. Haka<sup>2,3</sup>, Linda H. Kidder<sup>1</sup>, and E. Neil Lewis<sup>1,2</sup>

<sup>1</sup> Spectral Dimensions, Inc., 3416 Olandwood Ct. Suite 210, Olney MD 20832, USA 

Laboratory of Chemical Physics, National Institute of Diabetes and Digestive and Kidney Diseases, National Institutes of Health, Bethesda, MD 20892-6000, USA 

<sup>3</sup>Massachusetts Institute of Technology, 77 Massachusetts Avenue, George Harrison Spectroscopy Laboratory Rm. 6-014, Cambridge, MA 02139-4307, USA

#### **ABSTRACT**

We have applied Fourier transform infrared (FTIR) spectroscopic imaging, coupling a mercury cadmium telluride (MCT) focal plane array detector (FPA) and a Michelson step scan interferometer, to the investigation of various states of malignant human prostate tissue. The MCT FPA used consists of 64 x 64 pixels, each 61 µm², and has a spectral range of 2-10.5 microns. Each imaging data set was collected at 16 cm⁻¹ resolution, resulting in 512 image planes and a total of 4096 interferograms. In this article we describe a method for separating different tissue types contained within FTIR spectroscopic imaging data sets of human prostate tissue biopsies. We present images, generated by the Fuzzy C-Means clustering algorithm, which demonstrate the successful partitioning of distinct tissue type domains. Additionally, analysis of differences in the centroid spectra corresponding to different tissue types provides insight into their biochemical composition. Lastly, we demonstrate the ability to partition tissue type regions in a different data set using centroid spectra calculated from the original data set. This has implications for the use of the Fuzzy C-Means algorithm as an automated technique for the separation and examination of tissue domains in biopsy samples.

**Keywords:** infrared spectroscopic imaging, FT-IR spectroscopy, prostate cancer, Fuzzy C-Means clustering, infrared focalplane array

# 1. INTRODUCTION

Cancer will develop in approximately one in three persons now living in the United States, one in five will die from the disease. Over the last thirty years the number of cancer deaths has doubled and it presently exceeds 550,000 per year. Considering the scope and gravity of this disease, relatively little is known about the etiology of cancer and the prospect for a cure remains remote. Although significant research has been devoted to the search for a cure, currently the most effective means of increasing survival rates continues to be early detection. Much of the recent interest in cancer detection techniques has focused on spectroscopy to potentially augment current protocols for cancer diagnosis. Vibrational spectroscopy is particularly appealing since it has the capability to probe early changes in the biochemical composition of tissue that accompany disease progression. The incorporation of this type of quantitative parameter provides an ideal adjunct to conventional cancer diagnosis methodologies which are empirical and largely subjective because they rely heavily on the visual examination of stained tissue sections.

Several vibrational spectroscopic studies have been performed in an attempt to elucidate differences between normal, benign, and malignant tissues. Examination of cell lines, homogenized tissue, as well as microscopy and bulk measurements of tissue biopsies have provided notable insight into the biochemical changes associated with malignancy.<sup>2-6</sup> Although these approaches are well accepted within the spectroscopic community, applications in the medical sciences have been limited due, in large part, to a lack of cross discipline understanding. The substantial language and terminology barriers associated with such specialized fields as medicine and spectroscopy lead to inefficient communication amongst communities and hinder the progress of such multidisciplinary lines of study. Overcoming these barriers will not only facilitate superior research but will also result in improved patient care through superior diagnostic methods.

In an effort to surmount these barriers, we present a method based on infrared spectroscopic imaging microscopy which may have great benefits as an adjunct to current cancer diagnostic methodologies. The incorporation of an imaging approach is significant as it allows for the rapid pathological assessment of tissue biopsies, through image visualization, while simultaneously incorporating quantitative parameters that reflect changes in the molecular composition of the tissue. This hybrid approach is particularly attractive from a clinical standpoint since it embraces and enhances standard pathological protocols and does not attempt to supplant them. It can be easily integrated into the histopathological diagnosis routine, in which tissue is fixed, stained, visually examined and evaluated for abnormalities. These visible images of the stained tissue biopsy can be simultaneously compared and correlated with the corresponding IR images either by the pathologist or by other automated computational means.

As an example of this approach, we present FTIR spectral imaging data derived from a series of human prostate biopsies. Like single point FTIR spectroscopic techniques, FTIR spectroscopic imaging quantitatively assesses biochemical variance within the sample, but unlike conventional spectroscopic methods it preserves spatial information and allows the data to be displayed as an image. Implementation is a relatively straightforward adaptation of single-point instrumentation. The low energy associated with IR radiation also means that the sample is not damaged during data acquisition, allowing questionable areas within the tissue sections to be examined multiple times. Additionally, data acquisition is considerably more rapid than single point spectroscopic techniques that attempt to spatially map the tissue and therefore, the possibility exists that the technique could evolve into a real-time diagnostic aid. Further, because thousands of spectra are generated within each data set, statistical analyses to accurately assess trends and differences in the tissue in question can be employed. This results in a powerful methodology with the potential to provide both rapid and accurate diagnostic information.

A preliminary impediment to the application of FTIR spectroscopic imaging as an aid for cancer diagnosis is the separation of data into classes associated with each tissue type. In other words, because the tissue sampled within any given field of view is heterogeneous, and biochemical variance is known to occur across these tissue types as well as with disease progression, spatial domains must be examined independently. The two basic tissue types which comprise the prostate can be described as connective tissue, or non-glandular tissue, and epithelial tissue, or glandular tissue. The two basic tissue types which comprise the prostate can be described as connective tissue, or non-glandular tissue, and epithelial tissue, or glandular tissue. Connective tissue provides structural and metabolic support for other tissues and organs throughout the body and usually contains blood vessels which mediates the exchange of nutrients, metabolites, and waste products between tissues and the circulatory system. Additionally, loose connective tissues act as a biological packing material between cells and other tissues with more specific functions. The epithelia are a diverse group of tissues which, with rare exceptions, cover or line all body surfaces and cavities. Epithelium, such as the epithelium found in the prostate, is primarily involved in secretion, and is arranged into structures called glands. Glands are invaginations of epithelial surfaces which are formed during embryonic development by proliferation of the epithelium into underlying tissues. Epithelia in the prostate are almost entirely composed of closely packed cells with minimal intercellular material between them. The majority of prostatic malignancies are adenocarcinomas which originate in the epithelial tissues.

Separation of tissue types presents particular difficulties in glandular organs such as the prostate because the epithelial regions are distributed throughout the entire organ and not concentrated solely on the surface. This is in contrast to organs such as cervix, colon, and esophagus, in which the epithelium lines the organ cavity in a more clearly delineated manner. Thus, prostate tissue is much more heterogeneous than tissue types which consist of a discrete bilaminar pattern. Because the glandular to non-glandular tissue ratio alters dramatically between different zones of the prostate, biopsy samples routinely contain variable amounts of the two tissue types. Differences resulting from the incorporation of varying amounts of these tissue types into each infrared spectrum has previously been mistaken as variation resulting from disease progression. As a result, separation of tissue types is the first critical step in making a meaningful spectral classification scheme for comparisons between normal and malignant tissue.

In this manuscript, we apply Fuzzy C-Means clustering, a particular form of Cluster Analysis, to the separation of distinct tissue types in human prostate biopsies. The need to group or classify data within complex and overlapped data sets is a problem that constantly arises in mathematics and science. Significant research has been devoted to the development of algorithms which attempt to automatically select a series of parameters that divide data into classes in such a way that the objects grouped in the same class are very similar, and the objects in different classes are quite distinct. Cluster analysis, and in particular Fuzzy C-Means clustering, are techniques that can be applied to this end. Fuzzy C-Means clustering is an unsupervised, iterative classification algorithm that can be used to partition a set of spectra into groups of similar spectra, creating a fuzzy membership map and a centroid spectrum for each of a specified number of classes. The algorithm relies on the Euclidean distances between the test spectrum and the centroid spectra to generate a fuzzy membership vector, which

describes the relative probabilities of membership of that spectrum to each of the classes. The elements of the fuzzy membership vectors are used to construct weighting factors, which in turn are used to calculate new centroids for the classes. The new centroids are subsequently used to calculate a modified set of fuzzy membership indices, and the algorithm goes through this iterative process until these indices converge. In this manuscript, we will present infrared spectral images which illustrate the effectiveness of Fuzzy C-Means clustering in partitioning the connective and epithelial tissues in a sample of human prostate tissue. Furthermore, the spectral differences evident in the centroid spectra derived for each tissue type will be discussed. Finally, we will apply the centroid spectra from one data set to the separation of tissue types in a different data set. These approaches provide a much more exact and statistically robust means to compare similar tissue types across many different tissue sections and provide a basis whereby comparisons and therefore a distinction can be made between normal and malignant tissue.

# 2. MATERIALS AND METHODS

# 2.1 Tissue preparation

Human prostate tissue samples were obtained from subjects already undergoing sextant needle biopsy or excisional biopsy surgical procedures. The tissue was immediately frozen, and kept frozen until sectioning. Sections were cut ( $10 \mu m$ ) on a cryostat, mounted onto 2 mm thick calcium fluoride ( $CaF_2$ ) disks, and stained with a standard pathological stain, hematoxylin and eosin (H&E), prior to performing FTIR imaging experiments. Tissue samples were processed in complete accordance with conventional histopathologic protocols, the only deviation being the use of a  $CaF_2$  window as substrate instead of a glass slide.

# 2.2 Chemical samples

Collagen type II from bovine nasal cartilage, glycogen from rabbit liver, DNA sodium salt from human placenta, RNA from calf liver, and mucin from bovine submaxillary glands were all purchased from Sigma-Aldrich, Inc. Spectra were recorded at  $16~\mathrm{cm^{-1}}$  spectral resolution using a Bomem Michelson MB series FTIR spectrometer equipped with a liquid nitrogen cooled MCT detector. This spectral resolution was chosen so that the data could be compared using similar conditions to those used to record the imaging data.

#### 2.3 Data acquisition and analysis

FTIR imaging data were collected with a spectroscopic imaging system developed in this laboratory and described previously.  $^{10,11}$  The instrument consists of a step scan interferometer, microscopic image formation optics, and an IR FPA detector. In this arrangement, the emission from a ceramic globar is modulated by a modified step scan interferometer (Manning Applied Technology Inc, Troy ID and Spectral Dimensions, Inc, Olney, MD) and focused onto the sample by a Cassegranian 15x objective (Spectra-Tech, Shelton, CT). The transmitted radiation is then imaged onto a liquid nitrogen cooled MCT FPA detector (Santa Barbara Focal Plane, Goleta, CA) using a matched Cassegranian objective. The MCT FPA detector, consisting of 64x64 pixels each 61x61 µm, has a spectral range of 2-10.5 microns. Data were collected at  $16 \text{ cm}^{-1}$  spectral resolution with an interferometer step rate of 1 Hz. At each interferometer step, a total of 128 frames were collected at 210 Hz, using a 0.14 ms integration time per frame. The total data collection time per each individual image cube was approximately eight minutes and consisted of 512 image planes and a total of 4096 interferograms, corresponding to the 64x64 image pixels.

Individual interferograms were apodized and Fourier transformed to create a series of frequency resolved images and spectra. These single beam spectra were divided by an averaged background spectrum to yield transmittance spectra and images, which were subsequently converted to absorbance (OD) images and spectra. A simple two point baseline correction was applied and the spectra were normalized to the Amide I peak at approximately 1650 cm<sup>-1</sup>. All data analysis was performed with ISys (Spectral Dimensions, Inc, Olney, MD), a spectral image processing program which integrates the acquisition, visualization, preprocessing (spatial and spectral), and classification of hyperspectral image cubes. ISys is written in the Matlab (Mathworks, Natick, MA) programming language, and can import and export a variety of different file formats. It supports spatial and spectral Fourier Transforms, Kramers-Kronig transforms, a variety of cube, image, and spectral arithmetic operations, and spatial and spectral filtering options. Classification options include both chemometric (PCA, PLS, MLR, Factor Analysis) and statistical pattern recognition (Mahalanobis Distance, Linear Discriminant Analysis, Fuzzy C-Means) algorithms.

# 3. RESULTS AND DISCUSSION

The initial centroid spectra used in the Fuzzy C-Means algorithm were defined from a data set containing well delineated epithelial and connective tissue domains. A total of twelve high quality infrared spectra, four from epithelial tissues, four from regions corresponding to connective tissues, and four from the lumen of ducts were selected according to pathological classifications. These starting spectra were then used to partition all the data within the same image cube, containing 4096 spectra, into three distinct classes; secretions, epithelial, and connective tissues. An inherent problem in the use of clustering algorithms in practice is the difficulty of validating the resulting data partition. FTIR spectroscopic imaging, however, circumvents this drawback because the resulting data separation can be displayed as an image and compared with sample morphology. In this manner cluster validity can be readily assessed. Comparison of the visible H&E stained images to the IR images generated by the Fuzzy C-Means clustering algorithm was used to evaluate the success of the separation. Figure 1 demonstrates such a comparison, highlighting the separation of the three domains in the data set from which the initial spectra were chosen. By viewing the images, it is clear that the domains classified as secretions by the Fuzzy C-Means algorithm, shown in image 1B, correlate with the lumen of the ducts as seen in the visible image displayed in figure 1A. Additionally, the epithelial tissue domain generated by the algorithm, image 1C, corresponds to cellular regions of the ducts. Likewise the connective tissue image, shown in 1D, highlights the areas of supporting tissue surrounding the ducts. These

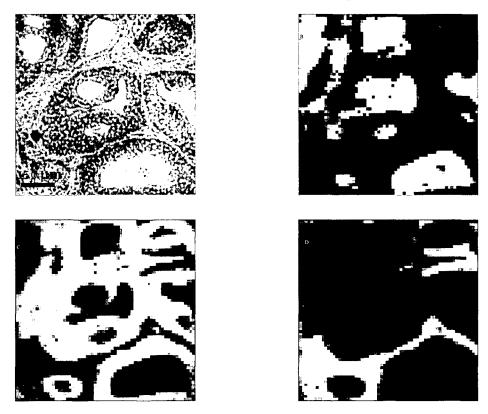


Figure 1. Visible brightfield image of an H&E stained section of malignant human prostate tissue, image A, and corresponding IR spectroscopic images. The IR images generated by the Fuzzy C-Means algorithm delineate B. prostatic secretions, C. epithelial tissues, D. connective tissue

separations are consistent with the pathologically defined morphology and demonstrate the success of the Fuzzy C-Means algorithm in automatically partitioning data acquired from an inhomogeneous prostate biopsy sample with the use of a few 'seed' spectra. While this particular implementation is partially supervised by the use of three small starting classes it is also possible to perform the same analysis in a completely unsupervised manner using randomly selected spectra from within a given data set.

Proc. SPIE Vol. 4259

Figures 2, 3, and 4 display the Fuzzy C-Means centroid spectra of the epithelial, connective tissue, and fluid filled domains as well as IR spectra of some of the major biochemical components present in the tissue. Because the Fuzzy C-Means algorithm continuously refines the initial centroid spectra based on class membership, their examination can assist in the identification and visualization of trends particular to a tissue type or region of the sample. By viewing the centroid spectra it is clear that the spectra of all three domains are dominated by contributions from protein moieties. This is consistent with the known chemical composition of the three tissue types and is witnessed by the characteristic strong protein, amide I and amide II absorption bands, present at approximately 1650 cm<sup>-1</sup> and 1530 cm<sup>-1</sup> respectively.

Although all three centroid spectra are dominated by protein absorptions, closer examination reveals subtle differences characteristic of their origin from a particular tissue type. For instance, epithelial tissue is typically composed of approximately 60% protein and 25% nucleic acids, although the composition will vary depending on the organ type, the cell division cycle, and several other factors. The epithelial centroid spectrum, shown in 2A, does have significant protein contributions but it also contains absorption bands characteristic of DNA and RNA (spectra shown in figures 2B and 2C respectively). Nucleic acid contributions are seen as increased absorption intensities at 1071, 1084, 1095, and 1245 cm<sup>-1</sup>. Increased spectral intensity attributable to nucleic acids is thought to be indicative of cancer progression due to the presence of more nuclear material as a result of enhanced cell proliferation. Another component which is generally considered to be a specific cellular differentiation material is glycogen. Molecules such as glycogen provide the energy for ATP synthesis, which is upregulated in malignant tissues. Thus as the epithelium in diseased regions commence rapid division, both

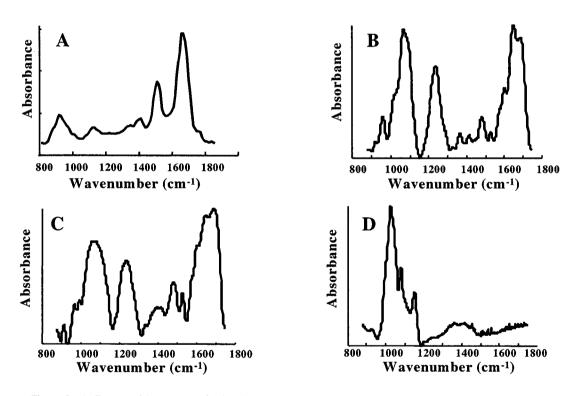


Figure 2. A. IR centroid spectrum of epithelial tissue generated from the data set shown in figure 1. Also shown are several IR spectra of pure components found in the epithelial tissues in the prostate gland; B. DNA, C. RNA, D. glycogen

glycogen and nucleic acid concentrations vary. Glycogen peaks can be seen at 1028, 1045, 1078, and 1115 cm<sup>-1</sup>, illustrated in figure 2D, and in addition to nucleic acids may be responsible for the increase in intensity in the 900 to 1300 cm<sup>-1</sup> spectral region seen in the epithelial tissue centroid spectrum (2A).

In contrast to epithelial tissues, connective tissue has little or no contribution from cellular materials such as glycogen or nucleic acids. The fibrous components of connective tissue consist predominately of collagen and elastin. Collagen is the main fiber type found in most supporting tissues and is the most abundant protein in the human body. Its most notable function is the provision of tensile strength. Elastin is not abundant in the prostate and is typically found in viscera whose function necessitates stretching and elastic recoil such as the lungs and blood vessels. Comparison of the connective tissue centroid spectrum, shown in 3A, with a spectrum of pure collagen, figure 3B, shows the expected similarity. Also, the increase in intensity in the 900-1300 cm<sup>-1</sup> spectral region resulting from the presence of nucleic acids and glycogen is considerably less pronounced in the connective tissue centroid spectrum.

The secretory cells of the prostate contribute a wide variety of products to the seminal plasma, some of which are thought to have diagnostic significance. Variations in the chemical composition of these secretions can be probed by examining regions which correspond to the lumen of ducts. The most widely recognized seminal plasma in the prostate is prostate-specific antigen (PSA) which is measured in serum prostate-specific antigen testing. PSA is a glycoprotein made almost exclusively by prostate tissue, which, in high concentrations, is associated with the presence of prostate cancer. Although PSA screening has been widely embraced by medical and lay communities alike for the early detection of prostate cancer, it has several drawbacks. The most notable is that its elevation is not specific to malignancy and can occur in several benign conditions such as benign prostatic hyperplasia (BPH), prostatitis, prostate infarction, and urinary retention, or just simply as a result of aging. It is possible that coupling a PSA measurement with the concentration of other chemicals thought to vary with prostate cancer progression will provide increased diagnostic accuracy. One example is the appearance of mucin secretions, Several types of prostate cancer are known to secrete a distinctive pale blue mucin. The presence of mucin is clinically significant since normal prostate tissue and benign prostate conditions are rarely characterized by mucin secretions. Thus, it is possible that elevated levels of both mucin and PSA, or the coupling of these parameters with changes identified in the connective tissues and epithelium could be more diagnostically rigorous than PSA testing alone. Figure 4 displays the centroid spectrum of prostatic secretions as well as a pure component spectrum of mucin. Although it doesn't appear that the secretion centroid spectrum contains mucin in this instance, the distinctive appearance of mucin indicates the ease with which it should be identifiable.

As a further test of the utility of these techniques to classify tissue types, we apply the previously calculated centroid spectra shown in figures 2, 3, and 4 to the classification of tissue obtained from the same biopsy, but from a completely different

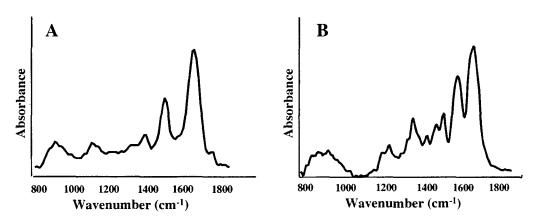


Figure 3. A. IR centroid spectrum of connective tissue in the human prostate gland B. IR spectrum of collagen

spatial location. The ability to use the centroid spectra generated from one data set to partition another data set is important because tissue type domains are often highly convoluted, and in some cases it is difficult or impossible to confidently identify the initial spectra to be used in the classification. Even in normal histological samples, morphologic features can be challenging to evaluate. Studies have concluded that focal atrophy in the prostate is a manifestation of both aging and inflammation. Deviations from normal morphology are often present as early as 30 years of age. This is particularly relevant since the incidence of prostatic adenocarcinoma is positively correlated with age. Because the prevalence, extent, and severity of focal atrophy progressively increase with age, most prostates sampled by needle biopsy are quite heterogeneous in histologic composition. Although these deviant histologic patterns seldom have clinical significance, their distinction from adenocarcinoma or BPH is sometimes difficult. Thus, as it is difficult enough to define normal tissue

domains in this age group, it is even more troublesome to differentiate tissue heterogeneity from disease progression. Further complications arise once metastasis has occurred because the epithelial and connective tissues become highly intermingled,

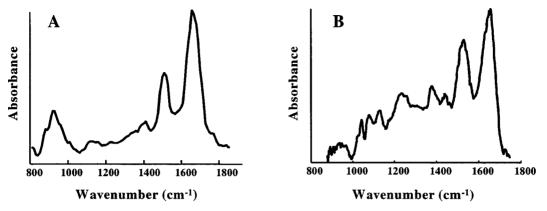


Figure 4. A. IR centroid spectrum of prostatic secretions B. IR spectrum of mucin

making the identification of pure tissue type domains even more challenging. In order to accomplish the separation necessary for spectral diagnosis, an unsupervised rapid method for separation of various tissue domains is often necessary. For these reasons, it is important to be able to easily separate highly convoluted tissue domains in histological sections in which abnormalities may exist, without having to define centroid spectra from the data set. The ability to numerically compare spectral profiles from known tissue types from within a database, with unknown spectra from new tissue sections provides a powerful tool to begin to untangle these issues.

Figure 5 shows the Fuzzy C-Means algorithm separation of tissue types in an FTIR imaging data set obtained from a different location on the same biopsy sample. This region was classified as malignant and poorly differentiated, and from viewing the visible image, it is apparent that the tissue type domains are much less well delineated than in image 1A. Thus, it is advantageous to be able to separate the tissue type regions without having to define centroid spectra from this data set. As before, we can get some indication of the success of the classifications by comparison of the IR images with the visible stained H&E image. Again, the domains displayed in figure 5 generated by the Fuzzy C-Means algorithm appear to correlate well with the visible image. The success of the separation serves as an important preliminary test for application of such an algorithm to an automated medical process.

# 4. CONCLUSIONS

Although existing cancer diagnostic procedures are highly successful, room for significant improvement exists. In order to gain widespread acceptance in the medical community, cancer detection techniques must be amenable to analysis by pathologists. For this reason, FTIR spectral imaging is particularly attractive because it can work seamlessly in conjunction with standard histopathological protocols. However, because the human prostate gland is a composite organ, made up of several glandular and non-glandular tissue types which vary in abundance and appearance with a number of factors, a means of examining spectral variance particular to each tissue type is needed as a perfunctory step in the application of FTIR spectral imaging as an augment to cancer diagnosis methodologies. The rationale for the examination of chemical variance in each tissue type independently lies in the fact that all tissue types have chemical components in common. These components change distinctly in each tissue type with disease progression and thus it is important that the trends be examined for each specific tissue type. For instance, as an important energy source for cells, glycogen is also stored in high concentrations in some forms of connective tissues where it is used to provide energy for such activities as the contractile motion of muscles. Changes in glycogen levels may only be diagnostically significant in epithelial tissue and the contamination of the spectrum from multiple tissue types might result in an incorrect diagnosis. This example explicitly illustrates the motivation for the examination of biochemical trends in each tissue type independently. In addition, the combination of the assessment of changes in several biochemical markers simultaneously may provide higher accuracy than reliance on a single moiety, such as PSA.

We have demonstrated a preliminary step in the application of FTIR spectroscopic imaging as an adjunct technique for prostate cancer diagnosis. The ability to examine chemical variation in different tissue types in an unsupervised manner is a necessary first step in the implementation of any spectral imaging technique as an adjunct to current cancer diagnosis

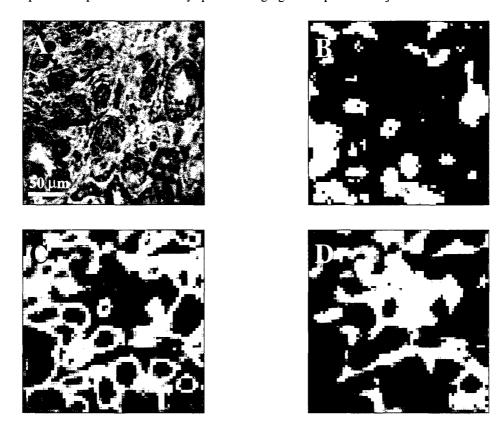


Figure 5. Visible brightfield image of an H&E stained section of malignant human prostate tissue and corresponding IR spectroscopic images. The IR images again delineate tissue types, but are generated by the Fuzzy C-Means algorithm using centroid basis spectra shown in figures 2, 3, and 4.

protocols. With the routine incorporation of computers and digital imaging methods into hospitals and other clinical settings it is easy to envision how FTIR spectral imaging could be readily adopted by the medical community and how the technique might be employed for the real-time analysis of biopsy samples. Examination of the visible H&E stained image will allow continued pathological assessment of the tissue, while comparison of the visible and infrared images can substantiate questionable diagnoses. With further research and development we anticipate that infrared spectroscopic imaging will ultimately provide a strong foundation for visualizing the presence, and quantifying the extent of carcinoma.

# **ACKNOWLEDGEMENTS**

We would like to acknowledge the contributions of Dr. John Gillespie, NCI and Dr. Ira Levin, NIDDK.

#### REFERENCES

- 1. Cancer Manual 9th Edition, R.T. Osteen Ed., American Cancer Society, Boston, MA, 1996.
- 2. L. Chiriboga, P. Xie, H. Yee, D. Zarou, D. Zakim, and M. Diem, "Infrared spectroscopy of human tissue: IV. Detection of dysplastic and neoplastic changes of human cervical tissue *via* infrared microscopy", *Cell. Mol. Biol.*, 44, 219-229, 1998.
- 3. E. Benedetti, E. Bramanti, F. Papineschi, I. Rossi, and E. Benedetti, "Determination of the Relative amount of Nucleic Acids and Proteins in Leukemic and Normal Lymphocytes by Means of Fourier Transform Infrared Microspectroscopy", *Appl. Spectrosc.*, **51**, 792-797, 1997.

- 4. P.T. Wong, R.K. Wong, T.A. Caputo, T.A. Godwin, B. Rigas, "Infrared spectroscopy of exfoliated human cervical cells: Evidence of extensive structural changes during carcinogenesis", *Proc. Natl. Acad. Sci. USA*, **88**, 10988-10992, 1991.
- 5. K. Yano, S. Ohoshima, Y. Shimizu, T. Moriguchi, H. Katayama, "Evaluation of glycogen level in human lung carcinoma tissues by an infrared spectroscopic method", *Cancer Letters*, **110**, 29-34, (1996).
- R. Manoharan, K. Shafer, L. Perelman, J. Wu, K. Chem, G. Deinum, M. Fitzmaurice, J. Myles, J. Crowe, R.R. Dasari, M.S. Feld, "Raman Spectroscopy and Fluorescence Photon Migration for Breast Cancer Diagnosis and Imaging", Photochem. Photobiol., 67, 15-22, 1998.
- 7. H.G. Burkitt, B. Young, and J.W. Heath, Wheater's Functional Histology 3<sup>rd</sup> Edition, Churchill Livingstone, New York, NY, 1993.
- 8. H.G. Burkitt, A. Stevens, J.S. Lowe, B. Young, Wheater's Basic Histopathology 3<sup>rd</sup> Edition, Churchill Livingstone, New York, NY, 1996.
- 9. R. Bezdek and F. Ehlich, "FCM: The fuzzy C-means clustering algorithm", Comp. Geoci., 10, 191-203, 1984.
- 10. E.N. Lewis, P.J. Treado, R.C. Reeder, G.M. Story, A.E. Dowrey, C. Marcott, I.W. Levin, "Fourier transform spectroscopic imaging using an infrared focal-plane array detector", *Anal Chem.*, **67**, 3377-3381 1995.
- 11. E.N. Lewis, I.W. Levin, P.J. Treado, "Spectroscopic imaging devices employing imaging quality spectral filters", U.S. Patent No. 5,377,003, 1994.
- 12. M. Diem, S. Boydston-White, and L. Chiriboga, "Infrared spectroscopy of cells and tissues: shining light onto a novel subject", *Appl. Spectrosc.*, **53**, 148A-161A, 1999.
- 13. G.B. Baretton, T. Vogt, S. Blasenbreu, U. Lohrs, "Comparison of DNA ploidy in prostatic intraepithelial neoplasia and invasive carcinoma of the prostate: an image cytometric study", *Hum. Pathol.*, **25**, 506-513, 1994.
- 14. D.C. Malins, N.L. Polissar, and S.J. Gunselman, "Models of DNA structure achieve almost perfect discrimination between normal prostate, benign prostatic hyperplasia (BPH), and adenocarcinoma and have a high potential for predicting BPH and prostate cancer", *Proc. Natl. Acad. Sci. USA*, 94, 259-264, 1997.

# Spectral Karyotyping (SKY) in Hematologic Neoplasia.

Birgitte S. Preiss\*<sup>a</sup>, Rikke K. Pedersen<sup>a</sup>, Gitte B. Kerndrup<sup>a</sup>
<sup>a</sup>Institute of Pathology – Chromosome Laboratory, Odense University Hospital

\*Institute of Pathology - Chromosome Laboratory, Odense University Hospital, DK-5000 Odense C. Phone: +45 6541 4824, Fax: +45 6591 2943, E-mail: birgitte.preiss@ouh.dk.

#### **ABSTRACT**

From November 1, 1997 till November 1. 2000 we have investigated 204 cases of acute myeloid leukemia (AML) (n=95), acute lymphatic leukemia (ALL) (n=40), myelodysplastic syndrome (MDS) (n=11), chronic myeloid leukemia (CML) (n=9), chronic lymphatic leukemia (CLL) (n=4) and non-Hodgkin lymphoma (NHL) (n=45) cytogenetically, using G-band analysis and spectral karyotyping (SKY). By SKY we were able to detect the abnormal clones in all cases but 9. In the G-band preparations these cases showed very few abnormal mitoses. The SKY either extended or confirmed the G-band findings in 94% of those with an abnormal karyotype. Cryptic translocations (translocations not suspected from the G-band karyotype) were found in 71 cases (26 AML, 9 ALL, 5 MDS, 2 CLL and 29 NHL).

We find SKY a powerful adjuvant diagnostic tool that does not compromise one of the advantages of karyotyping techniques, the analysis of the entire genome which, in contrast to molecular biological techniques, still leaves the possibility to get more answers than questions posed.

Keywords: G-band cytogenetics, hematologic neoplasia, leukemia, lymphoma, myelodysplastic syndrome, spectral karyotyping,

# 1. INTRODUCTION

In solid tumors and also in hematologic neoplasia it is often difficult to characterize the chromosomal abnormalities in full. In acute myeloid (AML) and acute lymphatic leukemia (ALL) it is important to obtain a complete karyotype since the clonal chromosome aberrations are of independent prognostic significance and they may also allocate the patients to different treatment regimens [1.2]. Although we, in our institution, obtain mitoses in almost all acute leukemias, myelodysplastic syndromes (MDS) and chronic myeloid leukemia (CML) patients at diagnosis we find that e.g. 37% and 43% of the AML and ALL patients with clonal chromosome aberrations show an incomplete karyotype by G-banding. By single- or oligotarget FISH it will be impossible to characterize but a few cases, money and amount of material being the limiting factors. Instead multi-target FISH seems an attractive solution as an adjuvant diagnostic tool.

# 2. MATERIAL AND METHODS

# 2.1 Patients

From November 1, 1997 till November 1, 2000 we have investigated 204 cases of AML (n=95), ALL (n=40), MDS (n=11), CML (n=9), chronic lymphatic leukemia (CLL) (n=4) and non-Hodgkin lymphoma (NHL) (n=45). As we consider as complete a G-band karyotype as possible paramount in our diagnostic investigations, we did not have material left to perform a SKY analysis on all cases with a G-band karyotype during this period.

The AML, ALL and NHL cases are derived from population based materials covering approximately 1/3 of the adult Danish population and 1/2 of the children, and we therefore know that the primary adult AML and pediatric ALL cases included in this study represents 58% (88/151) and 39% (27/69), respectively. All primary adult ALL cases diagnosed in the period are included.

# 2.2 Methods

G-band karyotyping was carried out after direct harvest and/or short-term culture of bone marrow or lymph node tissue as described earlier [3]. Mitoses karyotyped for the 204 cases: range 20-38, mean 25, median 25. The SKY analysis was carried out according to the manufacturer's instructions (Applied Spectral Imaging<sup>TM</sup>, Mikdal HaEmek, Israel).

# 3. RESULTS

From Table 1 appears the FAB-subtypes, M/F ratio, median age and age range for the patient groups investigated in this material. The AML subtypes of the 88 primary diagnoses were: M0 - 7% (8% in all patients diagnosed in the period (n=151)), M1 - 19% (23%), M2 - 43% (42%), M3 - 3% (2%), M4 - 8% (7%), M5 - 6% (5%), M6 - 5% (5%), M7 - 9% (8%). M/F ratio, median age and age range for all AML patients diagnosed in the period were 1.04, 69 years and 16-93 years, respectively.

Diagnosis		Patient no.	M/F-ratio	Age-range	Median age
AML <sup>1</sup>		n=91 <sup>2</sup>	0.78	16-88y	66y
ALL <sup>3</sup>		n=39 <sup>4</sup>	0.95	1-68y	5y
MDS <sup>5</sup>		n=10	1.5	25-95y	66y
CML <sup>6</sup>	Chronic phase Blast crisis	n=5 n=4	0.8	39-84y	52y
CLL <sup>7</sup>		<b>n=</b> 4	3.0	56-85y	59y
NHL8		n=45	1.37	11-97y	65y

Footnote to Table 1.

Table 1: Diagnoses, subtypes, M/F-ratio, age range and median age for the 198 patients included in this study.

Table 2 shows the frequencies of abnormal karyotypes according to diagnosis and the percentage of cases where SKY extended or confirmed the G-band findings. In the largest patient group, AML, 145 (96%) diagnosed in the period had a cytogenetic investigation performed at diagnosis. 63 (43%) patients had a normal karyotype and 82 (57%) an abnormal karyotype.

	Diagnosis	G-band Karyotype			Nos. where SKY extended or	
	9	Abnormal /		% Abnormal	confirmed G-banding (%)	
	$AML^1$	70	25	74	91 (96) <sup>2</sup>	
1	ALL <sup>3</sup>	34	6	83	37 (93) <sup>4</sup>	
	MDS <sup>5</sup>	10	1	91	11 (100)	
	CML	9	0	100	9 (100)	
	CLL	4	0	100	4 (100)	
	NHL	44	1	98	43 (96) <sup>6</sup>	

Footnote to Table 2.

<sup>1.</sup> AML: Acute myeloid leukemia. 2. M0: 6, M1: 17, M2: 38, M3: 3, M4: 7, M5: 5, M6: 4, M7: 8, Relapse: 3. 3. ALL: Acute lymphatic leukemia. 4. 2 patients were investigated in relapse only. 5. MDS: Myelodysplastic syndromes. 6. CML: Chronic myeloid leukemia. 7. CLL: Chronic lymphatic leukemia. 8. NHL: Non-Hodgkin lymphoma.

<sup>1. 4</sup> patients were investigated twice. 2. Excluding 4 patients where the abnormal clone was not found in the SKY preparation. 3. 1 patient was investigated twice. 4. Excluding 3 patients where the abnormal clone was not found in the SKY preparation. 5. 1 patient was investigated twice. 6. Excluding 2 patients where the abnormal clone was not found in the SKY preparation.

Table 2: Diagnoses, nos. with abnormal G-band karyotype and nos. with spectral karyotyping (SKY) extending or confirming the G-band karyotype.

A normal G-band karyotype was found in 33 of the 204 cases investigated, and in all these cases, except one, SKY confirmed the normal karyotype. This ALL patient with a normal G-band karyotype, showed a t(12;21) by SKY. The SKY extended or confirmed the abnormal karyotype in 91 AML and 37 ALL cases, respectively. In the remaining patients (MDS, CML, CLL and NHL) SKY extended or confirmed G-band karyotypes in 97% (MDS: 100%, CML: 100%, CLL: 100% and NHL: 96%). In 9 of the 204 cases the abnormal clone could not be found in the SKY preparation. These cases showed 2 – 16 abnormal mitoses (median 6) out of a median of 25 G-band analysed mitoses (range 25 – 28). The rest of the cases with chromosomal aberrations showed 2 – 38 abnormal mitoses (median 21.5).

71 of the 204 cases showed a total of 206 cryptic translocations. 126 of the 132 marker chromosomes found by G-banding were characterized by SKY. In 3 cases the marker chromosome was too small to be characterized by SKY. In 2 cases the origin of the chromosomal material could be established, but the origin of the centromeres could not. In 1 case the clone with a marker chromosome consisted of only 2/25 mitoses in the G-band preparation and could not be found in the SKY preparation (hybridization area 10x10 mm).

Fig. 1 shows the number of times individual chromosomes were involved in an aberration in G-band and SKY preparations, respectively, in the investigated AML cases. The chromosomes most often involved in G-band aberrations were: #5, #21, #7, #8, #17, #12, #11 and #15 in descending order. The chromosomes most often involved when SKY was carried out were: #5, #8, #7, #17, #21, #12, #11 and #3 in descending order.

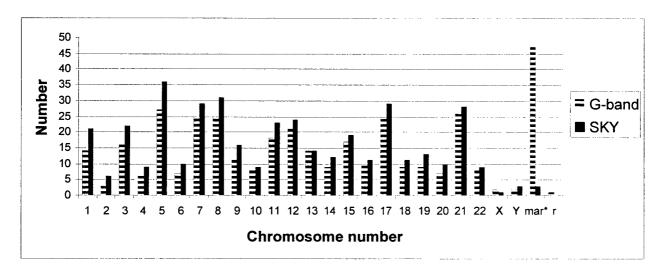


Fig. 1: Shows the number of times each chromosome was involved in an aberration in G-band and SKY preparations, respectively, in AML cases. \* In 2 cases the origin of the chromosomal material could be established but the origin of the centromeres could not and in 1 case the marker chromosome was too small to be characterized by SKY.

#### 4. DISCUSSION

For more than ten years cytogenetic aberrations have been recognized as independent prognostic factors in AML and ALL [4, 5]. Since 1986 and 1992 cytogenetic investigation by G-band has been one of the routine diagnostic tools used in ALL, AML and NHL patients in our institution. G-band karyotyping at our laboratory has a success rate of nearly 100% in AML and 99% in ALL and our frequencies of abnormal karyotypes correspond to literature published data of around 55-75% [4, 5, 6]. Over the years we have experienced, that in more than 1/3 of the AML and ALL patients with cytogenetic aberrations it has not been possible to fully characterize the chromosomal aberrations as marker chromosomes and added material are found in a substantial proportion of cases, and this is also the case for NHL and MDS patients. Therefore, to supplement the cytogenetic investigation in an attempt to characterize chromosomes involved in structural aberrations SKY was implemented from November 1, 1997. During the three year period that has passed since then, 151 patients have been diagnosed with AML at our institute. The 91 AML patients in this study have almost the same median age and age range as the 151 AML patients and they also have the same distribution of FAB subtypes. There are, however, more female patients,

relatively, among the 91 study patients, giving a lower M/F ratio, than in the background material. The single reason for performing SKY in only 91 AML patients was lack of material after G-banding in the remaining 54 cytogenetically investigated cases.

We performed 95 and 40 SKY investigations in 91 AML and 39 ALL patients, respectively, and we have been able to characterize all 62 marker chromosomes found by G-band karyotyping in these patients, except 3. In addition to characterizing marker chromosomes, SKY has also revealed 56 and 23 cryptic translocations in 26 AML and 9 ALL patients, respectively. By characterizing marker chromosomes and cryptic translocations, SKY extended the findings in 44% and 35%, respectively, of the AML and ALL cases with an abnormal G-band karyotype. This is in agreement with our earlier impression [7]. In the remaining AML and ALL cases with an abnormal G-band karyotype, SKY confirmed the findings except in 7 cases (4 AML and 3 ALL), where the abnormal clone could not be found by SKY. This was either due to the abnormal clones being small, or to the fact that there were only few and normal mitoses in the SKY preparation.

In all cases with a normal G-band karyotype, SKY confirmed the normal karyotype except in 1 ALL patient. By G-band analysis this patient showed 25 normal mitoses, however by SKY a t(12;21) was revealed in 4 mitoses.

In MDS, CLL and NHL cases with an abnormal karyotype, SKY extended the karyotype in 70%, 75% and 70%, respectively. In NHL the abnormal karyotypes are often more complex than in AML and ALL, which may explain this discrepancy.

In NHL patients the number of cryptic translocations is relatively higher (97 cryptic translocations in 29/45 patients) than in AML (56 cryptic translocations in 26/91 patients) and ALL (28 cryptic translocations in 9/39 patients) patients. This may also be explained by more complex karyotypes in NHL.

In conclusion, in hematologic neoplasia SKY is a valuable adjuvant diagnostic tool that does not compromise one of the advantages of karyotyping techniques, the analysis of the entire genome in one hybridization. This is in contrast to single or oligotarget FISH and PCR techniques where you may only investigate for the presence or absence of a limited number of specific aberrations at once. Further, as clonal chromosomal aberrations are among the factors used at Odense University Hospital to stratify AML and ALL patients to different treatment protocols, it is important to obtain as complete a karyotype as possible. The SKY is in this respect a valuable technique. Lastly, the prognostic value of SKY remains to be elucidated in larger cohorts of patients with hematologic neoplasia.

# **ACKNOWLEDGEMENTS**

We are greatly indebted to laboratory assistants Birthe Faurskov, Ulla Munk, Anne Nibe and Anne Grethe Sørensen for their expert technical assistance.

# REFERENCES

- 1. K. G. Schmidt, B. S. Preiss, G. B. Kerndrup, "Treating AML patients with repeated courses of mitoxantrone and high-dose cytosine arabinoside yields promising results in an unselected population of patients with normal karyotype," *Blood.* 94 (suppl 1), 298a, 1999.
- 2. K. G. Schmidt, "High-risk AML patients treated with fludarabine-etoposide-G-CSF-mitoxantrone-high-dose ara C ("FLEGMA")," *Blood.* 94 (suppl 1), 237b, 1999.
- 3. R. K. Pedersen, A. G. Sorensen, N. T. Pedersen, K. G. Schmidt, G. B. Kerndrup, "Chromosome aberrations in adult Hodgkin disease in a Danish population based study," *Cancer Genet Cytogenet.* 110, pp. 128-132, 1999.
- 4. D. Grimwade, H. Walker, F. Oliver, K. Wheatly, C. Harrison, G. Harrison, J. Rees, I. Hann, R. Stevens, A. Burnett, A. Goldstone, "The importance of diagnostic cytogenetics on outcome in AML: Analysis of 1,612 patients entered into the MRC AML 10 trial," *Blood.* 92, pp. 2322-2333, 1998.
- 5. L. M. Secker-Walker, H. G. Prentice, J. Durrant, S. Richards, E. Hall, G. Harrison, "Cytogenetics adds independent prognostic information in adults with acute lymphoblastic leukaemia on MRC trial UKALL XA," *Br. J. Haematol.* **96**, pp. 601-610, 1997
- 6. C.-H. Pui, W. M. Crist, "Cytogenetic abnormalities in childhood acute lymphoblastic leukaemia correlates with clinical features and treatment outcome," *Leukemia Lymphoma*. 7, pp. 259-274, 1992.
- 7. G. B. Kerndrup, E. Kjeldsen, "Acute leukemia cytogenetics An evaluation of combining G-band karyotype with multi-color spectral karyotyping," *Cancer Genet Cytogenet*. In press, 2000.

Structure of mouse spleen investigated by 7 color fluorescence imaging

Hiromichi Tsurui\*a, d, Shin-ichiro Niwab, Sachiko Hirosea, Ko Okumurac, d, Toshikazu Shirai

<sup>a</sup>Dept. of Pathology, Juntendo Univ. Sch. Med.; <sup>b</sup>Sumitomo Electric Industries, Ltd.

<sup>c</sup>Dept. of Immunology, Juntendo Univ. Sch. Med.; <sup>d</sup>CREST, JST

**ABSTRACT** 

Multi-color fluorescence imaging of tissue samples has been an urgent requirement in current biology. As far as fluorescence

signals should be isolated by optical bandpass filter-sets, rareness of the combination of chromophores with little spectral

overlap has hampered to satisfy this demand. Additivity of signals in a fluorescence image accepts applying linear unmixing of

superposed spectra based on singular value decomposition, hence complete separation of the fluorescence signals fairly

overlapping each other. We have developed 7-color fluorescence imaging based on this principle and applied the method to the

investigation of mouse spleen. Not only rough structural features in a spleen such as red pulp, marginal zone, and white pulp,

but also fine structures of them, periarteriolar lymphocyte sheath (PALS), follicle, and germinal center were clearly pictured

simultaneously. The distributions of subsets of dendritic cells (DC) and macrophages (M\(\phi\)) were investigated by their

subset-specific antibodies such as NLDC-145, CD8, and CD11b. They were not identical as reported previously by other authors.

The expressions of general M\phi markers such as BM8, F4/80, MOMA2 and Mac3 around the marginal zone were imaged

simultaneously. Their inhomogeneous expressions were clearly demonstrated. These results show the usefulness of the method

in the study of the structure that consists of many kinds of cells and in the identification of cells characterized by multiple

markers.

Keywords: fluorescence spectral imaging, singular value decomposition, Fourier spectroscopy, linear unmixing, hyperspectral

imaging, hyper multicolor imaging

1. INTRODUCTION

Biological higher-order function is performed through the interaction of many components. So, it is indispensable to observe

many components simultaneously to understand the mechanism under which the system is operated. As for free cells,

fluorescence-activated cell sorter (FACS) has made it possible to identify even more than 10 molecules surface or inside of cells.

However, the number of colors simultaneously used for histological investigation is quite limited because the combination of

dyes having little spectral overlap is rare.

A fluorescence image can be described as a vector space and each spectrum in it behaves as a vector. This fact allows us to

isolate superposed spectra with large spectral overlap using linear unmixing based on singular value decomposition. Based on

Correspondence: E-mail: tsurui@med.juntendo.ac.jp; Telephone: 81-3-5802-1039; Fax: 81-3-3813-3164

Biomarkers and Biological Spectral Imaging, Gregory H. Bearman, Darryl J. Bornhop, Richard M. Levenson, Editors, Proceedings of SPIE Vol. 4259 (2001) © 2001 SPIE · 1605-7422/01/\$15.00

60

this principle, we have developed 7-color fluorescence imaging of tissue samples<sup>1</sup>. Here we show some hyper-multicolor images obtained by applying this method illustrating the detailed structure of the mouse spleen.

# 2. MATERIALS AND METHODS

#### 2.1 Instrumentation

Instruments used for data acquisition were almost same as described previously<sup>1</sup>. In brief, an imaging spectrometer SD-200 (ASI, Inc.) was attached to epi-fluorescence microscopy BX-60WI (Olympus Optical Co. Ltd.). The objective lenses used were Uplan Apo 20X/0.70 and Uplan Apo 40X/0.85. Memory of the computer attached to the system was increased to 512MB as to accept 628 X 488 pixels image. In addition to 3 filter sets Bl, Gr and Rd used in the previous study<sup>1</sup>, a filter-set, UV was used for obtaining the spectrum of UV-excited chromophore, Marina Blue. The constructions of these filter-sets are shown in Table 1 and the spectra of filter-set UV and Marina Blue are illustrated in Fig. 1.

Table 1. Construction of filter-sets

Filter set	Exciter	Dichroic mirror	Emitter
UV	330WB80	400DCLP	400ALP
ВІ	470F35	505DRLP	515EFLP
Gr	546F10	560DRLPO2	565EFLP
Rd	640F20	660DRLP	665EFLP

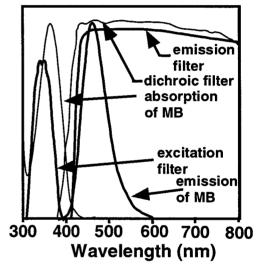


Figure 1. Spectra of Marina Blue and filter-set UV

# 2.2 Reagents

Monoclonal antibodies (mAbs) to CD4 (RM4-5), CD11b (M1/70), CD11c (HL3), CD16/32 (2.4G2), CD21/35 (7G6), CD45R/B220 (RA3-6B2), I-A<sup>d</sup>/I-E<sup>d</sup> (2G9), and Mac3 (M3/84) were purchased from BD Pharmingen (Franklin Lakes, NJ). MOMA-2 and F4/80 from Serotec Ltd. (Oxford, UK) and BM8 from Bachem, AG (Bubendorf, Switzerland), respectively. FDCM2 and CR-Fc, the fusion protein of mannose's cystein-rich domain and IgG's Fc-portion, were kindly provided by Dr. Marier H. Kosco-Virbois. Succinimidyl ester dyes Marina Blue, Alexa488, Alexa532, Alexa546, Alexa568 and Alexa594 and succinimidyl ester dyes Cy5 and Cy5.5 were purchased from Molecular Probes Inc. (Eugene, OR) and from Amersham Pharmacia-Biotech (Uppsala, Sweden), respectively. Peanut agglutinin (PNA) was obtained from Vector Laboratories Inc. (Burlingame, CA) and keyhole limpet hemocyanin (KLH) from Pierce Chemical Company (Rockford, IL), respectively. For Fig.

3, Zymosan BioParticle (Molecular Probes Inc.), Mac3, anti-CD11c, anti-CD4 and anti-CD45R/B220 were directly labeled with Marina Blue, Alexa546, Alexa568, Cy5 and Cy5.5, respectively. CD11b was indirectly labeled with Alexa488 through NHS-digoxygenin and anti-digoxygenin antibody (Roche Diagnostics, Mannheim, Germany). CR-Fc was indirectly labeled with Alexa594-conjugated anti-human IgG. For Fig. 4, FDCM2, anti-CD16/32, anti-CD11c, PNA and anti-CD45R were directly labeled with Alexa488, Alexa546, Alexa568, Alexa594 and Cy5 respectively. Anti-CD21/35 and anti- I-A<sup>d</sup>/I-E<sup>d</sup> were indirectly labeled with Alexa532 and Cy5.5 via biotin-streptavidin and digoxygenin-anti-digoxygenin systems, respectively. For Fig. 5, MOMA2 and Mac3 were directly labeled with Alexa488 and Alexa546, respectively. BM8 and F4/80 were indirectly labeled with Alexa532 and Alexa594 via biotin-streptavidin and digoxygenin-anti-digoxygenin systems, respectively.

#### 2.3 Specimens

For Fig. 3 and Fig. 5, an 8 weeks old female Balb/C mouse was injected i.v. with 200 µg of Zymosan BioParticle. Two hours later, its spleen was removed, embedded in OTC compound and frozen rapidly in liquid nitrogen. For Fig. 4, splenic tissues from Balb/c mice preimmunized twice at 8 and 11 weeks of age by applying intraperitoneal injections of 100 µg per mouse of KLH in Freund complete and incomplete adjuvants, respectively, were embedded in OCT compound—and rapidly frozen in liquid nitrogen. Blocks prepared as mentioned above were sliced at 4 µm thick, air-dried for 1 hour and stored at -20 C until use. After being fixed by acetone for 10 min, the cryosections were stained with several antibodies simultaneously by adding the mixture of labeled or tagged antibodies. Single color-stained specimen for each dye was also made for obtaining the authentic spectra to construct the spectral library.

# 3. RESULTS

# 3.1 Construction of the spectral libraries

Fig. 2 shows the spectral libraries constructed from the spectra obtained from single-color-stained images. Spectrum of each dye was the average of the 6 brightest points of the image. When excited with UV (Fig. 2a), Marina Blue-labeled Zymosan particle generated signals strong enough to provide a clear image at wavelength 450-500 nm. However, to remove the effect of auto-fluorescence completely, linear unmixing was performed using its cognate spectral library. In Fig. 3, auto-fluorescence of tingible body in some subset of M\$\phi\$ was used to evaluate their phagocytic activity toward apoptotic cells. Even though we have not thoroughly characterized auto-fluorescence in a mouse spleen yet, this auto-fluorescence was highly specific and found in the cells always adjoining apoptotic cells (not shown), and we tentatively call this phagosome "tingible body". When excited with BI (Fig. 2b), the spectrum of tingible body was remarkably differ from that of Alexa488. When excited with Gr (Fig. 2c), the spectrum of tingible body was differ from that excited with BI. This is not strange because tingible body may be a mixture of fluorogenic substances and its spectrum varies according to the excitation wavelength. The spectrum of tingible body was very close to those of Alexa568 and Alexa594 (Fig. 2c), yet could be isolated from them by linear unmixing. Fig. 2d shows the spectra of Cy5 and Cy5.5 obtained from images.

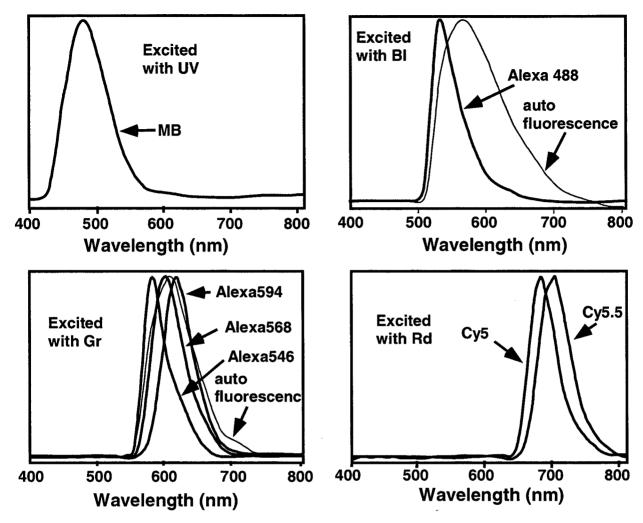


Figure 2. Spectra of dyes from images

# 3.2 Structure of white pulp

Fig. 3 shows isolated images of all the dyes used to stain, antibodies conjugated with which are indicated at lower-right corner of the images, respectively. Uplan Apo 20X/0.70 was used as objective lens. By assigning pseudo-color and superposing, any two or three images of them, one can construct color images (not shown). These images illustrate typical structure in a mouse spleen of a follicle lying astride a periarteriolar lymphocyte sheath (PALS). B220 was strongly expressed within the follicle and slightly suppressed in the marginal zone. Dendritic cells, characterized by CD11c<sup>+,</sup> distributed both in the PALS and in the marginal zone. It is notable that CD11b<sup>+</sup> dendritic cells located not only in the marginal zone, but in the PALS. Moreover, CD8<sup>+</sup> dendritic cells were recognized not only in the PALS, but in the marginal zone (not shown). CD4<sup>+</sup> cells, chiefly composed of T cells, are a major component of PALS. They distributed mainly in the PALS, however, a small fraction of them scattered in the

follicle. CR-Fc, the ligand of which is Sialoadhesin, specifically binds to marginal metallophilic M $\phi$  (MMM) in spleen. MMMs are situated at the margin of the white pulp running along the inner border of the marginal sinus (not shown). The image indicated "Auto-fl" was constructed of signals characteristic of tingible body. By superposing the images of CR-Fc, Zymosan-BP, and auto-fl, it was found that a little portion of MMMs bore tingible body or Zymosan-BP (not shown). Mac3 is mainly expressed on the marginal zone M $\phi$  (MZM) and the red pulp M $\phi$  (RPM). However, a very little portion of M $\phi$  in a follicle expressed Mac3.

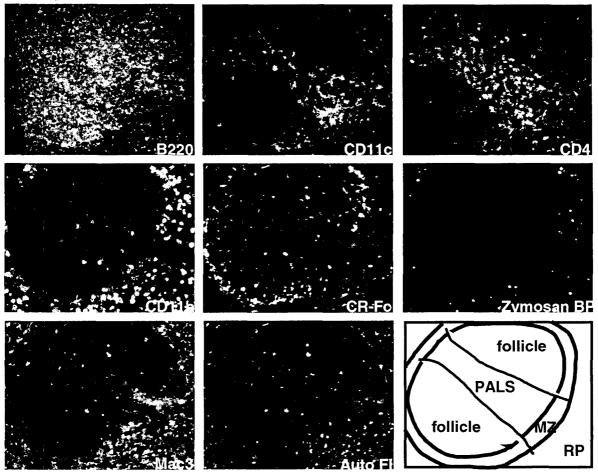


Figure 3. Structure of white pulp in mouse spleen

# 3.3 Structure of germinal center

A typical structure of a germinal center (GC) in a mouse spleen is illustrated in Fig. 4. It shows isolated images of all the dyes used for staining. Antibodies conjugated with the dyes are indicated respectively. Uplan Apo 20X/0.70 was used as objective lens. Germinal center is the site where affinity maturation of B cell receptor takes place. The essence of affinity maturation is the selection of the clones having the highest affinity to the stimulating antigen and the allowance of the survival authorized by

CD4<sup>+</sup> T cells. The affinity of B cell receptor (BCR) is thought to be evaluated by the interaction with the antigen or immune complex attached to the surface of follicular dendritic cells (FDC) via immunoglobulin receptors or complement receptors. Both a follicle and the marginal zone surrounding the white pulp were shown in the image stained with anti B220. Dendritic cells, specified by CD11c<sup>+</sup>, were seen both in the T cell area and in the marginal zone. It is worthy of notice that class II<sup>+</sup> cells fairly overlapped with dendritic cells. FDCs, characterized by FDCM2, extended to whole of the follicle. FDCM2 was highly expressed specifically in the GC, which was identified by B cells binding PNA strongly. Complement receptor<sup>+</sup> cells, represented as CD21/35<sup>+</sup>, also spread to whole the follicle, however, the intensity of the expression was divided into two levels. Strongly expressed cells covered the GC and they, as a whole, looked like a meshwork. The expression level of immunoglobulin receptor (FcγRII/III, represented as CD16/32) was also divided into two, however, the cells expressing stronger were more concentrated on the GC than CD21/35<sup>+</sup> cells were.

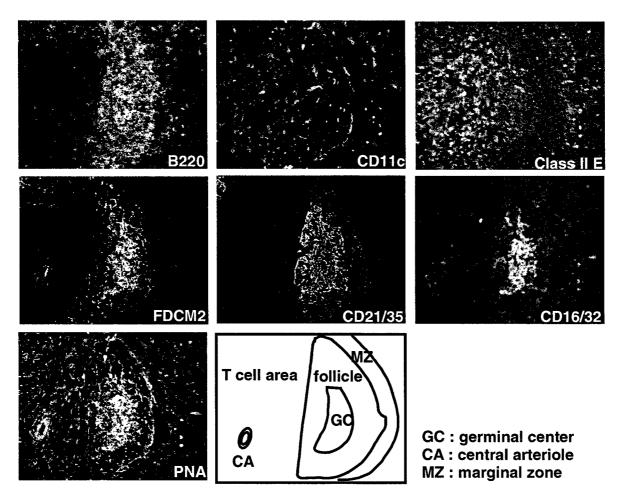


Figure 4. Structure of germinal center in mouse spleen

# 3.4 Expression of general $M\phi$ markers around the marginal zone

Fig. 4 shows the expressions around the marginal zone of F4/80, Mac3, MOMA2 and BM8, which are thought to be general Mφ marker. Uplan Apo 40X/0.85 was used as an objective lens. According to the hypothesis proposed by Leenen et al.², there locate RPM, red pulp marginal Mφ, MZM, MMM, and Mφ that distributes follicle and PALS. One third of the right side of the image shows the white pulp and two thirds of the left side shows the marginal zone and the red pulp. It is obvious that the expression of those markers vary from cells to cells. Mac3 was expressed on the largest subset, BM8 chiefly on MZM and RPM, MOMA2 on RPM, MZM and Mφ of follicle and PALS, respectively. F4/80 was expressed mainly on RPM, but also on a very limited subset of Mφ in the white pulp.

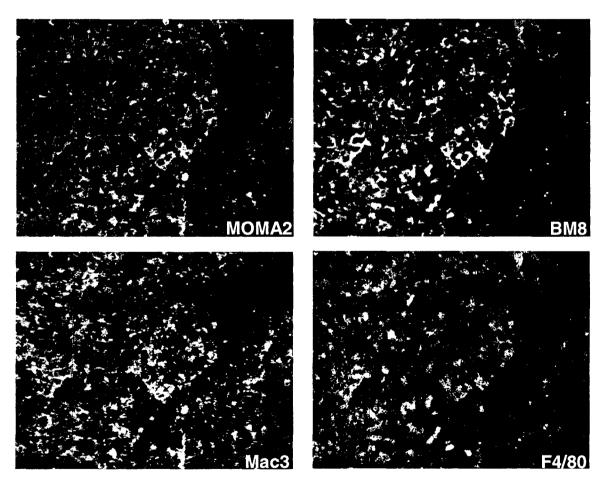


Figure 5. Expression of general  $M\phi$  markers around marginal zone

# **CONCLUSIONS**

Here we showed 8-color, 7-color and 4-color fluorescence images of mouse spleen. They demonstrated the complete separation of fluorescence signals having very close spectra each other. Even an auto-fluorescence from tissue can be used as a signal to investigate the distribution of some particular substance or cell population. Precise characterization of cell subsets in a tissue has come practicable only through this method. These results show the usefulness of the method in the study of the structure that consists of many kinds of cells and in the identification of cells characterized by multiple markers.

# REFERENCES

- 1. Tsurui H, Nishimura H, Hattori S, Hirose S, Okumura K, Shirai T. Seven-color fluorescence imaging of tissue samples based on Fourier spectroscopy and singular value decompositon, J Histochem Cytochem 48:653-662, 2000
- 2. Leenen PJM, Radosevic K, Voerman JSA, Salomon B, Rooijen N, Klatzmann D, Ewijk W, Heterogeniety of mouse spleen dendritic cells: In vitro phagocytic activity, expression of macrophage markers, and subpopulation turnover, J Immunol 160:2166-2173

# Multimodal multispectral imaging of the cervix in vivo for the detection of neoplasia

Anant Agrawal<sup>\*1</sup>, Tim Harrell<sup>1</sup>, Shabbir Bambot<sup>1</sup>, Mark Faupel<sup>1</sup>, Daron Ferris<sup>2</sup>
<sup>1</sup>SpectRx, Inc., Norcross, GA; <sup>2</sup>Medical College of Georgia, Augusta, GA

# **ABSTRACT**

Optical spectroscopy has been shown to be an effective method for detecting neoplasia of epithelial tissues. Most studies to date in this realm have applied fluorescence or reflectance spectroscopy alone as a preferred method of disease detection. We have been developing instrumentation which can acquire both reflectance and fluorescence images of the human cervix *in vivo*, with the goal of combining multispectral information from the two spectroscopic modalities. This instrumentation has been tested on a group of patients in a clinical setting. We have applied spectral and spatial analysis techniques to the acquired images to assess the capabilities of this technology to discriminate neoplastic from normal cervical tissue.

Keywords: cervix, neoplasia, fluorescence, reflectance, spectral imaging

#### 1. INTRODUCTION

Cervical cancer is one of the most common malignancies in women, represented annually as at least 370,000 new cases globally<sup>1</sup> and as 12,900 new cases in the US alone<sup>2</sup>. The implementation of annual screening using the Papanicolau (Pap) smear has significantly reduced cervical cancer mortality rates in the US, primarily by identifying women with precancerous changes, also known as cervical intraepithelial neoplasia (CIN) or, more concisely, cervical dysplasia. Despite the success of the Pap smear in reducing mortality rates, the test has demonstrated high false positive rates, which causes women with benign conditions to unnecessarily proceed to more expensive and invasive procedures. In a meta-analysis conducted by Fahey et al<sup>3</sup>, they reported an average sensitivity of 58% (95% CI 49-67%) and average specificity of 69% (95% CI 62-77%) of the Pap smear for detecting dysplasia in a screening setting. A more accurate, point-of-care test for cervical dysplasia has the potential to not only improve cervical cancer prevention but also reduce costs of health care.

Various forms of steady-state optical spectroscopy have been shown to be efficacious in the detection of CIN, as well as similar abnormalities of other epithelial tissues<sup>4-14</sup>. Fluorescence-based methods<sup>4-11</sup> and diffuse reflectance (or elastic scattering)-based methods<sup>12-14</sup> are among the most common spectroscopic techniques in this area. Nearly all studies have exploited either fluorescence or reflectance alone to provide information about the tissue relevant to the presence of disease. Measuring fluorescence and reflectance concurrently could offer a more complete picture of the biochemical and morphologic conditions of the interrogated tissue.

We have developed instrumentation to acquire both fluorescence and reflectance images of the cervix *in vivo* at a number of different ultraviolet (UV) and visible wavelengths. This multimodal multispectral imaging (MMI) system has been used in a clinical setting to acquire images from a cohort of patients with a broad distribution of cervical abnormalities, including those with a normal cervix and those with various grades of CIN. We have analyzed the images from these patients and present results of the analysis which indicate the ability of our system to discriminate normal from dysplastic tissue.

<sup>\*</sup>Correspondence: <a href="mailto:agrawal@spectrx.com">agrawal@spectrx.com</a>; phone (770) 242 8723; fax (770) 242 7075; <a href="http://www.spectrx.com">http://www.spectrx.com</a>; SpectRx, Inc., 6025A Unity Drive, Norcross, GA 30329

# 2. MATERIALS AND METHODS

#### 2.1 Instrumentation

Wavelength bands for fluorescence imaging were chosen based on the excitation and emission wavelengths of endogenous fluorophores present in cervical epithelium. Fluorescent species include tryptophan, collagen, elastin, reduced nicotinamide adenine dinucleotide (NADH), oxidized flavin adenine dinucleotide (FAD) and porphyrins. A number of studies have shown that the measured fluorescence intensity from these fluorophores may be significantly modulated by the onset and progression of dysplasia<sup>4,7,8,15,16</sup>.

The diffuse reflectance properties of the cervix, as with most other human tissues, are dominated by hemoglobin absorption. Because increased vascularity has been associated with dysplastic processes, we considered it essential to acquire reflectance images at one or more visible wavelength bands corresponding to the absorption peaks of hemoglobin. We also wanted to acquire reflectance images at other wavelength bands across the UV-visible spectrum, especially those not as strongly affected by hemoglobin, wherein effects such as epithelial scattering might indicate the presence of dysplasia.

We designed and constructed an imaging system capable of providing illumination and detection at a variety of UV-visible wavelength bands and suitable for use in a clinical setting. A layout of the optical system is shown in Figure 1. The illumination path consists of a xenon flashlamp as a broadband illumination source followed by a collimating mirror, optical filter, and finally a beamsplitter which directs light to the tissue. Fluorescent or reflected light passes back through the beamsplitter, followed by an optical filter and then an imaging lens system which places an image onto a CCD camera (512 x 512 pixels). Motorized filter wheels were used to independently select both illumination and collection filters. A tube was placed in front of the foreoptic to shield the exposed light path from ambient light.

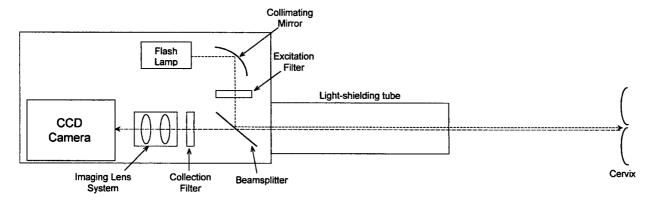


Figure 1. Optical system layout.

All the major electro-optical components of the MMI system were mounted in a contained unit on top of a vertical pole stand with wheels so it could be positioned in front of the patient like a standard colposcope used to examine the cervix. The imaging system could be manipulated via height and tilt adjustment. The stand was tethered to a base unit which contained power supplies, control circuitry, and a computer. Custom software was written to provide a simple user interface for system control and data acquisition. Ten fluorescence images and seven reflectance images were acquired per patient, with a total image acquisition time of approximately 1.5 minutes.

Because our system uses UV excitation wavelengths, we conducted an analysis to ensure patients would not be exposed to unsafe levels of UV light during the course of measurements. For the benefit of researchers developing electro-optical systems for detecting CIN, the Food and Drug Administration (FDA) has published a draft guidance document<sup>17</sup> which recommends a UV exposure limit for cervical tissue. This limit is equivalent to a threshold limit value set by the American Conference of Governmental Industrial Hygienists (ACGIH) for UV light incident on the eye and skin by non-laser light sources. The FDA draft guidance document states specifically that the device emission spectrum weighted with the action spectrum published by the ACGIH should be less than 3 mJ/cm<sup>2</sup>. Upon measuring the output of the MMI system at the UV

excitation wavelengths, we determined that the effective radiant exposure of our system was approximately 0.5 mJ/cm<sup>2</sup>, well below the threshold limit value.

# 2.2. Clinical data collection

After obtaining institutional review board-approved informed consent, non-pregnant women 18 years of age or older with an intact cervix scheduled for colposcopy were enrolled in our study. Colposcopy involves examination of the cervix *in situ* with low power magnification (3X-15X), typically after applying acetic acid to the cervix. Acetic acid acts as a contrast agent by temporarily whitening (acetowhitening) areas which tend to be suspicious of CIN. The colposcopic examination included digital color image capture with a video colposcope for documentation and data analysis purposes. When clinically indicated, either a biopsy was performed if CIN was suspected, or an excision treatment was performed to remove already-confirmed dysplastic tissue. Some patients were also scheduled for hysterectomy, usually for reasons unrelated to dysplasia or cancer. All biopsies and excised specimens underwent histologic analysis by pathologists at the clinical site.

Image acquisition with the MMI system took place before colposcopy. After the vaginal speculum was inserted, but prior to image acquisition, a mark was placed on the cervix to ensure all the images could be properly registered. The MMI system was then positioned so that the front of the tube was just inside the opening of the speculum and a test image of the cervix appeared in focus. Figure 2 shows some typical images acquired with the MMI system. Because we acquired images before colposcopy, they were without the contrast enhancement offered by acetic acid. For the purposes of this study, we wanted to determine if the native, unbiased properties of cervical tissue could provide adequate information to permit detection of dysplasia. In addition, since acetowhitening is a transient phenomenon typically lasting only several minutes, there was concern that there would be variable amount of acetowhitening influencing each image in an acquisition sequence.



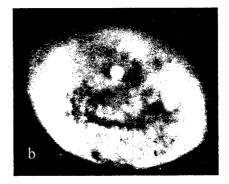


Figure 2. MMI system images of cervix in vivo: (a) reflectance image, (b) fluorescence image.

# 2.3. Data analysis

Images from 34 patients have been analyzed for this study. This group consists of 18 with a normal cervix, eight with only non-dysplastic lesions (metaplasia, inflammation), and eight with dysplasia. Of the dysplastic cases, one had only mild dysplasia (CIN 1, low grade) and seven had moderate to severe dysplasia (CIN 2+, high grade). Two of the CIN 2+ cases also had CIN 1 lesions, and another two of the CIN 2+ cases also had non-dysplastic lesions. The presence of dysplasia was always confirmed by histopathology; however, histologic specimens were typically not available to confirm non-dysplastic or normal conditions. Normal epithelium and non-dysplastic lesions were identified by colposcopy.

For each patient, the colposcopist drew a detailed colposcopic impression directly on the captured digital color image. The boundaries of any dysplastic or non-dysplastic lesions, as well as the boundary between the two normal cervical epithelial types (squamous and columnar) were recorded. This information was then transferred to the MMI system image set to delineate image regions and classify each region into one of five categories: normal squamous, normal columnar, non-dysplastic lesion, CIN 1 lesion, CIN 2+ lesion. It should be noted nearly every cervix contained multiple regions, and many times more than one category was present. During this classification process, image areas were also excluded from subsequent analysis for any of the following reasons: non-cervical tissue, registration mark, excessive blood or mucus, specular reflection artifact (CCD saturation), unknown/uncertain classification.

Prior to applying quantitative analysis techniques, images were first corrected by subtracting the offset introduced by the CCD. In addition, 5 x 5 pixel binning was applied to all images for data smoothing and data reduction purposes. Any mentions of the term "pixel" in the remainder of this paper are referring to the average of a 5 x 5 pixel block. Table 1 lists the number of patients, regions, and pixels in each category that were analyzed in this study.

	# Patients	# Regions	# Pixels
Normal squamous	34	44	24372
Normal columnar	9	11	551
Non-dysplastic	10	16	386
CIN 1	3	5	254
CIN 2-3	7	8	836

Table 1. Sample sizes for this study.

An expected source of intensity variability in the images was that arising from intrinsic differences in fluorescence yield between patients. This variability is unrelated to and can be larger than the fluorescence intensity differences between dysplastic and normal tissue. To investigate the possibility of reducing the effects of this variability, we generated a complementary set of images in which each pixel was normalized by the mean intensity of all pixels located on normal squamous epithelium from the same image. Normal squamous epithelium was selected as the normalization category because every cervix in the study population, and practically every cervix in the general population, contains some amount of this native epithelium.

Because the cervix has an irregular surface and its anatomical orientation varies significantly between patients, we expected and observed spatial intensity variations unassociated with system variability or relevant biological factors. In other words, there was intra- and inter-patient variability of excitation-collection geometry in every image. Therefore, we believed our best opportunity to extract useful quantitative information from the images was by analyzing ratio images, i.e. one image divided by another, pixel-by-pixel.

For both the original and squamous normalized image sets, all possible ratio images (excluding inverses) were generated from the ten fluorescence and seven reflectance image types, giving rise to 272 total ratio images per patient. For each ratio image type, all pixels from all patients together were then grouped by category. After separating the categories into two groups (i.e. normal squamous vs. all others, non-dysplasia vs. dysplasia), we applied the Mann-Whitney test, a non-parametric analog to the Student's *t*-test. The p-value from this test provided a metric which indicated how separate the two groups were for each ratio image type. The ratio image types were then ranked by p-value in order to select one or more types for basic discrimination algorithms.

### 3. RESULTS

We first wanted to determine an algorithm using the original images to discriminate normal squamous epithelium from all other tissue types. This was expected to be the simplest of our tasks at hand, because normal squamous can be visually identified on the cervix by even a minimally trained eye. Combining two ratio image types provided improved discrimination most critically between normal squamous and dysplasia, and also separated normal columnar and non-dysplastic lesions from normal squamous as well. Figure 3 plots all the pixels from the two ratio image types in feature space. With the decision lines shown, the discrimination performance of non-squamous normal (positive) from squamous normal (negative) was 87% sensitivity and 88% specificity.

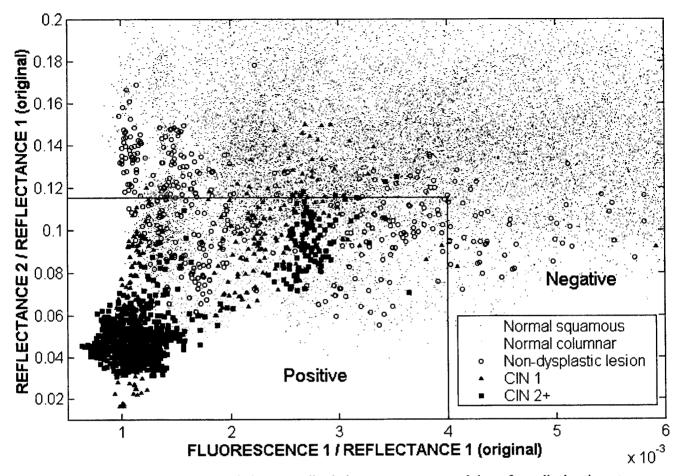


Figure 3. First algorithm using two ratio images to discriminate squamous normal tissue from all other tissue types.

Having completed our simpler task, our second task was to discriminate the remaining non-dysplastic pixels from the dysplastic pixels. Two different ratio image types were found, one from the original image set and the other from the squamous normalized image set, which again provided improved discrimination when combined. Figure 4 plots all the pixels from the two ratio images, again in feature space. Note that only pixels called positive by the first algorithm are plotted here, including normal squamous false positives. Similarly, pixels called negative by the first algorithm are excluded here, including dysplastic false negatives. For the decision line shown, the performance of this algorithm is 86% sensitivity and 86% specificity. The combined performance of these two algorithms to discriminate dysplasia from non-dysplasia is 83% sensitivity and 98% specificity.

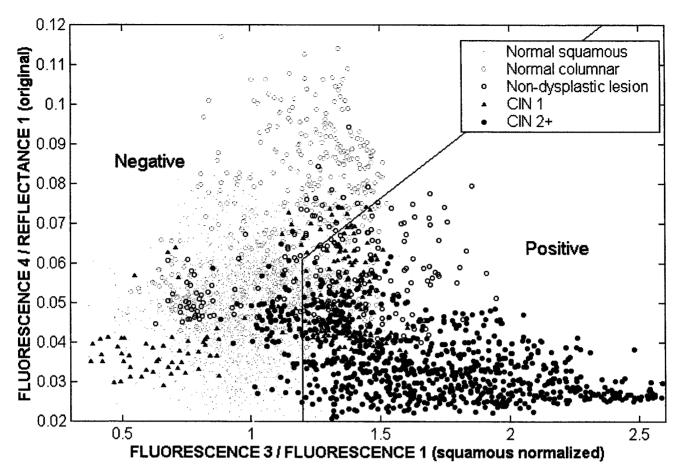


Figure 4. Second algorithm using two ratio images to discriminate dysplasia from non-dysplasia.

# 4. CONCLUSIONS

With basic analysis approaches, we were able to develop simple algorithms to demonstrate feasibility of discrimination between non-dysplastic and dysplastic tissue in this data set. The algorithms incorporated both fluorescence and reflectance information, thereby exploiting the multimodal capability of the MMI system. It is important to note that this level of discrimination was achieved even without the use of acetic acid, which is known to be essential for visual assessment of the cervix at colposcopy and has been shown benefit spectroscopic techniques<sup>18</sup>. The sensitivity and specificity as demonstrated in this study can potentially reduce the number of false positive cases and improve the detection rate of cervical dysplasia.

### **ACKNOWLEDGEMENTS**

We gratefully acknowledge Welch Allyn for funding to support this project. The authors would also like to thank Eileen Dickman, Candis Kapsner, Stan Mack, Sandy Roach for additional assistance on this project.

#### REFERENCES

- 1. D. Parkin, P. Pisani, and J. Ferlay, "Estimates of the worldwide incidence of 25 major cancers in 1990," *International Journal of Cancer* 80, pp. 827-841, 1999.
- 2. Cancer Facts and Figures, American Cancer Society, 2000.

- 3. M. Fahey, L. Irwig and P. Macaskill, "Meta-analysis of Pap test Accuracy," *American Journal of Epidemiology* **141**, pp. 680-689, 1995.
- 4. N. Ramanujam, M. Mitchell, A. Mahadevan, S. Warren, S. Thomsen, E. Silva and R. Richards-Kortum, "In vivo diagnosis of cervical intraepithelial neoplasia using 337-nm-excited laser-induced fluorescence," *Proceedings of the National Academy of Science USA* 91, pp. 10193-10197, 1994.
- 5. N. Ramanujam, M. Mitchell, A. Mahadevan-Jansen, S. Thomsen, G. Staerkel, A. Malpica, T. Wright, N. Atkinson and R. Richards-Kortum, "Cervical precancer detection using a multivariate statistical algorithm based on laser-induced fluorescence spectra at multiple excitation wavelengths," *Photochemistry and Photobiology*, **64**(4), pp. 720-735, 1996.
- 6. J. Dhingra, D. Perrault Jr., K McMillan, E. Rebeiz, S. Kabani, R. Manoharan, I. Itzkan, M. Feld, and S. Shapshay, "Early diagnosis of upper aerodigestive tract cancer by autofluorescence," *Archives of Otolaryngology and Head and Neck Surgery*, 122, pp. 1181-1186, 1996.
- 7. D. Ingrams, J. Dhingra, K. Roy, D. Perrault Jr., I. Bottrill, S. Kabani, E. Rebeiz, M. Pankratov, S. Shapshay, R. Manoharan, I. Itzkan, and M. Feld, "Autofluorescence characteristics of oral mucosa", *Head & Neck* 19, pp. 27-32, 1997
- 8. S. Schantz, V. Kolli, H. Savage, G. Yu, J. Shah, D. Harris, A. Katz, R. Alfano and A. Huvos, "In vivo native cellular fluorescence and histological characteristics of head and neck cancer," Clinical Cancer Research 4, pp.1177-1182, 1998.
- 9. D. Heintzelman, U. Utzinger, H. Fuchs, A. Zuluaga, K. Gossage, A. Gillenwater, R. Jacob, B. Kemp and R. Richards-Kortum, "Optimal excitation wavelengths for in vivo detection of oral neoplasia using fluorescence spectroscopy," *Photochemistry and Photobiology* 72(1), pp. 103-113, 2000.
- 10. K. Schomaker, J. Frisoli, C. Compton, T. Flotte, J. Richter, N. Nishioka, and T. Deutsch, "Ultraviolet laser-induced fluorescence of colonic tissue: basic biology and diagnostic potential," *Lasers in Surgery and Medicine* 12, pp. 63-78, 1992.
- 11. T. Wang, J. Crawford, M. Feld, Y. Wang, I. Itzkan, and J. Van Dam. "In vivo identification of colonic dysplasia using fluorescence endoscopic imaging," *Gastrointestinal Endoscopy* **49**, pp. 447-455, 1999.
- 12. J. Mourant, I. Bigio, J. Boyer, R. Conn, T. Johnson and T. Shimada, "Spectroscopic diagnosis of bladder cancer with elastic light scattering," *Lasers in Surgery and Medicine* 17, pp. 350-357, 1995.
- 13. F. Koenig, R. Larne, H. Enquist, F. McGovern, K. Schomacker, N. Kollias, and T. Deutsch, "Spectroscopic measurement of diffuse reflectance for enhanced detection of bladder carcinoma," *Urology* 51(2), pp. 342-345, 1998.
- 14. M. Wallace, L. Perelman, V. Backman, J. Crawford, M. Fitzmaurice, M. Seiler, K. Badizadegan, S. Shields, I. Itzkan, R. Dasari, J. Van Dam, and M. Feld, "Endoscopic detection of dysplasia in patients with Barrett's esophagus using light-scattering spectroscopy," *Gastroenterology* 119(3), pp. 677-682, 2000.
- 15. B. Banerjee, B. Miedema, H. Chandrasekhar, "Emission spectra of colonic tissue and endogenous fluorophores," *The American Journal of the Medical Sciences* **316**(3), pp.220-226, 1998.
- 16. D. Heintezelman, R. Lotan, and R. Richards-Kortum, "Characterization of the autofluorescence of polymorphonuclear leukocytes, mononuclear leukocytes and cervical epithelial cancer cells for improved spectroscopic discrimination of inflammation from dysplasia," *Photochemistry and Photobiology* 71(3), pp. 327-332, 2000.
- 17. U.S. Department of Health and Human Services Food and Drug Administration, Center for Devices and Radiological Health, "Electro-Optical Sensors for the *In Vivo* Detection of Cervical Cancer and its Precursors: Submission Guidance for an IDE/PMA," May 1999.
- 18. A. Agrawal, U. Utzinger, C. Brookner, C. Pitris, M. Mitchell and R. Richards-Kortum, "Fluorescence spectroscopy of the cervix: influence of acetic acid, cervical mucus, and vaginal medications," *Lasers in Surgery and Medicine* 25, pp. 237-49, 1999.

# Skin hydration imaging using a long-wavelength near infrared digital camera

Michael Attas,\* Trevor Posthumus, Bernie Schattka, Michael Sowa, Henry Mantsch, Shuliang Zhang<sup>a\*\*</sup>

Institute for Biodiagnostics, National Research Council Canada, Winnipeg, Canada <sup>a</sup>Unilever Research U.S.

# **ABSTRACT**

Skin hydration is a key factor in skin health. Hydration measurements can provide diagnostic information on the condition of skin and can indicate the integrity of the skin barrier function. Near-infrared spectroscopy measures the water content of living tissue by its effect on tissue reflectance at particular wavelengths. Imaging has the important advantage of showing the degree of hydration as a function of location. Short-wavelength (650-1050 nm) near infrared spectroscopic reflectance imaging has previously been used in-vivo to determine the relative water content of skin under carefully controlled laboratory conditions. We have recently developed a novel spectroscopic imaging system to acquire image sets in the long-wavelength region of the near infrared (960 to 1700 nm), where the water absorption bands are more intense. The LW-NIR system uses a liquid-crystal tunable filter in front of the objective lens and incorporates a 12-bit digital camera with a 320-by-240-pixel indium-gallium arsenide array sensor. Custom software controls the camera and the tunable filter, allowing image sets to be acquired and displayed in near-real time. Forearm skin hydration was measured in a clinical context using the long-wavelength imaging system, a short-wavelength imaging system, and non-imaging instrumentation. Among these, the LW-NIR system appears to be the most sensitive at measuring dehydration of skin.

Keywords: spectroscopic imaging, near infrared, liquid crystal tunable filter, skin hydration

# 1. INTRODUCTION

Skin hydration is a key factor in skin health. Skin with too much water may be an indication of edema (swelling); dehydrated skin may be an indication of compromised barrier function. Hydration measurements provide diagnostic information on the health of skin and are an indicator of the integrity of the skin barrier function. Near-infrared spectroscopic methods can measure the water content of living tissue by its effect on tissue reflectance at particular wavelengths. Infrared spectra are analyzed to isolate and quantify the portion of the signal resulting from the water in the skin. 2

Imaging has two important advantages over point-source spectroscopic measurements using fiber optic probes: it is a non-contact measurement technique, and it can show the degree of hydration as a function of location. Short-wavelength (650-1050 nm) near infrared spectroscopic reflectance imaging has previously been used in-vivo to determine the relative water content of skin under carefully controlled laboratory conditions.<sup>3</sup> In that work, the success of reconstructive surgery on skin was studied using an animal model. The likelihood of eventual survival of a skin flap could be predicted from its degree of dehydration. This was measured as a function of location using the intensity of the water absorption band near 980 nm. Measurements at longer wavelengths in the near infrared region were expected to provide superior hydration information, since the water absorption bands in that region are more intense.<sup>4</sup>

<sup>\*</sup> Michael.Attas@nrc.ca; phone 204-984-5191; fax 204-984-5472; Institute for Biodiagnostics, National Research Council of Canada, 435 Ellice Avenue, Winnipeg, Manitoba, Canada R3B 1Y6

<sup>\*\*</sup> Shuliang.Zhang@unilever.com; phone 201-840-2247; Unilever Research U.S., 45 River Road, Edgewater, NJ, USA 07020

#### 2. BACKGROUND

Spectroscopic images can be considered as a three-dimensional data set, or data cube. Two of the dimensions are spatial and the third is the wavelength. With a digital imaging system, the two spatial dimensions are acquired simultaneously at a particular wavelength. The wavelength setting is then changed, and a new image is acquired. This process is repeated until a stack of images, one for each wavelength, has been acquired. The spatial resolution of this procedure is a function of the sensor array, and the spectral resolution depends on properties of the wavelength selector. For the short-wavelength near infrared, by far the most popular sensor is the silicon charge coupled device, or CCD. CCD cameras are available with high resolution, high sensitivity, and relatively low cost. Wavelength selection is most simply accomplished using an assortment of narrow-pass filters. However, proper interpretation of the data in the spectral dimension is facilitated by having numerous slices at various wavelengths through the spectral region of interest. This is termed hyperspectral imaging (in contrast to multispectral imaging, where only a few wavelengths are required).

Tunable filters of high optical quality are the keys to obtaining sufficient wavelength slices for biological hyperspectral imaging. Several technologies are available; we have used liquid-crystal tunable filters (LCTFs) with good results. Since they have no moving parts, are rapidly tunable, and do not distort the image, they are convenient to use. The wavelength can be set by a simple digital command under computer control.

#### 3. INSTRUMENTATION

In developing a spectroscopic imaging system to work in the longer wavelength region of the near infrared, we adapted the overall design of the short-wavelength near infrared (SW-NIR) systems already in use in our laboratory. The wavelength range of interest was 960 to 1700 nm. The LW-NIR system uses a liquid-crystal tunable filter for this wavelength range designed by Cambridge Research and Instrumentation, Inc. (Boston MA). The filter is mounted in front of the objective, a standard C-mount video lens (Figure 1). Since CCD arrays are not sensitive in this wavelength range, an alternate camera technology was employed. The spectroscopic imaging instrument incorporates a 12-bit digital camera with a 320-by-240-pixel indium-gallium arsenide array sensor (Sensors Unlimited, Inc., Princeton NJ). Custom software controls the camera and the tunable filter, allowing image sets to be acquired and displayed in near-real time. This software was written using the LabView programming environment (National Instruments, Austin TX). This environment allowed rapid development, debugging, and implementation of the code, as well as providing a smooth and consistent user interface. More details of the instrumentation can be found elsewhere.

# 4. MEASUREMENTS

The LW-NIR spectroscopic imaging system was first tested in the laboratory where it was assembled, but a full functional test required a clinical setting, since that is its ultimate destination. A simple protocol was devised to explore the performance characteristics of the instrument. The protocol was approved by the Winnipeg Research Ethics Board. In accordance with the protocol, forearm skin hydration was measured in a clinical context using the long-wavelength imaging system, a short-wavelength imaging system, and non-imaging instrumentation. The objectives of the study were the following: to determine if LW-NIR spectroscopic imaging could be used to determine superficial skin hydration in vivo; to compare LW-NIR hydration imaging with the corresponding SW-NIR hydration imaging method; and to compare these non-contact hydration measurement methods with the traditionally used contact electrical measurements of skin hydration (conductance and capacitance). The Skicon 200 (IBS, Japan) with MT8C probe (Measurement Technologies, Cincinnati) was used to measure skin conductivity and the Corneometer 820 (Courage and Khazaka, Germany) was used to measure skin capacitance.

The study was carried out at the facilities of Hill Top Research in Winnipeg. Eight subjects were recruited, 4 male and 4 female. After informed consent was obtained, three test sites were marked on the inner, or volar, surface of one of the forearms of each subject (Figure 2). The sites were squares approximately 25 mm on a side, approximately 5

mm apart. They were randomly assigned for treatment using application of acetone (0.1 mL) or Curel<sup>®</sup> lotion (0.8 mL) or no treatment (control). Baseline measurements were made of these sites before treatment, and then at 30, 90, 180, and 300 minutes after treatment. The subjects remained in a climate-controlled room for the duration of the study.

A single LW-NIR measurement consisted of a stack of 75 image frames, each 320 × 240 pixels, covering the wavelength range from 960 to 1700 nm at 10-nm intervals. Each of these frames was the sum of ten sequential 17-ms exposures. The file size was 22.5 megabytes. A reference measurement was also taken and used to normalize the measurements of the subjects' forearms. The reference measurement consisted of a stack of 75 image frames of a white reference card (Kodak, Rochester NY) placed at the same distance from the camera as the forearms. Throughout the study the camera remained mounted on a photographic copy stand pointing vertically downward (Figure 3). Its distance approximately 600 mm above the subjects' arms allowed the three treatment sites to fit in the same image frame. Illumination was provided by a pair of quartz halogen lamps arranged to either side of the subject's arm and adjusted to minimize shadows. The subjects placed their arms in a padded plastic cradle during the measurements to reduce movement and increase reproducibility while maintaining comfort. Despite the arm cradle, some movement occurred, particularly between measurements, and the image sets required registration as part of the processing sequence (see below). The reflective dots placed at the corners of the squares marking the product application sites also served as registration markers.

The SW-NIR measurements were performed in a similar manner. Each was a stack of 41 image frames of  $256 \times 256$  pixels covering the wavelength range from 650 to 1050 nm at 10-nm intervals. Each frame was a 200-ms exposure using a digital camera (Photometrics, Tucson AZ) with a thermoelectrically cooled CCD sensor and a standard (35-mm) Nikon photographic lens. The liquid-crystal tunable filter (Cambridge Research & Instrumentation, Boston, MA) was mounted in front of the lens. The file size was 5.2 megabytes per image set.

Measurements with the Skicon and Corneometer were taken in triplicate at each treatment site, recorded manually, and later transcribed into a computer spreadsheet.

#### 5. DATA PROCESSING

The mathematical software package MATLAB (The MathWorks, Natick MA) was used to process the image data. The first step in the data processing sequence was the conversion of the raw reflection intensity data to optical density format. This was accomplished by first calculating the ratio of the pixel intensity in the subject to the intensity of the corresponding pixel in the reference measurement, and then taking the negative logarithm of this ratio. A simple linear registration algorithm was used to align the converted image frames within each data set and from one data set to another. It required some user input; namely, to identify the registration markers in each frame by mouse clicks. Cropping the registered frames to eliminate much of the background reduced file sizes and shortened processing times.

Selected image frames were examined visually at each step in this process. Qualitative variations in reflectance were evident, and could be related to the skin treatments. However, the principal means of quantifying the skin hydration level was by calculating the net peak area of the spectral water bands. The band near 980 nm was used in the SW-NIR data, and the more intense band near 1450 nm was used in the LW-NIR data (Figure 4). For each pixel, the integrated area of the water band was calculated, and a linear baseline subtracted. The resulting values for each pixel were plotted to generate a hydration image, with pixel intensity indicating the area of the water peak.

The non-image data were treated using the software package Statistica (StatSoft, Tulsa OK). Population means and variances were calculated and normalized to the baseline values, for both Skicon and Corneometer results. Statistica was also used to calculate the significance of changes in the mean pixel intensities of the hydration images.

# 6. RESULTS

Selected hydration images are presented to illustrate the range of skin response and the performance of the instrumentation. Subject no. 4 demonstrated a typical response to the skin treatments. The long-wavelength and short-wavelength imaging results are shown in Figures 5 and 6 respectively. In all the images, the registration markers define the borders of the treatment sites. Red areas in the false-color images have the highest water content, whereas blue areas have the lowest. In the pre-treatment images taken with both camera systems, the skin of subject no. 4 shows a gradient of water content along the length of the forearm. This interferes somewhat with the interpretation of the results. Nevertheless, the hydration image taken using the LW-NIR instrumentation 30 minutes after the treatments shows clear changes in water content. The acetone-treated area, at the top, has reduced hydration, while the Curel-treated area, at the bottom (nearest the wrist), has increased hydration. These differences confirm our expectations that the LW-NIR infrared hydration imaging technique is sensitive to induced changes in skin moisture.

The SW-NIR method is less sensitive to water content, as shown in Figure 6. Again, the intensity gradient along the length of the forearm is somewhat of a distracting factor. Changes in skin hydration can be detected visually between the pre-treatment image and the image taken 30 minutes after the treatments, but the changes are much less pronounced than for the LW-NIR instrument. By 90 minutes after treatment, the effects are difficult to distinguish.

The sequence of LW-NIR images of the forearm of subject no. 8 best shows the effects of the skin treatments and how they changed with time through the day. In the pre-treatment image (Figure 7a), the skin in the three squares is of fairly uniform intensity, indicating a fairly uniform hydration level: i.e., little or no gradient. This allows more subtle changes to be detected visually for this subject than for the others. The hydration image taken 30 minutes after the treatments (Figure 7b) shows the greatest change from the pre-treatment image. The site treated with Curel is at the top of the image. It has higher hydration than the middle, untreated site, and also higher hydration than it did in the pre-treatment image. The acetone-treated site, at the bottom of the image (nearest the wrist), has much lower hydration than it did before treatment, and also lower hydration than the untreated site beside it.

For subject 8, the changes resulting from the two skin treatments can be followed through the day in the LW-NIR hydration images (Figure 7). Acetone has a pronounced drying effect, which persists to the last measurement, made five hours after treatment (upper site in Figure 7). The slight increase in hydration resulting from application of Curel appears to fade in the images, and the hydration level of the Curel-treated site (lower site, nearest the wrist) is indistinguishable from that of the untreated site (center) after three hours or even earlier. This is evident to the eye in the images, and has been confirmed by statistical analysis (to be published elsewhere). To perform the statistical analysis, relatively uniform regions were defined within each treatment site, and the mean hydration intensities were calculated over these regions. Although for subject 8 differences between acetone, Curel, and untreated sites are visible in at least some of the hydration images, in the population as a whole (n=8) the Curel-induced differences in hydration were not significant. As anticipated by visual examination of the images, the statistical analysis also confirmed that treatment effects were much more difficult to discern by using the short-wavelength water absorption band than by using the long-wavelength band.

The results of the non-imaging measurements are easiest to appreciate when presented in graphical form. Figures 8 and 9 show how the Corneometer and Skicon readings for subject no. 1 change following the skin treatments. The trends in these graphs are similar from subject to subject (statistical analysis to be published elsewhere), but quite different from the imaging data trends. The acetone effect is barely discernable, while the effect of Curel is significant and lasts throughout the day. This is a surprising result, given that in the imaging measurements, the Curel treatment showed less effect than the acetone treatment.

# 7. DISCUSSION

The performance of the LW-NIR imaging system was expected to be superior to that of the SW-NIR system at determining changes in skin hydration. The main reason for this was postulated to be the higher intensity of the water absorbance band in the LW-NIR region of the spectrum relative to the one in the SW-NIR region. Nevertheless, the short-wavelength system had been successful in following hydration changes resulting from elevations of skin flaps

in the earlier rat studies.<sup>3</sup> In the present study, however, the changes in hydration were more superficial than in the flap elevation work. After all, we were not examining skin on its way to necrosis, but rather skin whose surface moisture was being altered. The acetone and Curel treatments affected only the outermost layers of the skin. The chief factor limiting the penetration through tissue of near-IR light beyond 900 nm is its absorption by water. Where the water bands are weak, the absorption is relatively low and the light penetrates more deeply. As a result, the light collected from the subjects at the shorter wavelengths near 980 nm is affected by the composition of a thicker layer of tissue, and the surface hydration plays a smaller part in the overall response. At longer wavelengths, only the superficial tissue layer contributes to the infrared reflectance, and changes in the degree of hydration are more noticeable. This explanation, while reasonable, requires verification. If it is correct, then measurement of a water band at intermediate wavelength should show response of intermediate intensity. We plan to generate hydration images based on the water band near 1200 nm as a test of this hypothesis.

The differences in the sensitivity to hydration changes of the imaging and the non-imaging methods were also surprising. It appears that the LW-NIR imaging system is more sensitive to dehydration (at least as caused by acetone application), while the Corneometer and Skicon instruments are more sensitive to moisturization (at least as caused by application of Curel). Possible reasons for this may be related to the side effects of the treatments, or to the mode of operation of the non-imaging instruments, or both. For example, application of acetone would tend to dissolve or otherwise rearrange the lipid component of the skin as well as reducing the skin's water content. This delipidization might affect the infrared spectrum somewhat, through changes in scattering properties; nevertheless, the net area of the water bands should not change. However, delipidization might also affect the nature of the contact between the skin surface and the Corneometer and Skicon probes, and therefore affect the readings they produce. This hypothesis remains to be tested.

Application of Curel also causes changes beyond simply increasing the water content of the skin. The ingredients of Curel are listed on the label as follows: glycerin 12%, white petrolatum 4 %, water, distearyldimonium chloride, isopropyl palmitate, cetyl alcohol, dimethicone, sodium chloride, methylparaben, and propylparaben. The presence of these constituents on the skin may change the scattering aspects of the infrared spectrum somewhat, though again the net area of the water bands should not be affected, since the water contained in the Curel would evaporate in the half hour between application and measurement. On the other hand, changes in skin elasticity and surface ionic content resulting from Curel application might affect the operation of the Corneometer and Skicon probes. Although these instruments are commonly used in studies of skin moisturization, they actually measure electrical properties of the skin. These properties are correlated with water content, but other changes in skin properties caused by the lotion may have more of an effect on the Corneometer and Skicon measurements than changes in hydration. Additional investigations of these postulated effects are required to elucidate the mechanism of operation of the different skin hydration measurement methods.

#### 8. CONCLUSIONS

The performance of the long-wavelength near infrared spectroscopic imaging system was tested in a clinical setting using a skin hydration protocol. The measurements indicated that the instrument could determine skin hydration non-invasively, in fact completely without contact. The resulting hydration images have high visual impact for immediate comprehension. The images also provide information on moisture distribution, which can be non-uniform. The infrared imaging method appears to be quite sensitive to changes in hydration caused by application of acetone. It is relatively insensitive to changes caused by application of Curel moisturizing lotion.

The LW-NIR system was found to be considerably more sensitive to these superficial changes in skin hydration than the SW-NIR system. Relative to contact measurements using Corneometer and Skicon instruments, the LW-NIR system appears to have greater sensitivity to skin dehydration caused by application of acetone but less sensitivity to changes caused by application of Curel moisturizing lotion. Further investigations into these phenomena are underway.

#### ACKNOWLEDGMENTS

We wish to acknowledge the kind assistance of L. Leonardi for image registration and of the expert staff of Hill Top Research in Winnipeg for hosting the hydration study. Financial assistance from Unilever Research US is gratefully acknowledged.

#### REFERENCES

<sup>&</sup>lt;sup>1</sup> J. de Rigal, M.J. Losch, R. Bazin, C. Camus, C. Sturelle, V. Descamps, and J.L. Lévêque, "Near-infrared spectroscopy: A new approach to the characterization of dry skin," J. Soc. Cosmet. Chem. 44. pp. 197-209, 1993.

<sup>&</sup>lt;sup>2</sup> K.A. Martin, "Direct measurement of moisture in skin by NIR spectroscopy," J. Soc. Cosmet. Chem. 44, pp. 249-261, 1993.

<sup>&</sup>lt;sup>3</sup> M.G. Sowa, J.R. Payette, and H.H. Mantsch, "Near-infrared spectroscopic assessment of tissue hydration following surgery," J. Surgical Research 86, pp. 62-69, 1999.

<sup>&</sup>lt;sup>4</sup> F.O. Libnau, O.M. Kvalheim, A.A. Christy, and J. Toft, "Spectra of water in the near- and mid-infrared region," Vibrational Spectroscopy 7, pp. 243-254, 1994.

<sup>&</sup>lt;sup>5</sup> P. Colarusso, L.H. Kidder, I.W. Levin, J.C. Fraser, J.F. Arens, and E.N. Lewis, "Infrared spectroscopic imaging: from planetary to cellular systems," Appl. Spectroscopy 52, pp. 106A-120A, 1998.

<sup>&</sup>lt;sup>6</sup> M.G. Sowa, J.R. Mansfield, G.B. Scarth, and H.H. Mantsch, "Noninvasive assessment of regional and temporal variations in tissue oxygenation by near-infrared spectroscopy and imaging," Appl. Spectroscopy 51, pp. 143-152, 1997.

<sup>&</sup>lt;sup>7</sup> H.R. Morris, C.C. Hoyt, and P.J. Treado, "Imaging spectrometers for fluorescence and Raman Microscopy acoustooptic and liquid-crystal tunable filters," Appl. Spectroscopy 48, pp. 857-866, 1994.

<sup>&</sup>lt;sup>8</sup> J.R. Mansfield, M.G. Sowa, and H.H. Mantsch, "Development of visible and near-IR LCTF-based spectroscopic imaging systems for macroscopic samples," Spectral Imaging: Instrumentation, Applications, and Analysis, eds. G.H. Bearman, D. Cabib, and R.M. Levenson, Vol.3920, pp. 99-107, SPIE, Bellingham WA, 2000.

<sup>&</sup>lt;sup>9</sup> H.R. Morris, C.C. Hoyt. P. Miller, and P.J. Treado, "Liquid crystal tunable filter Raman chemical imaging," Appl. Spectroscopy 50, pp. 805-811, 1996.

<sup>&</sup>lt;sup>10</sup> M.G. Sowa, J.R. Payette, M.D. Hewko, and H.H. Mantsch, "Visible-near infrared multispectral imaging of the rat dorsal skin flap," J. Biomedical Optics 4, pp. 474-481, 1999.

<sup>&</sup>lt;sup>11</sup> M. Attas, T. Posthumus, B. Schattka, M. Sowa, H. Mantsch, and S. Zhang, "Long-wavelength near-infrared

spectroscopic imaging for in-vivo skin hydration measurements," *Vibrational Spectroscopy*, 2001, in press.

12 K. Martin, "In-vivo measurements of water in skin by near-infrared reflectance," *Appl. Spectroscopy* 52, pp. 1001-1007, 1998.

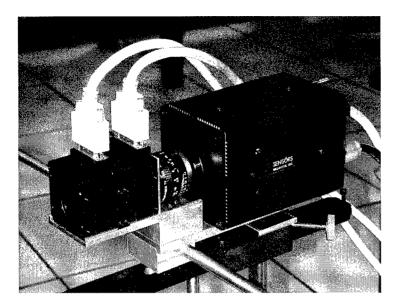


Figure 1. Filter, lens, and infrared camera (1-r).

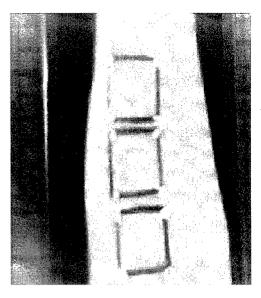


Figure 2. Test sites on forearm.

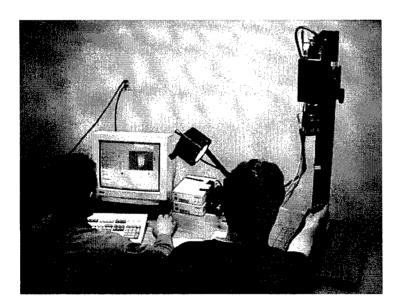


Figure 3. LW-NIR hydration imaging system in use.

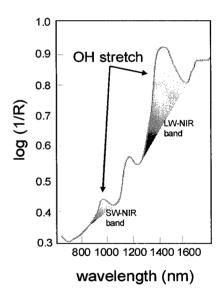


Figure 4. Skin optical density spectrum showing NIR water bands used for hydration imaging.

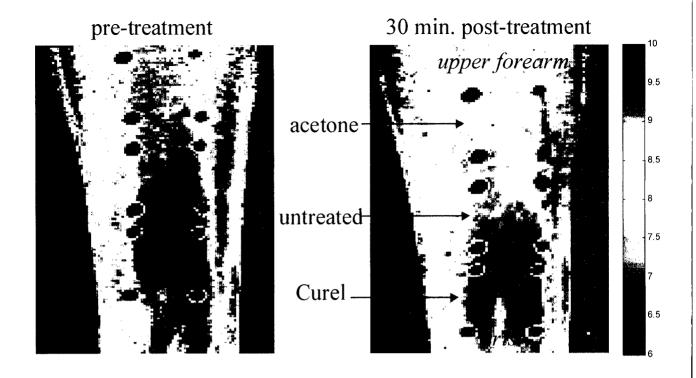


Figure 5. LW-NIR hydration images for subject no. 4 before and after product application.

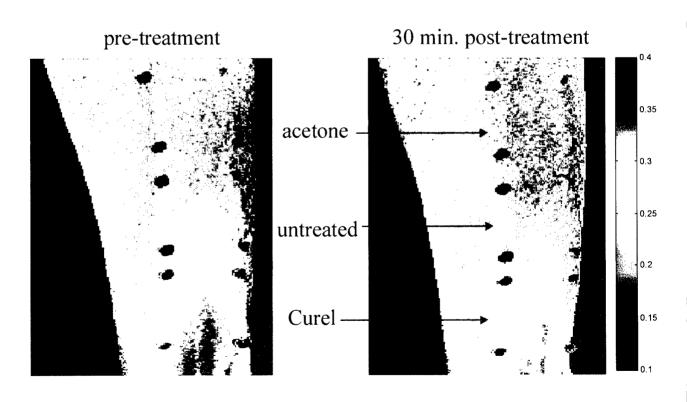


Figure 6. SW-NIR hydration images for subject no. 4 before and after product application.

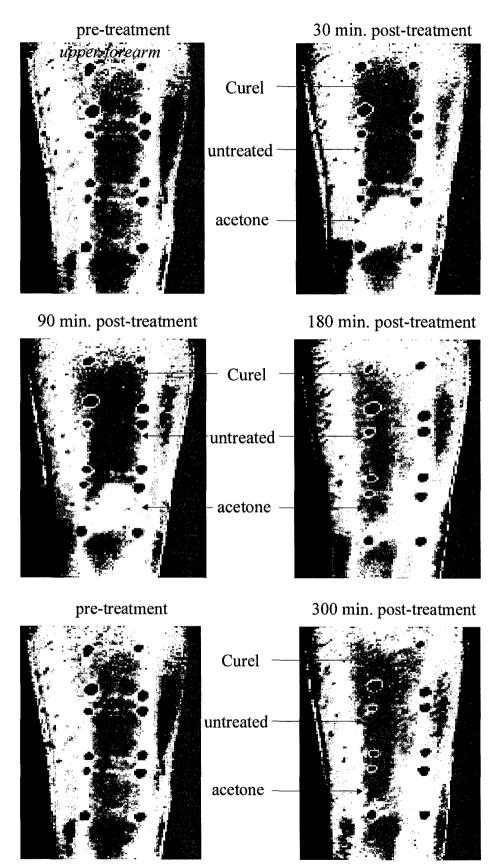


Figure 7. LW-NIR hydration image time series for subject no. 8.

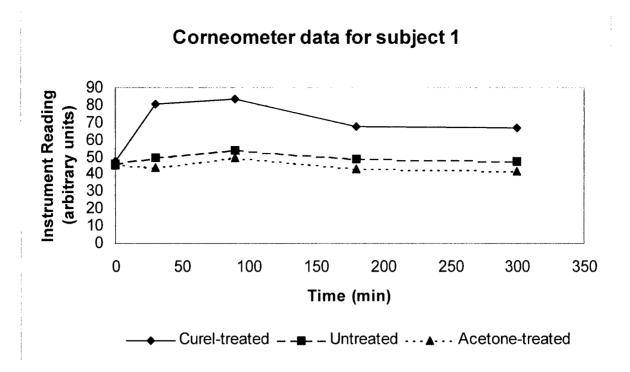


Figure 8. Corneometer data for subject no. 1.

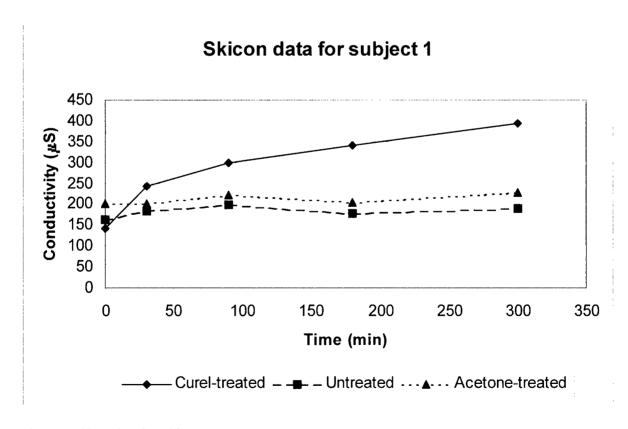


Figure 9. Skicon data for subject no. 1.

# Brain tissue characterization using Spectral Imaging: A potential clinical tool

Anita Mahadevan-Jansen, J. David Mongin, E. Duco Jansen, Dawn Pedrotty, Wei-Chiang Lin

Department of Biomedical Engineering, Vanderbilt University, Nashville, TN 37235

#### ABSTRACT

Spectral imaging as a modality combines two powerful techniques of imaging and fluorescence spectroscopy. By generating a 2-D image of an object with fluorescence information at every pixel, spectral imaging has the potential to provide clinicians with a valuable tool which can not only diagnosis the tissue but also provide an image of the boundary of where the normal and cancerous tissue intersect. The system used in these experiments was a modified spectral imaging system from Applied Spectral Imaging (SD-200, Carlsbad, CA). The system was mounted in an off-microscope configuration so that instead of performing microscopic measurements of tissue, macroscopic measurements on the order of several millimeters in size were collected. Preliminary results indicate that the spectra acquired from human brain tissues in vitro at individual pixels of the spectral image cube appear similar to that acquired using the single pixel system. Based on the findings of this study, spectral imaging has the potential to be a useful tool for tissue diagnosis and is currently limited by the speed of the data acquisition and size of the data.

Keywords: spectral imaging, fluorescence spectroscopy, tissue diagnosis, brain tumor demarcation

# INTRODUCTION

It is estimated that approximately 17,000 malignant brain tumors are diagnosed in adults and 1,500 in children every year in the United States [1-3] Although brain cancer only accounts for approximately 1.4% of all cancer [3], the 5-year survival rate of brain cancer patients (35%) is low. Surgical removal of brain tumor is the most common initial treatment received by brain cancer patients, typically followed by radiation therapy and chemotherapy. Many studies show that the degree of resection significantly influences recurrence and overall survival of brain tumor patients [4-6]. The surgical goal of brain tumor resection, hence, is to remove the maximum amount of tumor mass without sacrificing the patient's neurologic function. Incomplete resection implies the continued presence of tumor cells in the brain, which could later produce another tumor. In current practice, brain tumor margins are usually determined by the surgeon based on visual inspection and information provided by the CT/MR-image-based surgical navigation system [7] and/or intraoperative ultrasound (IOUS) [8]. However, several limitations in current guidance techniques prevent surgeons from successfully performing complete or high degree tumor resection. First, the infiltrating margins of primary tumors may not be visible on CT/MR images, even T2weighted MR images, unless tumor cells are sufficiently dense. Secondly, registration errors and intraoperative brain shift can drastically degrade the accuracy of the surgical navigation system by as much as 1 cm [9, 10]. Thirdly, unlike metastatic tumors, glioblastomas are typically diffuse in IOUS images. Fourthly, it is typically difficult to visually differentiate many low-grade gliomas and associated tumor margins from normal brain tissues. Although on-site pathology provides accurate diagnosis, it is time-consuming and expensive and as such is used less frequently for tumor margin detection in current practice. Hence, there is a clear need for the development of a real time guidance tool that allows intraoperative detection of brain tumor margins with high accuracy facilitating complete or high degree brain tumor resection.

# **Optical Spectroscopy**

One potential candidate for such tumor resection guidance is optical spectroscopy because it can detect alterations in tissue architecture and biochemical composition associated with the progression of disease. Tissue diagnosis using optical spectroscopy, also known as optical biopsy, has been widely investigated by several research groups in various organ systems in vivo [11, 12]. Intrinsic tissue fluorescence (autofluorescence) has been used to differentiate normal and non-normal tissues in the human breast and lung [13], bronchus [14], oral mucosa [15], cervix [16-18] and gastrointestinal tract [19-21]. Diffuse

reflectance spectroscopy is a fast and noninvasive method that can be detected by illuminating a sample (e.g., tissue) with a broad-band white light source and can be used to determine the optical properties of a sample [22], which reflect its structure and chemical composition. This has led to the application of diffuse reflectance spectroscopy alone for cancer detection in the bladder [23, 24], breast [25, 26] and skin [27-29].

Based on the promising results of the *in vitro* study [30], the applicability of optical spectroscopy for intra-operative detection of brain tumors/tumor margins was investigated in a pilot clinical trial consisting of 26 brain tumor patients [31]. The results of this clinical trial suggest that brain tumors and infiltrating tumor margins can be effectively separated from normal brain tissues *in vivo* using combined autofluorescence and diffuse reflectance spectroscopy [31]. A two-step empirical discrimination algorithm based on autofluorescence and diffuse reflectance at 460 nm and 625 nm was developed. This algorithm yields a sensitivity and specificity of 100% and 76% respectively in differentiating infiltrating tumor margins from normal brain tissues. Blood contamination was found to be a major obstacle that attenuates the accuracy of brain tumor demarcation using optical spectroscopy. Overall, this study indicates that optical spectroscopy has the potential to guide brain tumor resection intraoperatively with high sensitivity.

# Spectral Imaging (SI)

Although the results from the spectroscopy study showed extremely promising results and large scale clinical trials are currently in progress, single pixel spectroscopy is limited in its applicability especially as a guidance tool. Conventional optical spectroscopy is the measurement of light intensity as a function of wavelength at high spectral resolution but with very little spatial information. Multi-fiber spectroscopic probes provide some spatial information although conventional imaging is the technique used when spatial information is needed. However, imaging provides limited spectral information. Spectral imaging is a promising new method by which light spectrum at every picture element i.e. pixel, of a two-dimensional image is measured. The images acquired using such a method consists of a cube of information  $I_{x,y}(\lambda)$ , which contains the full spectrum at each pixel position (x, y) [32]. Thus spectral imaging combines the features of spectroscopy and imaging to provide new insights into the dynamics of tissue pathology by applying algorithms developed using spectral and imaging information from the same data cube. Thus the imaging capabilities of spectral imaging allows the spatial detection of subtle spectral changes.

Spectral Imaging may be performed in several ways depending on the method used for separating light into its spectral components. Two traditional methods of spectral imaging are the use of grating and spectral filters, which are based on spectral dispersion. Grating based systems use one axis of a CCD detector for spectral data and on axis for spatial data. Thus an image is obtained by scanning the grating parallel to the spectral axis of the CCD. Such a technique requires mechanical scanning capabilities and disallows the prior selection of regions of interest. In filter based techniques, discrete or continuous filters may be used. Multiple images are acquired for each wavelength where the wavelength selection is performed using filters. Inherent problems with filter-based techniques include difficulties in performing image registration and long integration times.

Spectral imaging can also be accomplished using interferometer based techniques. One such commercially available tool has been developed by Applied Spectral Imaging (ASI). This ASI system consists of an optical head, which contains (1) an interferometer, (2) a CCD array detector and (3) collection and imaging optics. The interferometer along with Fourier transform techniques are used to separate the light into its spectral components. The interferometer divides the incoming beam into two coherent beams with variable optical path differences (OPD) between them [32]. The beams are then recombined to interfere with each other. The interferogram obtained, which is a plot of the interference intensity as a function of OPD, is Fourier transformed to yield the spectrum. The interferogram is measured at each pixel in the CCD array, which upon Fourier transformation results in the spectrum at each pixel. Advantages of this technique include (1) high optical throughput, (2) high and variable spectral resolution and a wide spectral range. One disadvantage of the Fourier technique is the need for mathematical Fourier transformation required to obtain the spectrum, which leads to signification computation time and memory [32]. The acquisition of a spectral cube takes a greater length of time than a single shot CCD image measurement. This is because the spectral image has to be obtained for different OPDs and hence for different wavelengths. This acquisition time is dependent on the exposure time, data transfer time, and any other overhead time required to vary the OPD and the number of frames that need to be measured. In addition it should be noted that each frame of 512 x 512 requires about 256K bytes of memory for storage. Thus for the acquisition of 30 - 100 frames (a typical range) memory of 7.68 - 25.6 MB is required. However, this method has the potential to be a powerful guidance tool for brain tumor demarcation.

Thus, the overall goal of this project is to investigate the potential of a spectral imaging system (SD 200, ASI Inc. Carlsbad, California) in the acquisition of spectral images from gross brain tissues as a guidance tool during tumor resection. The specific objectives of this investigation are to (1) design and build an off-microscopic device for gross tissue measurement and (2) collect spectral images from brain tissues in vitro to assess the potential for discrimination of normal, tumor margins, and tumor tissues.

# MATERIALS AND METHODS

In order to view large regions of tissue instead of the microscopic sections analyzed by the original configuration of the spectral imaging system under investigation, an off-microscope system needed to be designed and constructed. However, retrofitting a system that is constructed to be used on a microscope or microscope like device so that it can be used in a free standing manner posed several problems including overall size of the final system and general feasibility issues. Figure 1 displays a schematic of the setup designed and constructed for the off-microscope configuration. A post that provides a stable platform for the optical head was built so that it provided minimum physical interference with maximal support.

Illumination was provided by a 100 W mercury arc lamp (Atto Arc 100W, Atto, Inc.) and a liquid light guide (Edmund Scientific) was used to deliver the light. The mercury lamp provided greater than 2mW at 360 nm using a 360 nm (±10 nm) bandpass filter (Omega Optical, Brattleboro, VT), which was found to be adequate for the spectral images acquired. The liquid light guide was employed as it provided even illumination at the sample. In order to deliver excitation light from the lamp and collect fluorescence light from the sample, a dichroic filter at 380 nm (380DCLP, Omega Optical, Brattleboro, VT) 380nm, was used. In addition a 380 nm longpass

filter was placed in front of the optical head so that all excitation light was rejected.

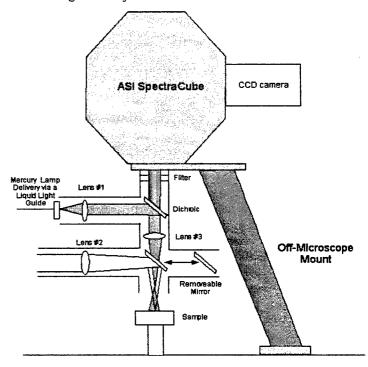


Figure 1: Schematic of the off-microscope configuration.

For the initial calibration experiments, canine brain tissue was obtained under the guidelines of the Animal Care Committee. Brain tissue obtained was snap frozen in liquid nitrogen and then stored in a ultra-low temperature freezer until use. Prior to spectral measurements, the tissue was thawed slowly to room temperature and hydrated with saline. The samples were used for no more than 15 minutes each to insure that the measured fluorescence was not influenced by dehydration of the tissue. The samples were placed in a petri dish containing saline during fluorescence measurements. For the actual spectral measurements, human brain tissues were used. These were acquired from patients undergoing temporal lobectomy or craniotomy procedures according to a protocol approved by the Vanderbilt Institutional Review Board. The tissues were stored and used as described above.

The spectral measurements were acquired using the setup described in Figure 1. All measurements were made at a center wavelength of 360nm with an illumination power of 2.5 mW at the level of the tissue. No photo bleaching was observed with this level of illumination as there was no significant drop in the overall fluorescence intensity during measurements. In conjunction with the acquisition of spectral images, the *in vivo* single pixel fluorescence spectroscopy system was used to measure the fluorescence spectra of the samples in order to validate the results using the ASI system to ascertain that it provides accurate diagnostic information. This *in vivo* system is described in detail in reference [31]. The acquired spectral data were calibrated for the spectral response of the detection systems using an NIST calibrated tungsten lamp. Rhodamine 6G was used as reference for all fluorescence measurements.

# **Acquisition Parameter Determination and Effect**

Many of the system parameters including step size of the interferometer, number of frames, spectral range, acquisition time per frame, virtual frames (zero padding), and scaling factor can be manipulated in software and needs to be set appropriately for accurate spectral information using the ASI system. For spectral image acquisition of brain tissue, the parameters that contributed to the overall quality of the spectra are step size, number of frames, and acquisition time [32]. The relationship of the number of steps between frames with the number of frames proved to be the most important factor in pixel-to-pixel variations. The number of steps between frames (s) controls the amount of angular movement that is performed by the beam splitter. The number of frames (f) defines the number of interferogram points that will be gathered for each spectral image. Figure 2 shows the effect of varying s and f on the spectral shape. The graphs show that when the product of

the number of steps and the number of frames increases; the signal to noise decreases. Canine brain tissue was used to determine optimal values in achieving spectral shape and reasonable signal to noise of the spectra.

It was found that the product of the number of steps and the number of frames that consistently provided reasonable signal to noise and the ability to perform pixel-to-pixel measurements was equal to 3000. The optimal set of parameters was determined to be number of steps=12 and number of frames=250. This parameter set proved to stabilize the spectra obtained from samples so that pixel-to-pixel measurements could be performed.

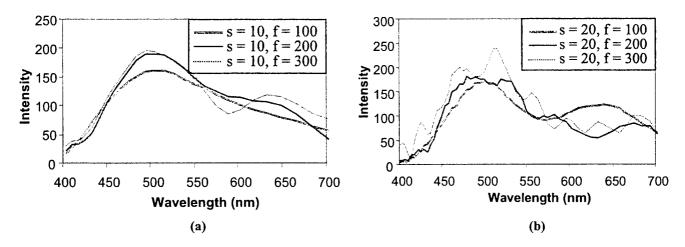
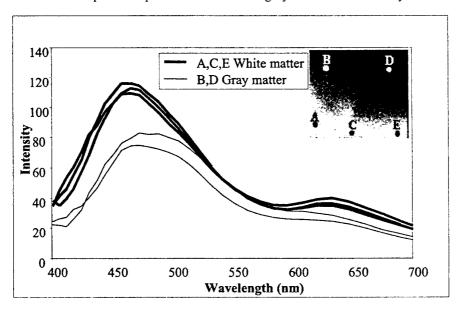


Figure 2: Fluorescence spectra of canine brain tissue acquired with (a) s = 10, f = 100, 200 and 300 respectively and (b) s = 30, f = 100, 200 and 300 respectively.

#### RESULTS

The human brain tissues used in this study were obtained from patients undergoing tumor resection and immediately frozen until time of study. The samples were thawed and cleaned of residual blood with saline for spectral image acquisition. Two samples of normal human brain tissue and two glioblastoma samples were studied. All human brain tissue spectral cubes were acquired using s = 12 and f = 250. Acquisition times were typically about 100 ms per frame and the total build time were typically on the order of about 60 seconds. Figure 3 shows the spectral image and fluorescence spectra of normal human brain tissue. Fluorescence spectra acquired from white and gray matter can be clearly differentiated.



**Figure 3:** (a) Spectral image of normal human brain tissue. (b) Fluorescence spectra at 5 representative pixels where pixels A, D and E are from white matter and pixels B and C are from gray matter.

Figure 4 shows the spectral image and fluorescence spectra of brain tissue with glioblastoma multiforme. Fluorescence spectra acquired from several tumor regions are shown.

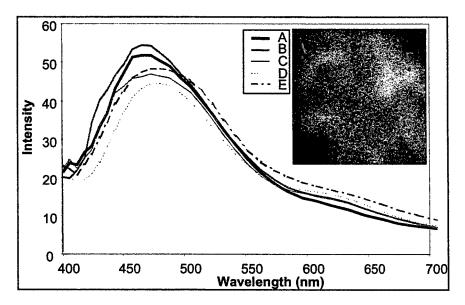


Figure 4: (a) Spectral image of tumor brain tissue. (b) Fluorescence spectra at 5 representative pixels.

Fluorescence spectra were also acquired with the single pixel fluorescence system described in reference [31] for 2 of the human brain tissue samples; one normal and one tumor. The fluorescence spectra acquired using both systems were essentially similar for normal as well as glioblastoma human brain tissue except below 420 nm.

#### DISCUSSION

Spectral imaging of biological tissue has the potential to greatly enhance the feasibility of using optical spectroscopic signal for diagnosis and therapeutic guidance. In most cases, physicians and scientist alike would rather see a spectral image of a given sample versus just a spectrum associated with the sample. By obtaining a spectral image of an object, it is possible to visualize the regions of interest based on their fluorescence signature and the images can be processed and false colored for discrimination. Acquisition parameters play an important part in the accurate representation of the fluorescence spectra for pixel-to-pixel comparison. The illumination intensity coupled with the exposure time per frames controlled the overall signal to noise level, which proved to be a concern in dimly fluorescent samples such as large sections of gray matter and glioblastoma, which have a lower fluorescence. Other parameters that played a significant role in the overall line shape of the spectrum are the number of steps between frames and the number of frames. When the product of these two parameters is kept constant the spectrum does not change greatly; however for tissue samples as the product increases the signals become more noisy due to over-sampling. In principle, as the product increases, the ability to separate small differences in wavelength characteristics increases if the signals have a narrow FWHM, such as a laser or narrow expressing dye [3]. However, for tissue, which typically has a more broad fluorescence emission, high spectral resolution can be sacrificed in order to yield signals that do not vary from pixel-to-pixel unless the fluorescence emission is truly different.

When the fluorescence spectra acquired from the ASI system were compared with that acquired using the single pixel fluorescence system, the spectra appeared very similar. However, it should be noted that in comparing spectra across different acquisition system, calibration for the spectral response of the system becomes extremely critical. This was particularly challenging for the spectral cube as pixel-by-pixel calibration needs to be performed. The similarity of the fluorescence spectra indicates the potential for applying the results and the developed algorithms using the single pixel fluorescence system [31] to data acquired using the ASI system. This then presents a challenging but promising avenue of development of optical techniques for brain tumor demarcation.

Before this system can be applied *in vivo* several limiting factors of using the ASI system in a clinical setting need to be addressed. In the current study the area of investigation is restricted to a few millimeters. In order to obtain a more reasonable region of study the area of illumination needs to be increased to the order of 2 X 2 cm which would require a much more powerful light house as compared with that used here. While the off-microscope configuration described here is useful for

research purposes, it is somewhat impractical for use in the operating room. Two potential system configurations include one with the operating microscope and the other coupled to an endoscope. Both options are currently under study. The overall acquisition of spectral images from human brain tissue and diagnosis determination using the acquired data could prove to be challenging *in vivo* due to the inherent curvature of the brain. Thus some form of distance measurement for correction of the fluorescence data (since fluorescence diminishes as the square of the distance) needs to be incorporated [7]. This may be performed using ultrasound, etc.

Spectral imaging thus presents an opportunity to provide real time, diagnostic and spatial information for surgical guidance. Spectral information can be utilized for brain tumor demarcation provided the spectra are carefully calibrated and the acquisition parameters are carefully selected for the given tissues. At this time, imaging time is still too long. Although acquisition time is reasonable (100 ms per frame), the build time associated with performing the Fourier transform on the interferogram is a problem. While the continued development of the ASI camera for spectral imaging based brain tumor demarcation will progress, tunable filters in conjunction with CCD systems are also suggested as potential future directions. The development of the off-microscope setup of the ASI system described above provides an initial step towards spectral imaging of brain tissue in a clinical setting. Based on the success of the single pixel *in vivo* fluorescence spectroscopy system, spectral imaging can provide diagnostic capabilities similar to fluorescence spectroscopy; however the main advantage over fluorescence spectroscopy is that associated with the fluorescence information, an image of the object is also acquired so that processing of the image can yield clear delineation of the border between normal and tumor tissues.

# REFERENCES

- 1. Chamberlain, M. and P. Kormanik, "Practical Guidelines for the Treatment of Malignant Gliomas", West J Med, 168(2): p. 114-120, 1998.
- 2. Duffner, P., et al., "Postoperative Chemotherapy and Delayed Radiation in Children less than three years of Age with Malignant Brain Tumors", N Engl J Med, 328: p. 1725-1731, 1993.
- 3. ACS, Brain and Spinal Cord Cancers of Adults, American Cancer Society 1998.
- 4. Selch, M., et al., "Gangliogliomas: Experience with 34 patients and Review of the Literature", Am J Clin Oncol, 21(6): p. 557-564, 1998.
- 5. Mohan, D., et al., "Outcome in Elderly Patients undergoing Definitive Surgery and Radiation Therapy for Supratentorial Glioblastoma Multiforme at a Tertiary Care Institution", Int J Radiat Oncol Biol Phys, 42(5): p. 981-987, 1998.
- 6. Freeman, C., J. Farmer, and J. Montes, "Low-grade astrocytomas in children: evolving management strategies", Int J Radiat Oncol Biol Phys, 41(5): p. 979-987, 1998.
- 7. Barnett, G. H., C. P. Steiner and D. W. Roberts (1998) Surgical navigation system technologies. in *Image-guided neurosurgery : clinical applications of surgical navigation*. (Edited by G. H. Barnett, D. W. Roberts and R. J. Maciunas), pp. 17-32. Quality Medical Publishing, Inc., St. Louis, MO.
- 8. Auer, L. M. and V. v. Velthoven (1990) Intraoperative Ultrasound Imaging in Neurosurgery: Comparison with CT and MRI. Springer-Verlag, Berlin.
- 9. Hill, D., C. J. Maurer, R. Maciunas, J. Barwise, J. Fitzpatrick and M. Wang (1998) Measurement of intraoperative brain surface deformation under a craniotomy. *Neurosurgery* 43, 514-526.
- 10. Dorward, N., O. Alberti, B. Velani, F. Gerritsen, W. Harkness, N. Kitchen and D. Thomas (1998) Postimaging brain distortion: magnitude, correlates, and impact on neuronavigation. *J Neurosurg* 88, 656-662.
- 11. Richards-Kortum, R. and E. Sevick-Muraca (1996) Quantitative optical spectroscopy for tissue diagnosis. *Annu. Rev. Phys. Chem.* 47, 555-606.
- 12. Ramanujam, N. (2000) Fluorescence spectroscopy of neoplastic and non-neoplastic tissues. Neoplasia 2, 89-117.
- 13. Alfano, R.R., et al., "Fluorescence Spectra from Cancer and Normal Human Breast and Lung Tissues", *IEEE Journal of Quantum Electronics*, **QE-23**(10): p. 1806 1811, 1987.
- 14. Hung, J., et al., "Autofluorescence of Normal and Malignant Bronchial Tissue", Lasers Surg Med, 11: p. 99-105, 1991.
- 15. Roy, K., et al. "Diagnostic Fluorescence Spectroscopy of Oral Mucosa", SPIE 2395, Bellingham, 1995.

- 16. Lohmann, W., et al., "Native Fluorescence of the Cervix Uteri as a Marker for Dysplasia and Invasive Carcinoma", Euro Jour Obstet Gynecol Reprod Biol, 31: p. 249-253, 1989.
- 17. Ramanujam, N., et al., "Spectroscopic Diagnosis of Cervical Intraepithelial Neoplasia (CIN) in vivo using Laser-induced Fluorescence Spectra at Multiple Excitation Wavelengths", Lasers Surg Med, 19(1): p. 63-74, 1996.
- 18. Ramanujam, N., et al., "Development of a Multivariate Statistical Algorithm to Analyze Human Cervical Tissue Fluorescence Spectra Acquired in vivo", Lasers Surg Med, 19(1): p. 46-62, 1996.
- 19. Schomacker, K.T., et al., "Ultraviolet Laser-Induced Fluorescence of Colonic Tissue: Basic Biology and Diagnostic Potential", Lasers in Surg Med, 12: p. 63-78, 1992.
- 20. Feld, M.S. "Early Detection of Dysplasia in Colon and Urinary Bladder", SPIE 1426, Bellingham, 1991.
- 21. Panjehpour, M., et al., "Spectroscopic Diagnosis of Esophageal Cancer: New Classification Model, Improved Measurement System", Gastrointest Endosc, 41(6): p. 577-81, 1995
- 22. Bigio, I.J. and J.R. Mourant, "Untraviolet and Visible Spectroscopies for Tissue Diagnostics: Fluorescence Spectroscopy and Elastic-Scattering Spectroscopy", *Phys Med Biol*, 42: p. 803-814, 1996.
- 23. Koenig, F., et al., "Spectroscopic Measurement of Diffuse reflectance for enhanced detection of bladder carcinoma", Urology, 51(2): p. 342-5, 1998.
- 24. Mourant, J.R., et al., "Spectroscopic Diagnosis of Bladder Cancer with Elastic Llight Scattering", Lasers Surg Med, 17(4): p. 350-7, 1995.
- 25. Svaasand, L.O., et al., "Reflectance Measurements of Layered Media with Diffuse Photon-density Waves: a Potential Tool for Evaluating Deep Burns and Subcutaneous Lesions", Phys Med Biol, 44(3): p. 801-13, 1999.
- 26. Peters, V.G., et al., "Optical Properties of Normal and Diseased Human Breast Tissues in the Visible and Near Infrared", Phys Med Biol, 35(9): p. 1317-34, 1990.
- 27. Manchesini, R., et al., "In vivo Spectrophotometric Evaluation of Neoplastic and Non-neoplastic Skin Pigmented Lesions. III. CCD Camera-based Reflectance Imaging", *Photochem Photobiol*, **62**(1): p. 151-4, 1995.
- 28. Tomatis, S., et al., "Spectrophotometric Imaging of Cutaneous Pigmented Lesions: Discriminant Analysis, Optical Properties and Histological Characteristics", J Photochem Photobiol B, 42(1): p. 32-9, 1998.
- 29. Bono, A., et al., "The Invisible Colours of Melanoma. A Telespectrophotometric Diagnostic Approach on Pigmented Skin Lesions", Eur J Cancer, 32A(4): p. 727-9, 1996.
- 30. Lin WC, Toms SA, Motamedi M, Jansen ED, Mahadevan-Jansen A, "Brain tumor demarcation using optical spectroscopy; an in vitro study," J Biomedical Optics, Vol. 5, No. 2, 214-220, 2000.
- 31. Lin WC, Toms SA, Jansen ED, Mahadevan-Jansen A, "In vivo brain tumor demarcation using optical spectroscopy," *Photochemistry and Photobiology* (in press), 2001.
- 32. Garini, Y., et al., Spectral Bio-Imaging, in Fluorescence imaging spectroscopy and microscopy, X.F. Wang and B. Herman, Editors. 1996, John Wiley: New York. p. 87-124

# The influence of the refractive index on EGFP fluorescence lifetimes in mixtures of water and glycerol

Klaus Suhling<sup>a</sup>, Daniel M. Davis<sup>b</sup>, Zdeněk Petrášek<sup>a</sup>, Jan Siegel<sup>c</sup> and David Phillips<sup>a</sup>

<sup>a</sup>Department of Chemistry, Imperial College of Science, Technology & Medicine, London SW7 2AY, UK,

bDepartment of Biology,
 Sir Alexander Fleming Building,
 Imperial College of Science, Technology & Medicine,
 London SW7 2AZ, UK,

 $^c$  Femtosecond Optics Group The Blackett Laboratory, Imperial College of Science, Technology & Medicine, London SW7 2BW, UK

# ABSTRACT

As a precursor to applying fluorescence lifetime imaging (FLIM) to studies of intercellular communication in molecular immunology, we have investigated the fluorescence lifetime of enhanced green fluorescent protein (EGFP) in mixtures of water and glycerol using time-correlated single photon counting (TCSPC). We find that the EGFP lifetime decreases with increasing glycerol content. This is accounted for quantitatively by the refractive index dependence of the fluorescence lifetime as predicted by the Strickler Berg formula which relates the fluorescence lifetime to the absorption spectrum. The solvent viscosity has no influence on the fluorescence lifetime.

We also discuss the refractive index dependence of the GFP fluorescence lifetime in more complex systems. The findings are particularly relevant for the interpretation of FLIM of GFP expressed in environments such as bacteria and cells.

**Keywords:** EGFP fluorescence lifetime. GFP, TCSPC, FLIM, immune synapse, Strickler Berg formula, inter- and intra-cellular communication

# 1. INTRODUCTION

An emerging theme in contemporary molecular immunology is that knowledge of protein structures and the physical chemistry of soluble receptor/ligand pairs are insufficient in predicting outcomes of intercellular communications.<sup>1</sup> As cells from the immune system survey other cells for signs of disease, proteins accumulate and organize in distinct patterns in the region of contact between the two cells. This formation of segregated molecular domains at intercellular contacts between immune cells is emerging as a critical molecular mechanism of immune recognition.<sup>2–4</sup> Using the green fluorescent protein (GFP).<sup>5</sup> redistribution of receptors and ligands at immune synapses between live cells have recently been imaged by time-lapse laser scanning confocal fluorescence microscopy.<sup>4</sup>

However, such imaging based on measuring fluorescence intensity only reveals the location of proteins at immune synapses. The fluorescence emission is a multi-parameter signal which can be characterized by intensity, position, lifetime, wavelength or polarization. Fluorescence lifetime imaging (FLIM)<sup>6-9</sup> is a technique that, in addition to position and intensity, also captures the fluorescence lifetime which allows the local physical environment of the fluorescence probe or fluorophore-tagged proteins to be studied.<sup>10</sup>

The fluorescence lifetime can report on, for example, microviscosity, refractive index, pH, polarity, or the orientation of the probe and its interaction with either the environment or with other probe molecules.<sup>11</sup> The interpretation of data can be complex,<sup>12</sup> particularly in a biological or biomedical context, so to interpret FLIM images for cell biology, parameters that affect the GFP fluorescent lifetime must be determined.

A number of studies of GFP fluorescence lifetimes have been reported. It has, for example, been found that it is insensitive to pH over a range from 5 to  $10,^{13}$  i.e. within the physiological range expected in live cells. In addition, time-resolved fluorescence anisotropy studies of GFP in mammalian cells, have been undertaken in order to obtain information about the viscosity of the GFP environment. The rotational correlation time of GFP in solution, around 15-17 ns, agrees well with theoretical calculations based on the shape of GFP. It increases in cells and bacteria.

GFP has been used in water/glycerol mixtures to study its diffusion coefficient using dynamic light scattering and fluorescence recovery after photobleaching.<sup>18</sup> It was found that its diffusion coefficient accurately obeys the Stokes Einstein equation which relates the diffusion coefficient to the solvent viscosity.

In this paper, we report a quantitative study of the refractive index influence on the fluorescence lifetime of the enhanced GFP (EGFP) in water/glycerol mixtures. The natural radiative lifetime of EGFP is calculated from the absorption and emission spectra and compared to the well characterized dye fluorescein. There is no evidence for a fluorescence lifetime dependence on the viscosity.

# 2. THEORETICAL BACKGROUND

The natural radiative lifetime  $\tau_0$  of molecules is defined as the reciprocal radiative transition probability  $k_0^{11}$ :

$$k_0 = \frac{1}{\tau_0} = \frac{8000 \pi c_0 \ln 10}{N_A} \frac{n_{fl}^3}{n_{abs}} \frac{g_{ex}}{g_{gr}} \langle \tilde{\nu}^{-3} \rangle^{-1} \int \frac{\varepsilon(\tilde{\nu})}{\tilde{\nu}} d\tilde{\nu}, \tag{1}$$

where  $c_0$  is the speed of light in vacuum,  $N_A$  the Avogadro number,  $g_{ex}$  and  $g_{gr}$  are the multiplicities of the excited and ground states,  $n_{fl}$  the mean refractive index over the fluorescence spectrum,  $n_{abs}$  the mean refractive index over the absorption spectrum,  $\varepsilon(\tilde{\nu})$  is the extinction coefficient and  $\tilde{\nu}$  is the wave number. The reciprocal mean value  $\langle \tilde{\nu}^{-3} \rangle^{-1}$  of the fluorescence spectrum is

$$\langle \tilde{\nu}^{-3} \rangle^{-1} = \frac{\int I(\tilde{\nu}) d\tilde{\nu}}{\int I(\tilde{\nu}) \tilde{\nu}^{-3} d\tilde{\nu}}.$$
 (2)

Equation 1 is a modified version of the case for sharp atomic transitions and is applicable to molecules (where the absorption band is broad and the emission Stokes shifted). The relationship is calculated from the Einstein A and B coefficients for spontaneous emission and for the probability of absorption. It uses the Born-Oppenheimer approximation where the wave function of each vibronic state can be written as the product of electronic and vibrational wave function. The derivation also assumes that the nuclear configurations of the ground state and the excited state are similar (Franck Condon principle). The multiplicities of the ground and excited states  $g_{gr}$  and  $g_{ex}$  are 1 for normal fluorescence transition between singlet states. The refractive index dependence is due to the medium in which the absorption and emission processes occur.

The formula can be used to predict the fluorescence lifetime from the absorption spectrum. Neglecting optical dispersion  $(n_{fl} = n_{abs} = n)$  and calculating the constants yields an often quoted form of the equation proposed by Strickler and Berg<sup>19</sup>:

$$\frac{1}{\tau_0} = 2.88 \times 10^{-9} \, n^2 \, \langle \tilde{\nu}^{-3} \rangle^{-1} \int \frac{\varepsilon(\tilde{\nu})}{\tilde{\nu}} \, d\tilde{\nu}. \tag{3}$$

An alternative equation has been proposed by Förster when the fluorescence and absorption spectra bear a mirror-image relationship to each other at wave number  $\tilde{\nu}_0^{20}$ :

$$\frac{1}{\tau_0} = 2.88 \times 10^{-9} \, n^2 \, \int \frac{(2\tilde{\nu}_0 - \tilde{\nu})^3}{\tilde{\nu}} \, \varepsilon(\tilde{\nu}) \, d\tilde{\nu}. \tag{4}$$

The natural fluorescence lifetime  $\tau_0$  is the fluorescence lifetime in the absence of non-radiative de-excitation. Radiative de-activation of the excited state with a rate constant  $k_0$  can compete with internal conversion with a rate constant  $k_{ic}$ , intersystem crossing to the triplet state  $(k_{isc})$ , or interaction with other molecules  $(k_{quench})$ . These non-radiative processes shorten the natural radiative lifetime  $\tau_0$  to the measured lifetime  $\tau_m$ . The quantum yield is the ratio of the radiative and non-radiative rate constants and relates the natural radiative lifetime  $\tau_0$  to the measured lifetime  $\tau_m$ :

$$\phi = \frac{k_0}{k_0 + k_{ic} + k_{isc} + k_{quench}} = \frac{\tau_m}{\tau_0},\tag{5}$$

with  $\phi \leq 1$  and, consequently,  $\tau_m \leq \tau_0$ . The Strickler Berg formula equation 3 thus places an upper limit on the fluorescence lifetime.

# 3. EXPERIMENTAL

The EGFP (GFP, F64L, S65T, Clontech) is a mutant of the GFP from the jellyfish Aequorea victoria. 1  $\mu$ l of EGFP were injected into a range of typically 0.8 ml of pre-prepared mixtures of water (distilled and passed through an Elgastat UHQ II water purifier (Elga Ltd), pH 7) and glycerol (Sigma) using a 5  $\mu$ l microsyringe. The EGFP concentration for the fluorescence lifetime measurements was typically  $5 \times 10^{-8}$  mol l<sup>-1</sup>. The fluorescein (Aldrich) concentration was  $5.6 \times 10^{-5}$  mol l<sup>-1</sup> in 0.1 M NaOH (BDH).

The EGFP absorption spectrum was measured on a Shimadzu UV-2501PC spectrophotometer, and the fluorescein absorption spectrum was measured on a Hewlett Packard HP8453 spectrophotometer. Excitation and emission spectra (bandwidth 5 nm) were measured on a SPEX Fluoro $\mathrm{Max}^{TM}$  spectrofluorometer using 10 mm pathlength quartz cuvettes (Hellma). The fluorescein sample was measured in a 1 mm pathlength quartz cuvette.

The fluorescence lifetimes were measured with time-correlated single photon counting (TCSPC)<sup>21,22</sup> using a solid state (10 W Coherent Verdi)-pumped, mode-locked, tunable Ti:sapphire laser (Coherent Mira 900) as excitation source. The pulse width was about 180 fs. The laser repetition rate of 76 MHz was reduced to 3.8 MHz using a pulse picker (APE, 60 % diffraction efficiency). The excitation wavelength was 470 nm, obtained by frequency doubling the 940 nm Mira output using an angle-tuned lithium iodate crystal, and the average power was 35  $\mu$ W. The emission was measured at 510 nm using a monochromator with 10 nm bandwidth. The detector was a side-on photomultiplier (model R955, Hamamatsu) with a commercial dynode chain and the photocathode at -1200 V. The TAC was triggered from a fast photodiode monitoring the excitation pulses. The maximum stop rate was 0.4 % of the start rate (for the 80 % water/20 % glycerol sample), and all other stop to start ratios were below this value. Vertical polarization was used on the excitation side, and the emission was collected at the magic angle of 54.7° to avoid depolarization effects.<sup>22</sup> Data analysis was performed on reconvolution software using a hybrid grid search algorithm (IBH).

A C++ program was used for the integration of absorption and emission spectra to calculate the natural radiative lifetime according to the Strickler Berg formula equation 3 and the Förster equation 4, with a resolution of 0.2 nm for the EGFP absorption spectrum and 1 nm for all other spectra.

The refractive index of the water/glycerol mixtures were taken from references [23] and [24] and extrapolated to 510 nm and 18°C.

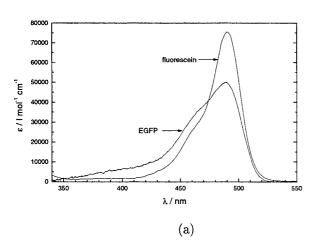
# 4. RESULTS

# 4.1. EGFP and fluorescein absorption and emission spectra

The absorption spectrum of EGFP in water is shown in figure 1(a). The EGFP concentration for this measurement was 0.0333 mg/ml  $[1.23 \times 10^{-6} \text{ mol } l^{-1}]$  ( $M_W^{EGFP} = 27 \text{ kDa}$ ). The absorbance at 489 nm was 0.0617, yielding an extinction coefficient  $\varepsilon_{EGFP} = 50~000~l~\text{mol}^{-1}\text{cm}^{-1}$ . This value is in good agreement with a value of (53 000±4 000) l mol $^{-1}$ cm $^{-1}$  quoted in references [25] and [26], but lower than 55 000-57 000 l mol $^{-1}$ cm $^{-1}$  as cited in reference [5].

The value for the absorption integral in equation 3 over a range from 340 nm to 530 nm is 6578 l mol<sup>-1</sup>cm<sup>-1</sup>. This can be compared to the value for fluorescein which has a similar absorption spectrum, as shown in figure 1(a). Using a fluorescein extinction coefficient  $\varepsilon_{fl} = 75\,500\,\mathrm{l\,mol^{-1}cm^{-1}}$  at 490 nm.<sup>19</sup> the value for the absorption integral from 360-540 nm is 6239 l mol<sup>-1</sup>cm<sup>-1</sup>, in good agreement with the value of 6183 l mol<sup>-1</sup>cm<sup>-1</sup> quoted in previous studies.<sup>19</sup> The fluorescein absorption integral value is slightly lower than its EGFP counterpart despite the latter's lower extinction coefficient. This is because the EGFP spectrum is broader and extends further into the blue than fluorescein.

The EGFP emission spectrum is shown in figure 1(b). The corresponding integral from 520-660 nm as calculated from equation 2 is  $7.00 \times 10^{12}$  cm<sup>-3</sup>. The fluorescein emission integral (from the spectrum in figure 1(b)) is  $6.71 \times 10^{12}$  cm<sup>-3</sup>, in good agreement with  $6.70 \times 10^{12}$  cm<sup>-3</sup> quoted in previous studies.<sup>19</sup> Despite having almost identical spectral shapes, the EGFP integral value is higher due to its spectrum's blue-shift relative to that of fluorescein. In



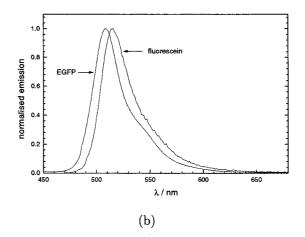


Figure 1. (a) The absorption spectra of EGFP in water and fluorescein in 0.1 M NaOH. (b) The corresponding emission spectra. The natural radiative lifetime  $\tau_0$  calculated from these spectra according to equation 3 is 4.23 ns for EGFP and 4.66 ns for fluorescein.

contrast to the absorption spectrum, the intensity of the emission spectrum does not influence the integral value, whereas the shape and wavelength do.

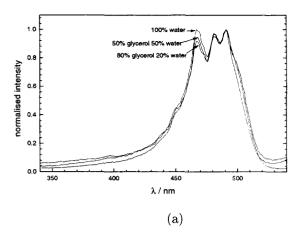
Using the Strickler Berg formula equation 3, a natural radiative lifetime of  $\tau_0^{EGFP}=4.23$  ns can be calculated. In water with a refractive index of about 1.336 at 510 nm at room temperature, and a quantum yield  $\phi_{EGFP}=0.60,^{5,25}$  this is shortened to  $\tau_{EGFP}=2.54$  ns (see table 1). This predicted value is about 7 % shorter than the measured value of  $(2.73\pm0.03)$  ns obtained in this work. Other authors quote a measured fluorescence lifetime of 2.81 ns for EGFP in water.<sup>16</sup> (A more detailed discussion of fluorescence lifetime studies can be found below.)

One reason for the apparent discrepancy between calculated and measured fluorescence lifetime could be the value of the quantum yield. If this is higher than the quoted 60 %, then the lifetime is longer. In addition, as the linear relationship between the extinction coefficient and the absorption integral extends to the error, a 7.5 % error  $^{25,26}$  in  $\varepsilon_{EGFP}$  translates into a 7.5 % error in the absorption integral, and hence the lifetime. Adding the quantum yield error to this results in an error range in which the theoretical and experimental values agree.

The Förster formula equation 4 yields a value of  $\tau_0 = 4.67$  ns for the fluorescein natural radiative lifetime, in good agreement with the value from the Strickler Berg formula equation 3 and previous work.<sup>27</sup> This is because the absorption and emission spectra bear a good mirror image relation to each other around  $\tilde{\nu}_0^{-1} = 503$  nm. The Förster formula equation 4 predicts 4.50 ns for the natural radiative lifetime of EGFP ( $\tilde{\nu}_0^{-1} = 495$  nm). The higher value compared to the Strickler Berg equation 3 is due to deviations from the mirror image relation.

fluorophore	$\int rac{arepsilon( ilde{ u})}{ ilde{ u}}d ilde{ u}$	$\langle \tilde{\nu}^{-3} \rangle^{-1}$	solvent	n	$ au_0$	φ	$\tau$
	$l  mol^{-1} cm^{-1}$	$cm^{-3}$			ns		ns
EGFP	6578	$7.00 \times 10^{12}$	water	1.336	4.23	0.60	2.54
EGFP	6578	$7.00\times10^{12}$	-	1	7.54	0.60	4.52
fluorescein	6239	$6.71\times10^{12}$	0.1 M NaOH	1.336	4.66	0.93	4.33
fluorescein <sup>19</sup>	6183	$6.70\times10^{12}$	0.1 M NaOH	1.336	4.70	0.93	4.37

Table 1. The integrals and natural radiative lifetimes  $\tau_0$  as determined from the absorption and emission spectra of EGFP and fluorescein in figure 1, using the Strickler Berg formula equation 3 with an extinction coefficient  $\varepsilon_{EGFP} = 50~000~l~mol^{-1} cm^{-1}$  and  $\varepsilon_{fl} = 75~500~l~mol^{-1} cm^{-1}$ . n is the refractive index,  $\phi$  the quantum yield and the calculated fluorescence lifetime  $\tau = \phi \tau_0$ . The n = 1 value is included for comparison with the gradient obtained from a straight line fit of the data in figure 4.



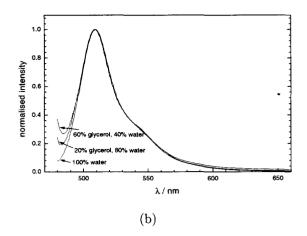


Figure 2. (a) The normalised excitation spectra (emission wavelength  $\lambda_{em} = 560$  nm) and (b) the normalised emission spectra (excitation wavelength  $\lambda_{ex} = 470$  nm) of EGFP in different glycerol/water mixtures.

# 4.2. EGFP excitation and emission spectra in different glycerol/water mixtures

Figure 2(a) shows the normalised excitation (emission wavelength  $\lambda_{em} = 560$  nm), and figure 2(b) shows the normalised emission spectra (excitation wavelength  $\lambda_{ex} = 470$  nm) of EGFP in a range of different glycerol water mixtures from 100 % water to 20 % water/80 % glycerol (by volume). There is no shape change or shift of the emission peak, the position of which remains at 509 nm, irrespective of the glycerol content of the solution.

EGFP in 100 % glycerol appears to denature the protein as the fluorescence emission spectrum was altered, and the intensity was dramatically reduced by several orders of magnitude, so that the lifetime could not be determined. In addition, after an attempt to degas the EGFP in 100 % water by successive freeze pump thaw cycles, no fluorescence emission could be detected at all.

# 4.3. EGFP fluorescence lifetime studies in different glycerol/water mixtures

Figure 3 shows the fluorescence decays of EGFP in different glycerol water mixtures. A gradual decrease of the fluorescence lifetime as the glycerol content increases is evident even without data analysis. A fit to a single exponential decay law yields  $(2.73\pm0.03)$  ns for the EGFP fluorescence lifetime in water. Other workers propose a 3-exponential fit to the EGFP fluorescence decays (excited at a shorter wavelength (450 nm) than this work), the longest and most intense component of which is 2.81 ns. <sup>16</sup> However, a single exponential decay model gave an adequate fit to the data for our current experimental set-up with a photomultiplier, in agreement with fluorescence lifetime studies on the S65T mutant. <sup>14,17</sup>

The fluorescence lifetime decreases to  $(2.48 \pm 0.03)$  ns for 60 % water/40 % glycerol, and to  $(2.25 \pm 0.03)$  ns for 20 % water/80 % glycerol (table 2). Importantly, the decrease in fluorescence lifetime with increasing glycerol content is gradual and does not occur suddenly at a certain water/glycerol mixture. This indicates that the bulk solvent properties affect the EGFP fluorescence lifetime, rather than, for example, a local solvation effect.

# 5. DISCUSSION

The low concentration of  $5 \times 10^{-8}$  mol l<sup>-1</sup> makes interaction effects such as self-absorption or aggregation unlikely. The latter has for example been seen in aging samples of coral red fluorescent protein in bacteria and is accompanied by a shortening of the fluorescence lifetime.<sup>28</sup> Self-absorption only occurs at high fluorophore concentrations, and leads to an apparent increase of the fluorescent lifetime.<sup>11</sup>

The fluorescence can be dependent on the viscosity of the solvent if internal molecular rotation is allowed, e.g. in certain dyes.<sup>29</sup> This in effect enables a charge transfer process to compete with radiative de-excitation and results in a non-radiative pathway  $k_{quench}$  in equation 5.<sup>30</sup> However, such a scenario can be excluded in the case of EGFP. Firstly, EGFP does not show any such possibility of rotation as the fluorophore in buried inside the rigid

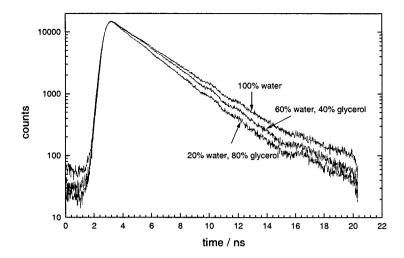


**Figure 3.** The fluorescence decays of EGFP in different glycerol/water mixtures showing a decrease of the fluorescence lifetime as the glycerol content of the medium increases.

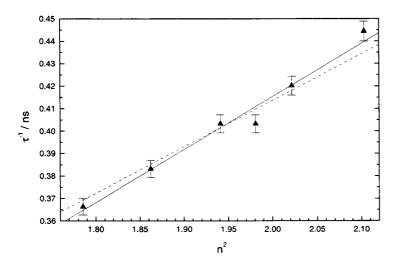
% water	% glycerol	au	n
100	0	2.73	1.3362
80	20	2.61	1.3647
60	40	2.48	1.3933
50	50	2.48	1.4075
40	60	2.38	1.4218
20	80	2.25	1.4503
0	100	-	1.4788

Table 2. The measured fluorescence lifetimes  $\tau$  from a monoexponential fit to the fluorescence decays in figure 3. The error (3 standard deviations) is about 1 %. The refractive index values are from references [23] and [24] and extrapolated to 510 nm and 18°C. The water/glycerol percentages are by volume.

barrel shaped protein structure where, according to time-resolved fluorescence anisotropy studies, it does not rotate independently.<sup>17</sup> Secondly, the theory predicts an increase of fluorescence lifetime with viscosity<sup>30</sup> since the internal molecular rotation is hindered in a more viscous medium, reducing  $k_{quench}$  and thus, according to equation 5, increasing  $\tau$ . However, this is the opposite of the trend we measured, in our work the fluorescence lifetime decreases with increasing viscosity.

However, there are several studies on the refractive index dependence of the fluorescence lifetime.<sup>31–34</sup> For example, it was found that the fluorescence lifetime of 9,10 diphenylanthracene in xylene scaled with the square of the refractive index when varying the temperature between 23°C and 127°C, as predicted by the Strickler Berg equation 3. The same effect was observed when using different solvents.<sup>31</sup> In addition, supersonic free jet spectroscopy shows the ratio of the fluorescence lifetime of isolated anthracene derivatives in a supersonic free jet divided by the lifetime of the same molecule in a solvent is proportional to the square of the refractive index of the solvent.<sup>34</sup>

Following this approach, according to the Strickler Berg equation 3, a plot of the inverse fluorescence lifetimes versus the square of the refractive index should yield a straight line, provided the quantum yield  $\phi$  and the extinction coefficient remain constant. (The Förster formula equation 4 has the same refractive index dependence.) The



**Figure 4.** The inverse EGFP fluorescence lifetime  $\tau^{-1}$  versus the square of the refractive index of the glycerol/water mixture.

intercept of the straight line is zero, and the gradient m is then given by

$$m = \frac{2.88 \times 10^{-9}}{\phi} \langle \tilde{\nu}_{av}^{-3} \rangle^{-1} \int \frac{\varepsilon(\tilde{\nu})}{\tilde{\nu}} d\tilde{\nu}, \tag{6}$$

combining equation 3 and equation 5. Note that whilst a refractive index of zero and an infinite fluorescence lifetime have no physical meaning, the intercept being zero is a mathematical requirement arising from the treatment of the data with equation 3.

A plot of the inverse lifetimes versus the squared refractive index of the solvent is shown in figure 4. A fit with both the intercept and gradient as variable parameters yields an intercept of  $(0.56 \pm 0.36)$  ns<sup>-1</sup> and a gradient of  $(0.235 \pm 0.016)$  ns<sup>-1</sup> (solid line in figure 4). A fit through zero with only the gradient as variable parameter yields a value of  $(0.207 \pm 0.004)$  ns<sup>-1</sup> (dashed line in figure 4).

The value derived directly from the absorption and emission spectra in figure 1 using the Strickler Berg formula is  $0.223 \text{ ns}^{-1}$ , the reciprocal value of  $\tau$  for n=1 in table 1. This is in good agreement with the gradients of the straight line fits to figure 4. Thus two entirely different methods, one based on steady state measurements, the other on time-resolved measurements, give the same result for m in equation 6.

Errors in this treatment could arise from the quantum yield or the extinction coefficient not being constant. They could, for example, decrease with increasing glycerol content. pH titration experiments with S65T GFP have indeed shown that the extinction coefficient appears to decrease with decreasing pH while the fluorescence lifetime remains constant.<sup>13</sup> If this is the case in our work, it would lead to a downward curvature in of the plot in figure 4. The intercept of a two parameter straight line fit is indeed below zero, but this could also be due to experimental errors, and further experiments would be needed to elucidate this matter.

Furthermore, it has been claimed that the refractive index dependence can depend on the shape of the molecule, and may deviate from its quadratic form. Although this has been subject of some theoretical attention, <sup>32</sup> supersonic free jet spectroscopy studies appear to indicate that the refractive index dependence is indeed very close to  $n^2$ . <sup>34</sup>

# 6. THE REFRACTIVE INDEX DEPENDENCE OF GFP FLUORESCENCE LIFETIMES IN MICROHETEROGENEOUS SYSTEMS

# 6.1. Reverse micelles

A dependence of the EGFP fluorescence lifetime on the medium has also recently been observed in reverse micelle systems.<sup>16</sup> There the fluorescence decays were analysed in terms of a 3-exponential decay law, it was found that

the longest and strongest of these EGFP fluorescence lifetime in bulk ( $\tau_{buffer}$ =2.81 ns) decreased to around 2.5 ns in the water pool of the reversed micelles.<sup>16</sup> The authors do not explicitly attribute this effect to the refractive index. However, the refractive index dependence of the fluorescence lifetime may explain why the EGFP fluorescence lifetime is lower in the water pool of reverse micelles than in bulk water.

Using a refractive index of n=1.483 for AOT,<sup>35</sup> a lower limit  $\tau_{min}$  can be placed on the EGFP fluorescence lifetime in micelles:  $\tau_{min}=(\frac{n_{water}}{n_{AOT}})^2\tau_{buffer}=2.28$  ns. This value is only correct if the EGFP were entirely surrounded by AOT. However, as it resides in the water pool inside the micelle, the effective refractive index of the micelle is lower than that of AOT, but higher than that of water. Consequently, the corresponding fluorescence lifetime is expected to be somewhere inbetween. Indeed, all of the quoted fluorescence lifetimes of EGFP in micelles of different sizes are above the minimum value  $\tau_{min}=2.28$  ns and below  $\tau_{buffer}=2.81$  ns.<sup>16</sup>

# 6.2. Cells

Considering the above, the lifetime of GFP in cells may also be expected to be different in different locations. For example, it has been reported that the GFP S65T mutant lifetime in PBS buffer is  $(2.93 \pm 0.02)$  ns, whereas the same mutant in cytoplasm is  $(2.6 \pm 0.1)$  ns.<sup>14,36</sup> If the refractive index explanation is applicable in this case, then  $n_{cytoplasm} = \sqrt{\frac{2.93}{2.6}} n_{PBS}$ . Say  $n_{PBS} = 1.336$ , then  $n_{cytoplasm} = 1.418$ . This opens up the possibility of using fluorescence lifetime measurements to determine the refractive index.

The EGFP mutant expressed in bacteria and cells has been found to have a fluorescence lifetime of 2.4-2.5 ns, <sup>28,36</sup> which is shorter than the EGFP fluorescence lifetime obtained in water. Again, a refractive index for the cells and bacteria could be calculated.

# 7. CONCLUSIONS AND RELEVANCE TO FLIM

We find that the refractive index dependence of the radiative lifetime of EGFP as predicted by the Strickler Berg formula, within experimental error, quantitatively matches the EGFP lifetime decrease in water/glycerol mixtures. Both steady state and time-resolved fluorescence measurements yield the same results for the absorption and emission integrals. There is no evidence that the EGFP fluorescence lifetime depends on the viscosity of the solvent. These findings are relevant for the interpretation of FLIM of GFP expressed in environments such as bacteria and cells.

We are ultimately interested in measuring the fluorescence lifetimes of GFP-tagged ligands and receptors to elucidate mechanisms of initiating intra- and intercellular signalling such as redistribution of proteins and lipids within the cell surface membrane or receptor oligomerisation. It is important to understand which factors affect the GFP lifetime, and here we show that the refractive index is one factor - on which, to the best of our knowledge, little work appears to have been done so far.

In this context, it would be interesting to study the lifetime of GFP in different locations in cells to see if the lifetime is shorter when located in the cell membrane rather than the cyctoplasm, for example. It would also be of interest to see if there are any inhomogeneities in the distribution of the fluorescence lifetime. This could easily be done with FLIM.

FLIM reporting on the physical environment of proteins as they redistribute into immune synapses appears to be a highly promising technique to study this immune synapses formation. This is ultimately relevant for understanding disease and for designing means to cure and prevent them.

#### **ACKNOWLEDGEMENTS**

KS, ZP and DP would like to acknowledge support from the UK's Engineering and Physical Sciences Research Council (EPSRC). DMD is supported by the Medical Research Council (MRC), the Biotechnology and Biological Sciences Research Council (BBSRC) and the Royal Society. We would also like to thank Paul French and Mary Cole from the Femtosecond Optics Group at Imperial College for stimulating discussions.

# REFERENCES

- 1. D. Davis, "Molecular recognition of disease at natural killer cell immune synapses," *Science Progress* **83**(4). pp. 303–316, 2000.
- 2. C. Monks, B. Freiberg, H. Kupfer, N. Sciaky, and A. Kupfer, "Three-dimensional segregation of supramolecular activation in T cell clusters," *Nature* **395**, pp. 82–86, 1998.
- 3. A. Grakoui, S. Bromley, C. Sumen, M. Davis, A. Shaw, P. Allen, and M. Dustin, "The immunological synapse: a molecular machine controlling T cell activation," *Science* 285, pp. 221–227, 1999.
- 4. D. Davis, I. Chiu, M. Fassett, G. Cohen, O. Mandelboim, and J. Strominger, "The human natural killer cell immune synapse," *Proceedings of the National Academy of Sciences* **96**, pp. 15062–15067, 1999.
- 5. R. Tsien, "The green fluorescent protein," Annual Reviews in Biochemistry 67, pp. 509-544, 1998.
- 6. A. Scully, A. MacRobert, S. Botchway, P. O'Neill, R. Ostler, and D. Phillips, "Development of a laser-based fluorescence microscope with subnanosecond time resolution," *Journal of Fluorescence* 6(2), pp. 119–125, 1996.
- 7. A. Scully, A. MacRobert, S. Botchway, P. O'Neill, R. Ostler, and D. Phillips, "Application of fluorescence lifetime imaging microscopy to the investigation of intracellular PDT mechanisms," *Bioimaging* 5, pp. 9–18, 1997.
- 8. K. Dowling, M. Dayel, S. Hyde, P. French, M. Lever, J. Hares, and A. Dymoke-Bradshaw, "High resolution time-domain fluorescence lifetime imaging for biomedical applications," *Journal of Modern Optics* **46**(2), pp. 199–209, 1999.
- 9. K. Dowling, M. Dayel, M. Lever, P. French, J. Hares, and A. Dymoke-Bradshaw, "Fluorescence lifetime imaging with picosecond resolution for biomedical applications," *Optics Letters* **23**(10), pp. 810–812, 1998.
- 10. P. Bastiaens and A. Squire, "Fluorescence lifetime imaging microscopy: spatial resolution of biochemical processes in the cell," *Trends in Cell Biology* **9**, pp. 48–52, 1999.
- 11. J. Birks, Photophysics of Aromatic Molecules, Wiley-Interscience, Chichester, 1970.
- 12. P. Verveer, A. Squire, and P. Bastiaens, "Global analysis of fluorescence lifetime imaging microscopy data," *Biophysical Journal* 78(4), pp. 2127–2137, 2000.
- 13. M. Kneen, J. Farinas, Y. Li, and A. Verkman, "Green fluorescent protein as a non-invasive intracellular pH indicator," *Biophysical Journal* 74, pp. 1591–1599, 1998.
- 14. R. Swaminathan, C. Hoang, and A. Verkman, "Photobleaching recovery and anisotropy decay of green fluorescent protein GFP-S65T in solution and cells: Cytoplasmic viscosity probed by green fluorescent protein translational and rotational diffusion," *Biophysical Journal* 72, pp. 1900–1907, 1997.
- 15. J. Mullaney, R. Thompson, Z. Gryczynski, and L. Black, "Green fluorescent protein as a probe of rotational mobility within bacteriophage T4," *Journal of Virological Methods* 88, pp. 35–40, 2000.
- 16. M. Uskova, J. Borst, M. Hink, A. van Hoek, A. Schots, N. Klyachko, and A. Visser, "Fluorescence dynamics of green fluorescent protein in AOT reversed micelles," *Biophysical Chemistry* 87, pp. 73–84, 2000.
- 17. A. Volkmer, V. Subramaniam, D. Birch, and T. Jovin, "One- and two-photon excited fluorescence lifetimes and anisotropy decays of green fluorescent proteins," *Biophysical Journal* 78, pp. 1589–1598, 2000.
- 18. N. Busch, T. Kim, and V. Bloomfield, "Tracer diffusion of proteins in DNA solutions. 2. Green fluorescent protein in crowded DNA solutions," *Macromolecules* **33**(16), pp. 5932–5937, 2000.
- 19. S. Strickler and R. Berg, "Relationship between absorption intensity and fluorescence lifetime of molecules," *Journal of Chemical Physics* **37**(4), pp. 814–820, 1962.
- 20. T. Förster, Fluoreszenz Organischer Verbindungen, Vandenhoeck and Ruprecht. Göttingen, 1951.
- 21. D. O'Connor and D. Phillips, Time-correlated single photon counting, Academic Press, London, 1984.
- 22. D. Birch and R. Imhof, "Time-domain Fluorescence Spectroscopy Using Time-Correlated Single Photon Counting" in "Topics in Fluorescence Spectroscopy: Techniques, Vol 1", Plenum Press, New York, 1991.
- 23. CRC Handbook of Chemistry and Physics, 59th edition, CRC Press, Florida, 1979.
- 24. J. Timmermans, Physico-chemical constants of pure organic compounds, Elsevier, 1950.
- 25. G. Patterson, S. Knobel, W. Sharif, S. Kain, and D. Piston, "Use of the green fluorescent protein and its mutants in quantitative fluorescence microscopy," *Biophysical Journal* 73, pp. 2782–2790, 1997.
- 26. E. Peterman, S. Brasselet, and W. Moerner, "The fluorescence dynamics of green fluorescent protein," *Journal of Physical Chemistry A* **103**(49), pp. 10553–10560, 1999.
- 27. W. Ware and B. Baldwin, "Absorption intensity and fluorescence lifetimes of molecules," *Journal of Chemical Physics* **40**(6), pp. 1703–1705, 1964.

- 28. S. Jakobs, V. Subramaniam, A. Schönle, T. Jovin, and S. Hell, "EGFP and DsRed expressing cultures of escherichia coli imaged by confocal, two-photon and fluorescence lifetime microscopy," FEBS Letters 479, pp. 131–135, 2000.
- 29. W. Sibbett and J. Taylor, "Synchroscan streak camera study of potential saturable absorbers in the blue spectral region," *Journal of Luminescence* 28, pp. 367–375, 1983.
- 30. B. Wilhelmi, "Influence of solvent viscosity on excited state lifetime and fluorescence quantum yield of dye molecules," *Chemical Physics* **66**, pp. 351–355, 1982.
- 31. R. Lampert, S. Meech, J. Metcalfe, D. Phillips, and A. Schaap, "The refractive index correction to the radiative rate constant in fluorescence lifetime measurements," *Chemical Physics Letters* **94**(2), pp. 137–140, 1983.
- 32. T. Shibuya, "The refractive index correction to the radiative rate constant," *Chemical Physics Letters* **103**(1), pp. 46–48, 1983.
- 33. S. Hirayama and D. Phillips, "Correction for refractive index in the comparison of radiative lifetimes in vapour and solution phases," *Journal of Photochemistry* **12**, pp. 139–145, 1980.
- 34. S. Hirayama, Y. Iuchi, F. Tanaka, and K. Shobatake, "Natural radiative lifetime of anthracene derivatives and their dependence on refractive index," *Chemical Physics* **144**, pp. 401–406, 1990.
- 35. J. Rička, M. Borkovec, and U. Hofmeier, "Coated droplet model of microemulsions: optical matching and polydispersity," *Journal of Chemical Physics* **94**(12), pp. 8503–8509, 1991.
- 36. R. Pepperkok, A. Squire, S. Geley, and P. Bastiaens, "Simultaneous detection of multiple green fluorescent proteins in live cells by fluorescence lifetime imaging microscopy," *Current Biology* **9**(5), pp. 269–272, 1999.

# Time-domain measurement of fluorescence lifetime variation with pH.

Alan G. Ryder \*a, Sarah Power a, Thomas J. Glynn a, and John J. Morrison b.

a Department of Physics, NUI- Galway, Ireland.
b Department of Obstetrics and Gynecology, NUI- Galway, Ireland.

#### ABSTRACT

Advances in the design and miniaturization of the lasers and electronics required for Time Correlated Single Photon Counting (TCSPC) measurement of fluorescence lifetime have simplified the use of the time domain method. We have assembled a compact portable system that is capable of measuring lifetimes down to ~200 ps (with deconvolution) and that can operate at a range of excitation and emission wavelengths. The excitation sources are pulsed LEDs and laser diodes with a maximum pulse rate of 40 MHz and are easily interchanged. Furthermore, the development of violet and blue GaN LEDs and laser diodes is expanding the range of fluorophores available for fluorescence lifetime measurement of ion concentrations.

pH sensitive fluorophores have a wide range of biological and clinical applications. The use of fluorescence lifetime rather than intensity to measure pH has a number of advantages including the reduction of effects due to photobleaching, scattering, and intensity variations in the excitation source. Using our compact TCSPC instrumentation we have measured the dependence of fluorescence lifetimes on pH for a range of dyes in phosphate buffer over the physiologically important range of 6.0 to 8.0. Most dyes exhibit only a small variation in lifetime (<1.0 ns) over the 6.0 to 8.0 pH range; however, acridine exhibits a large variation in lifetime and hence shows promise as a pH indicator.

Keywords: Fluorescence, lifetime, time correlated single photon counting, laser diode, light emitting diode, pH.

### 1. INTRODUCTION:

Fluorescence lifetimes in the nanosecond range have typically been measured by either of two methods, Time Correlated Single Photon Counting (TCSPC)<sup>1</sup> or phase modulation.<sup>2</sup> Phase modulation methods have enjoyed widespread success in the past for the relative simplicity of the instrumental setup. TCSPC, on the other hand, has been seen as the more complex method, relying on expensive detectors and complex electronics. Furthermore, the TCSPC method was generally implemented with either flash lamp sources (100 KHz pulse rates) which were very slow in data collection or with complex fast-pulsed lasers which were restricted to several distinct wavelength regions. In effect, TCSPC was a complex method confined (when using lasers) to large well-equipped laser laboratories and relied on a large degree of expertise. Recently, however, the emergence of new LED and laser diode technologies along with miniaturized electronics has enabled Time Correlated Single Photon Counting (TCSPC) methods to gain more widespread use.<sup>3, 4</sup> Such miniaturization of the electronics for TCSPC onto a single PC board with software control has at a stroke made the method much more accessible.<sup>5</sup> Semiconductor LEDs and lasers as fluorescence excitation sources have improved dramatically in the past decade and will revolutionize fluorescence lifetime measurement systems.<sup>6,7,8</sup> LED devices can now offer excitation wavelengths of between 380 nm and 600 nm with pulse rates in excess of 1 MHz and pulse widths of ~1 ns, which is ideal for mainstream biological

<sup>\*</sup> Corresponding author: <a href="mailto:alan.ryder@nuigalway.ie">alan.ryder@nuigalway.ie</a>; phone: 353-91-750469; fax: 353-91-750584; <a href="mailto:http://www.physics.nuigalway.ie/People/ARyder/index.html">http://www.physics.nuigalway.ie/People/ARyder/index.html</a>; Department of Physics, National University of Ireland-Galway, Galway, Ireland.

fluorescence lifetime studies. A further development has been the emergence of commercial violet GaN laser diodes in the past two years. These lasers are compact, capable of pulse widths less than 100 ps, and are easily incorporated into fluorescence lifetime systems.

The use of fluorescence lifetimes as a sensor method has attracted widespread interest in the past decade. <sup>9, 10, 11</sup> Analytes such as halides, <sup>12</sup> oxygen, <sup>13</sup> and carbon dioxide, <sup>14</sup> have been monitored using fluorescence lifetimes. Fluorescence lifetime based techniques have several advantages over more traditional fluorescence intensity methods which are susceptible to changes in excitation light intensity, to photobleaching, variation in light scattering and absorption of the sample.

#### 2. EXPERIMENTAL:

### 2.1 Apparatus and Procedure.

Fluorescence lifetimes were recorded using the Time Correlated Single Photon Counting (TCSPC) technique with a system that was assembled in-house using modular components (Figure 1).

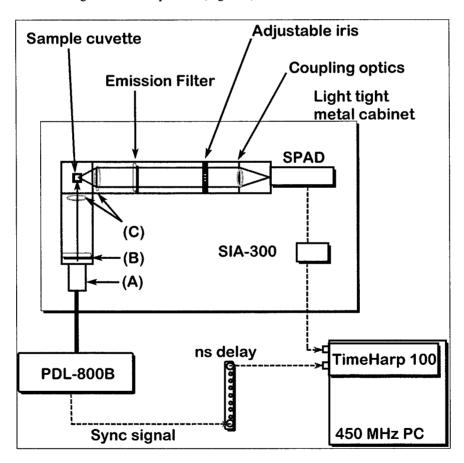


Figure 1: Schematic of fluorescence lifetime measurement apparatus: (A) Removable LED/ laser diode head, (B) Short pass filter, (C) Focusing optics.

The excitation sources were pulsed LEDs with center wavelengths of 380 and 460 nm or a pulsed 410 nm GaN laser diode, powered by a PicoQuant PDL-800B laser/LED driver. The emission of the LEDs was filtered using short pass filters to remove spurious longer wavelength emissions. The LEDs were operated at a variety of frequencies from 2.5 to 20 MHz for this study (maximum pulse rate = 40 MHz). A variable nanosecond delay unit was incorporated into the SYNC output from the laser driver. The fluorescence emission wavelength was selected with interference filters and detected using a Perkin Elmer SPCM-AQR-14 Single Photon Counting Module. The output TTL pulses from the SPAD were inverted and attenuated to NIM format using a SIA 300 inverter module before being fed into a TimeHarp 100 TCSPC module (both from PicoQuant). The card with a minimum channel resolution of 35 picoseconds was integrated into a standard PC, and the start/stop signals were inputted via RG58 SMA terminated cables. Light intensity at the detector was varied using an adjustable iris in front of the detector and by the use of ND filters. With the exception of the delay unit, laser driver and PC the complete unit was fitted into a light tight, 21x40x50 cm mild steel cabinet.

The Instrument Response Function (IRF) was obtained from a non-fluorescing suspension of alumina in water held in a 1 cm pathlength quartz cell and was assumed to be wavelength independent. Decay data were acquired until between 5 x  $10^3$  and 3 x  $10^4$  counts had been registered in the channel of maximum intensity. The determining factor as to the count maximum was the count rate, which was always <1% of the pulse rate. Count rates of  $10^4$  and  $10^5$  per second were routinely obtained from strongly fluorescing dyes yielding faster accumulating times by an order of magnitude or more when compared to flash-lamp systems. Lifetimes were obtained by deconvolution of the decay curves using the FluoFit software program (PicoQuant GmbH, Germany). All lifetimes were fit to a  $\chi^2$  value of less than 1.2 and with a residuals trace that was fully symmetrical about the zero axis.

#### 2.2 Materials:

Fifteen dyes in 0.1 M aqueous phosphate buffer were analyzed over a pH range from 5.8-8.0. The fluorophore concentration was maintained below 1 x 10<sup>-3</sup> M to rule out concentration effects. An absorption profile of each dye was recorded on a Shimadzu UV-1601 UV-visible spectrophotometer, and the excitation sources were chosen accordingly. Steady state fluorescence spectra of each dye were recorded on a Perkin Elmer LS 50B luminescence spectrometer to determine the correct emission filter for fluorescence lifetime measurements. All the dyes were surveyed in oxygenated and deoxygenated (nitrogen gas exchange) solutions at room temperature in 1 cm pathlength quartz cuvettes.

### 3. RESULTS & DISCUSSION:

The TCSPC system as developed was found to be user-friendly and required very little training for postgraduate student use. Once an operator had a sufficient grasp of TCSPC theory and methods, it required only one or two days to develop proficiency sufficient for routine measurements to be made. Apart from care needed to reduce reflection anomalies, the only other major concern is the requirement to ensure adequate filtering of the excitation sources to remove spurious long wavelength emissions and to remove the long wavelength 'tail' produced by LED emission. Figure 2(A) shows typical multi-exponential fits for two acridine decay curves at different pH values. The IRF curve shown (FWHM ~ 1.5 ns or less) is typical of the IRFs obtained with our instrumentation when LEDs were used as excitation sources.

	λ <sub>ex</sub> ( <b>nm</b> )	λ <sub>em</sub> ( <b>nm</b> )	τ(O <sub>2</sub> ) (ns)	τ(O <sub>2</sub> ) (ns)	τ (ns)	τ (ns)
рН			low	high	low	high
Fluorescein	460	550	3.6	4.2	3.6	4.2
Fluorescein Na salt	460	550	3.6	4.2	3.6	4.3
Fluorescein diacetate	460	550	3.5	4.0	3.5	4.0
Fluoresceinamine Isomer 1	460	550	3.3	3.9	3.3	3.9
Fluoresceinamine Isomer 2	460	550	3.0	3.9	3.0	4.0
FITC	460	550	3.4	4.1	3.4	4.1
6-Carboxyfluorescein	460	550	3.5	4.0	3.5	4.0
BCECF	460	550	3.0	3.8	3.0	3.8
SNAFL calcein	460	550	3.4	2.7	3.4	2.7
HPTS	410	500	5.4	5.4	5.4	5.4
10-(3-Sulfonyl) acridinium betaine	380	500	31.2	30.6	31.2	30.7
Acridine Orange	460	550	1.9	2.0	1.9	2.0
Rhodamine B	410	600	1.8	1.7	1.8	1.8
Acridine	380	450	26.3	13.7	26.3	14.0
Acridine	380	500	31.1	22.1	31.2	22.4

Table 1 Fluorescence lifetimes of a range of dyes at pH  $5.8 \pm 0.2$  (low) and  $7.9 \pm 0.2$  (high) in phosphate buffered solutions. The first two lifetime values are for oxygenated solutions while the last two represent the deoxygenated solutions. All decay curves were either single or bi-exponential fits. Lifetime measurements are accurate to better than  $\pm 0.1$  ns, as calculated by support plane analysis <sup>16</sup>.

With the exception of acridine, the majority of fluorophores show little lifetime variation over the pH range surveyed (table 1). Typical variation was less than one nanosecond while the lifetimes of acridine orange, Rhodamine B, and HPTS were found to be independent of pH over the 6.0 to 8.0 range. The results acquired for HPTS agree with those of other investigators. The majority of dyes surveyed are therefore unsuitable as fluorescence lifetime based pH sensors because of the small variation in lifetime. The presence of oxygen was not found to be a significant factor affecting the fluorescence lifetime of these dyes, except for the base form of acridine where there is a 0.3 ns increase in lifetime with deoxygenation.

Over this 6.0 to 8.0 pH range, acridine in solution exhibits interplay between two different chemical species that have a large difference in lifetime. The neutral acridine exhibits a lifetime of  $\sim 10$  ns, while the protonated form has a considerably longer lifetime of 31 ns. This is well illustrated in Figure 2(A) where it is clear that two decays are present at each pH value, with both decay curves fitting to bi-exponential terms.

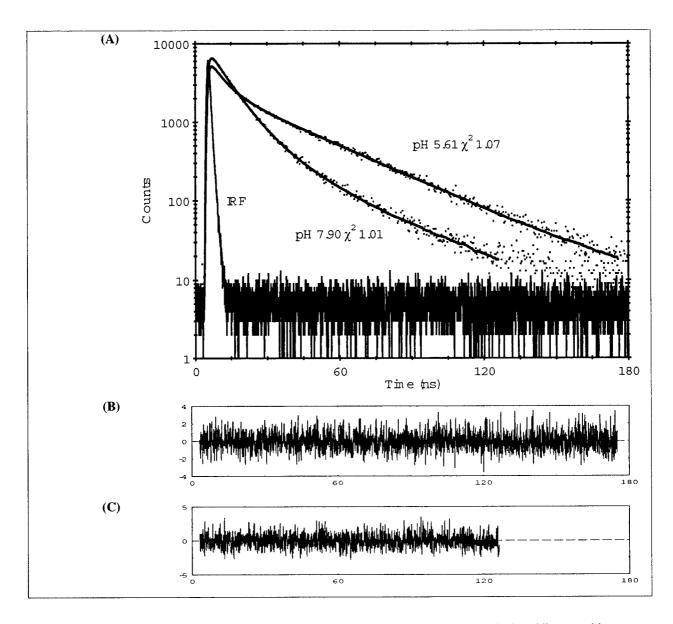


Figure 2: (A) Time domain intensity decay of acridine solutions at pH 5.61 & pH 7.90 (dotted lines), multi-exponential fit (solid lines), and the instrument response function. (B) Residuals for fit at pH 5.61, (C) Residuals for fit at pH 7.90. Data collected with 380 nm LED excitation at 2.5 MHz pulse rate, with the emission measured at 450 nm and a channel resolution of 70 ps.

The lifetime plots in Figure 3 show the change in average lifetime of acridine as a function of pH. At an emission wavelength of 450 nm the average lifetime is calculated from a two exponential decay fit which is a combination of fluorescence from both the neutral and protonated species. At an emission wavelength of 500 nm, there is a much greater contribution from the protonated rather than the neutral form of the dye, so the lifetime at any given pH is longer than that

measured at an emission wavelength of 450 nm. Measured at 500 nm, lifetimes in the pH range 5.8-6.4 fit to a single exponential therefore demonstrating negligible contributions from the neutral molecule. At pH values greater than 6.4 the fluorescence emission from the neutral species becomes a larger factor and so a bi-exponential fit is required. Both lifetime vs pH plots for acridine fit to 2<sup>nd</sup> order polynomial equations over this 6.0 to 8.0 range (Figure 3) which provides a simple and accurate method of pH measurement from the average fluorescence lifetime.

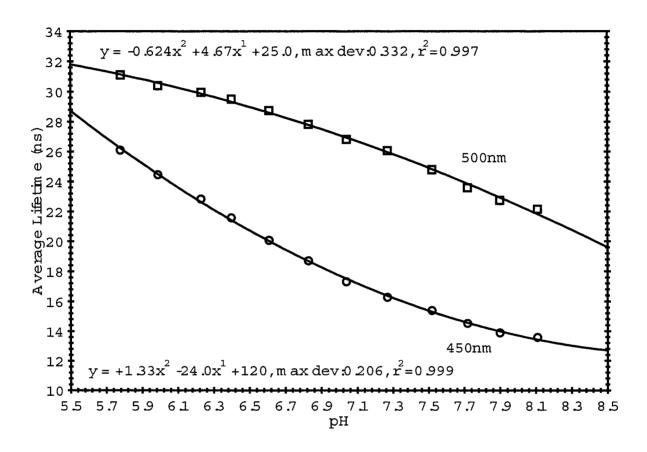


Figure 3: Plots of average fluorescence lifetime versus pH for acridine in phosphate buffer with 380 nm excitation and at two different emission wavelengths (450 & 500 nm). The two emission curves show different behaviour due to the two species in solution.

#### 4. CONCLUSIONS:

The compact nature and relative ease of use of the TCSPC system which we have built opens the way for this method to be employed by non-physicists for routine analysis. Although a thorough grounding in the principles and theory of TCSPC is necessary, very little knowledge of electronics and optics is required. The ease with which the excitation sources can be changed also demonstrates its versatility towards biological applications where a range of dyes may need analysis at the same

time. Although fast-pulsed lasers do exist, they tend to be very large, complex, and generally only provide a single wavelength, or range of wavelengths. By the use of pulsed LEDs and laser diodes, a range of dyes can be excited at visible and near-IR wavelengths between 380 nm and 750 nm with no change in the optical pathway and rapid exchange of sources.

The fluorophores which we have examined showed varying degrees of lifetime change with pH variation. Most dyes had a lifetime change of less than one nanosecond over the crucial physiological range of 6.0 to 8.0 pH units and we therefore discount them as potential lifetime based pH sensors. Acridine was found to have the largest lifetime variation of 12.5 ns over the range 5.8 to 8.0 pH units and because it can be excited with a 380 nm LED we consider it an excellent candidate as a pH indicator for a wide variety of biological applications.

#### 5. ACKNOWLEDGEMENTS:

The work was funded by grants from the Irish Higher Education Authority, under its Programme for Research in Third Level Institutions, and by a Millennium Research Fund grant from NUI-Galway.

#### 6. REFERENCES:

- 1 D.V. O'Connor and D. Phillips, Time-correlated Single Photon Counting, Academic Press, London, 1984.
- 2 J.R. Lakowicz and I. Gryczynski, Frequency-Domain Fluorescence Spectroscopy. In: Topics in fluorescence spectroscopy: Volume 1 Techniques, J. R. Lakowicz editor. pp. 293-335, Plenum Press, New York, 1991.
- 3 Y.L. Zhang, S.A. Soper, L.R. Middendorf, J.A. Wurm, R. Erdmann, M. Wahl, "Simple near-infrared time-correlated single photon counting instrument with a pulsed diode laser and avalanche photodiode for time-resolved measurements in scanning applications," *Appl. Spectrosc.* **53**, pp. 497-504, 1999.
- 4 W. Becker, H. Hickl, C. Zander, K.H. Drexhage, M. Sauer, S. Siebert, J. Wolfrum, "Time-resolved detection and identification of single analyte molecules in microcapillaries by time-correlated single-photon counting (TCSPC)," *Rev. Sci. Instrum.* 70, pp. 1835-1841, 1999.
- 5 Three companies which supply TCSPC electronics on a single board are: PicoQuant GmbH, Berlin Germany, Becker & Hickl, Berlin, Germany, and Edinburgh Instruments, UK.
- 6 T. Araki and H. Misawa, "Light emitting diode-based nanosecond ultraviolet light source for fluorescence lifetime measurements," *Rev. Sci. Instrum.* **66**, pp. 5469–1995.
- 7 H. Szmacinski and Q. Chang, "Micro- and sub-nanosecond lifetime measurements using a UV light-emitting diode," *Appl. Spectrosc.* **54**, pp. 106-109, 2000.
- 8 J. Sipior, G.M. Carter, J.R. Lakowicz, and G. Rao, "Blue light-emitting diode demonstrated as an ultraviolet excitation source for nanosecond phase-modulation fluorescence lifetime measurements," *Rev. Sci. Instrum.* **68**, pp. 2666-1997.
- 9 H. Szmacinski and J. R. Lakowicz, *Lifetime-Based Sensing*. In: *Topics in fluorescence spectroscopy: volume 4 Probe design and chemical sensing*, J. R. Lakowicz editor, p.295, Plenum Press, New York, 1994.
- 10 S. Draxler, M.E. Lippitsch. "Optical pH sensors using fluorescence decay time," Sens. Actuators B, 11, pp. 421-424, 1993.

- 11 J.R. Lakowicz, H. Szmacinski. "Fluorescence lifetime-based sensing of pH, Ca2+, K+ and glucose," *Sens. Actuators B*, **11**, pp.133-143, 1993.
- 12 H. Szmacinski, J.R. Lakowicz. "Potassium and sodium measurements at clinical concentrations using phase-modulation fluorometry," *Sens. Actuators B*, **60**, pp. 8-18, 1999.
- 13 G.A. Holst, T. Köster, E. Voges & D.W. Lübbers. "FLOX an oxygen-flux-measuring system using a phase-modulation method to evaluate the oxygen-dependent fluorescence lifetime," *Sens. Actuators B*, **29**, pp. 231-239, 1995.
- 14 J. Sipior, S. Bambot, M. Romauld, G.M. Carter, J.R. Lakowicz and G. Rao, "A lifetime-based optical CO2 gas sensor with blue or red excitation and stokes or anti-stokes detection," *Anal. Biochem.*, **227**, pp. 309-318, 1995.
- 15 O. S. Wolfbeis, E. Fürlinger, H. Kroneis, H. Marsoner, "Fluorimetric Analysis 1. A study on fluorescent indicators for measuring near neutral ("physiological") pH-values," *Fresenius Z Anal Chem*, **314**, pp.119-124, 1983.
- 16 J. R. Lakowicz, Principles of Fluorescence Spectroscopy, pp.122-125, Kluwer Academic/Plenum Publishers, New York, 1999.

# New approach to optical imaging of tumors

Samuel Achilefu, Joseph E. Bugaj, Richard B. Dorshow,\* Hermo N. Jimenez, and Raghavan Rajagopalan Mallinckrodt Inc., PO Box 5840, St. Louis, MO 63134-0840

### **ABSTRACT**

Site-specific delivery of drugs and contrast agents to tumors protects normal tissues from the cytotoxic effect of drugs, and enhances the contrast between normal and diseased tissues. In optical medicine, biocompatible dyes can be used as phototherapeutics or as contrast agents. Previous studies have shown that the use of covalent or non-covalent dye conjugates of carriers such as antibodies, liposomes, and polysaccharides improves the delivery of such molecules to tumors. However, large biomolecules can elicit adverse immunogenic reactions and also result in long blood clearance times, delaying visualization of target tissues. A viable alternative to this strategy is to use small bioactive molecule-dye conjugates. These molecules have several advantages over large biomolecules, including ease of synthesis of a variety of high purity compounds for combinatorial screening of new targets, enhanced diffusivity to solid tumors, and the ability to affect the pharmacokinetics of the conjugates by minor structural changes. Thus, we conjugated a near infrared absorbing dye to several bioactive peptides that specifically target overexpressed tumor receptors in established rat tumor lines. High tumor uptake of the conjugates was obtained without loss of either the peptide receptor affinity or the dye fluorescence. These findings demonstrate the efficacy of a small peptide-dye conjugate strategy for *in vivo* tumor imaging. Site-specific delivery of photodynamic therapy agents may also benefit from this approach.

**Keywords:** photodiagnostics, phototherapeutics, peptide-dye conjugates, targeting agents, contrast agents, tumor detection, dyes, fluorescence, indocyanine green, optical imaging

#### 1. INTRODUCTION

Innovative methods for targeting optical dyes to tumors for disease diagnosis and therapy are burgeoning. Clever schemes involving acid and enzyme cleavable conjugates of dye-biomolecule entities have been recently reported. Simpler schemes involving protein-dye conjugates or antibody-dye conjugates are also known.

Recently we pioneered the methodology of employing known tumor receptor-targeted peptides for the detection of *in vivo* tumors by optical imaging. It has been well-known that a radiolabel attached to such peptides can be used as a tumor marker in gamma scintigraphy (several commercial products are available). Our basic idea was to replace the radioactive label with a dye molecule. This approach has several advantages over the use of non-specific dyes, or the conjugation of dyes to large biomolecules, in the optical imaging of *in vivo* tumors. Such advantages include rapid localization on tumors, rapid clearance from blood and the possibility of synthesizing several peptide derivatives without resorting to expensive natural products. Dye-peptide conjugates synthesized previously, based on this concept, have been shown to effectively target and bind specifically to receptors of implanted tumors. Optical images of these tumors *in vivo* by exciting the fluorescence mode of the dye moiety were easily obtained. 5-7

In this article, we report on the development of novel near infrared dye-peptide compounds. The efficacy of these new fluorescent contrast agents was evaluated *in vivo* in well-characterized rat tumor lines using a simple continuous wave fluorescence imaging apparatus.

# 2. MATERIALS AND METHODS

# 2.1 Synthesis

# 2.1.1 Synthesis of bispropylcarboxymethylindocyanine dye (Cyhex)

Cyhex is a reactive analogue of Indocyanine Green (ICG, Figure 1A). It was prepared by the reaction of a mixture of 1,1,2-trimethyl-[1H]-benz[e]indole and 3-bromohexanoic acid in 1,2-dichlorobenzene. Reaction of the brown solid precipitate

obtained with glutaconaldehyde dianil monohydrochloride in ethanol gave a green solution. Evaporation of the solvent and lyophilization of the residue gave cyhex as dark green flakes (Figure 1B).

# 2.1.2 Synthesis of Cytate-66

Octreotate, a somatostatin receptor ligand, was prepared by standard Fmoc solid phase synthesis<sup>7</sup> and the two cystein residues per molecule were cyclized into a disulfide bond on solid support with thallium trifluoroacetate to give the cyclic peptide. Selective cleavage of the peptide from the resin, while leaving the protecting groups intact, except for the N-terminal amine, was effected with 5% trifluoroacetic acid in dichloromethane. Reaction of cyhex with the peptide in dimethylformamide and subsequent removal of peptide side chain protecting groups trifluoroacetic acid gave the crude product. The pure compound was isolated by HPLC (100% HPLC purity) and characterized by mass spectrometry. (Figure 1C).

# 2.1.3 Synthesis of Cybesin-66

A similar procedure described above was used to prepare cybesin-66, which has affinity for the bombesin receptor. This peptide is linear, hence, does not require the cyclization step described above. HPLC purity was >99.5% (Figure 1D).

Figure 1: Structures of ICG, cyhex, cytate and cybesin

#### 2.2 Animal models and agent administration protocols

# 2.2.1 Pancreatic acinar carcinoma (CA20948) tumor

Male Lewis rats (120-140 g) were implanted with the pancreatic acinar tumor by serial implantation of solid material from a donor animal to a recipient animal. This transplantable tumor line has previously been shown to express somatostatin (sst<sub>2</sub>) receptors, and has been widely used in *in vitro* and *in vivo* receptor binding assays. The number of binding sites has been determined at 489 fmol/mg protein. The procedure for transplantation and growth has been previously described. Palpable tumor masses are evident approximately 9 days post implant, and between 13-15 days post implant the tumor masses reach 2-2.5 g at which time they are used in the imaging studies described below. This tumor line has been maintained *in vivo* by serial implantation for more than 120 generations with no change in receptor expression.

# 2.2.2 Pancreatic acinar carcinoma (AR42-J) tumor

This cell line is derived from exocrine rat pancreatic acinar carcinoma. It can be grown in continuous culture or maintained *in vivo* in athymic nude mice, SCID mice or in Lewis rats. This cell line is particularly attractive for *in vitro* receptor assays as it is known to express a variety of hormone receptors including cholecystokinin (CCK), epidermal growth factor (EGF), pituitary adenylate cyclase activating peptide (PACAP), somatostatin (sst.) and bombesin.<sup>12</sup>

In this model, male Lewis rats were implanted with solid tumor material in a similar manner as described for the CA20948 rat model. Palpable masses were present 7 days post implant and imaging studies were conducted on animals at 10-12 days post implant when the mass had achieved ~2-2.5 g. This tumor line has been maintained *in vivo* for more than 30 generations without change in receptor expression.

# 2.2.3 Animal preparation

Prior to imaging, the animals were anesthetized with rat cocktail (xylazine; ketamine; acepromazine 1.5: 1.5: 0.5) at 0.8mL/kg via intramuscular injection. The area of the tumor (left flank) was shaved to expose tumor and surrounding surface area. The contralateral flank was shaved similarly to provide the negative control. A 21 gauge butterfly equipped with a stopcock and two syringes containing heparinized saline was placed into the lateral tail vein of the rat. Patency of the vein was checked prior to administration of any agent via the butterfly apparatus.

# 2.3 Imaging apparatus and procedure

A non-invasive *in vivo* fluorescence imaging apparatus was employed to assess the efficacy of contrast agents developed for tumor detection in animal models. A LaserMax Inc. laser diode of nominal wavelength 780 nm and nominal power of 40 mW was used. The detector was a Princeton Instruments model RTE/CCD-1317-K/2 CCD camera with a Rodenstock 10 mm F2 lens (stock #542.032.002.20) attached. A 830 nm interference lens (CVI Laser Corp. part # F10-830-4-2)) was mounted in front of the CCD input lens such that only emitted fluorescent light from the contrast agent was imaged. Typically, an image of the animal was taken pre-injection of contrast agent. This image was subsequently subtracted (pixel by pixel) from the post injection images. However, the background subtraction was never done once the animal had been removed from the sample area and returned at a later time for images taken several hours post injection.

# 3. RESULTS & DISCUSSION

#### 3.1 Cytate-66

112

We have previously shown that the cypate dye – octreotate peptide conjugate designated cytate-1 is a compound that selectively targets somatostatin receptor-rich tumors (CA20948 or AR42-J) and specifically binds to the sst<sub>2</sub> receptors, allowing for localized fluorescence at the tumor site. <sup>5-7</sup> Unlike cytate-1, the new dye-peptide conjugate, cytate-66, has two somatostatin receptor-avid octreotate ligands which increases the receptor affinity of the conjugate. This new dye-peptide conjugate was tested on rats with an AR42-J tumor on the flank. A 500  $\mu$ L dose of a 0.5 mg/mL aqueous concentration solution was administered. Time sequence images were taken. By one hour, localization of the compound in the tumor was evident. Figure 2 is the image at 22 hours post administration. Cytate-66 is seen to have accumulated and remained localized in the tumor tissue. Biodistribution images (not shown) demonstrate that the compound accumulates in the tumor, as well as

Proc. SPIE Vol. 4259

the liver (due to the cyanine component), and the adrenals and pancreas (due to the peptide affinity for the sst<sub>2</sub> receptors on these tissues).

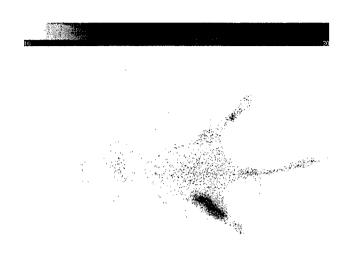


Figure 2. Rat with AR42-J tumor on left flank 22 hours post administration of Cytate-66.

# 3.2 Cybesin-66

We have previously shown that the cypate dye-bombesin peptide conjugate designated bombesinate (or cybesin-1) is a compound that selectively targets bombesin receptor-rich tumors (AR42-J) and specifically binds to the receptors, allowing for localized fluorescence at the tumor site. Cybesin-66 is similar to cytate-66, except that the peptide component is a bombesin receptor avid ligand, an octapeptide bombesin analogue. This new dye-peptide conjugate was tested on rats with an AR42-J flank tumor. A 500  $\mu$ L dose of a 0.5 mg/mL aqueous concentration solution was administered. Time sequence images were taken. Localization of the compound in the tumor was evident at 19 hours post administration as shown in Figure 3.

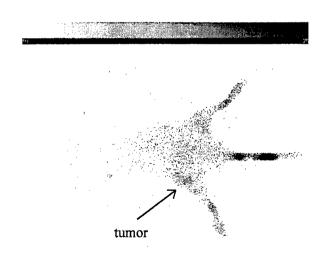


Figure 3: Rat with AR42-J tumor on left flank 19 hours post administration of Cybesin-66.

#### 4. SUMMARY

We have previously shown that cypate dye, like ICG, does not accumulate in either the somatostatin receptor rich CA20948 tumor or the bombesin/somatostatin receptor rich AR42-J tumor. In contrast, however, the new cyhex dye-peptide conjugates cytate-66 and cybesin-66 do accumulate in such tumors to the extent the tumors can be imaged using a simple continuous wave apparatus. These results further verify that small peptide-dye conjugates are effective in tumor detection by optical imaging, analogous to work performed in the nuclear medicine arena.

### 5. ACKNOWLEDGMENTS

The authors wish to thank Jill Johler and Randy Wilhelm for mass spectral analysis.

### REFERENCES

- 1. R. Weissleder, C-H Tung, U. Mahmood, A. Bogdanov Jr., "In vivo imaging of tumors with protease-activated near-infrared fluorescent probes," Nature Biotech. 17, pp. 75-378 1999.
- K. Licha, A. Becker, F. Kratz, and W. Semmler, "New contrast agents for optical imaging: Acid-cleavable conjugates of cyanine dyes with biomolecules," in *Biomedical Imaging: Reporters, Dyes, and Instrumentation*, Darryl J. Bornhop, Christopher Contag, Eva M. Sevick-Muraca, Editors, Proceedings of SPIE Vol. 3600, pp. 29-35 (1999).
- 3. A. Becker, B. Riefke, B. Ebert, U. Sukowski, H. Rinneberg, W. Semmler, and K. Licha, "Macromolecular contrast agents for optical imaging of tumors: Comparison of indotricarbocyanine-labeled human serum albumin and transferrin," *Photochemistry and Photobiology* 72, pp. 234-241, 2000.
- 4. B. Ballou, G.W. Fisher, A. S. Waggonner, D. L. Farkas, J.M. Reiland, R. Jaffe, R.B. Mujumdar, and T.R. Hakala, "Tumor labeling *in vivo* using cyanine-conjugated monoclonal antibodies," *Cancer Immunol. Immunother.* 41, pp. 257-263, 1995.
- 5. S. Achilefu, R.B. Dorshow, J.E. Bugaj, and R. Rajagopalan, "Tumor specific fluorescent contrast agents," in *Optical Biopsy III*, Robert R. Alfano, Editor, Proceedings of SPIE Vol. **3917**, pp. 1-7 (2000).
- 6. S. Achilefu, R.B. Dorshow, J.E. Bugaj, and R. Rajagopalan, "Novel receptor-targeted fluorescent contrast agents for *in vivo* tumor imaging," *Invest. Radiol.* **35**, pp. 479-485 (2000).
- 7. J.E. Bugaj, S. Achilefu, R.B. Dorshow, and R. Rajagopalan, "Novel fluorescent contrast agents for optical imaging of *in vivo* tumors based on a receptor-targeted dye-peptide conjugate platform," submitted Journal of Biomedical Optics, August, 2000.
- 8. J-C Reubi, U. Horrisberger, C.E. Essed, J. Jeekel, J.G. Klijn, and S.W. Lamberts, "Absence of somatostatin receptors in human exocrine pancreatic adenocarcinomas," *Gastroenterology* **95**, 760-763 (1988).
- C.J. Anderson, L.A. Jones, L.A. Bass, E.L.C. Sherman, D.W. McCarthy, P.D. Cutler, M.V. Lanahan, M.E. Cristel, J.S. Lewis, and S.W. Schwarz, "Radiotherapy, toxicity and dosimetry of copper-64-TETA-octreotide in tumor-bearing rats," J. Nucl. Med. 39, 1944-1951 (1998).
- 10. M. De Jong, W.A.P. Breeman, B.F. Bernard, E.J. Rolleman, L.J. Hofland, T.J. Visser, B. Setyono-Han, W. H. Bakker, M.E. van der Pluijm, and E.P. Krenning, "Evaluation *in vitro* and in rats of <sup>161</sup>Tb-DTPA-octreotide, a somatostatin analogue with potential for intraoperative scanning and radiotherapy," *Eur. J. Nucl. Med.* **22**, 608-616 (1995).
- 11. B. Stolz, G. Weckbecker, P.M. Smith-Jones, R. Albert, F. Raulf, and C. Bruns, "The somatostatin receptor-targeted radiotherapeutic [90YDOTA-DPhe1, Tyr3] octreotide (90Y-SMT 487) eradicates experimental rat pancreatic CA 20948 tumors," *Eur. J. Nucl. Med.* 25, 668-674 (1998).
- 12. J-B Deitrich, "AR4-2J cells: A model to study polypeptide hormone receptors," Bioscience Reports 16, 273-288 (1996).
- 13. S. Achilefu, J.E. Bugaj, R.B. Dorshow, H.N. Jimenez, R. Rajagopalan, R. Wilhelm, E.G. Webb, and J.L. Erion, "Site-specific tumor targeted fluorescent contrast agents," Proceedings of SPIE Volume 4156, in press.

<sup>\*</sup>Correspondence: Email: Richard.Dorshow@mkg.com; Phone: (314) 654-3338; Fax: (314) 654-8900

# Monoclonal antibody-tagged receptor-targeted contrast agents for detection of cancers

N. S. Soukos, M. R. Hamblin, T. F. Deutsch, and T. Hasan

Wellman Laboratories of Photomedicine, Department of Dermatology, Massachusetts General Hospital, Harvard Medical School, Boston, MA 02114, USA

#### **ABSTRACT**

Oral cancer and precancer overexpress the epidermal growth factor receptor (EGFR) and monoclonal antibodies against EGFR coupled to photoactive dyes may have a potential both as diagnostic and treatment modalities for oral premalignancy. We asked whether an anti-EGFR Mab (C225) conjugated with the fluorescent dye indocyanine Cy5.5 could detect dysplastic changes in the hamster cheek pouch carcinogenesis model. Secondly, we tested whether the same antibody conjugated with the photosensitizer chlorin(e6) could be used together with illumination to reduce levels of expression of EGFR as evaluated by the immunophotodetection procedure.

Increased fluorescence appeared to correlate with development of premalignancy when the C225-Cy5.5 conjugate was used. Areas with increased fluorescence signal were found in carcinogen-treated but clinically normal cheek pouches, that revealed dysplastic changes by histology. The immunophotodetection procedure was carried out after photoimmunotherapy with the C225-ce6 conjugate, and showed a significant reduction in fluorescence in the illuminated compared to non-illuminated areas in the carcinogen-treated but not the normal cheek pouch. The results demonstrate that the use of anti-EGFR Mab targeted photoactive dyes may serve as a feedback controlled optical diagnosis and therapy procedure for oral premalignant lesions.

**Keywords:** Fluorescence diagnosis, oral pre-cancer, hamster cheek pouch, photodynamic therapy, photoimmunotherapy, carcinogenesis

# 1. INTRODUCTION

Monoclonal antibodies that recognize tumor-associated antigens and that are conjugated to fluorescent dyes may have several uses in medical imaging. These may include the detection of early malignant or pre-cancerous lesions, the, delineation of tumor margins, measuring the response to treatment, and the early detection of recurrence. Although oral cancer occurs in a region of the body that is accessible to physical examination, most oral cancers are moderately advanced at the time of diagnosis <sup>1</sup>. This is due to failure to detect and treat early recognizable or unrecognizable premalignant signs of squamous cell carcinoma (SCC). On the other hand, the management of field cancer of the oral cavity, with multicentric foci of invasion, presents a considerable problem. Surgical resection of synchronous or metachronous SCC, along with premalignant lesions, is likely to be associated with considerable mutilation.

The epidermal growth factor receptor (EGFR), a glycoprotein of 170,000 MWt with an intrinsic tyrosine-specific protein kinase activity stimulated upon EGF binding <sup>2</sup>, has been shown to be overexpressed in head and neck cancers including oral cancer and precancer <sup>3, 4</sup>. EGFR was upregulated in human normal epithelium adjacent to tumor, retained elevated through hyperplasia and dysplasia and was dramatically increased from dysplasia to SCC <sup>5</sup>. EGFR overexpression has also been found in the chemically induced malignant transformation carcinoma in the hamster cheek pouch model <sup>6</sup>. These data suggest that the EGFR overexpression might be a useful marker for detection and treatment of early invasive oral premalignancy.

Correspondence: T. Hasan. Other author information: N.S.S. Email: <a href="mailto:soukos@helix.mgh.harvard.edu">soukos@helix.mgh.harvard.edu</a>; Telephone: 617-724-2881; Supported by U.S. Dept of Energy Grant DE-FG02-91-ER61228. M.R.H. Email: <a href="mailto:hamblin@helix.mgh.harvard.edu">hamblin@helix.mgh.harvard.edu</a>; Telephone: .617-726-6182; Supported by U.S. Dept of Defense Medical FreeElectron Laser Program under Contract N 00014-94-1-0927 and U.S. National Institute of Health Grant R01 AR40352. T.F.D. Email: <a href="mailto:deutsch@helix.mgh.harvard.edu">deutsch@helix.mgh.harvard.edu</a>; Telephone: 617-726-6167; Supported by U.S. Dept of Defense Medical FreeElectron Laser Program under Contract N 00014-94-1-0927. T.H. Email: <a href="mailto:hasan@helix.mgh.harvard.edu">hasan@helix.mgh.harvard.edu</a>; Telephone: .617-726-6696; Supported by U.S. National Institute of Health Grant R01 AR40352.

MAbs against the EGFR coupled to radioisotopes <sup>7, 8</sup> have been used for diagnostic purposes. Anti-EGFR MAbs labeled with radioisotopes have also been used to inhibit tumor growth <sup>9</sup> and enhance the antitumor activity of chemotherapy <sup>10</sup>. MAbs coupled to fluorescent dyes, such as fluorescein <sup>11, 12</sup> and indocyanine <sup>13</sup>, have been used for diagnosis of cancer. In addition, enhancement of the selectivity of photodynamic therapy (PDT) has been observed in vitro <sup>14, 15</sup> and in vivo <sup>16, 17</sup> using MAbs conjugated with PS such as chlorins. Recently, a conjugate between an anti-EGFR Mab and the PS benzoporphyrin derivative improved the selectivity and efficacy of the PS for SCC in the hamster cheek pouch model <sup>18</sup>. The specific aims of this study were twofold. First, to determine whether a conjugate between an anti-EGFR chimeric MAb (C225) and the fluorescent dye indocyanine Cy5.5 could deliver, after injection, sufficient amounts of the marker dye into clinically unrecognizable early premalignant lesions in the hamster cheek pouch carcinogenesis model to make them detectable by fluorescence imaging. Second, to investigate the photodynamic effects of a conjugate between the C225 and the PS chlorin e6 (ce6) on early premalignant lesions of the hamster cheek pouch, and to assess by the immunophotodetection procedure the effectiveness of PIT after the injection of the C225-Cy5.5 conjugate into hamsters.

## 2. MATERIALS AND METHODS

# 2.1. Animal model

The Syrian golden hamster cheek pouch carcinogenesis closely replicates events involved in the development of premalignancy in human oral cancer <sup>19</sup>. Male Syrian golden hamsters (*Mesocricetus auratus*) (80 to 100 g) were obtained from the Charles River Animal Research Facility, (Boston, MA) at 4 to 6 weeks of age. Animals were housed four to a cage at room temperature with wood chips for bedding and with a 12-hour light/dark cycle. Water and laboratory chow were given *ad libitum*. All procedures received approval from the Subcommittee on Research Animal Care of Massachusetts General Hospital prior to the start of the study.

Epithelial changes characteristic of the progress to early premalignancy were induced by thrice weekly (Mon, Wed and Fri) topical application using a Q-tip of 50 - 100 μl of a 0.5% solution of 7,12-dimethylbenz(a)anthracene (DMBA) (Sigma Chemical Co., St. Louis, MO) in mineral oil on the right buccal pouch mucosa for 6 weeks. Initial studies also used 12 weeks application of DMBA to give papillary tumors measuring 4-6 mm in diameter. Injection of drugs into the subclavian vein as well as immunophotodiagnosis and photoimmunotherapy (PIT) studies were performed under intraperitoneal anesthesia with a cocktail of ketamine, xylazine and atropine (80-100 mg/Kg, 5-10 mg/Kg and 0.04 mg/Kg respectively). The hamsters were euthanized in a CO<sub>2</sub> chamber. At the time of euthanasia animals weighed between 180 and 220 g. After euthanasia the cheek pouches were excised along with the underlying connective tissue and musculature and routine histology (H&E staining) was performed.

# 2.2. Chemicals

The MAb C225 was kindly provided by ImClone Systems, Inc. (Somerville, NJ). Cy5.5 FluoroLink Dye (bisfunctional NHS ester in sealed foil packets) was obtained from Amersham Life Science (Arlington Heights, IL). Chlorin<sub>e6</sub> was obtained from Porphyrin Products (Logan, UT). BSA and mouse IgG were obtained from Sigma (St. Louis, MO).

# 2.3. Preparation of conjugates

Cy5.5 conjugates were prepared by dissolving 2 mg protein (C225, BSA or mouse IgG) in 2 ml sodium bicarbonate buffer (0.1M, pH=9.3). The content of one Cy5.5 foil pack was dissolved in sodium bicarbonate buffer (200  $\mu$ l) and added to the protein solution with shaking. The mixture was incubated in the dark at room temperature for 3 h, whereupon it was dialyzed 3 times against 5 l phosphate buffer (0.01M, pH=7.4) to remove any unbound dye.

 $C_{e6}$ -NHS ester was prepared as a solution in DMSO as previously described  $^{20}$ . C225 (2mg) were dissolved in 2 ml sodium bicarbonate buffer and DMSO solution containing NHS ester of 200  $\mu$ g  $c_{e6}$  equivalent was added with stirring. This is a 25 fold molar excess of  $c_{e6}$  to IgG. After 24 h incubation in the dark at room temperature the preparation was exhaustively dialyzed (at least 3 times) against 5 l phosphate buffer (0.01M, pH=7.4). After characterization by spectrophotometry, Cy5.5 and  $c_{e6}$  conjugates were stored at  $^{40}$ C in the presence of 10% v/v horse serum (to prevent aggregation) and 15 mM sodium azide.

# 2.4. Cell lines

The human epidermoid squamous cell carcinoma line A431 was obtained from the American Type Culture Collection (Rockville, MD). The hamster cheek pouch carcinoma cell line (HCPC-1) was developed from culture of an experimentally induced epidermoid carcinoma of the buccal pouch  $^{21}$  and was a generous gift of Dr. Joel Schwartz (Dept. of Oral Pathology, Harvard School of Dental Medicine, Boston, MA). Cells were grown in Dulbecco's modified Eagle's medium (DMEM) with high glucose (Gibco, Grand Island, NY) supplemented with 10% fetal calf serum (FCS) (Gibco), 100 units/ml penicillin G and 100  $\mu$ g/ml streptomycin (Sigma). Medium was changed every 2-3 days and cells were passaged weekly using trypsin-EDTA (Gibco). All cells were maintained in 10 cm diameter petri dishes with 12 ml growth medium and kept at  $37^{\circ}$ C in a humidified 95% air, 5% CO<sub>2</sub> atmosphere.

# 2.5. In vitro immunoreactivity of the C225-Cy5.5 conjugate with tumor cells

HCPC-1 and A431 cells were grown in P35 dishes containing 5 ml of growth medium and a 22 mm square glass coverslip until they were 60-70% confluent. The C225-Cy5.5, BSA-Cy5.5 or mouse IgG-Cy5.5 conjugates were added at a final concentration of 0.1  $\mu$ g Cy5.5 equivalent /ml in serum-containing medium for 3 h at 37°C. The coverslips were then washed three times with PBS, were put on histological slides in PBS and examined with an epi-illumination fluorescence microscope (Axiophot; Zeiss, Oberkochen, Germany) equipped with a cooled charge-coupled device camera (CE200; Photometrics, Tucson, AZ). Images were obtained using excitation light provided by a mercury vapor lamp and a 670  $\pm$  5 nm band-pass filter and the emission was collected with a long-pass filter at 700 nm.

# 2.6. Fluorescence imaging

Imaging was conducted with a Pulnix room temperature CCD camera (model TM 745, Pulnix America Inc., Sunnyvale, CA) with the anesthetized hamster placed on a movable stage approximately 50 cm below the camera. To avoid any reflectance the cheek pouches were put on a black cloth covering a polystyrene platform and were firmly attached to it using pins with a diameter of 100 µm. The CCD camera was interfaced to an integration system (Pulnix) allowing integration of the signal for up to one second. The cheek pouches were illuminated with 670 nm light from an argon-ion (Innova 100; Coherent, Inc., Palo Alto, CA) pumped dye laser (CR-599; Coherent) at a power density of 15 mW/cm<sup>2</sup> (450 mW total power) measured with a power meter (model 200, Coherent). The light was delivered to the imaging plane through a 1 mm diameter fiber optic and expanded to give homogenous spot of 5 cm diameter using a 45 objective lens with numerical aperture of 0.1.

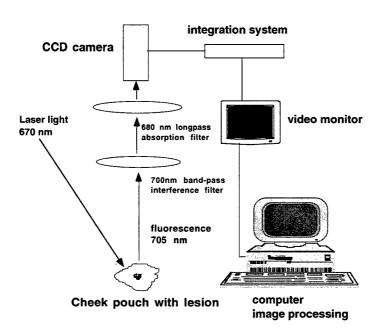


Figure 1. Schematic representation of fluorescence imaging set-up.

Fluorescence images were captured with an integration time of 1 second and with two filters placed before the camera lens. The first filter was a 700 nm bandpass interference filter with a bandwidth of 10 nm full width half maximum (Andover Corporation, Salem, NH) and the second was a longpass absorption filter with a 50% cut-off wavelength at 690 nm (Andover Corporation) and was used to remove fluorescence induced in the first filter. Excitation at 670 nm gave the optimum balance of power from the laser and excitation light rejection by the filters and allowed fluorescence images to be captured at a low level of background light. A white-light image of each specimen was first captured to inspect the cheek pouch. Fluorescence images from the CCD camera were captured using an 8-bit/pixel frame grabber (model DT 2867, Data Translation, Marlboro, MA) controlled by the computer program Global Lab Image (v2.20, Data Translation). The laser beam rested on each cheek-pouch for 5 seconds in order to acquire each image, therefore since the tissue was illuminated with 15 mWcm<sup>-2</sup> it receives a fluence of 0.075 Jcm<sup>-2</sup> of energy. Each hamster was imaged before injection and on days 1, 2, 4, 6, and 8 after injection.

Each image series was analyzed by image analysis software (Global Lab Image v2.20) which measured the mean pixel intensity (measured on a 256 gray-scale) in a pre-defined region (3 mm 5 4 mm) and gave the standard deviation. Measurements of average pixel intensity on the black background cloth surrounding the cheek pouch were taken for background correction. Each measurement of tissue fluorescence had the background measurement subtracted from it yielding what is referred to as the absolute fluorescence.

# 2.7. Immunophotodetection of premalignant lesions

Before fluorescence imaging was undertaken the cheek pouch mucosae were inspected to evaluate the lesions and photographed. Initial fluorescence imaging studies used 3 hamsters that had developed gross papillary tumors after 12 weeks painting of the cheek pouch. These animals were injected with 670 µg of C225-Cy5.5 conjugate (the average Cy5.5: MAb ratio was 2.1) corresponding to 12 µg of Cy5.5 and imaged 2 days later. For imaging of oral premalignant lesions 27 hamsters bearing lesions produced by painting the right cheek pouches for 6 weeks were studied. Nine hamsters were injected with C225-Cy5.5 as described above. Six control animals received 610 µg of irrelevant mouse IgG-Cy5.5 conjugate (the average Cy5.5: IgG ratio was 2.3) also corresponding to 12 µg of Cy5.5. Another groups of six control animals were injected with 390 µg BSA-Cy5.5 conjugate (the average Cy5.5: BSA ratio was 1.6) corresponding to 12 µg of Cy5.5 in order to distinguish between EGFR binding and increased vascular permeability. In all cases the overall dose of Cy5.5 injected was 100 µg per kg body weight.

At the end of the fluorescence imaging studies, biopsies (approximately 25 mm<sup>2</sup>) were obtained in order to correlate the fluorescent signals with the histologically determined stage of the lesions. In the case of cheek pouches that showed a fluorescent hot-spot, one biopsy was taken from the hot-spot and another from a part of the cheek pouch distant from the hot-spot. Tissue samples were immediately placed in 10% formalin followed by routine processing for paraffin embedding and histologic study. Sections were stained with hematoxylin-eosin and examined by light microscopy.

# 2.8. PIT in vivo

A pilot study investigated the photodynamic effect of the C225- $c_{e6}$  conjugate on EGFR expression in early premalignant lesions (6 weeks of DMBA treatment) of the hamster cheek pouch of 11 hamsters. Before injection of C225- $c_{e6}$  the visible area of each cheek pouch (DMBA-treated and normal) was divided in two equal parts using India ink and the outer part of each cheek pouch to be exposed to light was marked, while the inner part was protected from light by a black cloth. Animals were injected with 3.38 mg C225- $c_{e6}$  conjugate (the average  $c_{e6}$ : MAb ratio was 4.8 corresponding to 65  $\mu$ g of  $c_{e6}$ ) and 666 nm light was applied 2 days later (total fluence = 100 J/cm² delivered at a power density of 50 mW/cm²). The effectiveness of the treatment was assessed by immunophotodiagnosis by injecting the C225-Cy5.5 conjugate as described above at 5 days post treatment. Fluorescence imaging was performed 3 days after injection of the C225-Cy5.5 conjugate.

# 2.9. Statistics

Standard deviations of ratios of two means were calculated by the use of addition in quadrature  $^{22}$ . Differences between two means were tested for significance by a two-sided Students t-test assuming equal or unequal variances as appropriate. Means of ratios were tested to see if they were significantly > 1 by one-sided Students t-test.

#### 3. RESULTS

# 3.1. Preparation and characterization of conjugates

The absorption spectra of the C225-Cy5.5 and BSA-Cy5.5 conjugates together with free Cy5.5 are shown in Fig.1a. The conjugates have a distinct peak at 284 nm due to the protein absorbance by IgG and BSA, and the peak due to the Cy5.5 is at 675 nm for all conjugates. The number of dyes per protein molecule can be calculated assuming extinction coefficients of 2.5 5 10<sup>5</sup> M<sup>-1</sup>cm<sup>-1</sup> for Cy5.5 at 675 nm, 1.7 5 10<sup>5</sup> M<sup>-1</sup>cm<sup>-1</sup> for IgG (corrected for absorbance of Cy5.5 at 284 nm) and 1.2 5 10<sup>5</sup> M<sup>-1</sup>cm<sup>-1</sup> for BSA at 284 nm (likewise corrected for absorbance of Cy5.5). The C225-Cy5.5 conjugate had 2.1 molecules of Cy5.5 attached to each IgG, while BSA had 1.6 molecules per protein molecule.

Because the effectiveness of the  $c_{e6}$  conjugates in the destruction of premalignant tissue may depend on the amount of PS able to be delivered to the lesion, it was desired to have as high a loading of  $c_{e6}$  as possible, consistent with the MAb still retaining its immunoreactivity. In the present case the loading of the  $c_{e6}$  conjugates was limited by their tendency to aggregate when the ratio increased beyond 5 molecules of  $c_{e6}$  per IgG. The absorption spectra of C225- $c_{e6}$  and free  $c_{e6}$  are shown in Fig. 1b. The conjugate has a distinct absorbance at 284 nm due to the protein in the IgG, the intensity of the Soret band is somewhat reduced, and the long wavelength Q band is red shifted to 666 nm as opposed to 654 nm. It can be calculated assuming extinction coefficients of 1.5 5  $10^5$  Imol<sup>-1</sup>cm<sup>-1</sup> for  $c_{e6}$  at the Soret band and 2.4 x  $10^5$  Imol<sup>-1</sup>cm<sup>-1</sup> for IgG at 280 nm. The C225- $c_{e6}$  conjugate had a loading of 4.8 molecules of  $c_{e6}$  to each IgG.

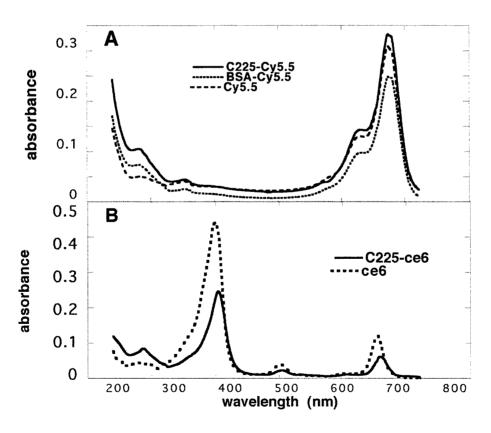


Figure 2. Ultraviolet-visible absorption spectra in 0.1 M NaOH/0.1% sodium dodecyl sulfate. (a) C225-Cy5.5, mouse IgG-Cy5.5, BSA-Cy5.5 conjugates and unconjugated Cy5.5; (b) C225- $c_{e6}$  and  $c_{e6}$ .

# 3.2. Fluorescence localization in living cells

\_The fluorescence images of A431 and HCPC-1 cells that had been incubated with the C225-Cy5.5 conjugate at a final concentration of 0.1 μg Cy5.5 equivalent in serum-containing medium for 3 h at 37°C are shown in Fig. 2 a and c along with the corresponding bright-field images (Fig. 2, b and d). The conjugate showed a strong affinity for A431 cells, which was expected since these cells have a high number of EGFRs <sup>23</sup>. In addition a significant fluorescence was seen with HCPC-1 cells indicating the suitability of the conjugate for targeting the DMBA tumor model. Neither cell showed fluorescence after incubation with BSA-Cy5.5 or mouse IgG-Cy5.5 conjugates (data not shown).

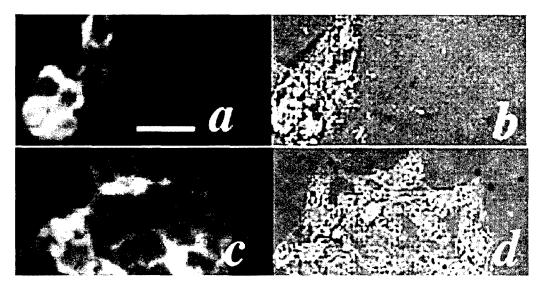


Figure 3. Fluorescence localization of C225-Cy5.5 with A431 and HCPC-1 cells. Cells were incubated with the conjugate at a final concentration of 0.1  $\mu$ g Cy5.5 equivalent in serum-containing medium for 3 h at 37°C (670 nm band-pass filter excitation and 700 nm long-pass filter emission). A431 cells with the C225-Cy5.5 conjugate, (a) fluorescence; (b) bright-field. HCPC-1 cells with the C225-Cy5.5 conjugate, (c) fluorescence; (d) bright-field. Bar = 50  $\mu$ m.

# 3.3. Immunophotodiagnosis of oral precancer in vivo

Initially, immunophotodiagnosis was performed on three animals with gross papillary tumors obtained after painting of cheek pouches for 12 weeks. A representative image from an animal with a papillary tumor measuring 5 mm in diameter is shown in Fig. 4. The normal cheek pouch has no visible fluorescence, while the tumor-bearing pouch has a clearly delineated tumor in the fluorescence image. Note that the fluorescence from the tumor is not completely uniform and this non-uniformity does not appear to be due to the illumination conditions, suggesting that the expression of the EGFR is heterogeneous or the perfusion is non-uniform.

To examine the use of immunophotodiagnosis in animals with hyperplastic or dysplastic lesions we used hamsters that had been painted with DMBA for an average of 6 weeks. Animals were injected with C225-Cy5.5 or the control dye conjugates (mouse IgG-Cy5.5 or BSA-Cy5.5) and imaged on days 1, 2, 4, 6, and 8 after injection.

A series of fluorescent images captured from both DMBA-treated cheek pouch and control cheek pouch in one animal (No. 5) at different time points is shown in Fig.5. At day 1 fluorescence was obtained from tissue, but it was evident that the C225-Cy5.5 conjugate still circulated in the cheek pouch vessels. As time progressed the contrast between carcinogen-treated and normal cheek pouches became greater. The multi-layered structure at the junction of the cheek-pouch mucosa and the rest of the oral mucosa has significantly higher fluorescence than the single layered cheek pouch. This is due to the additive effect of many tissue layers when fluorescence is measured with near-infrared excitation and emission wavelengths that penetrate well through tissue. However the single layer of the cheek pouch is the part painted with carcinogen and was the area that was analyzed for fluorescence quantification. The increased fluorescence of the multi-layered structure did not interfere with detection of increased fluorescence in DMBA treated pouches. At day 8 the fluorescent signals were very weak although there was still good contrast between normal and carcinogen treated cheek pouches.

Proc. SPIE Vol. 4259

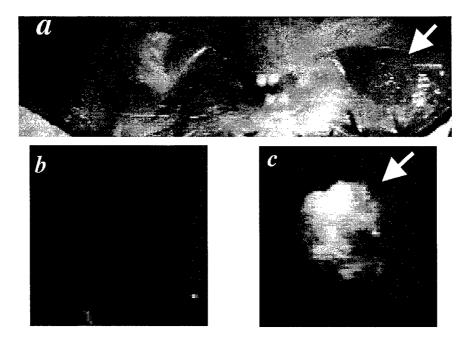


Figure 4. Fluorescence image of hamster with gross papillary tumor obtained after 12 weeks painting of cheek pouch with DBMA. Hamsters were injected with 670 μg of C225-Cy5.5 and imaged 2 days later. (a) White light image of both cheek pouches. (b) Fluorescence image of normal cheek pouch. (c) Fluorescence image of carcinogen-treated cheek pouch with papillary tumor (arrow).

The mean values of the ratios of fluorescence from DMBA-treated to the fluorescence from normal cheek pouches from groups of hamsters injected with the EGFR-targeted C225-Cy5.5 and non-targeted conjugates (mouse IgG-Cy5.5 and BSA-Cy5.5) are shown in Figure 6. The ratios from the C225-Cy5.5 group were significantly (p<0.05) greater than 1 for all time points except 1 day after injection. None of the control groups had mean ratios that were statistically > 1. The histological diagnoses of the animals in the control groups were similar with about 50% of the hamsters in each group showing focal dysplasia or hyperplasia.

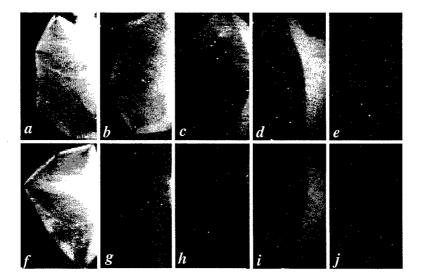
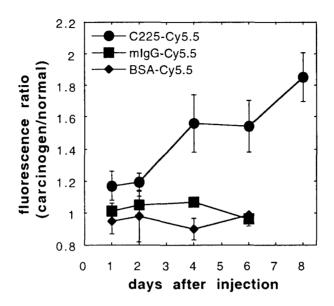


Figure 5. Pairs of fluorescence images taken from premalignant (a-e) and control cheek pouch (f-j) of hamster (no. 5) at 1 (a, f), 2 (b, g), 4 (c, h), 6 (d, i) and 8 (e, j) days after the administration of the C225-Cy5.5 conjugate.

Five out of nine animals in the C225-Cy5.5 group showed a distinct and circumscribed area of increased fluorescence (termed a hot-spot) within the overall increased fluorescence of the clinically normal DMBA-treated cheek pouch (see Fig. 7).



**Figure 6.** Ratios of fluorescence intensities from DMBA-treated and normal cheek pouches. Ratios of mean fluorescence values (DMBA-treated cheek pouch/normal cheek pouch) from groups of hamsters at different time intervals after the injection of the specified conjugate. Values are means and SEM calculated in quadrature.

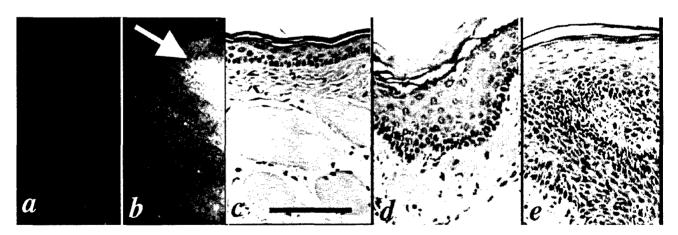


Figure 7. Fluorescence images of normal (a) and DMBA-treated (b) cheek pouches in hamster #6 at 6 days after the injection of the C225-Cy5.5 conjugate. A fluorescence hot-spot (area of increased fluorescence) can be seen within the DMBA-treated cheek pouch (arrow). H&E histology shows (c) normal mucosal epithelium for the DMBA-untreated cheek pouch, bar =  $100 \mu m$ ; (d) mild dysplasia for the DMBA-treated cheek pouch; and (e) moderate dysplasia for the hot-spot.

Table 2 shows the correlation between the fluorescence ratios on days 1, 4, and 6 (DMBA-treated/normal) and the histological diagnosis of biopsies taken from whole (clinically normal) cheek pouches and from fluorescent hot-spots located within cheek pouches of five hamsters. As can be seen four out of five of the hot-spots showed evidence of dysplasia in the hot-spot tissue, while only one (#6) showed dysplasia outside of the hot-spot. The remaining hot-spot (#3 which had the lowest fluorescence ratio) showed only hyperkeratosis and an inflammatory infiltrate.

**Table 2.** Ratios of fluorescence intensities from DMBA-treated and normal cheek pouches in individual animals injected with C225-Cy5.5. Ratios of fluorescence values (DMBA-treated cheek pouch/normal cheek pouch) from individual hamsters at different time intervals after the injection of the C225-Cy5.5 conjugate correlated with the histologically determined stage of the premalignant lesion. Values are means and SD calculated in quadrature.

Ratio of mean fluorescence intensities (DMBA-treated/normal pouches)		es (DMBA-	Microscopic diagnosis from H&E stained fixed slides		
	Day 1	Day 4	Day 6		
1	1.2	1.53	1.16	hyperkeratosis	
2	1.06	1.09	0.92	hyperkeratosis	
3*	0.94	1.08	1.23	hyperkeratosis	
4	1.23	1.23	1.02	hyperkeratosis	
5	0.94	1.07	1.9	hyperkeratosis	
6*	1.06	2	2.18	dysplasia <sup>†</sup>	
7*	1.76	2.09	1.74	hyperkeratosis, hyperplasia	
8*	1.17	2.45	1.99	hyperkeratosis	
9*	1.17	1.48	1.68	hyperkeratosis	
Fluorescence cheek pouch)	ratios from	hot-spot (hot-	-spot/normal	Microscopic diagnosis from hot-spot	
3		1.57	1.87	hyperkeratosis, strong inflammatory infiltrate	
6		2.3	3.31	dysplasia¶	
7		2.68	2.4	dysplasia <sup>‡</sup>	
8	1.63	3.54	2.66	dysplasia§	
9	1.45	1.63	1.87	dysplasia¶	
mean ±S.D	1.54 ±0.13	2.34± 0.81	$2.42 \pm 0.6$		
P values for Mean > 1		P <0.001	P <0.001		

<sup>\*</sup> Areas within DMBA-treated cheek pouches that showed an increased fluorescence signal (hot spots) were found.

The fluorescence values from these hot-spots were separately calculated and the resulting mean absolute values together with the overall (whole cheek pouch) mean absolute fluorescence values from both DMBA-treated and normal pouches are plotted against time after injection in Fig. 8. The fluorescence intensities were highest 1 day after the injection of the C225-Cy5.5 conjugate (2 days after in the hot-spots) and then dropped in an apparent exponential decay.

<sup>†</sup> hyperkeratosis, hyperplasia, drop-shaped rete processes.

<sup>¶</sup> hyperkeratosis, irregular epithelial downgrowth, loss of basal cell polarity, increased nuclear-cytoplasmic ratio, small number of abnormal mitoses.

<sup>‡</sup> hyperkeratosis, irregular epithelial downgrowth, loss of basal cell polarity

<sup>§</sup> hyperkeratosis, hyperplasia, nuclear hyperchromatism, strong inflammatory infiltrate.

<sup>¶</sup> hyperkeratosis, hyperplasia, irregular epithelial downgrowth, deep cell keratinization, enlarged prickle cells.

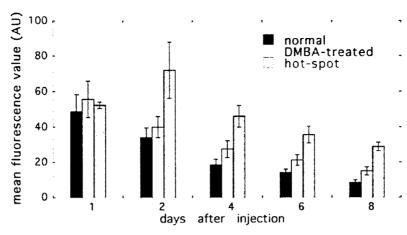


**Figure 8.** Time course of mean absolute fluorescence values in the hot spots, whole DMBA-treated and DMBA-untreated cheek pouches after the injection of the C225-Cy5.5 conjugate. Values from normal and DMBA-treated are from 9 hamsters while values of hot-spot fluorescence are from 5 hamsters. Values are expressed as means ± SEM.

# 3.4. PIT studies

These experiments were performed in order to test the hypothesis that C225 could selectively deliver a photosensitizer to the EGFR in these early premalignant lesions, and that after illumination the resultant photodynamic effect would reduce the expression of the EGFR. Furthermore, immunophotodiagnosis could be used as a feedback tool for the photoimmunotherapy, and the tissue fluorescence level may act as a surrogate marker for efficacy. We hypothesized that the effects of PIT on EGFR levels could be demonstrated by comparison of fluorescence images produced by C225-Cy5.5 in the cheek pouches at 5 days after treatment. Eleven hamsters had one cheek pouch painted with carcinogen for 6 weeks and then each animal was injected with C225-  $c_{e6}$  and 3 days later part of each cheek pouch (carcinogen-treated and normal) was illuminated with red

light (100 J/cm<sup>2</sup>). Five days later animals were injected with C225-Cy5.5 as before, and after another 3 days, fluorescence images were obtained. Four mean fluorescence values from the areas of cheek pouches were obtained and are shown in Figure 9.

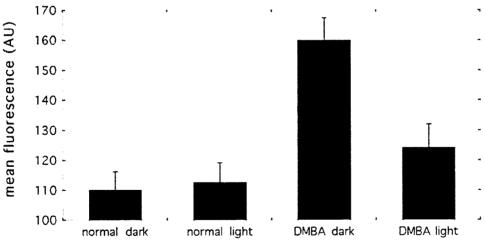


**Figure 9.** Mean absolute fluorescence values from illuminated and non-illuminated, carcinogen-treated and normal cheek pouches treated with PIT followed by immunophotodiagnosis. Values are means and SEM.

As expected there was a highly significant difference between the mean fluorescence values of the non-light exposed areas of the normal and DMBA-treated cheek pouches ( $110 \pm 21$  vs  $160 \pm 29$ , p < 0.0005). The mean fluorescence values of the light-treated and non-light treated areas of the normal cheek pouches were almost the same ( $112 \pm 22$  vs  $110 \pm 21$ ). When the light-exposed DBMA-treated areas were compared to the non-light-exposed DMBA-treated areas there was a significant reduction in fluorescence ( $124.2 \pm 26$  vs  $160 \pm 29$ , p < 0.01) and interestingly there was no significant difference between the

light-exposed DMBA-treated areas and either the light-exposed or the dark areas of the normal cheek pouches. This latter result suggests that the overexpression of the EGFR found after DMBA treatment has been reduced to background levels after PIT. After completion of the fluorescence imaging the animals were sacrificed and the cheek pouches subjected to histological examination. All eleven hamsters had hyperkeratosis and focal hyperplasia in the DMBA treated pouches, and two animals had in addition focal dysplasia. The light-exposed areas of both normal and DMBA-treated pouches revealed in addition a submucosal edema and inflammatory infiltrate.

#### DISCUSSION

The results obtained in this study show that fluorescence immunophotodetection of oral precancer could be possible using an anti-EGFR MAb coupled to the fluorescent dye indocyanine Cy5.5 in a DMBA-induced hamster cheek pouch carcinogenesis model. The use of an anti-EGFR MAb to deliver a fluorophore applied equally well to the PS ce6 making possible reduction of tissue EGFR levels by a photodynamic effect. The immunophotodetection procedure was used to assess response to PIT.

Fluorescent dyes recently used for diagnostic purposes are fluorescein <sup>11</sup>, <sup>12</sup> and a family of dyes called indocyanines <sup>13</sup>. The indocyanine dyes have advantages over fluorescein in that they emit a more penetrating fluorescent signal, have high quantum yields and good solubility <sup>24</sup>, <sup>25</sup>. A recent member of the indocyanine family called indocyanine Cy5.5 emits a penetrating fluorescent red signal at 702 nm after excitation at 675 nm and has an extremely high absorption coefficient of more than 250,000. The advantage here is that both emission and absorption peaks of Cy5.5 are located in a region of the spectrum where background endogenous fluorescence from most cellular pigments is very low. In addition, the fluorescence signal of the marker dye Cy5.5 detected on tissues is amplified because an increased number of molecules are localized deeper into them. In this study the indocyanine:MAb molar ratio in the C225-Cy5.5 conjugate was 2.1. This ratio was efficient in detection of oral premalignant lesions as well as in detection of tumors in nude mice using the marker dye Cy5 with excitations and emission wavelengths at 640 and 667 nm respectively <sup>13</sup>.

The injection of the C225-Cy5.5 conjugate was well tolerated by the animals and gave sufficiently high levels of tissue fluorescence to allow quantitative imaging. The fluorescence photomicrographs indicated that at both 30 min (data not shown) and 24 h the C225-Cy5.5 conjugate was distributed primarily within and near the vasculature. The same observations were also obtained using the BSA-Cy5.5 conjugate as well as free Cy5.5. The average fluorescent intensity values showed high standard deviations in both DMBA-treated and normal cheek pouches because fluorescence was mainly obtained from the cheek pouch capillaries. Control cheek pouches contained a plexus of capillaries with uniform diameters that were connected to larger vessels. The capillaries in DMBA-treated cheek pouches were larger than those of control cheek pouches. All these microvascular changes observed at 6 weeks after the application of DMBA were similar to those observed by <sup>26</sup> in the same model. We did not observe any striking difference in fluorescence obtained from both control and premalignant tissue 24 h after the injection of the conjugate. This was in contrast with some reported immunophotodetection studies in animals and humans where contrast was seen 24 h after the injection of Mabs labeled either with fluorescein 11, 12, 26, 27 or with indocyanine 13, 24, 25. At 2 days after the injection of the conjugate the fluorescent signal mainly originated from extravascular dye within the tissue and there was some contrast between normal and premalignant tissue. The best contrast was obtained at 4-8 days, which may be due to the metabolism or clearance of unbound conjugate. Certain types of tumor vasculature have shown a dramatic increased permeability to macromolecules<sup>28</sup>, <sup>29</sup>. However, early premalignant lesions may not demonstrate hyperpermeability of blood vessels. In this study a BSA-Cy5.5 conjugate as well as free Cy5.5 were used to distinguish between EGFR binding and increased vascular permeability.

Distinction between premalignant lesions and normal cheek pouches was possible using our fluorescence imaging system. Areas of increased fluorescence intensity within the premalignant tissue could also be detected. These fluorescence-hot spots revealed dysplasia on histologic examination. It seems that increased levels of the C225-Cy5.5 conjugate retained in these lesions due to increased numbers of EGFRs. Other studies have used PS designed for PDT for fluorescence detection of premalignancy in the hamster cheek pouch model <sup>30-34</sup>. Although our imaging system was not able to differentiate hyperkeratotic and inflammatory lesions from normal tissue, in two animals with hyperkeratosis and inflammatory changes hot areas were detected in the DMBA-treated cheek pouches. These areas revealed strong infiltrate in the lamina propria. The observed increased fluorescence intensity from these inflamed areas may be largely due to increased supply of blood that may lead to the enhancement of the permeability of the C225-Cy5.5 conjugate. Increased fluorescence signals were also observed in two controls animals injected with free Cy5.5 whose DMBA-treated cheek pouch revealed mild inflammatory response.

The EGFR has also been used in several studies as a therapeutic target. Several anti-EGFR murine MAbs administered alone were able to inhibit the proliferation of a variety of human cancer cell lines in culture and in xenograft

models <sup>35</sup>. A link between EGFR signaling and angiogenesis has recently been identified <sup>36</sup>, <sup>37</sup>. Systemic administration of the MAb C225 inhibited growth and metastasis of human transitional cell carcinoma established in the bladder wall of athymic nude mice in part by inhibition of angiogenesis <sup>38</sup>. The use of conjugates between an anti-EGFR MAb and a PS to target photodynamic treatment to the EGFR is an approach with many advantages. Damage is limited to the illuminated volume of tissue in the absence of side effects. In addition, these immunoconjugates may not need to be internalized in order to impose their effect. Our goal in this study was to reduce the levels of EGFR expression in premalignant lesions by a targeted photodynamic effect. The hypothesis is that destruction of EGFRs will result in a significant reduction of growth signals in the nucleus that may lead to regression of the lesions. In this study, PIT had reduced the immunoreactivity of EGFR in early premalignant lesions of the hamster cheek pouch. Laser-induced immunophotodetection appeared to be an effective tool for the assessment of the response to PIT. Five days after PIT the reduction of EGFR functionality was 25% in the premalignant tissue indicating that the signaling pathway has endured serious damage. The photodynamic effects of a conjugate between an anti-EGFR MAb and the photoactivatable compound benzoporphyrin derivative have been studied on squamous cell carcinoma in the hamster cheek pouch model <sup>18</sup>. The conjugate proved to be effective and led to an 80% rate of complete response after illumination.

Our results suggest that immunophotodiagnosis using indocyanine-labeled anti-EGFR MAb may have potential as a technique for the detection of early oral precancer. In the longterm it could be used to identify populations at high risk, to improve diagnostic accuracy, to stage tumors more precisely for prognostic and therapeutic decisions and to monitor more effectively the responses to therapy. Preliminary data suggest that immunophotodiagnosis could be usefully incorporated into an efficient PIT protocol also using EGFR as a target. These results encourage further studies that will explore whether innunophotodiagnosis can monitor the progress of dysplastic lesions as well as follow-up response to treatment of dysplastic lesions subjected to PIT.

### **ACKNOWLEDGEMENTS**

We thank Michael P. Bamberg, Jaimie L Miller, and Bart Johnson for technical assistance, ImClone Systems, Inc. for the gift of MAb C225 and Coherent Inc. for the loan of the argon-pumped dye laser. The authors are grateful to Dr. Brian W. Pogue for useful advice and suggestions concerning the set up of the fluorescence imaging system, to Dr Suzanne Keel for help with histopathology, and Dr Richard L. Fabian for support.

#### REFERENCES

- 1. C. Scully, "Clinical diagnostic methods for the detection of premalignant and early malignant oral lesions," *Community Dent Health*, **10 Suppl 1**, pp. 43-52, 1993
- 2. G. Carpenter, "Receptors for epidermal growth factor and other polypeptide mitogens," *Annu Rev Biochem*, **56**, pp. 881-914, 1987
- 3. A. Eisbruch, M. Blick, J. S. Lee, P. G. Sacks, and J. Gutterman, "Analysis of the epidermal growth factor receptor gene in fresh human head and neck tumors." *Cancer Res*, **47**, pp. 3603-3605, 1987
- 4. K. Shirasuna, Y. Hayashido, M. Sugiyama, H. Yoshioka, and T. Matsuya, "Immunohistochemical localization of epidermal growth factor (EGF) and EGF receptor in human oral mucosa and its malignancy," *Virchows Arch A Pathol Anat Histopathol*, **418**, pp. 349-353, 1991
- 5. D. M. Shin, J. Y. Ro, W. K. Hong, and W. N. Hittelman, "Dysregulation of epidermal growth factor receptor expression in premalignant lesions during head and neck tumorigenesis," *Cancer Res*, **54**, pp. 3153-3159, 1994
- 6. D. M. Shin, I. B. Gimenez, J. S. Lee, K. Nishioka, M. J. Wargovich, S. Thacher, R. Lotan, T. J. Slaga, and W. K. Hong, "Expression of epidermal growth factor receptor, polyamine levels, ornithine decarboxylase activity, micronuclei, and transglutaminase I in a 7,12-dimethylbenz(a)anthracene-induced hamster buccal pouch carcinogenesis model," *Cancer Res*, 50, pp. 2505-2510, 1990
- 7. C. R. Divgi, S. Welt, M. Kris, F. X. Real, S. D. Yeh, R. Gralla, B. Merchant, S. Schweighart, M. Unger, S. M. Larson, and et al., "Phase I and imaging trial of indium 111-labeled anti-epidermal growth factor receptor monoclonal antibody 225 in patients with squamous cell lung carcinoma," *J. Natl. Cancer Inst.*, 83, pp. 97-104, 1991
- 8. A. Goldenberg, H. Masui, C. Divgi, H. Kamrath, K. Pentlow, and J. Mendelsohn, "Imaging of human tumor xenografts with an indium-111-labeled anti- epidermal growth factor receptor monoclonal antibody," *J Natl Cancer Inst*, **81**, pp. 1616-1625, 1989

- 9. Z. Fan, H. Masui, I. Altas, and J. Mendelsohn, "Blockade of epidermal growth factor receptor function by bivalent and monovalent fragments of 225 anti-epidermal growth factor receptor monoclonal antibodies," *Cancer Res*, **53**, pp. 4322-4328, 1993
- J. Baselga, D. Pfister, M. R. Cooper, R. Cohen, B. Burtness, M. Bos, G. D'Andrea, A. Seidman, L. Norton, K. Gunnett, J. Falcey, V. Anderson, H. Waksal, and J. Mendelsohn, "Phase I studies of anti-epidermal growth factor receptor chimeric antibody C225 alone and in combination with cisplatin," J Clin Oncol, 18, pp. 904, 2000
- 11. S. Folli, G. Wagnieres, A. Pelegrin, J. M. Calmes, D. Braichotte, F. Buchegger, Y. Chalandon, N. Hardman, C. Heusser, and J. C. Givel, "Immunophotodiagnosis of colon carcinomas in patients injected with fluoresceinated chimeric antibodies against carcinoembryonic antigen," *Proc Natl Acad Sci USA*, **89**, pp. 7973-7977, 1992
- 12. A. Pelegrin, S. Folli, F. Buchegger, J. P. Mach, G. Wagnieres, and H. van den Bergh, "Antibody-fluorescein conjugates for photoimmunodiagnosis of human colon carcinoma in nude mice," *Cancer*, 67, pp. 2529-2537, 1991
- 13. S. Folli, P. Westermann, D. Braichotte, A. Pelegrin, G. Wagnieres, H. van den Bergh, and J. P. Mach, "Antibody-indocyanin conjugates for immunophotodetection of human squamous cell carcinoma in nude mice," *Cancer Research*, 54, pp. 2643-2649, 1994
- 14. M. Del Governatore, M. R. Hamblin, E. E. Piccinini, G. Ugolini, and T. Hasan, "Targeted photodestruction of human colon cancer cells using charged 17.1A chlorin e6 immunoconjugates [In Process Citation]," *Br J Cancer*, **82**, pp. 56-64, 2000
- 15. M. R. Hamblin, J. L. Miller, and T. Hasan, "Effect of charge on the interaction of site-specific photoimmunoconjugates with human ovarian cancer cells," *Cancer Res*, **56**, pp. 5205-5210, 1996
- 16. K. L. Molpus, M. R. Hamblin, I. Rizvi, and T. Hasan, "Intraperitoneal photoimmunotherapy of ovarian carcinoma xenografts in nude mice using charged photoimmunoconjugates," *Gynecol Oncol*, **76**, pp. 397-404, 2000
- 17. M. Del Governatore, M. R. Hamblin, C. R. Shea, I. Rizvi, K. G. Molpus, K. K. Tanabe, and T. Hasan, "Experimental photoimmunotherapy of hepatic metastases of colorectal cancer with a 17.1A chlorin(e6) immunoconjugate," *Cancer Res*, **60**, pp. 4200-4205, 2000
- 18. A. Hemming, N. Davis, B. Dubois, N. Quenville, and R. Finley, "Photodynamic therapy of squamous cell carcinoma. An evaluation of a new photosensitizing agent, benzoporphyrin derivative and new photoimmunoconjugate," *Surg Oncol*, 2, pp. 187-196, 1993
- 19. G. Shklar, E. Eisenberg, and E. Flynn, "Immunoenhancing agents and experimental leukoplakia and carcinoma of the hamster buccal pouch," *Prog Exp Tumor Res*, **24**, pp. 269-282, 1979
- 20. N. S. Soukos, M. R. Hamblin, and T. Hasan, "The effect of charge on cellular uptake and phototoxicity of polylysine chlorin(e6) conjugates," *Photochem. Photobiol.*, **65**, pp. 723-729, 1997
- 21. O. Odukoya, J. Schwartz, R. Weichselbaum, and G. Shklar, "An epidermoid carcinoma cell line derived from hamster 7,12- dimethylbenz[a]anthracene-induced buccal pouch tumors," *J Natl Cancer Inst*, 71, pp. 1253-1264, 1983
- 22. J. R. Taylor, An introduction to error analysis., p. 57. Mill Valley, CA: University Science Books, 1982.
- 23. T. Kawamoto, J. D. Sato, A. Le, J. Polikoff, G. H. Sato, and J. Mendelsohn, "Growth stimulation of A431 cells by epidermal growth factor: identification of high-affinity receptors for epidermal growth factor by an anti-receptor monoclonal antibody," *Proc Natl Acad Sci U S A*, 80, pp. 1337-1341, 1983
- 24. B. Ballou, G. W. Fisher, T. R. Hakala, and D. L. Farkas, "Tumor detection and visualization using cyanine fluorochrome-labeled antibodies," *Biotechnol Prog.* 13, pp. 649-658, 1997
- 25. B. Ballou, G. W. Fisher, J. S. Deng, T. R. Hakala, M. Srivastava, and D. L. Farkas, "Cyanine fluorochrome-labeled antibodies in vivo: assessment of tumor imaging using Cy3, Cy5, Cy5.5, and Cy7," *Cancer Detect Prev*, **22**, pp. 251-257, 1998
- 26. A. G. Lurie, M. Tatematsu, T. Nakatsuka, R. M. Rippey, and N. Ito, "Anatomical and functional vascular changes in hamster cheek pouch during carcinogenesis induced by 7, 12-dimethylbenz(a)anthracene," *Cancer Res*, **43**, pp. 5986-5994, 1983
- 27. M. Tatsuta, H. Iishi, M. Ichii, M. Baba, R. Yamamoto, S. Okuda, and K. Kikuchi, "Diagnosis of gastric cancers with fluorescein-labeled monoclonal antibodies to carcinoembryonic antigen," *Lasers Surg Med*, **9**, pp. 422-426, 1989
- 28. H. F. Dvorak, J. A. Nagy, J. T. Dvorak, and A. M. Dvorak, "Identification and characterization of the blood vessels of solid tumors that are leaky to circulating macromolecules," *Am J Pathol*, **133**, pp. 95-109, 1988
- 29. F. Yuan, M. Leunig, S. K. Huang, D. A. Berk, D. Papahadjopoulos, and R. K. Jain, "Microvascular permeability and interstitial penetration of sterically stabilized (stealth) liposomes in a human tumor xenograft," *Cancer Res*, **54**, pp. 3352-3356, 1994
- 30. D. H. Crean, C. Liebow, R. B. Penetrante, and T. S. Mang, "Evaluation of porfimer sodium fluorescence for measuring tissue transformation," *Cancer*, **72**, pp. 3068-3077, 1993
- 31. T. S. Mang, C. McGinnis, C. Liebow, U. O. Nseyo, D. H. Crean, and T. J. Dougherty, "Fluorescence detection of tumors. Early diagnosis of microscopic lesions in preclinical studies," *Cancer*, 71, pp. 269-276, 1993

- 32. K. Furukawa, H. Yamamoto, D. H. Crean, H. Kato, and T. S. Mang, "Localization and treatment of transformed tissues using the photodynamic sensitizer 2-[1-hexyloxyethyl]-2-devinyl pyropheophorbide-a," *Lasers Surg Med*, **18**, pp. 157-166, 1996
- 33. V. V. Lazarev, R. A. Roth, Y. Kazakevich, and J. Hang, "Detection of premalignant oral lesions in hamsters with an endoscopic fluorescence imaging system," *Cancer*, **85**, pp. 1421-1429, 1999
- 34. S. Andrejevic Blant, J. P. Ballini, H. van den Bergh, C. Fontolliet, G. Wagnieres, and P. Monnier, "Time-dependent biodistribution of tetra(m-hydroxyphenyl)chlorin and benzoporphyrin derivative monoacid ring A in the hamster model: comparative fluorescence microscopy study," *Photochem Photobiol*, 71, pp. 333-340, 2000
- 35. J. Mendelsohn and J. Baselga Antibodies to growth factors and and receptors. *In:* A. P. J. DeVita, S. Hellman, and S. A. Rosenberg (eds.), Biologic therapy of cancer, 2nd edition, pp. 607-623. Philadelphia: J. B. Lippincott, 1995.
- 36. H. Masui, T. Kawamoto, J. D. Sato, B. Wolf, G. Sato, and J. Mendelsohn, "Growth inhibition of human tumor cells in athymic mice by anti-epidermal growth factor receptor monoclonal antibodies," *Cancer Res*, 44, pp. 1002-1007, 1984
- 37. A. M. Petit, J. Rak, M. C. Hung, P. Rockwell, N. Goldstein, B. Fendly, and R. S. Kerbel, "Neutralizing antibodies against epidermal growth factor and ErbB-2/neu receptor tyrosine kinases down-regulate vascular endothelial growth factor production by tumor cells in vitro and in vivo: angiogenic implications for signal transduction therapy of solid tumors," *Am J Pathol*, **151**, pp. 1523-1530, 1997
- 38. P. Perrotte, T. Matsumoto, K. Inoue, H. Kuniyasu, B. Y. Eve, D. J. Hicklin, R. Radinsky, and C. P. Dinney, "Anti-epidermal growth factor receptor antibody C225 inhibits angiogenesis in human transitional cell carcinoma growing orthotopically in nude mice," *Clin Cancer Res*, **5**, pp. 257-265, 1999

# Targeted Type 1 phototherapeutic agents using azido-peptide bioconjugates

Raghavan Rajagopalan\*, Samuel A. Achilefu, Hermo N. Jimenez, Elizabeth G. Webb, Michelle A. Schmidt, Joseph E. Bugaj\*\*, Richard B. Dorshow Mallinckrodt Inc., Saint Louis, Missouri

### **ABSTRACT**

Five peptides binding to somatostatin and bombesin receptors were conjugated to 4-azido-2,3,5,6-tetrafluorophenylbenzoic acid, a Type 1 photosensitizer, at the N-terminal position. The receptor affinities were determined by competition binding assay using two different pancreatic tumor cell lines, CA20948 and AR42-J, that express somatostatin-2 (SST-2) and bombesin receptors respectively All compounds exhibited high receptor specificity, i.e., the  $IC_{50}$  values ranged between 1.0 to 64.0 nM. These conjugates may be useful for targeted Type 1 phototherapy via the generation of nitrenes at the cell surfaces expressing these receptors.

### 1. INTRODUCTION

The use of visible and near-infrared (NIR) light in clinical practice is growing rapidly. <sup>1-3</sup> Compounds absorbing or emitting in the visible or NIR, or long-wavelength (UV-A, >350 nm) region of the electromagnetic spectrum are potentially useful for optical tomographic imaging, endoscopic visualization, and phototherapy. However, the major advantage of biomedical optics lies in its therapeutic potential. <sup>4-6</sup> Although the potential of cancer phototherapy has been recognized since early 1900's, <sup>7,8</sup> only recently has this technique been successfully applied to treat bladder, esophageal, and late-stage lung cancers in humans using Photofrin II, a hematoporphyrin photosensitizer recently approved by the United States Food and Drug Administration.

Photosensitizers operate via two distinct pathways as shown in Figure 1. Type 1 mechanism involves direct energy or electron transfer from the excited photosensitizer to the cellular components thereby causing cell death. Type 2 process

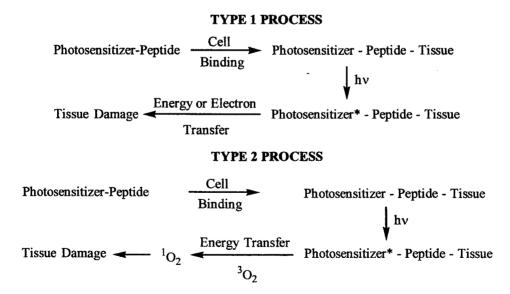


Figure 1: Phototherapeutic Processes

involves two distinct steps: (a) the generation of singlet oxygen by energy transfer from the triplet excited state of the photosensitizer to the oxygen molecules surrounding the tissues, and (b) collision of singlet oxygen with the tissue thereby promoting tissue damage. In either Type 1 or Type 2 mechanism, the photochemical reaction proceeds via the lowest triplet state of the sensitizer. Therefore, relatively long triplet lifetime is required for effective phototherapy whereas short triplet

lifetime is necessary for photodiagnostics in order to avoid photodamages. Phototherapeutic efficacy can be substantially enhanced if the excited state photosensitizers can generate reactive intermediates such as free radicals, nitrenes, carbenes, etc. which have much longer lifetimes than the excited chromophore and have been shown to cause considerable cell injury. 10

Most of the currently known photosensitizers belong to Type 2 category, commonly referred to as 'photodynamic therapy (PDT)' agents. These include monomeric porphyrin derivatives, corrins, cyanines, phthalocyanines, phenothiazines, rhodamines, hypocrellins, etc. 11,12 In contrast, only a small number of compounds belonging to the class of anthracylines antitumor that operates through Type I mechanism have been investigated. Surprisingly, there has not been much attention directed at developing Type 1 agents despite the fact that Type 1 process seems inherently more efficient than Type 2 for the following reasons: first, unlike Type 2, Type 1 photosensitizers do not require oxygen for causing cellular injury; and second, Type 1 involves two steps (photoexcitation and direct energy transfer) whereas Type 2 involves three steps (photoexcitation, singlet oxygen generation, and energy transfer). Furthermore, some tumors have hypoxic regions, which may render Type 2 mechanism ineffective. The ultimate objective of our current research is to develop highly selective and efficient phototherapeutic drugs based on Type 1 process. Accordingly, as the first step toward this goal, we wish to report the results of tumor cell binding assay of somatostatin bombesin receptor specific peptides bearing an azidotetraflurobenzoyl (ATFB) moiety, which can be excited by UV-A light in accordance with the procedure described for ATFB-human serum albumin conjugate. Photoexcitation of the aromatic chromophore effects rapid intramolecular energy transfer to the azido group which will result in the extrusion of N<sub>2</sub> molecule with concomitant production of the reactive intermediate, nitrene. The nitrogen that is released is in vibrationally excited state, which may also aid in additional cellular injury.

### 2. MATERIALS AND METHODS

# 2.1 Synthesis of azido-peptide bioconjugates

The structures of 4-azido-2,3,5,6-tetrafluorobenzamido (ATFB) bioconjugates are shown in Figure 2. The conjugates were synthesized by the standard automated solid-phase method and were purified by HPLC such that the chromatographic purity

Figure 2: Structures

of the compounds were >99%. Molecular weights were determined by electrospray mass spectrum. A typical procedure is described below for ATFB- conjugates 1-5. Preparation of 4-azido-2,3,5,6-tetrafluorophenylbenzoic acid has been reported previously.<sup>14</sup>

The conjugates were prepared by fluorenylmethoxycarbonyl (Fmoc) solid phase peptide synthesis strategy¹6 with a commercial peptide synthesizer from Applied Biosystems (Model 432A SYNERGY Peptide Synthesizer). The first peptide cartridge contained Wang resin pre-loaded with an amide resin on 25-µmole scale. The amino acid cartridges were placed on the peptide synthesizer and the product was synthesized from the C- to the N-terminal position. Coupling of the Fmoc-protected amino acids (75 µmol) to the resin-bound free terminal amine (25 µmol) was carried out with 2-(1H-benzotriazol-1-yl)-1,1,3,3-tetramethyluronium hexafluorophosphate (HBTU, 75 µmol)/N-hydroxybenzotriazole (HOBt, 75 µmol). Each Fmoc protecting group on solid support was removed with 20% piperidine in dimethylformamide before subsequent amino acid was coupled to it. The last cartridge contained 4-azido-2,3,5,6-tetrafluorobenzoic acid, which was successfully coupled to the peptide automatically, thus avoiding the need for post-synthetic manipulations. After the

synthesis was completed, the product was cleaved from the solid support with a cleavage mixture containing trifluoroacetic acid (85%):water (5%):phenol (5%):thioanisole (5%) for 6 hours. The ATFB-peptide conjugate was precipitated with mthyl t-butyl ether and lyophilized using water/acetonitrile (2:3) mixture. The conjugate was purified by HPLC and analyzed by LC/MS. The analytical data for the bioconjugates 1-5 are shown in Table 1 below.

Table 1: HPLC and Mass Spectral Data

ATFB-Peptide Conjugate	Chromatographic Purity (%)	m/Z (M+H)	
1. Bombesin (7-14)	99.5	1157	
2. Lys <sup>0</sup> -Bombesin (7-14)	99.5	1286	
3. Gly-ser-gly-Bombesin (7-14)	99.0	1358	
4. Tyr <sup>3</sup> -Octreotate	99.0	1266	
5. Lys <sup>0</sup> -Octreotate	99.9	1394	

# 2.2 Cell binding assay

Receptor affinities (IC<sub>50</sub> values) of ATFB-bioconjugates were determined by the standard competitive binding assay using cells expressing somatostatin and bombesin receptors. Receptor binding assays were carried using cultured AR42-J cells (ATCC) for the bombesin conjugates 1-3 and, membrane preparations of CA20948 tumor cells; for the octreotate conjugates 4,5. Assays were performed using the Millipore Multiscreen system (Bedford, MA) with radiolabled with <sup>111</sup>In-DTPA-Tyr<sup>(3)</sup>-octreotate or <sup>111</sup>In-DTPA-bombesin<sup>(7-14)</sup> as the labeled tracers, and ATFB-conjugates 1-5 as cold competitors. The IC<sub>50</sub> values were calculated using a four-parameter curve fitting routine using the program GraFit (Erithacus, UK).

# 3. RESULTS AND DISCUSSION

The IC<sub>50</sub> values for the ATFB bioconjuates (1-5) are shown in Table 2. All compounds, as would be expected from previous

Table 2: IC<sub>50</sub> Values

ATFB-Peptide Conjugate	IC <sub>50</sub> (nM)		
1. Bombesin (7-14)	64.0		
2. Lys <sup>0</sup> -Bombesin (7-14)	3.4		
3. Gly-ser-gly-Bombesin (7-14)	1.2		
4. Tyr <sup>3</sup> -Octreotate	2.7		
5. Lys <sup>0</sup> -Octreotate	1.0		

studies employing containing fluorescent dyes<sup>17</sup> or radionuclide chelates,<sup>18</sup> exhibited high binding to their corresponding receptors. The variation in the binding constants can be attributed to the differences in peptide sequence. The results indicate that ATFB-peptide conjugates have high affinity for their corresponding receptors and, therefore, they may be useful for targeted phtotherapy for those lesions expressing somatostatin and bombesin receptors. Even conjugate 1, which is the weakest among the series, should have sufficient affinity for targeted for targeted phototherapy.

# REFERENCES

- J.C. Hebden and D.T. Delpy, "Diagnostic Imaging with Light," The British Journal of Radiology 70, pp. S206-S214, 1997.
- 2. G. Freiherr, "The Light Stuff: Optical Imaging in Medical Diagnostics," Medical Devices & Diagnostic Industry, pp. 40-46, 1998.
- 3. F.F. Rubaltelli, "Photodiagnostic and Phototherapeutic Techniques in Medicine," in *Documento Editoriale*, G. Jori, C. Perria, Editors, pp. 101-107, Milano, 1995.
- 4. G. Jori, "Novel therapeutic modalities based on photosensitized process," EPA Newletter No. 60, pp. 12-18, 1997.
- 5. K.B. Trauner et al., "Photodynamic synovectomy using benzoporphyrin derivative in an antigen-induced arthritis model for rheumatoid arthritis," *Photochemistry and Photobiology* 67, pp. 133-139, 1998.
- 6. G.I. Stables and D.V. Ash, "Photodynamic therapy," Cancer Treatment Reviews 21, pp. 311-323, 1995.

- 7. M.D. Daniel and J.S. Hill, "A history of photodynamic therapy," Aust. N.Z. Journal of Surgery, pp. 340-348, 1991.
- 8. T.J. Dougherty, "Photoradiation therapy II. Cure of animal tumours with haematoporphyrin and light," *Journal of National Cancer Institute* 55, pp. 115-121, 1978.
- 9. T. Takemura, "Mechanism of photodynamic therapy: exploration by photophysicochemical study," *Frontiers of Photobiology*, pp. 503-506, 1993.
- 10. T. Parassasi, "Two photon microscopy of aortic fibers shows proteolysis induced by LDL hydroperoxides," *Free Radicals in Biology and Medicine* **28(11)**, pp. 1589-1597, 2000.
- 11. G. Jori and E. Reddi, "Second generation photosensitizers for the photodynamic therapy of tumours," in *Light in Biology and Medicine*, R.H. Douglas et al., Editors, pp. 253-266, Plenum Press, New York, 1991.
- 12. G.G. Miller, "Preclinical assessment of hypocrellin B and hypocrellin B derivatives as sensitizers for photodynamic therapy of cancer: progress update," *Photochemistry and Photobiology* **65(4)**, pp. 714-722, 1997.
- 13. A. Andreoni, "Tumour photosensitization by chemotherapeutic drugs," Biologia Nr 3, pp. 43-46, 1993.
- 14. R.S. Pandurangi, "Chemistry of bifunctional photoprobes 3: correlation between the efficiency of CH insertion by photolabile chelating agents. First example of photochemical attachment of 99mTc complex with human serum albumin," *Journal of Organic Chemistry* 63, pp. 9019-9030, 1998.
- 15. C.E. Dinerman, "Spectroscopic analysis of azide decomposition products for use in a pyrotechnically initiated carbon dioxide chemical laser," *Report AD780788 (RDTR NO. 269)*, Naval Ammunition Depot, Applied Sciences Department, Crane, Indiana. May 1974.
- 16. E. Atherton, Fluorenylmethoxycarbonyl-polyamide solid phase peptide synthesis: General principles and development, Information Press, Oxford, 1989.
- 17. S.A. Achilefu, Richard B. Dorshow, Joseph E. Bugaj, and Raghavan Rajagopalan, "Novel receptor-targeted fluorescent contrast agents for in vivo imaging of tumors," *Investigative Radiology* 35(8), pp. 479-485, 2000.
- 18. M. deJong, W.A.P. Breeman, W.H. Bakker, P.P.M. Kooij, B.F. Bernard, L.J. Hofland, T.J. Visser, A. Srinivasan, M.A. Schmidt, J.L. Erion, J.E. Bugaj, H.R. Macke, and E.P. Krenning, "Comparison of 111In-labeled somatostatin analogues for tumor scintigraphy and radionuclide therapy," Cancer Research 58, pp. 437-441, 1998.

Proc. SPIE Vol. 4259

132

<sup>\*</sup>rajagopalans@worldnet.att.net; phone 314 878-6119; fax 314 878-2609; 13031 Vinson Court, Maryland Heights, MO 63043; jebugaj@mkg.com; phone 314 654-2000; fax 314 654-7212; http://www.mkg.com; Mallinckrodt Inc., 675 McDonnell Blvd., P.O. Box 5840, St. Louis, MO 63134.

# Dimensions of calcium release domains in frog skeletal muscle fibers

Julio L. Vergara<sup>†</sup>, Marino DiFranco and David Novo

Department of Physiology, UCLA School of Medicine, Los Angeles, CA

# **ABSTRACT**

The spatiotemporal properties of the  $Ca^{2+}$  release process in skeletal muscle fibers were determined using an improved confocal spot detection system. Muscle fibers were loaded with the low affinity fluorescent  $Ca^{2+}$  indicator OGB-5N and localized action potential-induced fluorescence signals were recorded from consecutive locations separated by 200 nm within a single sarcomere. Three-dimensional reconstructions of the  $Ca^{2+}$  transients illustrate the existence of domains of increased fluorescence around  $Ca^{2+}$  release sites in the neighborhood of the T-tubules. We estimated the dimensions of these domains by drawing isochronal curves ( $\Delta F/F$  vs. spot position) and fitting Gaussian profiles to them. It was found that the earliest detectable full-width-at-half-maximum of these profiles was  $0.77 \pm 0.25 \mu m$  and increased rapidly with time to  $1.4 \pm 0.2 \mu m$  at their peak (18 °C). A brief, but statistically significant, delay of  $0.8 \pm 0.42 ms$  was observed between the onset of the fluorescence transients at the Z- and M-lines. Our results are compatible with the possibility that, in response to AP stimulation,  $Ca^{2+}$  is not released exclusively from the junctional region of the sarcoplasmic reticulum, but from a broader expanse of the triadic region.

Keywords: Confocal spot detection, calcium transients, skeletal muscle, calcium domains, excitation-contraction coupling

### 1. INTRODUCTION

A critical step in the excitation-contraction (E-C) coupling process in skeletal muscle is the release of Ca<sup>2+</sup> ions, stored at a high concentration in the lumen of the terminal cisternae (TC) of the sarcoplasmic reticulum (SR), in response to electrical depolarization of the transverse tubular system (T-system)<sup>1-3</sup>. The structures supporting this release phase of E-C coupling are proposed to be the regions of the SR adjacent to the T-tubule, known as T-SR junctions, where Ca<sup>2+</sup> release channels (ryanodine receptor channels, RyR) and voltage sensors (dihydropyridine receptors, DHPRs) are presumed to be linked through protein-protein interactions<sup>4-6</sup>. Under physiological conditions, the electrical signal for Ca<sup>2+</sup> release in the muscle fiber is an action potential (AP) that spreads longitudinally through the sarcolemma and radially through the membranes of the T-system<sup>7-10</sup>.

In frog skeletal muscle fibers, the T-SR junctions are remarkably well aligned with the Z-lines delimiting every sarcomere<sup>1,4,11</sup>; consequently, it is expected that in this preparation action potentials (APs) generate early increases in the Ca<sup>2+</sup> concentration ([Ca<sup>2+</sup>]) at regions of the sarcomere close to the Z-line and smaller and more delayed changes at more remote regions (M-lines). The localization of the sites of Ca<sup>2+</sup> release to the Z-lines was first demonstrated experimentally by Escobar *et al.* (1994)<sup>12</sup> using a spot detection method and fluorescent Ca<sup>2+</sup> indicators. These authors observed that the AP-elicited [Ca<sup>2+</sup>] increase at the M-line was not significantly delayed relative to that at the Z-line (Z-M delay) and proposed that a broad band of the SR may participate in the release process<sup>12</sup>. However, this suggestion has remained questionable since limitations in the spatial resolution of the spot detection method could hinder the visualization of small Z-M delays<sup>13-15</sup>. Thus, the hypothesis that Ca<sup>2+</sup> release is localized to the T-SR junction hinges on the careful measurement of these delays and on whether they can be accounted for by passive Ca<sup>2+</sup> diffusion-reaction mechanisms in the sarcomere. Alternatively, Ca<sup>2+</sup> ions released from one region of the SR may lead to activation of the release of additional Ca<sup>2+</sup> from other regions of the SR through, for example, the positive feedback process known as Ca-induced-Ca<sup>2+</sup>-release<sup>16-18</sup>.

The goal of the experiments described here is to measure the spatiotemporal properties of the [Ca<sup>2+</sup>] changes that occur within a single sarcomere in a frog skeletal muscle fiber following AP stimulation, and to quantitatively assess the magnitude of Z-M delays. We utilized an enhanced spot detection methodology<sup>12,19</sup> in which the spatial resolution is that inherent to a confocal epifluorescence system<sup>20,21</sup>.

<sup>&</sup>lt;sup>†</sup> <u>jvergara@mednet.ucla.edu</u>; phone (310) 825-9307; fax (310) 206-3788; Department of Physiology, UCLA School of Medicine, 10833 LeConte Ave., 53-263 CHS, Los Angeles, CA 90095-1751

### 2. METHODOLOGY

The general methodology and technical improvements of the confocal spot detection system utilized for the experiments presented below will be described extensively elsewhere 19. We provide here a brief account of the major features of the confocal technique inasmuch as they are required to understand the experimental data.

# 2.1 Muscle fiber preparation and electrophysiological methods.

The experimental chamber and muscle fiber dissection and mounting procedures were as previously described<sup>22</sup>. Briefly, segments of cut single fibers from the dorsal head of the semitendinosus muscle from *Rana Catesbeiana* were mounted in an inverted double vaseline-gap chamber. The fibers were stretched to 3.7-4 µm to prevent contraction. Two vaseline seals isolated 3 segments of the fiber. The lateral segments were permeabilized with saponin (100 µg/ml; 1-3 min) to allow for free exchange between the lateral pool's solution and the intracellular milieu of the central segment of the fiber. The central pool was perfused with normal Ringer, whereas the lateral pools contained internal solution (see below). Experiments were performed between 17-21 °C. APs were elicited by supra-threshold current pulses delivered to the muscle fiber through one lateral pool and recorded with a custom made electronic circuit<sup>22</sup>. The membrane potential at the central segment of the fiber was measured as the potential at the central pool minus the potential of lateral pool opposite to that used for current injection. APs were filtered at 10 kHz with an 8-pole Bessel filter (Frequency Devices, Haverhill, MA, USA) and digitized at 25-50 kHz using a PCI-MIO-16XE-10 data acquisition board (National Instruments, Austin, TX).

#### 2.2 Solutions.

Ringer's solution: 114 mM NaCl; 2.5 mM KCl; 10 mM MOPS-Na; 1.8 mM CaCl<sub>2</sub>, 10 mM dextrose. Isotonic high K: 110 mM K<sub>2</sub>SO<sub>4</sub>, 10 mM MOPS. *Internal solution:* 110 mM Aspartate-K; 20 mM MOPS-K: 1 mM MgCl<sub>2</sub>, 5 mM Na<sub>2</sub>-phosphocreatine, 5 mM K<sub>2</sub>-ATP, 100-500 μM EGTA, 0.1 mg/ml Creatine-phosphokinase. The osmolality and pH of the solutions were adjusted to 250 mOsm/kg and 7.0, respectively.

# 2.3 Optical setup and stage scanning system.

The optical system was based on an inverted epifluorescence microscope (Model IM, Zeiss, Oberkochen, Germany). In addition to the standard bright-field configuration, it could operate as a stage scanning confocal or standard fluorescence microscope. In confocal mode, the 488 nm line of an Argon laser (Model 95, Lexel, Freemont, CA, USA) was focused onto a 5 µm pinhole (PH-5, Newport Corporation, Irvine, CA, USA). The pinhole image was projected using a 5x objective through the illumination port of the microscope. A 505DRLP dichroic mirror (Omega Optical, Brattleboro, VT, USA) directed the excitation light to a 100x high NA oil immersion objective (Plan Fluor 100, 1.3 NA, Nikon, Japan) that focused it to a 0.6 µm spot on the preparation. The fluorescence image of the illumination spot was collected with the same lens, passed through a 515 nm long pass emission filter (Omega Optical) and centered on a 50 µm pinhole (04PIP013, Melles Griot, Rochester, NY, USA) used to mask the square active area (200 µm per side) of a PIN photodiode (HR008, United Detector Technology, Hawthorne, CA, USA), which served as the light detector. The photocurrent was amplified using an integrating patch-clamp unit (Axopatch 200B, Axon Instruments, Foster City, CA) and filtered at 2-5 kHz using an 8-pole Bessel filter (Frequency Devices). The optical signal and the AP were acquired simultaneously using the acquisition board described above. A shutter (22510A1S5, Vincent and Associates, Rochester, NY) was used to control the illumination time of the sample.

The experimental chamber and the electronic headstage were mounted on a custom-made microscope stage. Two open-loop motorized drives (860A-2, Newport) were used for coarse movement of the stage in the x- or y-direction (orthogonal to the optical axis of the microscope). In addition, a high-resolution nanotranslator (Model TSE-150, Burleigh Instruments, Inc., Fishers, New York), driven by an inchworm motor with a closed loop integral linear encoder, permitted positioning of the stage along the x-axis with 50 nm resolution. A 6000ULN controller (Burleigh Instruments) was used to drive the inchworm motor under computer control using custom-written software in G-language (Labview, National Instruments). This software was also used to control a stepper motor (Z-Axis1, Prairie Technologies, Waunakee, WI) driving the focusing mechanism of the microscope (z-axis) with 500 nm resolution. In stage scanning confocal mode, the specimen was moved in the x direction while the confocal spot remained stationary and the long axis of the muscle fiber was aligned parallel to the x-axis of the microscope stage. The lateral (x-y) and axial (z) resolution of the confocal system was determined in vitro using 0.1-2.0 μm (diameter) fluorescently labeled latex beads (Fluorospheres, size kit #2, Molecular Probes, Eugene, OR). The beads were attached to a glass coverslip and bathed in water or embedded in 40% glucose, 0.5% agarose in order to mimic the refractive index of the fiber<sup>15,23</sup>. Beads were scanned in the x- and z-directions in 100 and 500 nm steps, respectively. Plots of fluorescence vs. the spot position were fit to Gaussian functions and their full-width-at-half-maximum (FWHM) was used as evaluate the width of the intensity profile. For comparison, the plots of fluorescence of beads of different diameters were normalized to their maxima.

# 2.4 Measurement and analysis of Ca<sup>2+</sup>-dependent fluorescence transients.

The salt form of the  $Ca^{2+}$  indicator Oregon Green 488 BAPTA-5N (OGB-5N) (Molecular Probes) was added at 200-500  $\mu$ M concentrations to the cut ends and allowed to diffuse into the muscle fiber 45-60 minutes prior to optical

measurements being started. Figure 1 illustrates the typical experimental protocol used to acquire localized fluorescence transients in response to a single AP stimulation of the muscle fiber. Figure 1, traces a and b correspond to simultaneously acquired records of the AP and the OGB-5N fluorescence, respectively. Approximately 20 ms after starting the acquisition, and 60 ms before the stimulation of the fiber, the laser shutter was opened to acquire the baseline fluorescence (F<sub>rest</sub>, trace b). The AP elicited a rapid increase in fluorescence to a peak  $\Delta F_{peak}$ , which was followed by a decay to baseline within  $\sim$ 40 ms. Trace c of Figure 1 defines relevant parameters that will be used to define the kinetic features of the Ca2+ transient, expressed in terms of  $\Delta F/F^{24,25}$ . The amplitude of the transient was characterized by its ( $\Delta F/F$ )<sub>peak</sub> value and its specific duration by the full-duration-at-half-maximum (FDHM). The delay time (t<sub>d</sub>) corresponds to the period between the time of stimulus delivery (t = 0) and the initiation of the rising phase of the transient, defined as the first moment when the fluorescence is sustained for 1 ms at 3 standard deviations (SD's) above F<sub>rest</sub>. The rising phase of the transient was characterized by the rise time (rt), defined as interval between the initiation and the peak of the transient. All the kinetic parameters were calculated directly from the sampled data by a custom-made computer program written in Delphi (Borland, Scotts Valley, CA, USA).

To determine the spatial dependence of [Ca<sup>2+</sup>] changes, the illumination spot was initially focused in the z-axis to within 10 µm from the bottom coverslip and on a random location with respect to the fiber's sarcomere structure. Subsequently, individual fluorescent transients elicited by AP stimulation were recorded every 5-10 s from adjacent sites, separated by 100-200 nm, along the x-axis.

a  $\Delta F_{peak}$ b  $F_{rest}$ t=0 50 msc  $\Delta F/F_{peak}$ 1  $\Delta F/F$ 

Figure 1. Confocal detection of fluorescence transients. The action potential (trace a) and the Ca<sup>2+</sup>-dependent OGB-5N fluorescence changes (trace b) were simultaneously recorded when the detection spot was placed at a Z-line. The resting potential and the amplitude of the AP are 100 and 145 mV, respectively. The characteristic parameters of the fluorescence transient (trace c) are:  $t_d = 5$  ms; rt = 4.8 ms; ( $\Delta F/F$ )<sub>peak</sub> = 2.5; FDHM = 21 ms. Experimental conditions: [EGTA]: 100  $\mu$ M; [OGB-5N]: 500  $\mu$ M; temperature: 17°C; sarcomere spacing: 4.3  $\mu$ m.

10 ms

The combination of stretching and the use of exogenous intracellular Ca<sup>2+</sup> buffers (OGB-5N and EGTA) prevented any fiber movement, as evidenced by direct observation under the microscope and the lack of movement artifacts in the optical records.

To estimate the free  $[Ca^{2+}]$  underlying fluorescence transients, we used a deconvolution formula (based on an equilibrium approximation<sup>25</sup>) that requires independent measurements of the maximum and minimum fluorescence of the indicator ( $F_{max}$  and  $F_{min}$ , respectively).  $F_{max}$  was measured *in vivo* at the end of the experiment, as previously described<sup>25</sup>.  $F_{min}$  was assumed to correspond to the resting fluorescence of the fiber since OGB-5N is a  $Ca^{2+}$  indicator with very low affinity ( $K_d = 32 \, \mu M^{26}$ ) and the average resting  $[Ca^{2+}]$  of amphibian muscle fibers is ~100 nM<sup>27</sup>.

# 2.5 T-tubule staining and sarcomere length measurements.

In order to correlate the positional-dependence of the  $Ca^{2+}$  transients with specific structures of the sarcomere, the muscle fibers were stained with the non-permeant fluorescent potentiometric dye di-8-ANEPPS (Molecular Probes), which specifically labels the T-system<sup>10,28</sup>. Experiments involving di-8-ANEPPS were performed using either dual- or single-staining protocols. In the dual staining experiments, the fibers were intracellularly stained with OGB-5N and subsequently externally stained with di-8-ANEPPS (1-10  $\mu$ g/ml in Ringer) for ~30 minutes. Confocal spot measurements were performed as described above in order to localize the  $Ca^{2+}$ -dependent fluorescence transients with respect to the T-tubule fluorescence. In single staining experiments, the fiber was externally perfused for ~30 minutes with 1-10  $\mu$ g/ml di-8-ANEPPS in Ringer solution prior to mounting in the experimental chamber. The fiber was scanned with the confocal spot in 100 or 200 nm steps

and the fluorescence was acquired at every position. Since in these measurements the source of fluorescence (the T-tubule) represents a sub-resolution object 10,29,30, in principle it can be used to test the optical resolution of our microscope *in vivo*.

#### 3. RESULTS

#### 3.1 Evaluation of the spatial resolution of the confocal spot system.

To determine the lateral resolution of our spot detection system, we scanned beads of known sizes along the x-axis and determined the FWHM of their intensity profiles. Two examples of these scans are shown in Figure 2A for beads of 0.2

and 1.0 µm in diameter. It can be observed that the Gaussian fits to the data points for each bead are readily distinguishable, as reflected the significantly different FWHM values of 0.27 and 0.99 µm, respectively. The relationship between FWHM and bead diameter is shown in Figure 2B for a wide range of bead sizes. From this plot it can be deduced that the FWHM provides an accurate experimental measurement of the actual diameter for beads ranging in size between 0.5 and 2.0 µm, as illustrated by the close match between the linear regression and the equality line. However, the FWHM of beads smaller than 0.5 µm deviates from linearity and asymptotically approaches the limit of resolution of the optical system. It should be noted that, although 0.2 and 0.1 µm beads could not be distinguished from each other, they still appeared significantly smaller than 0.5 µm beads (p<0.005). Thus, the FWHM of 0.3 µm obtained with these very small beads represents the minimum fluorescence object that we can resolve, thus defining the lateral (xaxis) resolution of the microscope. A similar trend, but with a much more severe limitation in the resolution, was observed with the same size beads scanned in the zdirection (data not shown). In this case we determined19 that the axial (z-axis) resolution is  $\sim 0.75 \mu m$ , a

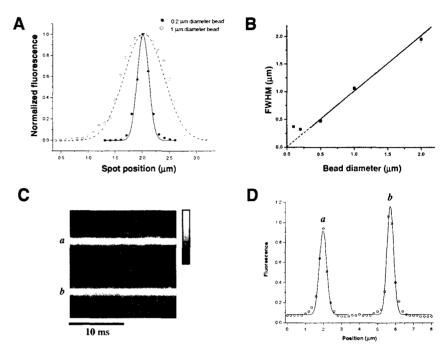


Figure 2: Assessment of the spatial resolution of the confocal system. A: Normalized fluorescence data obtained from x-axis scans of calibration beads. Closed and open circles represent data from 0.2 and 1.0 mm beads, respectively. Solid and dashed lines represent their respective Gaussian fits, with FWHM of 0.27 and 0.99 µm, respectively. B: Comparison of actual bead diameter to FWHM determined from the x-axis scans of several beads of 0.1 (n = 5), 0.2 (n = 16), 0.5 (n = 16), 1.0 (n = 6) and 2.0 (n = 5)  $\mu$ m in diameter. The solid line is a linear regression fit (slope = 1.01, intercept =  $5 \times 10^{-4}$  and r = 0.995) for the 0.5, 1.0 and 2.0 mm beads. The dashed line represents the equality y = x. C: Grayscale image of the T-tubule fluorescence built from traces acquired from 40 adjacent confocal spot positions in a fiber stained with di-8-ANEPPS. The acquisition time was 20 ms per trace, and the records were taken at positions separated by 200 nm. The direction of scan is vertical and time is horizontal. The calibration bar represents 50 grayscale levels, corresponding to fluorescence values from 0 to 1.2, and has a length of 4 µm. D: Time average of the fluorescence intensity in every record used to make up the image in C, plotted as a function of the spot position. The solid lines are Gaussian fits to the fluorescence data, yielding a FWHM of 0.48 and 0.44  $\mu$ m, for peaks a and b respectively.

result that is in good agreement with fluorescence confocal theory for a 1.3 NA objective<sup>20.31</sup>.

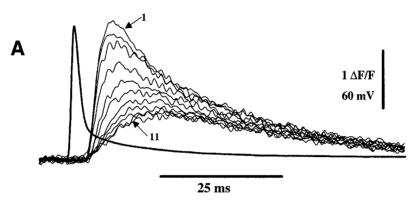
We measured the lateral dimension of T-tubules from fibers stained with di-8-ANEPPS  $^{10,28}$ , under the same conditions in which  $\text{Ca}^{2+}$  detection experiments are performed (see below), and verified if it was close to values obtained in vitro for very small beads. Figure 2C is an image constructed from typical stage-scan fluorescence traces, which depicts the fluorescence intensity (in grayscale levels) as a function of time and spot position. The total distance scanned was 8  $\mu$ m, corresponding to approximately two sarcomeres. The negligible fluorescence observed in the space between two adjacent T-tubules demonstrates that there is no apparent misregistration of sarcomeres above and below the focal plane of the illumination/detection spot. This is further documented in Figure 2D, which corresponds to a time-average fluorescence

profile of the scans in Figure 2C. In this figure, the T-tubules appear as very narrow peaks of fluorescence whose spatial distribution can be readily evaluated quantitatively by fitting to Gaussian functions. It can be seen that the background fluorescence is very low and the ratio between the peak fluorescence intensity and the baseline is ~10. Gaussian fits of pooled data from experiments like that shown in Figures 2C and 2D, yield a mean T-tubule FWHM of  $0.49 \pm 0.08$  (Mean  $\pm$  SD, n = 15).

#### 3.2 Location dependence of OGB-5N fluorescence transients.

Figure 3A shows a family of fluorescence transients obtained by scanning a fiber stained intracellularly with OGB-5N. The length of the scan spanned half a sarcomere from the Z-line (trace 1) to the M-line (trace 11). In agreement with

reports<sup>12,15</sup>. transients recorded at the Zline are significantly faster and larger than recorded at the M-line. The electrical trace shown in Figure 3A is the superposition of the 11 APs that elicited the fluorescence transients. They are identical within 1 mV, excluding variations on the electrical properties of the muscle fiber as a possible cause for the positional dependent variance in the evoked fluorescence transients. As illustrated in the kinetic **Figures** 3A. features of the transients recorded intermediate at locations between the M- and Z-line vary continuously from their extreme values at these positions. The rising phase of the evoked transients becomes slower (rt increases from 5.1 to 13.2 ms) as the recording position moves from the Z- to the M-line. It should be noted that the falling phases of the transients do not cross each other and there is no evidence of secondary release processes following the peak. The onset of the fluorescent transients at the M-line, seen in Figure 3A, is delayed by



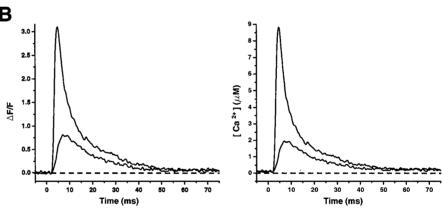


Figure 3. Positional dependence of fluorescence and  $[Ca^{2+}]$  transients detected form a single sarcomere in fiber perfused internally with 500  $\mu$ M OGB-5N. A: Superimposed OGB-5N  $\Delta$ F/F transients (1 through 11) and APs recorded at 10 adjacent spot positions every 200 nm along a line parallel to the fiber axis. Traces 1 and 11 correspond to transients recorded at the Z-line and M-line, respectively. The APs are a superimposition of the 11 APs that evoked the fluorescence transients. Temperature: 17°C; sarcomere spacing: 4.3  $\mu$ m; [EGTA]: 0.1 mM. **B:** Left panel, fluorescence transients ( $\Delta$ F/F) recorded at the Z- and M-lines from another fiber. Right panel, [Ca<sup>2+</sup>] traces calculated using the calibration procedures described in Methods and assuming a [Ca<sup>2+</sup>] baseline of 100 nM. The dashed lines represent the zero level for both plots. Temperature: 19.2°C, sarcomere spacing: 4  $\mu$ m; [EGTA]: 0.5 mM.

<0.7 ms with respect to the Z-line. Data pooled from 36 experiments performed under similar conditions (the [EGTA] was 0.5 mM instead of 0.1 mM and the temperature was 18°C) revealed that the mean Z-M delay, calculated as the average of the differences in  $t_d$  between Z- and M-line  $\Delta F/F$  transients, is only  $0.86 \pm 0.42$  ms. This is a surprisingly small number since, if we consider that the average distance between the Z- and M-lines is ~2  $\mu$ m, it would imply an average rate of spread of Ca<sup>2+</sup> along the sarcomere of ~2.3  $\mu$ m/ms. Finally, the large difference in  $(\Delta F/F)_{peak}$  between the Z- and the M-line fluorescence transients (2.5 vs. 0.8, respectively) demonstrates the existence of large intrasarcomeric Ca<sup>2+</sup> gradients. After ~30 ms these gradients collapse, as evidenced by the fact that the transients fuse together at this time.

In order to estimate the magnitude of the  $[Ca^{2+}]$  changes underlying localized fluorescence transients, we performed the calibration procedures described in Methods. Figure 3B shows a comparison between  $\Delta F/F$  transients recorded at the Z-and M-line (left panel) and their corresponding deconvoluted  $[Ca^{2+}]$  transients (right panel). The peak  $[Ca^{2+}]$  was 8.8  $\mu$ M for the Z-line and 2  $\mu$ M for the M-line. With the caveat that, within the detection spot, OGB-5N is at equilibrium throughout the time course of the transients, the apparent similarity in kinetics between  $[Ca^{2+}]$  and  $\Delta F/F$  transients indicates that the changes in  $[Ca^{2+}]$  were constrained to the linear range of the  $Ca^{2+}$ -dye saturation curve<sup>26</sup>. This is reinforced by the similarity of the ratio between  $(\Delta F/F)_{peak}$  at Z- and M-lines (3.9) and that between peak  $[Ca^{2+}]$  values (4.5). The  $[Ca^{2+}]$  transients shown in Figure 3B were calculated using a ratio between  $F_{max}$  and  $F_{rest}$  of 15, which is similar to the average value obtained in other 4 saturation experiments (15  $\pm$  1, n = 5).

#### 3.3 Dimensions of AP-evoked fluorescence domains.

The concept of a Ca<sup>2+</sup> domain, a localized increase in [Ca<sup>2+</sup>] as a function of space and time, has been introduced to characterize Ca<sup>2+</sup>-entry sites in excitable cells<sup>32,33</sup>. The experimental determination of the properties of AP-evoked

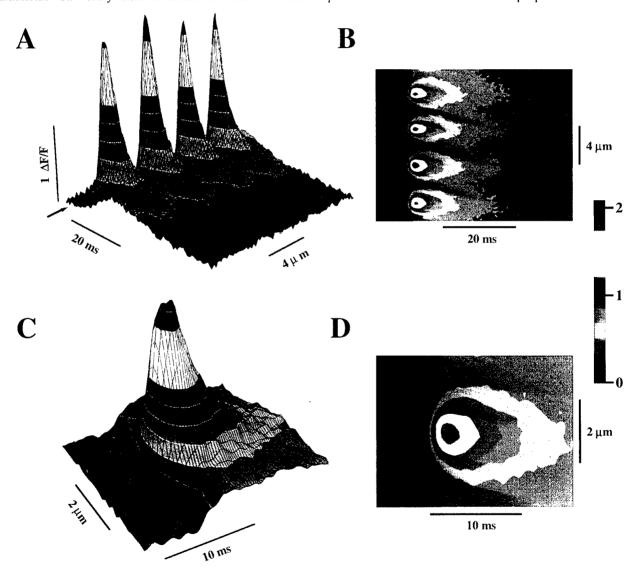


Figure 4.  $Ca^{2+}$ -dependent OGB-5N fluorescence domains. A and B: 3D and contour plots, respectively, of the  $Ca^{2+}$ -dependent OGB-5N fluorescence transients obtained by moving the muscle fiber across a distance of ~ 16  $\mu$ m with a scanning step size of 200 nm. Panels A and B show the same 4 domains. C and D: Enlarged view of the central domain shown in panels A and B. The stimulus time is indicated by an *arrow* in A and by a *red line* in B through D. The calibration bar represents 12 color levels corresponding to  $\Delta F/F$  values ranging from 0 to 2.2. Experimental conditions: [OGB-5N]: 500  $\mu$ M. [EGTA]: 100  $\mu$ M; sarcomere spacing: 4.4  $\mu$ m; temperature: 17°C.

presynaptic  $Ca^{2+}$  microdomains in a neuromuscular junction preparation has been recently accomplished using low affinity  $Ca^{2+}$  indicators and the spot detection method<sup>34</sup>. Analogously, when AP-evoked OGB-5N  $\Delta$ F/F transients are plotted as a function of distance (Figure 4), a clear portrait can be obtained of the topology of the inter- and intra-sarcomeric  $Ca^{2+}$  dynamics. There are defined regions, regularly spaced along the muscle fiber, in which the  $Ca^{2+}$  release originates and where the  $[Ca^{2+}]$  changes are most pronounced. These regions, henceforth termed  $Ca^{2+}$ -release domains, are shown in Figures 4 in different perspectives: 3D plots in panels A and C, and contour maps in panels B and D. Figures 4A and 4B illustrate how the  $Ca^{2+}$  domains originate in the region of the T-tubules for 4 consecutive sarcomeres and how they expand in time along the longitudinal axis of the fiber. The figure also provides evidence that the positional-dependence of the  $\Delta$ F/F transients is preserved identically across several sarcomeres. The contour maps presented in Figures 4B and 4D demonstrate that every individual  $Ca^{2+}$ -release domain is centered symmetrically on the Z-line and that the onset of the  $\Delta$ F/F transient at the M-line

is slightly delayed with respect to the Z-line. The regular pattern of the 4 Ca<sup>2+</sup> domains shown in Figure 4A, and the bilateral symmetry of each of them (Figures 4B and 4D), demonstrate the intrinsic symmetry of the Ca<sup>2+</sup> release regions of the SR with respect to the Z-line. Furthermore, these results prove that, during an x-axis scan, the laser intensity required to obtain each AP-evoked transient did not affect the record obtained from the adjacent position (separated by 200 nm). In other words, the intensity of the excitation light was low enough as to not induce significant photodamage to the fiber. However, this was not always the case and in some occasions domains were skewed in the direction of the scan; these results were discarded.

An important aspect of the overall process of  $Ca^{2+}$  release in skeletal muscle fibers that becomes patent in Figure 4 is the heterogeneous (yet stereotypical)  $Ca^{2+}$  distribution in the myoplasm that persist for ~30 ms after AP stimulation. After this time, although the  $[Ca^{2+}]$  gradients progressively dissipate, the  $[Ca^{2+}]$  remains elevated throughout each sarcomere for another ~40 ms (Figure 4B). Figures 4C and 4D show expanded renditions of the central domain in Figures 4A and 4B to depict in more detail the formation of the  $Ca^{2+}$  domain. It can be observed that the domain becomes first visible ~3 ms after the onset of the AP as a narrow region of increased  $\Delta F/F$  which widens in time, reaching at its peak a FWHM of ~1.4  $\mu$ m.

The spatiotemporal properties of Ca<sup>2+</sup>-release domains give valuable information about features of the physiological Ca<sup>2+</sup> release process, such as the extent and localization of the Ca<sup>2+</sup> sources along the muscle fiber, and the diffusion of Ca<sup>2+</sup> throughout the sarcomeres. We will focus now on the quantitative evaluation of the size and rate of expansion of the domains in order to assess some of these properties. To this end, the domains' isochronal cross sections were fit to Gaussian curves in order to yield their FWHM<sup>34</sup>. A plot of isochronal sections obtained at 5 different times after stimulation during the rising phase of a Ca<sup>2+</sup> domain are shown in Figure 5A. It can be observed that during the 2.4 ms rising phase, the Ca<sup>2+</sup> domain grows in amplitude from a  $\Delta F/F$  of 0.3 to 3, and in width, from a FWHM of 0.85 µm to 1.27 µm. Figure 5B shows another sequence of isochronal sections of the same domain, but in this case taken during its falling phase, that demonstrates the gradient dissipation from a  $(\Delta F/F)_{peak}$  of ~1.9 to ~0.9 with an associated widening from 1.27 to 1.44 µm. As

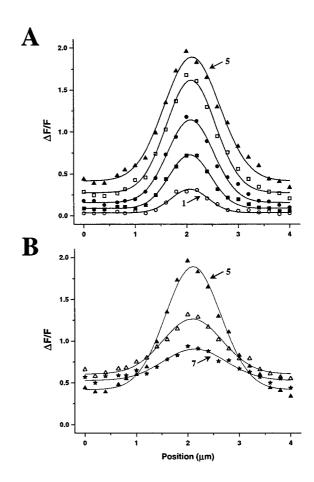


Figure 5. Dimensions of a Ca<sup>2+</sup>-release domain. A: Isochronal  $\Delta$ F/F plots of a single domain obtained at 5 different times after stimulation, from 3.4 ms (trace 1) to 5.8 ms, corresponding the peak time at the Z-line (trace 5). The FWHM of Gaussian curves fitted to the isochronal data (continuous lines) measured 0.85, 0.95, 1.05, 1.11 and 1.27  $\mu$ m for traces 1 to 5, respectively. B: Isochronal plots of the same domain in A, obtained at 2 times after the peak (trace 5). Trace 7 was obtained 11 ms after stimulation. The FWHM of Gaussian curves fitted to the isochronal data (continuous lines) measured 1.27, 1.36, and 1.44  $\mu$ m, for traces 5 to 7, respectively. Experimental conditions: [OGB-5N]: 500  $\mu$ M, [EGTA]: 0.5 mM; sarcomere spacing: 4  $\mu$ m; temperature: 18°C.

expected, all the isochronal spatial profiles are centered and symmetrical about the same position in the sarcomere (Z-line). At 18 °C the peak of the  $Ca^{2^+}$ -release domains occurred 5.4  $\pm$  0.8 ms (n = 38) after the AP stimulation, and 2.52  $\pm$  0.5 ms after the initiation of the transient. At this point the FWHM was  $1.4 \pm 0.2 \,\mu\text{m}$  (n = 28). Obviously, this value of FWHM does not directly reflect on the actual size of the  $Ca^{2^+}$  release since that isochronal measurement was made at a time that allowed for diffusional expansion of the domain. Using an approach analogous to the characterization of  $Ca^{2^+}$  entry sites in presynaptic terminals<sup>34</sup>, we could estimate the size of the  $Ca^{2^+}$  source by measuring the FWHM of the domain at the earliest time that it was detectable. We found for the data in Figure 5 that the expansion of the domain evolved at two different rates: a fast initial process, that occurs between the onset of the  $Ca^{2^+}$  release and the point at which the Z-line transient peaks (~4.8 ms), with an expansion rate of 0.15  $\mu$ m/ms, and a significantly slower process of steady expansion (during which the  $Ca^{2^+}$  gradients dissipate) whose approximated rate is 0.02  $\mu$ m/ms. Following the same approach, in 10 domains in 5 different fibers, the first isochronal cross section that was visible above the noise in fibers perfused with 500  $\mu$ m OGB-5N and 0.5 mM EGTA at ~18 °C, occurred at 3.24  $\pm$  0.56 ms (mean  $\pm$  SD). Remarkably, the mean FWHM of the earliest detectable isochronal cross sections was 0.77  $\pm$  0.25  $\mu$ m. This value is significantly larger than the optical resolution of our optical system as determined by fluorescent bead calibrations and from the FWHM of di-8-ANEPPS labeled T-tubules (Figure 2).

#### 4. DISCUSSION AND CONCLUSIONS

We have described the use of a stage scanning confocal microscope to measure AP-induced intrasarcomeric Ca<sup>2+</sup> transients in amphibian skeletal muscle fibers under physiological conditions. Using this optical setup, we obtained a detailed spatiotemporal portrait of the intrasarcomeric Ca<sup>2+</sup> movements that occur in response to an AP, which will allow us to initiate the quantitative assessment of processes that underlie Ca<sup>2+</sup> release in physiological E-C coupling.

The combination of a low capacitance PIN photodiode and a low noise integrating amplifier made it possible to measure fluorescence changes with a high signal-to-noise (s/n) ratio from a confocal detection volume as small as 0.3 µm diameter in the x-y plane and 0.75 µm in the x-z plane. This high spatial resolution and the use of nanopositioning actuators allowed us to discriminate time-dependent variations in the [Ca<sup>2+</sup>] from positions separated by 100-200 nm. These are significant improvements over the system described previously<sup>12</sup>. What makes the current confocal detection method ideal for studying AP-evoked Ca<sup>2+</sup> release in skeletal muscle fibers is not only its space resolution, which is comparable to other confocal microscopes, but its extremely low noise and the ability to acquire data at up to 50 kHz.

Our confidence in the spatial resolution of the spot detection system, based on extensive *in vitro* bead calibration experiments, was confirmed *in vivo* by staining of the T-tubules with the potentiometric indicator di-8-ANEPPS<sup>10,28</sup>. In this regard, an interesting result was that the FWHM of stained T-tubules, which are known to measure <100 nm in diameter, was significantly larger (0.49  $\pm$  0.08  $\mu$ m) than that of corresponding fluorescent beads of the same size (~0.3  $\mu$ m). Part of this discrepancy could be due to the tortuous geometry of the T-system, which makes it very unlikely to have a single T-tubule within the detection volume of our system. In fact, high magnification electron micrographs of frog skeletal muscle fibers show that the T-tubules wander around the Z-line in an arbitrary manner<sup>4,11,29,30</sup>. It could also be due to the fact that the fiber represents an anisotropic and complex optical media, which could alter the point spread function of the microscope. Nevertheless, a sucrose-agar solution designed to mimic the refractive index of the fiber had no effect on the spatial resolution as determined by in vitro bead calibrations (data not shown).

Although 4  $\mu$ m is not the physiological slack sarcomere length of frog skeletal muscle fibers, stretching doesn't seem to affect significantly the Ca<sup>2+</sup> release process, as evidenced by the large  $(\Delta F/F)_{peak}$  values obtained with OGB-5N at the Z-lines. On the contrary, our results indicate a robust Ca<sup>2+</sup> release, leading to peak [Ca<sup>2+</sup>] changes of ~9  $\mu$ M at the Z-line, and, surprisingly, ~ 2  $\mu$ M at the M-line. Besides not having deleterious effects, stretching affords several advantages for our experimental approach. Firstly, separating simultaneously activated adjacent sources of Ca<sup>2+</sup> release afforded us a larger number of spot positions sampled with our finite probe. Thus, increasing the sarcomere length was equivalent to increasing the lateral spatial resolution of the detection system, and allowed for a more detailed description of intrasarcomeric Ca<sup>2+</sup> movements. In addition, increasing the distance between the Z- and M-lines, favors the detection of Z-M delays. Finally, separating Ca<sup>2+</sup> sources minimizes the effect that adjacent sources have on each other. In other words, the Ca<sup>2+</sup> release domains described in this work closely represent the contribution of individual Ca<sup>2+</sup> release sites to the [Ca<sup>2+</sup>] profiles along the sarcomere, with only small effects arising from neighboring sites.

The characterization of Ca<sup>2+</sup> release domains using the confocal spot detection technique and the sampling protocol described in this work was only possible since the Ca<sup>2+</sup> release is a stereotyped process, both in time and space. Thus, following each AP stimulation, the release of Ca<sup>2+</sup> ions from the SR was repeated identically throughout the muscle fiber. Although, at the global detection level, this repeatability had been well documented previously<sup>25</sup>, our work shows, for the first time, that there is a high similarity between Ca<sup>2+</sup> signals recorded at equivalent positions of the sarcomere for different Ca<sup>2+</sup> release sites (Figure 4). This result indicates that the structures underlying a Ca<sup>2+</sup> release domain at each triad are

extraordinarily similar to each other, and that the activation of the E-C coupling by an AP proceeds in a highly repeatable fashion. Our work also shows for the first time, that at every particular sarcomere location, there is a reproducible Ca<sup>2+</sup> release process in response to every AP. This can be readily inferred from the characteristic bilateral symmetry and periodic distribution of the kinetic parameters for fluorescence transients recorded along a sarcomere. Any significant fluctuation in the Ca<sup>2+</sup> release in response to consecutive stimulations would have resulted in a random pattern.

After the introduction of localized detection methods to study E-C coupling in skeletal muscle 12 subsequent confocal fluorescence studies have been performed primarily using beam scanning (BS) confocal microscopes to investigate the spatiotemporal properties of spontaneous Ca<sup>2+</sup> release events (Ca<sup>2+</sup> sparks). The sparks are localized Ca<sup>2+</sup> release events, which have been proposed to represent elementary processes underlying Ca<sup>2+</sup> release during E-C coupling 35,36. In contrast, in this study we focus on the measurement of localized Ca<sup>2+</sup> domains evoked by the physiological activation of the Ca<sup>2+</sup> release mechanisms by an AP. As such, our work provides valuable reference data challenging the putative physiological role of the Ca<sup>2+</sup> sparks since both phenomena have been studied with comparable spatial resolution. The comparison between the spatiotemporal properties of Ca<sup>2+</sup> sparks and our Ca<sup>2+</sup> domains suggests that if sparks truly represent elementary events in skeletal muscle E-C coupling, their stochastic recruitment to yield an evoked physiological response must be exquisitely synchronized.

In 1994, our laboratory reported that the onset of AP-evoked Ca<sup>2+</sup>-dependent fluorescence signals recorded from skeletal muscle fibers at the M-line was not significantly delayed with respect to those at the Z-line 12. Although in a subsequent publication<sup>13</sup> we noticed that deblurred pulsed laser images of Ca<sup>2+</sup> gradients recorded early after AP stimulation showed some delay between M-line and Z-line fluorescence, and later confirmed the existence of a Z-M delay by improving the confocality of the spot detection system<sup>14</sup>, the issue has remained debatable ever since. Recently, Hollingworth et al. 15 measured localized AP-evoked Ca2+ transients using a BS microscope in intact frog skeletal muscle fibers injected with Fluo-3 and reported the existence of ~1 ms Z-M delay at 22 °C. In this paper we very carefully examined the kinetic properties of Z- and M-line transients using a confocal detection system with a resolution comparable (or slightly better) than these authors', a low affinity Ca<sup>2+</sup> indicator with an improved kinetic response with respect to Fluo-3<sup>37</sup>, and stretched muscle fibers to sarcomere spacings of ~4 µm. Moreover, we used a very stringent criterion to determine the onset time of the fluorescence transients (3 S.D. above baseline, see Methods). Under these conditions, we found Z-M delays to be detectable, but very short  $(0.86 \pm 0.42 \text{ ms at } \sim 18 \,^{\circ}\text{C}, \, p < 0.001)$ . If the increase in dye fluorescence along the sarcomere is visualized as a wavefront advancing from the Z-line towards the M-line, its speed of propagation would be ~2.3 μm/ms. This value is at least an order of magnitude larger than the speed of propagation of Ca<sup>2+</sup> waves (typically in the tens of µm/s) recorded in other biological preparations<sup>38,39</sup>. Moreover, a myofibril model of Ca<sup>2+</sup> diffusion in the sarcomere in which an infinitesimal release site is located at the Z-line, and which includes realistic kinetic binding parameters to myoplasmic proteins, predicts a Z-M delay of at least 3 ms for a half-sarcomere distance of 2 µm<sup>40</sup>. According to Hollingworth et al. 15, the inclusion of mobile Ca<sup>2+</sup> buffers in the model and corrections for distortions due to dye binding to intracellular proteins and misregistration between sarcomeres, leads to predicted Z-M delays of ~1 ms for a half-sarcomere distance of 1.6 um. Nevertheless, this value is still too large to explain ours, considering the larger sarcomere spacing in our measurements. Moreover, we independently demonstrated, from T-tubule staining experiments, that under our experimental conditions the upper limit for the uncertainty in the location of the release sites is 0.49 µm, and we have never observed the severe phase shifts along longitudinal scans that prompted these authors to introduce misregistration corrections. An alternative explanation to account for the short Z-M delays observed experimentally is to assume that a relatively broad band of Ca<sup>2+</sup> release sites (probably spanning both terminal cisternae of the triad) is rapidly engaged after the AP activation<sup>12</sup>. There are two lines of evidence in support of this possibility. Firstly, the presence of extra-junctional RvR Ca<sup>2+</sup> release channels has been demonstrated in the membranes of skeletal muscle SR<sup>41</sup>. Secondly, the surprising results obtained here indicating that the smallest detectable isochronal cross section of Ca<sup>2+</sup> domains has a FWHM of ~0.8 µm. This result cannot be readily explained by limitations in the axial resolution of the detection system since fluorescently stained T-tubules reported significantly narrower FWHM of ~0.5 um. Moreover, our bead calibration experiments demonstrated that the detection system in the x-axis is linearly accurate for objects of dimensions larger than 0.5 µm. It could be argued that the low affinity of OGB-5N might contribute to the large size of the earliest detectable width of the Ca<sup>2+</sup> domain since it could miss relatively small [Ca<sup>2+</sup>] changes occurring early after AP stimulation. However, we have performed control experiments using the high affinity indicator OGB-2<sup>26</sup> and found results similar to those with OGB-5N (data not shown). We are currently investigating the role of mechanisms that might be responsible for the existence of a relatively wide band of Ca<sup>2+</sup> release. We developed a 3D model of the sarcomere that includes localized or delocalized sources of Ca<sup>2+</sup> and takes into account the limitations of our optical detection system, which will be used to test this hypothesis<sup>42</sup>. Also, since the most likely candidate for the recruitment of extraiunctional RvR channels might be a Ca<sup>2+</sup>-induced-Ca<sup>2+</sup>-release mechanism, we are studying the effects of caffeine on localized Ca<sup>2+</sup> domains<sup>43</sup>.

#### **ACKNOWLEDGEMENTS**

This work was supported by the National Institutes of Health/National Institute of Arthritis and Musculoskeletal and Skin Diseases (NIAMS) grant AR-25201.

#### **REFERENCES**

- 1. Huxley, A. F. & Taylor, R. E. "Local activation of striated muscle fibers", J. Physiol. 144, pp. 426-451, 1958.
- 2. Sandow, A. "Excitation-contraction coupling in skeletal muscle", *Pharmacol. Rev.* 17, pp. 265-320, 1965.
- 3. Podolsky, R. J., Hall, T. & Hatchett, S. L. "Identification of oxalate precipitates in striated muscle fibers", *J. Cell Biol.* 44, pp. 699-702, 1970.
- 4. Peachey, L. D. "The sarcoplasmic reticulum and transverse tubules of the frog's sartorius", *Journal of Cell Biology* **25**, pp. 209-231, 1965.
- 5. Tanabe, T., Beam, K. G., Adams, B. A., Niidome, T. & Numa, S. "Regions of the skeletal muscle dihydropyridine receptor critical for excitation-contraction coupling", *Nature* **346**, pp. 567-9, 1990.
- 6. Rios, E., Ma, J. J. & Gonzalez, A. "The mechanical hypothesis of excitation-contraction", *J. Muscle Res. and Cell Mot.* 12, pp. 127-35, 1991.
- 7. Adrian, R. H., Chandler, W. K. & Hodgkin, A. L. "The kinetics of mechanical activation in frog muscle", *J. Physiol.* **204**, pp. 207-30, 1969.
- 8. Adrian, R. H. & Peachey, L. D. "Reconstruction of the action potential of frog sartorius muscle", *J. Physiol.* **235**, pp. 103-31, 1973.
- 9. Vergara, J. & Bezanilla, F. "Fluorescence changes during electrical activity in frog muscle stained with merocyanine", *Nature* **259**, pp. 684-6, 1976.
- 10. Kim, A. M. & Vergara, J. L. "Supercharging accelerates T-tubule membrane potential changes in voltage clamped frog skeletal muscle fibers", *Biophys. J.* **75**, pp. 2098-116, 1998.
- Zampighi, G., Vergara, J. & Ramon, F. "On the connection between the transverse tubules and the plasma membrane in frog semitendinosus skeletal muscle. Are caveolae the mouths of the transverse tubule system?", *J. Cell Biol.* **64**, pp. 734-40, 1975.
- 12. Escobar, A. L., Monck, J. R., Fernandez, J. M. & Vergara, J. L. "Localization of the site of Ca2+ release at the level of a single sarcomere in skeletal muscle fibres", *Nature* **367**, pp. 739-41, 1994.
- 13. Monck, J. R., Robinson, I. M., Escobar, A. L., Vergara, J. L. & Fernandez, J. M. "Pulsed laser imaging of rapid Ca2+ gradients in excitable cells", *Biophys. J.* 67, pp. 505-14, 1994.
- 14. Escobar, A. L., Vergara, J. L., Fernandez, J. & Monck, J. "Excitation-contraction coupling in single sarcomeres of frog skeletal muscle fibres", *J. Muscle Res. and Cell Mot.* 17, pp. 375, 1996.
- 15. Hollingworth, S., Soeller, C., Baylor, S. M. & Cannell, M. B. "Sarcomeric Ca2+ gradients during activation of frog skeletal muscle fibres imaged with confocal and two-photon microscopy", *J. Physiol.* **526**, pp. 551-60, 2000.
- 16. Endo, M., Tanaka, M. & Ogawa, Y. "Calcium induced release of calcium from the sarcoplasmic reticulum of skinned skeletal muscle fibres", *Nature* **228**, pp. 34-6, 1970.
- 17. Ford, L. E. & Podolsky, R. J. "Regenerative calcium release within muscle cells", *Science* 167, pp. 58-9, 1970.
- 18. Fabiato, A. & Fabiato, F. "Contractions induced by a calcium-triggered release of calcium from the sarcoplasmic reticulum of single skinned cardiac cells", *J. Physiol.* **249**, pp. 469-95, 1975.
- 19. DiFranco, M., Novo, D. & Vergara, J. L. "Characterization of the Calcium Release Domains during Excitation-Contraction Coupling in Skeletal Muscle Fibres", (submitted), pp., 2001.
- 20. Castleman, K. Digital Image Processing Prentice Hall, New York, 1979.
- 21. Wilson, T. Confocal Microscopy Academic Press, New York, 1990.
- 22. DiFranco, M. et al. "Inverted double-gap isolation chamber for high-resolution calcium fluorimetry in skeletal muscle fibers", *Pflugers Arch* 438, pp. 412-8, 1999.
- 23. Huxley, A. F. & Niedergerke, R. "Measurement of the striations of isolated muscle fibres with the interference microscope", *Journal of Physiology* **144**, pp. 403-425, 1958.
- 24. Vergara, J., Bezanilla, F. & Salzberg, B. M. "Nile blue fluorescence signals from cut single muscle fibers under voltage or current clamp conditions", *Journal of General Physiology* 72, pp. 775-800, 1978.
- 25. Vergara, J. & DiFranco, M. "Imaging of calcium transients during excitation-contraction coupling in skeletal muscle fibers", *Adv Exp Med Biol* **311**, pp. 227-36, 1992.

- 26. DiGregorio, D. A. & Vergara, J. L. "Localized detection of action potential-induced presynaptic calcium transients at a Xenopus neuromuscular junction", *J Physiol (Lond)* **505**, pp. 585-92, 1997.
- 27. Lopez, J. R., Alamo, L., Caputo, C., DiPolo, R. & Vergara, J. L. "Determination of ionic calcium in frog skeletal muscle fibers", *Biophys J* 43, pp. 1-4, 1983.
- 28. Kim, A. M. & Vergara, J. L. "Fast voltage gating of Ca2+ release in frog skeletal muscle revealed by supercharging pulses", *J Physiol (Lond)* 511, pp. 509-18, 1998.
- 29. Peachey, L. D. "Transverse tubules in excitation-contraction coupling", Fed. Proc. 24, pp. 1124-34, 1965.
- 30. Franzini-Armstrong, C. "Studies of the triad. 3. Structure of the junction in fast twitch fibers", *Tissue and Cell* 4, pp. 469-78, 1972.
- 31. Brakenhoff, G. J., Van Spronsen, A., Van der Voort, H. T. M. & Nanninga, N. "Three-dimensional confocal fluorescence microscopy", *Methods in Cell Biology* **30**, pp. 379-398, 1989.
- 32. Chad, J. E. & Eckert, R. "Calcium domains associated with individual channels can account for anomalous voltage relations of Ca-dependent responses", *Biophysical Journal* 45, pp. 993-9, 1984.
- 33. Augustine, G. J., Charlton, M. P. & Smith, S. J. "Calcium action in synaptic transmitter release", *Annual Review of Neuroscience* **10**, pp. 633-93, 1987.
- 34. DiGregorio, D. A., Peskoff, A. & Vergara, J. L. "Measurement of action potential-induced presynaptic calcium domains at a cultured neuromuscular junction", *Journal of Neurosciences* **19**, pp. 7846-59, 1999.
- 35. Tsugorka, A., Rios, E. & Blatter, L. A. "Imaging elementary events of calcium release in skeletal muscle cells", *Science* **269**, pp. 1723-6, 1995.
- 36. Klein, M. G. et al. "Two mechanisms of quantized calcium release in skeletal muscle", *Nature* 379, pp. 455-8, 1996.
- 37. Escobar, A. L. et al. "Kinetic properties of calcium indicators: rapid transient responses to flash photolysis of DM-nitrophen.", *Pflugers Archiv* **434**, pp. 615-631, 1997.
- 38. Blatter, L. A. & Wier, W. G. "Agonist-induced [Ca2+]i waves and Ca", American Journal of Physiology 263, pp. H576-86, 1992.
- 39. Girard, S. & Clapham, D. "Acceleration of intracellular calcium waves in Xenopus oocytes by calcium influx", *Science* **260**, pp. 229-32, 1993.
- 40. Cannell, B. M. & Allen, D. G. "Model of calcium movements during activation in the sarcomere of the frog skeletal muscle", *Biophysical Journal* 45, pp. 913-925, 1984.
- 41. Dulhunty, A. F., Junankar, P. R. & Stanhope, C. "Extra-junctional ryanodine receptors in the terminal cisternae of mammalian skeletal muscle fibres", *Proceedings of the Royal Society of London. Series B: Biological Sciences* 247, pp. 69-75, 1992.
- 42. Novo, D., DiFranco, M. & Vergara, J. L. "A 3-D cylindrical diffusion-reaction model of a single myofibril to study localized calcium signaling in skeletal muscle", *Proceeding of The Biophysical Society Meeting, Boston, MA*, 2001.
- 43. Vergara, J. L., DiFranco, M. & Novo, D. "Confocal study of the effects of caffeine on calcium release elicited by action potential stimulation", *Proceeding of the Biophysical Society Meeting, Boston, MA*, 2001.

# Fluorescent pH probes, Fluorescent Proteins, and Intrinsic Cellular Fluorochromes are Tools to Study Cytosolic pH (pH<sup>cyt</sup>) in Mammalian Cells.

Gloria M. Martinez<sup>a</sup>, Lauren S. Gollahon<sup>b,c</sup>, Keri Shafer<sup>a</sup>, Sowmini K. Oomman<sup>a</sup>, Christian Busch<sup>a</sup>, and Raul Martínez-Zaguilán<sup>a, c, d</sup>

Departments of <sup>a</sup>Physiology; <sup>b</sup>Biological Sciences, Texas Tech University, and <sup>c</sup>Southwest Cancer Center.

Texas Tech University Health Sciences Center, Lubbock, Texas, 79430 dCorresponding author.

#### **ABSTRACT**

Our understanding of intracellular pH homeostasis in eukaryotic systems has been enhanced since the introduction of carboxyfluorescein diacetate as a useful pH probe more than 20 years ago. BCECF, a derivative of this earlier fluoroprobe has dominated the field. In the past 10 years, SNARF-1 has emerged as an alternative pH probe. Recently, a novel derivative of BCECF, BCPCF has been developed. Green Fluorescent Proteins (GFP's) have also been used recently to monitor pH in a "non invasive manner" in several cell types. Here, we report that human mammary epithelial cells can be transfected with the gene encoding for cyan (CFP), green (GFP), and yellow (YFP), to study cytosolic pH. The novel red fluorescent protein (DsRed) is not sensitive to pH. Multidrug resistance (MDR) has been associated with altered cytosolic pH homeostasis. We show that experimental maneuvers that decrease pH<sup>in</sup> enhance the efficacy of chemotherapeutic drugs. We also show that short pulses of UV-B light elicited acidosis in cells, as evaluated by ratio ion cell imaging, and confocal/spectral imaging microscopy. During the course of these experiments we noticed that cells exhibit intrinsic fluorochromes that can be used to monitor pH in living cells.

Keywords: Intracellular pH, fluoroprobes, multidrug resistance, UV-B light

#### 1. Several Fluorescent pH Probes are Available to Study pH in Living Cells.

Most mammalian cells regulate their intracellular pH via the ubiquitous Na<sup>+</sup>/H<sup>+</sup> exchanger and several HCO3-based H<sup>+</sup>-transporting mechanisms<sup>1,2,3,4,5</sup>. Other exchangers such as K<sup>+</sup>/H<sup>+</sup>-ATPase, Cl'/H<sup>+</sup> co-transport, Ca<sup>2+</sup>/H<sup>+</sup> exchanger have also been found in some specialized cells<sup>5,6,7,8</sup>. Primary H<sup>+</sup>-transporting mechanisms such as H<sup>+</sup>/K<sup>+</sup>-ATPase in the kidney and gastric epithelia, and electrogenic Vacuolar type H<sup>+</sup>-ATPase found in acidic intracellular organelles (e.g., lysosomes, endosomes, Golgi apparatus) have also been implicated in pH regulation<sup>9,10,11</sup>. In addition to these H<sup>+</sup>-transporting systems, some cells with an invasive phenotype, i.e., osteoclasts, macrophages, tumors, and angiogenic microvascular endothelial cells, employ plasmalemmal vacuolar type H<sup>+</sup>-ATPase (pm-V-ATPase) to regulate their intracellular pH<sup>12,13,14,15,16,17,18</sup>. The understanding of the main intracellular pH<sup>in</sup> regulatory mechanisms in eukaryotic cells has rapidly progressed in the past 20 years since the introduction of the first useful pH fluorescent indicator (carboxyfluorescein diacetate)<sup>19</sup>. This probe was used by Thomas and colleagues in 1979 to monitor pH in the cytosol of living cells<sup>19</sup>. This probe was better retained that its parental compound (i.e., carboxy fluorescein), however it had a serious drawback: its pK<sub>a</sub> was low (ca. 6.4) and the pH in most normal cells is ca. 6.6-7.0. The development of a ratiometric pH

fluorescent indicator such as BCECF (pK ca. 7.0) and the ingenious conjugation of the free acid form of the dye to an acetoxy methyl ester (AM) group by Tsien and colleagues in 1982 further revolutionized this field<sup>20,21</sup>. This was partly due to the fact that BCECF has a pK<sub>a</sub> of ca 7.0, that is close to the pH<sup>in</sup> found in many normal cells (ranging from pH 6.7-7.2)<sup>21</sup>. Further, dye loading of cells was enormously facilitated by the introduction of the AM groups that allowed the fluoroprobe to freely permeate through the plasma membrane. Since cells exhibit esterase activities to hydrolyze AM groups, the free acid form of the dye is released in the cytosol by exploiting the cell's own chemistry. This free acid form of the dye is essentially cell impermeant. Thus allowing the pH<sup>in</sup> to be monitored from several minutes to hours. At the present time, BCECF and SNARF-1 are the most widely used pH fluorescent indicators. These dves are considered to be ratiometric<sup>20,21,22,23</sup>. Ion fluorescent indicators with ratiometric properties are highly desirable over non ratiometric probes (i.e., exhibiting single emission/single excitation properties) because in the latter, changes in fluorescence intensity can be due to either changes in dye concentration or to changes in [H<sup>+</sup>]. Since treatment of cells with agonists/antagonists may result in changes in cell volume, it is difficult, if not impossible, to assign changes in fluorescence of non-ratiometric probes to either changes in cell volume, pH, or both. The remarkable characteristic of a fluoroprobe with a ratiometric property is that upon changes in ion concentration, it exhibits increases and decreases in fluorescence intensity at distinct wavelengths whereas an ion insensitive wavelength (isoexcitation or isoemissive), remains unchanged (Fig 1). Thus, by by ratioing the ion sensitive wavelengths it has been assumed that we can obtain a ratio signal that increases with increasing pH in a relatively dye concentration-independent manner. As shown in Fig 1C, SNARF-1 is a good ratiometric dye since it exhibits a distinct ion insensitive wavelength (i.e., isoemissive point) with distinct emission wavelengths which increase and decrease. respectively, as pH increases. In contrast, BCECF does not have a distinct ion insensitive wavelength (isoexcitation point) and upon pH changes, there are large changes in the numerator excitation wavelength at 506 nm whereas the denominator excitation wavelength at 426 nm hardly changes (Fig 1A). Recently, a new pH derivative of BCECF, BCPCF, has been developed by Molecular Probes<sup>24</sup>. The carboxyethyl groups of BCECF have been substituted

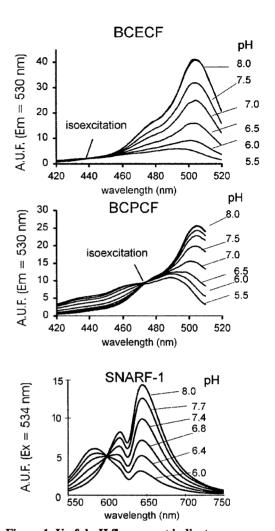


Figure 1. Useful pH fluorescent indicators. Fluorecent ion indicators (free acid form), were dissolved in high  $K^+$  buffer<sup>22</sup> at a final concentration of 2  $\mu$ M dye at the indicated pH values, and their fluorescence excitation and emission spectra were recorded in a spectrofluorometer (DMX-1000) using 4 nm slits and a rhodamine standard.

by methylene groups in BCPCF. This resulted in a shift in the isoexcitation point from 440 nm in BCECF to longer wavelengths in BCPCF (i.e., 454 nm *in vitro* and 468 nm *in situ*; Fig 1B). One of the consequences of this shift is that BCPCF is a better ratiometric dye than BCECF because the dynamic range of BCPCF at the denominator pH sensitive wavelength at 426 nm is larger (Fig 1B). We have performed *in situ* titrations of BCPCF in A7r5 Vascular smooth muscle cells and have determined a pK<sub>a</sub> of ca.7.2, which is larger than the one determined *in vitro* (pK<sub>a</sub> of ca. 7.0). This is in contrast to the behavior of BCECF, where the *in vitro* and *in situ* pK<sub>a</sub> remain unchanged at pK<sub>a</sub> ca 7.0. *in situ* characterization of the dye indicates the usefulness of monitoring the ion sensitive wavelengths of BCPCF since conditions that increase cellular pH resulted in increases and decreases in the fluorescence signals at 495 nm and 426 nm, respectively, when increasing pH. Importantly, the ion insensitive wavelength at 468 nm (isoexcitation) in BCPCF,

remains unchanged (cf., Fig 1B; not shown). This is a significant advantage when compared to BCECF, since the "ion insensitive wavelength" shifts following acid loading experiments, probably due to changes in cell volume (not shown). Because it has long been assumed that ratio corrects for differences in dye concentration, we decided to evaluate this phenomenon. As shown in Fig 2, ratio does not correct for differences in dye concentration in either BCECF or BCPCF, even after corrections for inner filter (Fig 2A and 2B). This complicates the determination of pH<sup>in</sup>, since in vitro titration parameters cannot be used without serious under- or over-estimations of pH values. Furthermore, the dye needs to be calibrated in situ at the end of every experiment, since the  $R_{max}$  and the  $R_{min}$ parameters needed to estimate pHin, vary with dye concentration. It must be emphasized that

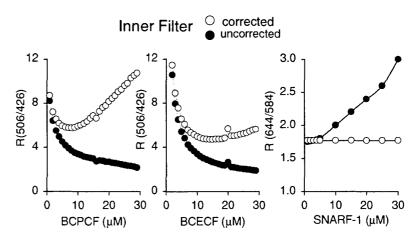


Figure 3. Effect of dye concentration on fluorescence ratios of popular and novel pH fluorescent indicators. Data were corrected for inner filter as described previously<sup>22</sup>.

the range of dye concentrations under which this phenomenon is observed are significant since the dye concentration (following a typical loading of cells with 2  $\mu$ M pH- or Ca<sup>2+</sup>-AM indicators), can result in intracellular accumulation of the free form of the dye as high as 100-500  $\mu$ M. The relevance of this inner filter phenomenon for ion measurements when dealing with single cells requires further evaluation. It can be argued that the pathlength of cells is very small (i.e., a few micrometers), however we must consider that the sensitivity of our detectors is also extremely high. Fortunately, SNARF-1 ratios are unaffected by dye concentration when corrected by inner filter (Fig 2C). Drawbacks of SNARF-1 as a pH indicator are its elevated pK<sub>a</sub> of ca. 7.5 and its poor quantum yield<sup>17,22</sup>. However, an elevated pK<sub>a</sub> is optimal to study tumor cells, since they typically exhibit a more alkaline pH than non-tumor cells<sup>17</sup>. Thus, SNARF-1 is more reliable than either BCECF and BCPCF as a ratiometric pH probe to study tumors.

Altogether, these data emphasize the need for careful selection of the pH fluoroprobe for particular applications, especially if large changes in dye concentration, due to cell volume or dye leakage, are expected.

# 2. Fluorescent Proteins Are Useful Tools to Study pH in Living Cells.

In addition to the fluorescent pH indicators that have been developed and synthesized with a rational chemical approach, recently it has been recognized that there are fluorescent proteins that can be used as pH probes. One of these bioluminescent proteins derived from marine invertebrates is the green fluorescent protein (GFP) from the jellyfish *Aequorea victoria*<sup>25,26</sup>. The GFP has been traditionally used as a non-invasive fluorescent probe for gene expression, protein localization, and intracellular protein targeting. Although the discoverers of GFP did not report its pH sensitivity<sup>27</sup>, recently we and others have evaluated the pH sensitivity<sup>25,26,28,29</sup>. As shown in Fig 3, a mutant of GFP, i.e.,  $\alpha$ GFP, is pH sensitive with a

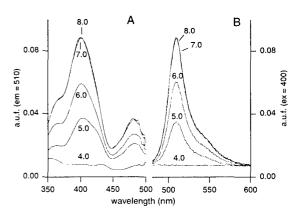


Figure 2. Fluorescence excitation (A) and emission spectra of GFP as a function of pH.  $\alpha$ GFP (1 $\mu$ g/ml) was dissolved in high K<sup>+</sup> buffer <sup>17,22</sup>. The pH was increased stepwise (0.2 pH unit at a time) using aliquots of 1M NaOH. Only selected tracings are presented.

pK<sub>a</sub> of ca. 6.5, that is in agreement with previous reports <sup>25,26</sup>. Other GFP mutants have been developed with distinct pH

sensitivities ranging from 4.5 to 6.5, as well as, with distinct spectral properties<sup>25,26,28</sup>. Recently, a ratiometric GFP has been developed by site directed mutagenesis 28. However, at the present time it is not commercially available. To evaluate the usefulness of GFP as a pH reporter, we have recently transfected cells with GFP and other fluorescent proteins targeted to discrete subcellular compartments, or to the cytosol to monitor their pH environment by using several imaging approaches (data not shown). Specifically, we have transiently transfected vascular smooth muscle cells with GFP targeted to the endoplasmic reticulum (ER)<sup>25,29</sup>. An example of the distribution of GFP-ER is shown in Fig 4. Notice that GFP is excluded from the cell nucleus. The extent of co-localization of GFP and the sarcoplasmic reticulum Ca<sup>2+</sup>-ATPase (SERCA) has been corroborated by immunocytochemistry. In these experiments, simultaneous images of GFP and SERCA (MaB-Texas Red fluorescence) are obtained with a Bio-Rad 1024 MRC confocal microscope. Sectional images (XYZ series) were collected and each section was analyzed on a pixel by pixel basis utilizing LaserSharp software (Bio-Rad, Hercules, CA) to assess colocalization of GFP and SERCA-Texas-Red<sup>29</sup>. These data indicate that we can reliable target GFP to ER compartments (not shown). We are in the process of characterizing the pH environment of these compartments to understand their response to Ca<sup>2+</sup> release/sequestration. We



Figure 4 GFP targeted to the ER in vascular smooth muscle cells. See text for details.

have also recently transfected cells with GFP targeted to the cytosol to be used as a reporter of pH in this compartment. These experiments are being undertaken using spectral imaging microscopy that offers unsurpassed spatial

As mentioned earlier, there are other variants of GFP that could be used as pH probes 30,31,32. As shown in Fig 5, Cyan Fluorescent Protein (CFP) exhibit considerable changes in the excitation and emission spectra in response to changes in pH. Specifically, as pH<sup>in</sup> is increased from 5.0 to 8.0, there is an increase in the fluorescence intensities at the excitation peak (436 nm), as well as, at the emission peak at 475 nm. Interestingly, the fluorescence properties of CFP in situ are similar to those observed in solution (not shown). We have further evaluated the usefulness of CFP as a pH probe in living cells. This is shown in Fig 6, where cells transfected with cytosolic CFP were transferred to the fluorometer cuvette and their excitation and emission spectra were acquired (Fig 6A and 6B). Then, a time course experiment was initiated (Fig 6C). Cells were initially perfused with buffer at pH<sup>ex</sup> 7.0. At the time indicated, perfusate was exchanged for one containing NH<sub>4</sub>Cl. This results in a rapid alkalinization of the cytosol that is similar to that

and spectral resolution.

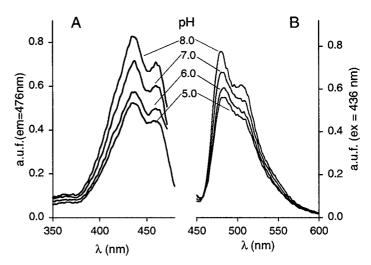


Figure 5. Fluorescence excitation and emission spectra of CFP. This was performed as a function of pH in human mammary ductal carcinoma cells whose pH gradients have been fully collapsed by the use of nigericin, valinomycin and high K<sup>+</sup>.

observed with pH indicators internalized in cells such as BCECF or SNARF-1<sup>6,7,17</sup>. Thereafter, the cells were washed to

remove NH<sub>4</sub>Cl. This resulted in a rapid acidification, followed by a pHin recovery towards baseline. This pHin recovery is due to several pH regulatory systems present in these cells (i.e., Na+/H+ exchanger and HCO<sub>3</sub><sup>-</sup>-based H<sup>+</sup>-transporting mechanisms.

More recently, a red fluorescent protein was isolated from a non-bioluminescent anthozoan species<sup>33</sup>. The rationale for searching for alternatives to GFP and its multiple variants was based on the knowledge that in the phylogenetic scale, earlier forms of non-bioluminescent proteins may have evolved. Indeed, Matz et al.<sup>33</sup> identified several novel proteins capable of emitting fluorescence in the yellow and red part of the spectrum, demonstrating that GFP-like molecules are not always functionally linked to bioluminescence. The characterization of the red fluorescent proteins (DsRed) in terms of pH sensitivity has not been fully evaluated. We therefore investigated whether, in analogy to GFP and its variants, DsRed

cells whose pH gradients have been fully collapsed by preincubation in high K<sup>+</sup> buffers containing nigericin and valinomycin, at determined pH values (Fig 6). From prior experiments, we know that these conditions fully collapse their pH gradients<sup>17,22</sup>. The salient characteristics of DsRed are the peaks at 585 nm and at 650 nm in the excitation and emission spectra, respectively (Fig 7). Importantly, as shown in Fig 7. DsRed is not affected by pH in the range of 5.0 to 9.0. We have not yet evaluated, the pH sensitivity of DsRed at pH values outside this range. This is needed, since there are subcellular compartments with pH values in the pH range of 2.0-5.0, such as the lysosomes. These studies are currently under way in our laboratory. The relevance of our current findings regarding the lack of pH sensitivity of DsRed within the pH range of 5.0-9.0 is that, unlike the GFP and its variants that exhibit various degrees of pH sensitivity, DsRed is not pH sensitive. Furthermore, if it is shown that DsRed is not affected by pH within a physiological range encompassing the pH of organelles such as lysosomes (pH 2-5) to mitochondria (pH ca. 8.0), the use of DsRed should significantly improve GFP, CFP, and YFP, since the changes in their fluorescence could be due to real changes in the levels of protein expression, or to pH changes. Moreover, DsRed can excitation (A) nor the emission (B) spectra. also be used in conjunction with GFP and/or some of its

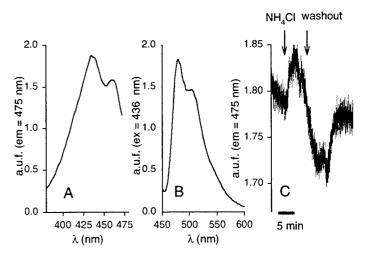


Figure 6. CFP is a useful tool to study cytosolic pH. Human mammary ductal carcinoma cells were used to assess the utility of CFP as an indicator of pH. (A) Excitation spectra, (B) emission spectra, and (C) NH<sub>4</sub>Cl experiment to show increases and decreases in pH<sup>in</sup> (see text for details).

may exhibit pH sensitivity. To do this, human breast cancer cells were transfected with the gene encoding for DsRed (pDsRed1-N1), that was driven by the CMV promoter vector, and their fluorescence properties in situ were evaluated in

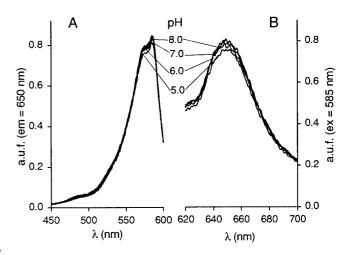


Figure 7. DsRed is not affected by pH. Human mammary ductal carcinoma cells were stably transfected with pDsRed-1-N1 and their pH gradients were fully collapsed with nigericine, valinomycin and high K<sup>+</sup>. Note that pH does not alter the

variants to perform ratiometric pH measurements. This, of course, will require careful consideration of the levels of expression of these probes, as well as knowledge of the subcellular distribution of these proteins. Fluorescence resonance energy transfer should also be considered when performing these type of experiments<sup>34,35</sup>. Fortunately, the previous experience with other ion indicators when used in combination with multiple fluoroprobes should facilitate the judicious selection of fluorescent proteins when co-expressed in the same cellular compartments, or in distinct compartments<sup>23,36</sup>.

## 3. Altered pH Homeostasis is Observed in Multidrug Resistance.

A major barrier for the effective treatment of cancer is multi-drug resistance (MDR) by tumor cells<sup>37,38</sup>. While some mechanisms of resistance allow cells to survive exposure to a single agent, the phenomenon of MDR confers upon cells the ability to withstand exposure to lethal doses of many structurally unrelated antineoplastic agents. Drugs commonly involved in the MDR phenotype are generally natural products or their derivatives. Some of the natural products include anthracyclines, vinca alkaloids, epidophyllotoxins, and actinomycin D<sup>38</sup>. Anthracycline derivatives include mitoxantrone and doxorubicin. Paclitaxel is a novel chemotherapeutic agent derived from the bark of the Western Yew tree<sup>39</sup>. It has been used successfully against ovarian carcinoma and breast cancer. Unfortunately, tumor cells also have developed MDR via classical (i.e. involving overexpression of the multidrug transport P-gp) and non classical mechanisms (i.e., involving non P-gp mechanisms)<sup>37,38,39,40</sup>. A common feature of MDR cells is a net decrease in the intracellular accumulation of drugs. Alterations in tubulin and microtubules following development of resistance to paclitaxel have also been demonstrated in several MDR cell lines<sup>40</sup>. Alterations in

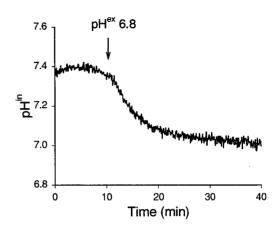


Figure 8. Acidic extracellular pH decreases pH<sup>in</sup> in human breast cancer cells. Cells were loaded with SNARF-1 and their fluorescence monitored as described previously. Perfusate was initiated at a pH<sup>ex</sup> = 7.4. At the time indicated by the arrow, perfusate was exchanged to pH<sup>ex</sup> = 6.8 (see text for details).

intracellular pH (PHin) homeostasis have also been implicated in MDR. For instance, it has been reported that MDR cells exhibit either similar or more alkaline pHin than their sensitive counterparts<sup>37,41</sup>. It is acknowledged that primary transport mechanisms are essential for maintenance of gradients and to energize secondary transporters. We therefore hypothesize that functional expression of a primary transport mechanism such as pmV-ATPase may serve to energize drug extrusion as a secondary phenomenon. Indeed, we have observed that V-H<sup>+</sup>-ATPase expression represents a non-classical mechanism of MDR in several types of human cancers, including: breast cancer, ovarian and uterine sarcoma cells rendered resistant by continuous gradual exposure to several chemotherapeutic drugs, including doxorubicin, mitoxanthrone, and paclitaxel<sup>38</sup>. We further hypothesize that suppression of this pump's activity or exposure of MDR cells to acidic pH<sup>ex</sup> to elicit cytosolic acidification, should sensitizes MDR cells to chemotherapeutic drugs. Our preliminary data indicate that 50 nM bafilomycin A<sub>1</sub> pre-treatment for 2 hrs enhances the cytotoxic effects of paclitaxel by ca. 2-3 fold when compared to untreated controls (Fig 7A). The selected concentration of bafilomycin effectively block V-H<sup>+</sup>-ATPase and affects pH<sup>in</sup> regulation<sup>11,17</sup>. Because it is known that decreasing pH<sup>ex</sup> can decrease pH<sup>in</sup> in most cell types, we evaluated whether preincubation of MDR cells at a mildly acidic pHex = 6.8 for 2 hrs would sensitize cells to chemotherapeutic drugs. This maneuver decreases their resistance to several unrelated chemotherapeutic drugs by ca. 3-5 fold when compared to cells maintained under control conditions (i.e.,  $pH^{ex} = 7.4$ ). The magnitude of the  $pH^{in}$  decrease elicited by exposure of cells to acidic pHex of 6.8 was ca. 0.4 pH unit (Fig 8). The kinetics of the pHin decrease following exposure to a mildly acidic pHex are however slow  $(t_{1/2} = 8-12 \text{ min})$ . Interestingly, this maneuver was more efficient than blockade of V-H<sup>+</sup>-ATPase by bafilomycin A<sub>1</sub>. Albeit the mechanisms responsible for conferring the enhanced sensitivity of MDR cells to chemotherapeutic drugs by acidic pHex are not clear, it is possible that these different effects may be related to different targets of action. Specifically, decreasing pHex may have had an effect on more than one pHin regulatory system involved in MDR such as the Na<sup>+</sup>/H<sup>+</sup> exchanger and/or HCO<sub>3</sub><sup>-</sup>-based H<sup>+</sup>-transporting mechanism, whereas bafilomycin treatment affects only V-H<sup>+</sup>-ATPase, hence its lower effect as a chemosensitizer. However, the treatment of MDR cells with

inhibitors of the Na<sup>+</sup>/H<sup>+</sup> exchanger (e.g. amiloride derivatives) or anion transport (i.e., stilbene derivatives) does not correlate with the degree of reversal of the MDR phenotype nor increases the efficacy of several chemotherapeutic drugs<sup>42,43</sup>. A simplistic model to explain MDR is based on the observation that most chemotherapeutic drugs are weak bases with an alkaline acid dissociation constant. As such, these drugs like to partition and remain in the more acidic extracellular environment that is prevalent in most tumors, thus not able to concentrate inside the cell to exert their cytotoxic effects<sup>43</sup>. Although such a model might be attractive to explain MDR in those cases of drugs with alkaline pH, it does not explain however those cases where the drugs have a more complex structure such as paclitaxel, that has both acidic and basic domains<sup>44</sup>. Recent work has indicated an important role of acidic pHin on apoptosis<sup>45</sup>. Regardless of the mechanism of action, our data suggest that acute acidosis may enhance the efficacy of chemotherapeutic drugs.

# 4. Experiments at the Single Cell Level Indicate that Ultraviolet (UV-B) Light Elicits Cytosolic Acidosis.

Our earlier experiments in multidrug resistance indicated that acidic pH enhances the efficacy of chemotherapeutic drugs. Unfortunately, for this approach to be successful in the clinic, it will require that one could elicit intracellular acidosis within a shorter timeframe than that elicited by acute exposure to acidic pH<sup>ex</sup>. It will also require that the acidosis be delivered at the target site. Earlier studies have indicated that wavelengths in the range of 280 nm - 320 nm (known as UV-B light), are responsible for the harmful effects associated with UV light exposure, i.e., sunburns, skin cancer, DNA mutation. The latter effect of UV on DNA has been studied extensively<sup>46</sup>. However, evidence is accumulating that ultraviolet light (UV) can also affect cytoplasmic and membrane structures. It has been

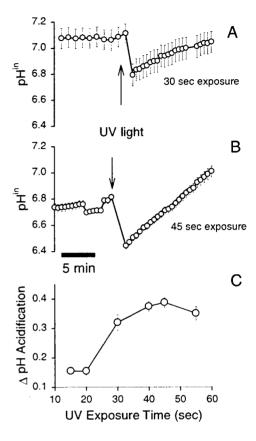


Figure 9. UV light exposure elicit cytosolic acidosis in human breast cancer cells. Cells were loaded with 2  $\mu$ M BCPCF(AM) and their fluorescence ratios were recorded and converted to pH values as described previously (see text for details).

shown that UV can directly affect cytoplasmic transcription factors, kinases associated with the cellular membrane and even membrane receptors<sup>47</sup>. Because it is known that acidic pH is clastogenic and it can cause DNA fragmentation, thereby increasing the probability of the rate of mutation, we decided to investigate whether short pulses of UV exposure may elicit intracellular acidosis that could be useful in chemotherapy. In these experiments, metastatic breast cancer cells (MDA-MB231) grown onto 25 mm round coverslips were loaded with BCPCF-AM and the fluorescence was monitored using a cell imaging system. The imaging system consists of the following: A high speed filter changer (lambda DG4; Sutter Instruments Co, Novato, CA) to rapidly change excitation filters (440 nm and 505 nm); a quartz fiber optic to deliver the light. Signal was collected at an emission of 530 nm, using a frame transfer charged coupled device (CCD) camera coupled to an intensifier (Princeton Instruments Intensifier Pentamax, ADC 5 MHZ). Cells were imaged with a inverted microscope (Olympus IX-70) using a 60x immersion oil objective (1.4 N.A.). In this imaging system, the excitation filters can be changed as fast as 1.5 msec. For these experiments, however, we used longer integration times (i.e., 100 msec exposure). Images were analyzed using Meta Imaging Systems software (ver 4.5; Universal Imaging Corporation, West Chester, PA). Cells loaded with BCPCF were transferred to the microscope cell chamber (PDMI-2, Medical Systems Corp. Greenvale, NY) and maintained at 37°C on the microscope stage. in situ calibration was performed at the end of every experiment. Cells were continuously perfused at 3.0 ml per min, and steady state pHin was monitored to obtain baseline (Fig 9). At the time indicated by the arrow, a short UV light pulse derived from the Xenon arc lamp (175 W) housed in the lambda DG4 (no excitation filters) was delivered to the cells. The light was reflected using a

dichroic mirror (290 nm-330 nm). As shown in Fig 9A and 9B, short pulses of UV light resulted in rapid acidosis. Because the dynamics of this experiment do not allow us to obtain rapid kinetics (since the UV light was shined onto the cells using a dichroic filter that was changed manually), we cannot determine the exact kinetics. Nevertheless, these data indicate that the decrease in pH<sup>in</sup> following UV exposure is immediate, and the magnitude of the acidosis is dependent on the length of the exposure, reaching a maximum of ca. 0.4 pH unit at 40 sec (Fig 9C). The magnitude of this acidification is similar to

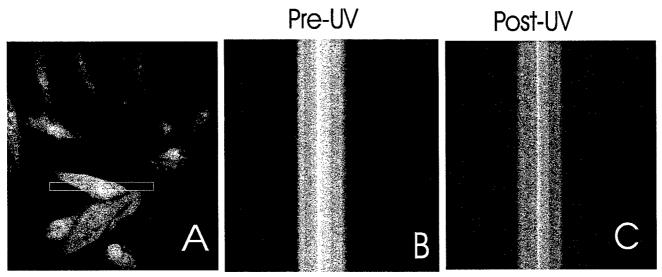
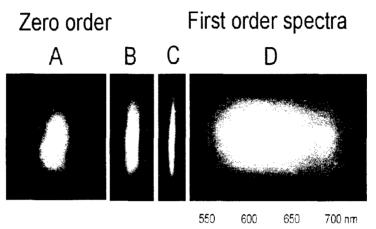


Figure 10 Line scanning confocal microscopy reveals that UV exposure of breast cancer cells elicit cytosolic acidifications. Cells were grown on round glass coverslips (25 mm). At sub-confluence they were loaded with SNARF-1, as described previously. Cells were transferred to the microscope cell chamber (PDMI-2, Medical Systems Corp. Greenvale, NY) and maintained at 37 °C on the microscope stage. Cells were continuously superfused with buffer. (A) Ratio image of a single cell. The white box indicates the region from which the line scan was obtained. (B) Line scanning of the region identified in (A) while cell was superfused with buffer to obtain baseline pH. (C) cells were exposed to 30 sec UV exposure using a Hg arc lamp (100 W) and the light was delivered using a dichroic filter (290-320 nm) while the ratio fluorescence image of SNARF-1 was continuously acquired. Notice that there are pH gradients from leading (left) to lagging (right) edge and that the fluorescence ratio i.e., intensity in the image, decreases after UV exposure (cf., Fig C). From in situ calibration of SNARF-1 at the end of the experiment, we have estimated that the pH magnitude of the cytosolic acidification is ca. 0.8 pH unit.

the one elicited by preincubating cells at acidic  $pH^{ex} = 6.8$ . This is therefore a significant improvement over our earlier approach since the kinetics of the acidosis is at least 2 orders of magnitude faster. We have determined that the amount of UV light delivered to the cells by this approach corresponds to 17.6 mJ and 26.4 mJ for a 30 and 45 sec exposure, respectively. The observation that UV exposure elicited a rapid acidification has been corroborated with line scanning confocal microscopy that offers unsurpassed temporal resolution. In these experiments, a cell can be scanned as fast as 2 msec from leading to lagging edge. As shown in Fig 10, these data indicate that UV elicits acidosis of ca. 0.6-1.0 pH unit, as determined from *in situ* titration performed at the end of the experiment.

The cytosolic acidosis following UV exposure in our previous experiments could be due to many different effects of UV light. We also noticed that UV exposure elicited dye-bleaching in both BCECF and SNARF-1 loaded cells. Thus, the observed phenomenon (i.e., decreases in BCPCF fluorescence signal and ratios) following UV exposure could be due to an artifact because the dye concentration was altered (vide supra). We therefore decided to use an alternative approach that employs monitoring the full spectrum of the pH indicator and the changes in spectral shape, as opposed to monitoring only changes in intensity (and ratios). This approach is known as spectral imaging microscopy. This technique allows measurements of ions in single cells, and in discrete subcellular regions <sup>23,36</sup>. This technique has proved to be superior to confocal microscopy and the previously described ratiometric approach, in that it allowed us to do longer experiments, perform in situ titrations, and simultaneously collect data from at least sixteen discrete subcellular regions. Although we

sacrificed temporal resolution (e.g., spectra from leading to lagging edge of a cell can be obtained in as little as 2 msec, but the refreshing rate of this CCD is ca. 1 sec), the improved spectral resolution and less damaging effects on cells have allowed us to better quantify differences in pH in discrete cellular regions. The fluorescence signal was evaluated using a spectral imaging microscope comprised of the following elements: A fluorescence inverted microscope (Olympus IX-70 with a 60x objective, N.A. 1.4). A 6.7 eyepiece was used to image the cell through the side port of the microscope onto the input slit of a grating monochromator (Chromex 250 IS/SM spectrograph, Albuquerque NM). The spectral output from the grating was imaged onto a liquid cooled CCD camera (Photometrics, Mod CH350, Tucson, AZ) equipped with a 512x512 element (27 μm<sup>2</sup>/pixel) imaging chip. These values are binned to obtain higher signal/noise since the fluorescence signal emitted from a single cell loaded with a pH indicator is focused onto the input slit of a monochromator (i.e. spectrograph) to diffract the light into its frequency components. Since spatial information is obtained along the length of the entrance slit (Fig 11), a single cell can be aligned so the spectra are acquired from unique subcellular locations (i.e. leading to lagging edge in invasive and metastatic cells). The optical filters were as follows: 488 nm narrow bandpass filter; 550 long bandpass dichroic. In the case of MB-231 cells (Fig 11), we find that at steady-state, pHin is more alkaline at the leading (pH 7.2) than at the lagging (pH 7.0) edge by ca.  $0.21 \pm$ 



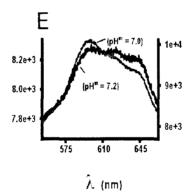


Figure 11. Spectral imaging microscopy to study pH<sup>in</sup> in discrete subcellular regions of the cell. Human breast cancer (MDA-MB235) cells were grown on glass coverslips to subconfluence and loaded with SNARF-1. (A) A single cell is aligned onto the entrance slit (2.0 mm) of the spectrograph, allowing identification of its leading and lagging edge (bottom and top of the cell, respectively). (B) Slit width is decreased (0.5 mm) to allow for increased spatial resolution and increased signal/noise ratio. (C) Final slit width is 0.2 mm. (D) Emission filters are removed and the fluorescence spectra are collected and de-convoluted from individual tracks. Notice that we can collect data from up to 54 tracks corresponding to distinct cellular regions from leading to lagging edge of the cell. (E) The emission spectra are collected and recorded from two distinct tracks in the cell corresponding to the leading and lagging edge. Note that the dye concentration (y axis) is larger in the lagging than at the leading edge, however, the spectral shape indicates that the pH is more alkaline at the leading than at the lagging edge (from *in situ* titrations performed in discrete cellular regions (not shown)

0.07 pH unit. With this set-up, we demonstrated that UV exposure elicits large cytosolic acidifications (0.6 to 1.0 pH unit;

Fig 12). The magnitude of this effect is dependent on the length of the UV exposure. The fact that larger cytosolic acidifications are observed with this approach than with the confocal laser scanning microscope is due to the use of Hg lamp which is a more powerful energy source than the Xenon arc lamp at these wavelengths (Fig 12 C).

#### 5. Cells Exhibit Intrinsic Fluorochromes That Are Sensitive to pH.

During the course of our experiments employing UV exposure, we noticed that cells exhibited autofluorescence that was distinct from the well recognized fluorescence due to NADH, FADH <sup>48</sup>. It is possible that this autofluorescence may be due to amino acid side chains of proteins (e.g., tryptophan, tyrosines),

although their pK, values are typically acidic. Although the nature of the fluorochrome is not known at the present time, it is interesting to note that it exhibits sensitivity to pH, since there is a decrease in the fluorescence excitation signal at 292 nm with increasing pH from 4.5 to 7.7. The emission spectra also changes since the fluorescence emission signal at 340 nm decreases with increasing pH. The small shoulder at ca. 500 nm in the fluorescence emission signal probably derives from the glass coverslips, and could be avoided with the use of quartz coverslips. We use the fluorescence signal at ca. 434 nm as a constant coverslip background to ratio the signal at 340 nm to 434 nm. As is apparent from both the excitation and the emission spectra, the inherent fluorochrome is not sensitive beyond pH > 7.5 due to its acidic pK<sub>a</sub> (ca. 6.5). This limits the use of this approach to cells with acidic pH. However, most tumor cells exhibit pH values > 7.2 whereas most normal cells exhibit pH values > 6.9 and < 7.2. Because the changes in fluorescence between this range of pH values is discrete, this may limit the potential use of these fluorochromes to discriminate between normal and tumor tissue pH. However, recently, our laboratory has shown that the pH differences in discrete cellular domains, as well as in pH oscillations due to intrinsic pH gradients (i.e., leading and lagging edge in invasive cells), can be as large as 0.4-0.5 pH unit. Further investigation is needed to address this issue at the cellular level. A more serious problem that impairs the use of intrinsic fluorochromes for monitoring pH is the difficulty of efficient excitation at 292 nm in most optical system. Multiphoton confocal microscopy may alleviate this problem because of the use of longer wavelengths for excitation. Nevertheless these and many other potential complications, these data indicate that inherent fluorochromes may be useful in understanding pH regulation and the progression of disease and or normal physiological changes.

To obtain some insight as to the subcellular location of the autofluorescence that is pH sensitive, we employed Mn $^{2+}$ , a known quencher $^{49}$ . As shown in Fig 14, Mn $^{2+}$  addition efficiently quenches the fluorescence in a concentration dependent manner. In these experiments, cells were grown on coverslips at confluency and then washed 3 times with perfusion media, and transferred to the fluorometer cuvette. Cells were perfused continuously at a rate of 3.0 ml/min and the initial excitation and emission spectra were taken (shown as "0 Mn $^{2+}$ ). After 5 min, perfusate was exchanged for one containing 1  $\mu M$  Mn $^{2+}$  and fluorescence excitation and emission spectra were taken after 1 min. This

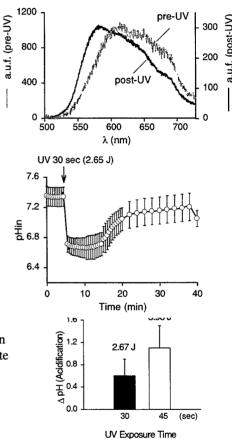


Figure 12. Exposure of human breast cancer cells to UV light. The extent of cytosolic acidosis was determined by spectral imaging microscopy. Cells were loaded with SNARF-1 for these experiments (see text for details).

process was repeated as necessary until  $10 \,\mu\text{M} \,\text{Mm}^{2+}$  was reached. Noticed that the fluorescence signals decrease as  $\text{Mn}^{2+}$  concentration increases in a concentration dependent fashion, suggesting that some type of quenching is occurring. We estimated the Stern-Volmer constant for this type of quenching by fitting the data into the following equation:

$$F_0/F = (1 + Kq) * [Q]$$
 eqn 1.

Where  $F_0$  represents the autofluorescence signal at the peak (either 340 nm for emission spectra or 286 nm for

excitation spectra) in the absence of the quencher, [O], and F is the fluorescence at the peak (either 340 nm for emission spectra or 286 nm for excitation spectra) in the presence of the quencher. From these experiments we have estimated the Stern Volmer constants (10<sup>5</sup> M<sup>-1</sup>) for the emission (Kq = 5.4) and excitation (Kq = 5.1) spectra. Albeit these experiments do not allow us to distinguish whether dynamic or static quenching (or a combination off both is occurring), these data indicate that the autofluorescence signal (i.e., inherent fluorochrome[s]) are readily accessible to the quencher. We have employed detergents such as digitonin 50 uM, to permeabilize the cells. This approach is used to release typical fluorescent ion indicators with a molecular weight of ca. 1,000 from the cytosol. These experiments have indicated that ca. 95% of the fluorescence signal remains after digitonir permeabilization of cells. We take this as an indication that the fluorochrome(s)

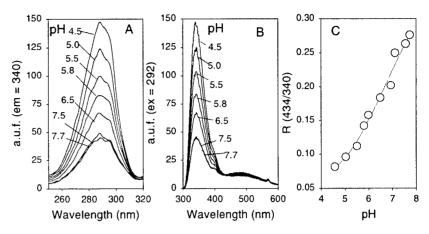


Figure 13. Human breast cancer cells (MDA-MB231) exhibit inherent fluorochromes that are pH sensitive. Cells grown onto coverslips at confluency were transferred to the fluorometer cuvette and their excitation (A) and emission (B) spectra were monitored. Collapsing of pH gradients was performed by exposing cells to High K+ buffer containing nigericin and valinomycin to perform in situ ne titrations (C).

responsible for this autofluorescence either has a molecular weight > 1,000 or that it is immobilized in the cytosol (i.e, bound to proteins). Further experiments are needed to evaluate these possibilities.

#### **ACKNOWLEDGMENTS**

The authors would like to acknowledge Mr. David Bennet for his technical assistance. This work is supported by AHA (National) 9750558N, ACS RPG-00-035-01CNE, and NIH(RO1-HL65695-01) to RMZ.

#### REFERENCES

- 1. A. Roos and W.F. Boron, "Intracellular pH," *Physiol Rev*, 61, pp. 296-434, 1981.
- 2. R. J. Gillies, R. Martínez-Zaguilán, E.P. Peterson, and R. Perona, "Role of intracellular pH in mammalian cell proliferation," *Cell Physiol Biochem*, 2, pp. 159-179, 1992.
- 3. S. Grinstein, O.D. Rotstein, M.J. Mason, "Na<sup>+</sup>/H<sup>+</sup> exchange and growth factor induced cytosolic pH changes: Role in cellular proliferation," *Biochim Biophys Acta*, 988, pp. 73-97, 1989.
- 4. W.F. Boron, "Intracellular pH regulation in epithelial cells," *Annu Rev Physiol*, 48, pp. 377-388, 1986.
- 5. R.J. Gillies and R. Martínez-Zaguilán, "Regulation of intracellular pH in Balb/c-3T3 cells: Bicarbonate raises pH via NaHCO<sub>3</sub>/HCl exchange and attenuates the activation of Na<sup>+</sup>-H<sup>+</sup> exchange by serum," *J Biol Chem*, 266, pp. 1551-1556, 1990.

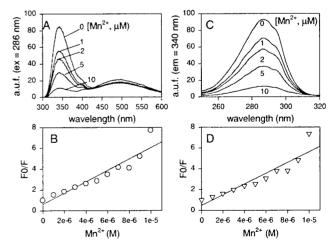


Figure 14. Mn<sup>2+</sup> efficiently quenches intrinsic flurorochromes in human breast cancer cells (see text for details).

- 6. Sanchez-Armass, R. Martínez-Zaguilán, G.M. Martinez, and R.J. Gillies, "Regulation of pH in rat brain synaptosomes. I. Role of sodium, bicarbonate, and potassium," *J.Neurophysiol.* 71, pp. 2236-2248, 1994.
- 7. Martínez-Zaguilán R., Gillies R.J., and Sanchez-Armass S. "Regulation of pH in rat brain synaptosomes. II. Role of Cl.". *J.Neurophysiol.* 71:2249-2257, 1994.
- 8. J. Mendlein and G. Sachs, "Interaction of a K<sup>+</sup> competitive inhibitor, a substituted imidazo[1,2α] pyridine, with phospho and dephosphoenzyme forms of H<sup>+</sup>-K<sup>+</sup>-ATPase," *J Biol Chem*, 265, pp. 20823-20826, 1990.
- 9. M. Forgac, "Structure and function of vacuolar class of ATP-driven proton pumps. *Physiol Rev*, 69, pp. 765-796, 1989.
- 10. I. Mellman. "Endocytosis and molecular sorting". Annu. Rev. Cell Dev. Biol. 12, pp. 575-625, 1996.
- E.J. Bowman, A. Siebers, and K. Altendorf, "Bafilomycins: a class of inhibitors of membrane ATPases from microorganisms, animal cells, and plant cells," *Proc Natl Acad Sci USA*, 85, pp. 7972-7976, 1988.
- 12 C.J. Swallow, S. Grinstein, and O.D. Rotstein, "A vacuolar type H<sup>+</sup>-ATPase regulates cytoplasmic pH in murine macrophages," *J Biol Chem*, 265, pp. 7645-7654, 1990.
- 13. A. Bidani and S.E. Brown, "ATP-dependent pH<sub>i</sub> recovery in lung macrophages: evidence for a plasma membrane H(+)-ATPase," *Am J Physiol*, 259, pp. C586-C598, 1990.
- 14. A. Nanda, A. Gukovskaya, J. Tseng, S. Grinstein, "Activation of vacuolar type proton pumps by protein kinase C. Role in neutrophil pH regulation," *J Biol Chem*, 267, pp. 22740-22746, 1992.
- 15. H.K. Vaananen, E.-K. Karhukorp, K. Sundquist, B. Wallmark, I. Roinen, T. Hentunen, J. Tuukkanen, and P. Lakkakorpi, "Evidence for the presence of a proton pump of the vacuolar H<sup>+</sup>-ATPase type in the ruffled borders of osteoclasts," *J Cell Biol*, 111, pp. 1305-1311, 1990.
- 16. T. Nordstrom, O.D. Rotstein, R. Romanek, S. Asotra, J.N.M. Heersche, M.F. Manolson, G.F. Brisseau, and S. Grinstein, "Regulation of cytoplasmic pH in osteoclasts. Contribution of proton pumps and a proton-selective conductance," *J Biol Chem*, 270, pp. 2203-2212, 1995.
- 17. R. Martínez-Zaguilán, R.M. Lynch, G.M. Martínez, R.J. Gillies, "Vacuolar-type H<sup>+</sup> ATPases are functionally expressed in plasma membranes of human tumor cells," *Am J Physiol*, 265, pp. C1015-C1029, 1993.
- 18. R. Martínez-Zaguilán, E.A. Seftor, Y.-W.Chu, M.J.C. Hendrix, and R.J. Gillies, "Acidic pH enhances the invasive behavior of human melanoma cells," *Clin Exp Metastasis*, 14, pp. 176-186, 1996
- 19. J.A. Thomas, R.N. Buchsbaum, A. Zimniak, and E. Racker, Biochemistry, 18:2210-2218, 1979
- 20. R.Y. Tsien, "Fluorescent Indicators of Ion Concentrations," Meth Cell Biol. 30, 127 156, 1989.
- 21. R. Haughland, "Intracellular ion indicators In: Fluorescent and luminescent probes for biological activity. *W.T. Mason ed.*" Academic Press, New York. 1993.
- 22. R. Martínez-Zaguilán, G.M. Martinez, F. Lattanzio, and R.J. Gillies, "Simultaneous measurement of intracellular pH and Ca<sup>2+</sup> using the fluorescence of Snarf-1 and Fura-2 in BALB/c-3T3 cells," *Am. J. Physiol.* 260, pp. C297-C307, 1991.
- 23. R. Martínez-Zaguilán, G. Parnami, and R.M. Lynch, "Selection of fluorescent ion indicators for simultaneous measurements of pH and Ca<sup>2+</sup>," *Cell Calcium.* 19, pp. 337-349, 1996.
- J. Liu, Z. Diwu, and D.H. Klaubert, "Fluorescent molecular probes III. 2',7'- BIS- (3-carboxypropyl)
   -5-(and-6)-carboxyfluorescein (BCPCF): A new polar dual-excitation and dual-emission pH indicator with a pK<sub>a</sub> of 7.0," *Bioorg Med Chem Lett*. 7, pp.3069-3071, 1997.
- 25. G.H. Patterson, S.M. Knobel, W.D. Sharif, S.R. Kain, and D.W. Piston, "Use of green fluorescent protein and its mutants in quantitative fluorescence microscopy," *Biophys. J.* 73, pp. 2782-2790, 1997.
- 26. M. Kneen, J. Farinas, and A.S. Verkman, "Green fluorescent protein as a noninvasive intracellular pH indicator" *Biophys. J.* 74, pp. 1591-1599, 1998.
- 27. G. Miesenböck, D.A. De Angelis, and J.E. Rothman, "Visualizing secretion and synaptic transmission with pH-sensitive green fluorescent proteins," *Nature*. 394, pp 192-195, 1998.
- 28. W.W. Ward, In: *Bioluminescence and Chemiluminescence* (eds. DeLuca, M.A. & McElroy, W.D.). Academic Press, New York. 1981.
- 29. J.D. Rojas, S. Sanka, S. Gyorke, D.E. Wesson, A. Minta, and R. Martinez-Zaguilan. "Intracellular pH (pH<sup>in</sup>) and Cytosolic Calcium ([Ca<sup>2+</sup>]<sup>cyt</sup>) Regulation via ATPases: Studies in Cell Populations, Single Cells and Subcellular Compartments". *Proc. Int. Soc. Opt. Engin.*, *SPIE* 3600, pp. 51-63.

- 30. Piston DW. Patterson GH. Knobel SM. "Quantitative imaging of the green fluorescent protein (GFP)". *Methods in Cell Biology*. 58, pp. 31-48, 1999.
- 31. Pepperkok R. Squire A. Geley S. Bastiaens PI. "Simultaneous detection of multiple green fluorescent proteins in live cells by fluorescence lifetime imaging microscopy". *Curr. Biol.*. 9, pp. 269-72, 1999
- 32. Beavis AJ. Kalejta RF. "Simultaneous analysis of the cyan, yellow and green fluorescent proteins by flow cytometry using single-laser excitation at 458 nm". *Cytometry*. 37, pp. 68-73, 1999
- 33. Matz MV. Fradkov AF. Labas YA. Savitsky AP. Zaraisky AG. Markelov ML. Lukyanov SA "Fluorescent proteins from nonbioluminescent Anthozoa species". *Nature Biotechnol.*, 17, pp. 969-73, 1999
- 34. Gordon GW. Berry G. Liang XH. Levine B. Herman B. "Quantitative fluorescence resonance energy transfer measurements using fluorescence microscopy". *Biophys. J.* 74, pp. 2702-13, 1998..
- 35. Sagot I. Bonneu M. Balguerie A. Aigle M. "Imaging fluorescence resonance energy transfer between two green fluorescent proteins in living yeast". *FEBS Letters*. 447, pp. 53-7, 1999
- 36. R. Martínez-Zaguilán, M.W. Gurule, and R.M. Lynch, "Simultaneous measurement of intracellular pH and Ca<sup>2+</sup> in insulin- secreting cell lines by spectral imaging microscopy," *Am.J.Physiol.* 270, pp. C1438-C1446, 1996.
- 37. Martínez-Zaguilán R., Raghunand N., Lynch R.M., Bellamy W., Martinez G.M., Rojas B., Smith D., Dalton W.S., and Gillies R.J. "pH and drug resistance I: Plasmalemmal V-type H\*-ATPase is functionally expressed in drug resistant human breast cancer cell lines". *Biochem Pharmacol.*, 57, pp. 1037-1046, 1999.
- 38. Gotessman M.M., Pastan I. "Biochemistry of multidrug resistance mediated by the multidrug transporter." *Annu. Rev. Biochem.*, 62, pp. 385-427, 1993.
- 39. Horwitz S.B. "Mechanism of action of taxol". Trends Pharmacol. Sci., 13, pp.134-136, 1992.
- 40. Dumontet C., and Sikic B.I.. "Mechanisms of action of and resistance to antitubulin agents: microtubule dynamics, drug transport, and cell death". *J. Clin. Oncol.*, 17, pp.1061-1070. 1999.
- 41. Roepe P.D., Weisburg J.H., Luz J.G., Hoffman M.M., and Wei L.-Y. "Novel Cl<sup>-</sup> dependent intracellular pH regulation in murine MDR1 transfectants and potential implications". *Biochemistry*, 33, pp. 11008-11015, 1994.
- 42. Vukovic V., and Tannock I.F. "Influence of low pH on cytotoxicity of paclitaxel, mitoxantrone and topotecan". *Br. J. Cancer*, 75, pp. 1167-1172, 1997.
- 43. Raghunand N., Martínez-Zaguilán R., Wright S.H., and Gillies R.J. pH and drug resistance II: turnover of acidic vesicles and resistance to weakly basic chemotherapeutic drugs. *Biochem Pharmacol.*, 57, pp.1047-1058, 1999.
- 44. Huizing M.T., Sewberath Misser V.H., Pieters R.C., Ten Bokkel Huinink W.W., Venhoff C.H.N., Vermoken J.B, Pinedo H.M., and Beijnen J.H. Taxanes: a new class of antitumor agents. *Cancer Invest.*, 13, pp. 381-404, 1995.
- 45. Rich IN. Worthington-White D. Garden OA. Musk P. "Apoptosis of leukemic cells accompanies reduction in intracellular pH after targeted inhibition of the Na(+)/H(+) exchanger". *Blood*, 95:1427-1434, 2000
- 46. Sarasin A. "The molecular pathways of ultraviolet-induced carcinogenesis". *Mutation Research.* 428, pp. 5-10, 1999
- 47. Schwarz T. "UV light affects cell membrane and cytoplasmic targets". *J. Photochem. Photobiol. B Biology.* 44, pp. 91-6, 1998
- 48. B.R. Masters and B. Chance. Redox confocal imaging: Intrinsic fluorescent probes of cellular metabolism. In: "Fluorescent and Luminescent Probes for Biological Activity". W.T. Mason, Ed. Academic Press, pp. 44-57,1993
- 49. J.R. Lakowicz. "Principles of Fluorescence Spectroscopy" Plenum Press, New York, 258-297, 1983.

## Study for usefulness of Indocyanine green as an infrared marker

Yuko Fukami, Manabu Heya and Kunio Awazu Institute of Free Electron Laser, Graduate School of Engineering, Osaka University 2-9-5 Tsuda-yamate, Hirakata, Osaka 573-0128, Japan

#### **ABSRTACT**

Indocyanine green (ICG) is widely used as a tracer for the non-invasive estimation of liver function. ICG has properties of binding with plasma protein, and has a large absorption peak at 805 nm. There were no reports, however, about the IR absorption peak of ICG at 7.1  $\mu$ m, which absorption coefficient amounts to ~13000 cm<sup>-1</sup>. In this study, ICG was exposed to free electron lasers (FELs) with wavelength of 7.1  $\mu$ m and usefulness of ICG as an IR-marker was discussed. ICG film sample was formed on IR-transparent BaF<sub>2</sub> crystal substrate and exposed to FELs with the wavelength of 7.1 $\mu$ m. After exposure, the sample was analyzed by FT-IR and film thickness measurements. As results, ICG ablated with the FEL of the power density of more than 5 W/cm<sup>2</sup> (=P<sub>dth</sub>), and that the molecular structure of ICG was still stable for the power density of less than P<sub>dth</sub>, 3 W/cm<sup>2</sup>. Therefore, ICG can be considered as a novel infrared marker (IR marker) to the living tissue which absorbs FEL photon energy without changing the IR absorption peak.

Keywords: free-electron laser (FEL), indocyanine green (ICG), photodynamic therapy (PDT), Infrared marker (IR marker)

#### 1. INTRODUCTION

Indocyanine green, ICG [1], which is stable when it binds with plasma protein and further to irradiation of visible and near infrared light, is the reagent widely used in clinical examinations of liver function [2-10]. ICG can be used as an sensitive absorber for vascular surgery or ophthalmology. However, conventional application used only properties in near infrared region, and there has been no researches in mid infrared, molecular vibrational energy region. We have suggested that the method to excite molecular vibrations with wavelength tunable free-electron lasers, FEL, is useful in biomedical fields [8]. This method is to excite certain target selectively to remove by FEL irradiation corresponding to absorption of special vibration mode in the target molecule. The target material must have strong absorption peaks in, which do not overlap those of other materials existing together.

On the other hand, IR marker is a reagent, which has characteristic absorption peak and a property binding to a specific molecule. Materials without appropriate absorption in mid IR region can be the targets of IR-PDT (photodynamic therapy) with these markers. A certain appropriate IR marker bind to aimed material to make it target materials, which absorb lasers to be detected, heated and removed via the IR markers. Further, with FELs which can adjust the wavelength of markers' absorption freely and continuously, any reagents which have a property binding to a specific molecule have possibility to be used as IR markers. Thus, FELs can expand potential field applied IR marker and FELs. IR markers must have (1) characteristic absorption peak, (2) a property binding to a specific molecule and (3) stability to IR laser irradiation. It is already known that ICG binds to specific molecule, plasma protein [2,3], which is one of the requests. In this study, we discussed other requests by FEL exposures to ICG and analyses using FT-IR, UV/VIS spectrometry and optical microscope.

fukami@fel.eng.osaka-u.ac.jp; phone +81 072 897 6415; fax +81 072 897 6419; Institute of Free Electron Laser, Graduate School of Engineering, Osaka University, 2-9-5 Tsuda-yamate, Hirakata, Osaka 573-0128, Japan.

#### 2. EXPERIMENTAL

#### 2.1 Material: indocyanine green, ICG

The molecular structure of ICG was shown in Figure 1 [1]. ICG (Daiichi Pharmaceutical Company; Diagnogreeu®) of 25mg was solved into 10ml water and volume of 10ul was dropped onto a BaF<sub>2</sub> crystal substrate. After water vaporization, a thin film of ICG was formed.

#### 2.2 FEL exposure

ICG films were exposed to FELs in air at room temperature. Changes of exposed area were monitored using optical microscope in real time (Figure 2). The FEL wavelengths were 7.1 and 7.9 µm which were absorbed by ICG strongly and weakly, respectively. The FEL power was adjusted not to damage, ablation or carbonization, on the sample surface. Exposure conditions were summarized in table 1.

Table 1 FEL exposure conditions

Wavelength, λ (μm)	7.1	7.9
Average power, P (mW)	2.5	1.5
Exposed area, S (cm <sup>2</sup> )	$0.9 \times 10^{-3}$	$0.5 \times 10^{-3}$
Power density, P <sub>d</sub> (W/cm <sup>2</sup> )	3.0	3.0
Exposed time, t (s)	10 60 300	10

#### 2.3 Measurements

UV/VIS absorption spectra of ICG solution were measured by UV/VIS spectrometer (Hitachi; U-3500). Before and after FEL exposure, IR absorption spectra and thickness of ICG film samples were measured by FT-IR spectroscope (Horiba; FT-520) and surface profile analyzer (Veeco; Dektak3). ICG film sample was heated from room temperature to 300 °C, and changes were monitored with optical microscope.

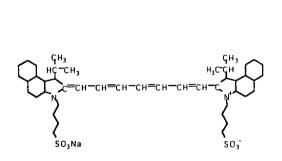


Figure 1 Structural formula of indocyanine green (ICG).

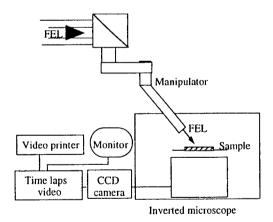


Figure 2 FEL exposure system onto the microscope. The FEL beam directed to an optical microscope through a multi-joint cylindri cal tube. A sample was placed on an inverted microscope stage and the changes caused by FELs were monitored continuously by a CCD camera in real time.

#### 3. RESULTS

#### 3.1 Sample Characeristics

#### UV to IR spectrum

ICG solution with solvent of water has absorption peaks at 0.71 and 0.78  $\mu$ m in visible light region (Figure 3). It is known that the absorption peaks shift to 0.805 $\mu$ m in plasma protein. In this study, we discussed optical properties in midinfrared light region. IR absorption spectrum of ICG film sample was shown in Figure 4. Large absorption peak which corresponds to CH<sub>2</sub> bending vibration was observed at 7.1 $\mu$ m. At this 7.1 $\mu$ m-wavelength, the absorption coefficient of the sample ( $\mu$ <sub>a</sub>) was calculated to be about 13000cm<sup>-1</sup> from absorbance and film thickness.

On heating, ICG film sample was not changed from room temperature to 250 °C in both of the structure and the amount, and turned to brown because of carbonization at 250 °C.

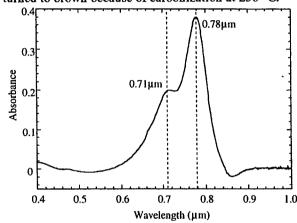


Figure 3 UV/VIS absorption spectrum of ICG solution with solvent of water. An overlap of broad absorption peaks was observed.

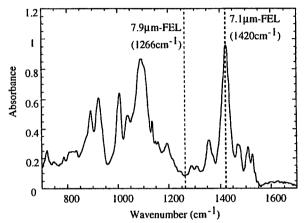


Figure 4 IR absorption spectrum of ICG. Dotted lines indicate the FEL wavelengths employer in this experiments. The wavelength of 7.1  $\mu$  m is corresponds to sharp absorption peak at 1420cm<sup>-1</sup>.

#### 3.2 FEL exposure effects

#### Observation by optical microscope

The threshold of FEL power density,  $P_{dth}$ , for ablation and carbonization varied depending on exposed wavelength. The values of  $P_{dth}$  were 5 and 14 W/cm<sup>2</sup> at 7.1 and 7.9  $\mu$ m, respectively.

On the sample surfaces exposed to FEL of 7.1  $\mu$ m at lower power density than  $P_{dth}$ , 3mW, the edges of exposed area were stamped. Further, bubble formations were observed at some exposed areas as shown in Figure 5. On the other hand, on the sample surfaces exposed to FEL of 7.9  $\mu$ m at lower power density than  $P_{dth}$ , 3mW, no changes were observed. Changes of IR absorption spectra

IR absorption spectra of the sample exposed to FEL of 7.1 µm for 10, 60 and 300 sec were shown in Figure 6. The ratios of absorbance of before and after FEL exposure were summarized in Table 2. Each absorption peaks decreased by similar ratio as the increase of the exposure time.

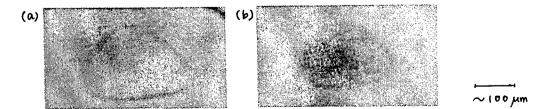


Figure 5 Observation of FEL exposed area through an optical microscope. Edges of the exposed areas were stamped on the surface (a), further, bubbles were formed in some samples (b).

Table 2 Ratio of IR absorbance before and after exposure of 7.1µm-FELs

Exposed time, t (s)	10	60	300
at 719cm <sup>-1</sup>	0.5	0.4	0.4
at 926cm <sup>-1</sup>	0.5	0.4	0.3
at 1007cm <sup>-1</sup>	0.5	0.4	0.3
at 1090cm <sup>-1</sup>	0.5	0.4	0.4
at 1420cm <sup>-1</sup>	0.4	0.4	0.3

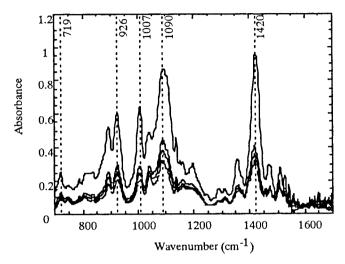


Figure 6 IR absorption spectra of ICG before and after FEL exposure of 7.1µm-FELs. Dotted lines indicate the wavelength of main absorption peaks. Table 3 summarizes the ratio of IR absorbance before and after exposure. All absorption peaks decreased similarly after FEL exposures.

#### Change of the sample thickness

Conditions of 7.1µ m-FEL exposures, changes of absorbance at 7.1 µm (1420cm<sup>-1</sup>) and sample thickness were summarized in Table 3. After FEL exposure of 7.1 µm and 3 W/cm<sub>2</sub>, the sample thickness decreased.

Table 3 Change of thickness and absorbance at 1420cm<sup>-1</sup> of ICG films exposed to FELs (7.1μm, 3.0W/cm<sup>2</sup>)

Change of thickne	ss (μm), (ratio%)	Change of absorbance at 1420cm <sup>-1</sup>	Microscopic observation
0.42 → 0.38	(90%)	$0.51 \rightarrow 0.31  (61\%)$	bubble formation
0.17 → 0.14	(83%)	$0.35 \rightarrow 0.26 (74\%)$	
0.30 → 0.22	(73%)	0.43 → 0.30 (70%)	
0.32 → 0.23	(72%)	0.47 → 0.33 (70%)	
0.92 → 0.73	(78%)	0.96 → 0.41 (43%)	bubble formation
0.89 → 0.56	(62%)	$0.96 \rightarrow 0.36  (38\%)$	bubble formation
0.99 → 0.56	(50%)	0.96 → 0.32 (33%)	bubble formation

#### 4. DISCUSSIONS

#### 4.1 Usefulness as an IR marker

As shown in Figure 6 and Table 2, IR absorbance decreased after FEL exposure while the shapes (ratios between peaks) of IR spectra did not change. This indicates that FEL exposure did not induced structural change but decrease of the amount of ICG. It was considered that ICG is stable chemically with 7.1 $\mu$ m-FEL exposure of the power density lower than threshold for ablation (i.e.  $P_d > P_{dth}$ ), and that during the Exposure temperature of the sample was lower than carbonization point, 250 °C.

These observations indicates that ICG seems to be useful as IR marker because of the properties (1) binding to the target molecule (plasma protein), (2) absorbing mid IR light strongly (at 7.1µm, 13000cm-1) and (3) keeping structural stableness.

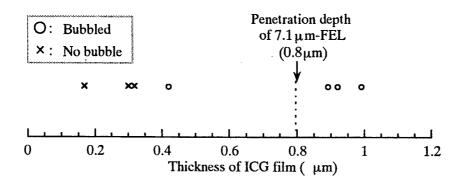


Figure 7 Plot of ICG film thickness before 7.1  $\mu$  m-FEL exposures and microscopic observation results during the exposures. The thickness of the bubbled samples was more than penetration depth of 7.1  $\mu$  m-FEL, 0.8 $\mu$  m.

By using ICG as IR marker, the target molecule, plasma protein, with ICG can be characterized and detected by large absorption at 7.1µm light, and further heated and removed with the light absorption. As such, materials with no characteristic absorption at appropriate wavelength in mid IR region can be the targets for mid-IR PDT. Particularly due to quite large absorbance of ICG at 7.1 µm which is hundreds or thousands times as large as those of typical components included in tissue, water, protein and lipid, selective light absorption can be effective for target materials via marker only.

#### 4.2 Mechanism of bubble formation

On some of sample surfaces exposed to FEL of 7.1 µm bubble formations were observed at some exposed areas. FEL exposed samples could be divided into two groups, according to whether bubble was formed or not, and the elements in each group had common tendencies: While the bubble group (1) had thickness of more than 0.4 µm before FEL exposure and (2) showed less decrease in thickness than in absorbance after FEL exposure, the no bubble group (1') had thickness of less than 0.3 µm, (2') showed comparable decrease in thickness and absorbance and (3') was stamped edge of exposed area.

It is considered that the bubble group did not decreased in thickness so much as in absorbance because the volume of the bubbles kept thickness during exposure. In the exposed area of thick samples much energy of FEL are absorbed to induce bubble formation inside.

The penetration depth (:  $\delta = 10000/\mu_a$  [µm]) of ICG for the light of 7.1µm-wavelength is approximately 0.8 µm. This value and thickness of the samples were summarized in Figure 7. There is a tendency that in the samples with thickness more than penetration depth FEL induced bubble formation. It is considered that following process occurred to form bubbles in the 'thick' sample films of ICG made from ICG solution with solvent of water: (1) Incident FEL energy was absorbed by ICG in nearly whole, (2) the temperature of the exposed area achieved boiling point of water, 100 °C, and (3) water vaporized explosively to form bubbles, and the exposed area seems to have kept the temperature lower than 100 °C during this process.

From these discussions, it is considered that ICG has possibility to be used in PDT as absorber of laser energy to limit the exposure area in depth. The method to control transmittance using light absorption properties of ICG without risk of caving is being researched in the near IR region and the effects have been reported [11,12]. The method of vaporization surgery is already applied to digestive organs, stomach and intestines, to expose NIR laser (805 nm in wavelength) to the surface of the organs injected ICG under the mucous [13,14]. Here we suggest the usefulness of ICG in the mid IR region in addition to that in near IR region, that 0.8µm-thick ICG can shield 7.1µm-wavelength-light which is transmit to deeper area. And due to absorbance of ICG at 7.1µm much larger than those of typical tissue components, water, protein and lipid, only a little amount of ICG can absorb laser light strongly to work as absorber.

#### 5. CONCLUTIONS

In this study, ICG was exposed to free electron lasers (FELs) with wavelength of 7.1  $\mu$ m and usefulness of ICG as an IR-marker was discussed. As results, ICG ablated with the FEL of the power density of more than 5 W/cm<sup>2</sup> (=P<sub>dth</sub>), and that the molecular structure of ICG was still stable for the power density of less than P<sub>dth</sub>, 3 W/cm<sup>2</sup>. Therefore, ICG can be considered as a novel infrared marker (IR marker) to the living tissue which absorbs FEL photon energy without changing the IR absorption peak.

#### **ACKNOWLEDGEMENTS**

We would like to thank S. Kuma and M. Tanaka at Mitsubishi Electric System & Service, Co., Ltd. for their skilful help in providing the FEL.

#### REFERENCES

- [1] I.J.Fox, L.G.S.Brooker, D.W.Heseltine: Fed Proc 16 (1957) 39.
- [2] T.Namihisa, K.Minabe, K.Iijima: Liver 5 (1963) 114.
- [3] Meeting of Japanese Pathology in Gastroenterology: Journal of Japan Gastroenterology 70 (1969) 573.
- [4] N.K.Takaki, C.W.Mathews, J.P.Semmens: Obstetrics and Gynecology 30 (1967) 220.
- [5] Y.Ishigami, M.Masuzawa, Y.Shinoyama, E.Satoh, M.Akiyama, M.Katoh, A.Terada, T.Okuyama, K.Tamura, A.Fukui, Y.Abe, M.Hatanaka, M.Kanda, K.Awazu, Y.Tanaka, M.Taniguchi: Medicine and therapy 16 (1988) 47.
- [6] K.Awazu, Y.Yokoi, S.Watanabe, T.Komada, A.Miyazaki, T.Namihisa: Liver 30 (1989) 1698.
- [7] K.Awazu, H.Matsubara, S.Tanba, K.Tomida, Y.Yotsuya, M.Osawa, Y.Miyagawa, J.Kurihara: Sumitomo Electronics 139 (1991) 1.
- [8] K.Awazu, A.Nagai, K.Aizawa: Lasers in Surgery and Medicine 23 (1998) 233.
- [9] C.M.Leevy, F.Smith, J.Longueville, G.Paumgartner, M.M.Howard: JAMA 200 (1967) 148.
- [10] M.L.J.Landsman, G.Kwant, G.A.Mook, W.G.Zijlstra: Journal of Applied Phisiology 40 (1976) 575.
- [11] T.Hayashi, T.Arai, M.Hino, N.Nakamura, M.Masuda, M.Kikuchi, H.Suzuki: Proceedings of 18th Meeting of Japan Society for Laser Surgery and Medicine (1997) 37.
- [12] S.Tokonabe, Y.Omichi, T.Hayashi, T.Arai, M.Kikuchi, H.Nakajima, M.Hayakawa, H.Nakamura: Proceedings of 18th Meeting of Japan Society for Laser Surgery and Medicine (1997) 149.
- [13] T.Hayashi, T.Arai, H.Tajiri: Proceedings of 16th Meeting of Japan Society for Laser Surgery and Medicine (1995) 349.
- [14] T.Hayashi, T.Arai, M.Kikuchi, K.Hino, M.Masuda, H.Sizuki: Proceedings of 17th Meeting of Japan Society for Laser Surgery and Medicine (1996) 103.

## **Addendum**

[4259-01]	Low-light imaging spectroscopy with standard video cameras R. H. Cormack, Chameleon Optics, Inc. (USA)
[4259-06]	Multivariate methods applied to hyperspectral FT-IR imaging for quantitative analysis  D. M. Haaland, F. W. Koehler, M. C. Celina, Sandia National Labs. (USA)
[4259-16]	Development of spectral color banding (SCAN) analysis and its application to cytogenetic analysis  N. Kakazu, Kyoto Prefectural Univ. of Medicine (Japan); I. Bar-Am, Spectral Imaging Ltd. (Israel); S. Hada, Kyoto Prefectural Univ. of Medicine (Japan)
[4259-24]	Highly sensitive detector with phased-array NIR systems B. Chance, Univ. of Pennsylvania (USA)
[4259-25]	Imaging cancer in vivo using optical markers in animal and human subjects D. A. Benaron, Stanford Univ. (USA)
[4259-27]	Three-dimensional localization of tissue volumes using near-infrared excitable fluorescent contrast agents E. M. Sevick-Muraca, Texas A&M Univ. (USA)
[4259-28]	In-vivo activatable optical probes for molecular imaging U. Mahmood, Massachusetts General Hospital (USA)
[4259-29]	Lanthanide chelates as topical agents for early disease detection D. J. Bornhop, S. Roberts, J. Griffin, T. S. Goebel, Texas Tech Univ. (USA); M. Motamedi, B. A. Bell, Univ. of Texas Medical Branch at Galveston (USA)
[4259-30]	Design of cyanine dye-based optical contrast agents: comparison of in-vivo imaging properties of highly hydrophilic contrast agents and receptor-targeted peptide contrast agents  K. Licha, M. Bauer, Freie Univ. Berlin (Germany); C. Hessenius, C. Groetzinger, Univ. Charite (Germany); U. Sukowski, B. Ebert, Physikalisch-Technische Bundesanstalt (Germany)
[4259-32]	Local field fluorescence microscopy: a new window for cardiac physiology (calcium and membrane potential indicators)  A. Escobar, Texas Tech Univ. Health Sciences Ctr. (USA)
[4259-33]	Glucose metabolism dynamics: insulin secretion using nonlinear laser microscopy D. W. Piston, Vanderbilt Univ. (USA)

[4259-34]	Surface pH measurements in epithelial cells by confocal and multiphoton microscopy M. H. Montrose, Indiana Univ. (USA)
[4259-38]	Adding another dimension to laser scanning microscopy implemented on a Zeiss LSM 510 G. Weiss, R. Wolleschensky, Carl Zeiss Jena GmbH (Germany)

### **Author Index**

Achilefu, Samuel A., 110, 129 Agrawal, Anant, 68 Attas, Michael, 75 Awazu, Kunio, 157 Bambot, Shabbir B., 68 Bar-Am, Irit, Addendum Bauer, Michael, Addendum Bell, Brent A., Addendum Benaron, David A., Addendum Bornhop, Darryl J., Addendum Bueeler, Michael, 22 Bugaj, Joseph E., 110, 129 Busch, Christian, 144 Celina, Mathias C., Addendum Chance, Britton, Addendum Claus, Richard O., 29 Conner, S., 29 Cormack, Robert H., Addendum Davis, Daniel M., 92 Deutsch, Thomas F., 115 DiFranco, Marino, 133 Dorshow, Richard B., 110, 129 Ebert, Bernd, Addendum Escobar, Ariel, Addendum Faupel, Mark, 68 Ferris, Daron, 68 Fukami, Yuko, 157 Gabbard, Joseph, 24 Gillenwater, Ann, 22 Glynn, Thomas J., 102 Goebel, Timothy S., Addendum Gollahon, Lauren S., 144 Griffin, John, Addendum Groetzinger, Carsten, Addendum Haaland, David M., Addendum Hada, Satoshi, Addendum Haka, Abigail S., 47 Hamblin, Michael R., 115 Harrell, Tim, 68 Harvey, Andrew R., 16 Hasan, Tayyaba, 115 Heintzelman, Douglas L., 22 Herman, Petr, 8 Hessenius, Carsten, Addendum Hewko, Mark D., 36 Heya, Manabu, 157 Hirose, Sachiko, 60 Jansen, E. Duco, 85 Jimenez, Hermo N., 110, 129 Kakazu, Naoki, Addendum Kerndrup, Gitte B., 56 Kidder, Linda H., 47 Koehler, Frederick W., Addendum Leonardi, Lorenzo, 36 Levenson, Richard M., 1

Lewis, E. Neil, 47 Licha, Kai, Addendum Lin, Wei-Chiang, 85 Mahadevan-Jansen, Anita, 85 Mahmood, Umar, Addendum Malak, Henryk M., 8 Mantsch, Henry H., 36, 75 Martinez, Gloria M., 144 Martínez-Zaguilán, Raul, 144 Matas, Anna, 36 Meissner, Ken E., 24, 29 Miller, Peter J., 1, 16 Mongin, J. David, 85 Montrose, Marshall H., Addendum Moore, Wayne E., 8 Morrison, John J., 102 Motamedi, Massoud, Addendum Niwa, Shinichirou, 60 Novo, David, 133 Okumura, Ko, 60 Oomman, Sowmini K., 144 Payette, Jeri R., 36 Pedersen, Rikke K., 56 Pedrotty, Dawn, 85 Petrášek, Zdeněk, 92 Phillips, David, 92 Piston, David W., Addendum Posthumus, Trevor, 75 Power, Sarah, 102 Preiss, Birgitte S., 56 Rajagopalan, Raghavan, 110, 129 Richards-Kortum, Rebecca R., 22 Roberts, S., Addendum Ryder, Alan G., 102 Schattka, Bernhard J., 36, 75 Schmidt, Michelle A., 129 Sevick-Muraca, Eva M., Addendum Shafer, Keri, 144 Shaw, Maurice A., 24 Shirai, Toshikazu, 60 Siegel, Jan, 92 Smith, S. C., 29 Soukos, N. S., 115 Sowa, Michael G., 36, 75 Spillman, William B., Jr., 24, 29 Suhling, Klaus, 92 Sukowski, Uwe, Addendum Tsurui, Hiromichi, 60 Utzinger, Urs, 22 Vecer, Jaroslav, 8 Vergara, Julio L., 133 Webb, Elizabeth G., 129 Weiss, Georg, Addendum Wolleschensky, Ralf, Addendum Zhang, Shuliang L., 75